Studies in Using Gold Nanoparticles in Treating Cancer and Inhibiting Metastasis

A Dissertation
Presented to
The Academic Faculty

by

Yue Wu

In Partial Fulfillment
of the Requirements for the Degree
Doctor of Philosophy in the
School of Chemistry and Biochemistry

Georgia Institute of Technology
May 2019

Studies in Using Gold Nanoparticles in Treating Cancer and Inhibiting Metastasis

Approved by:

Dr. Mostafa A. El-Sayed, Advisor
School of Chemistry and Biochemistry
Georgia Institute of Technology

Dr. Robert Dickson
School of Chemistry and Biochemistry
Georgia Institute of Technology

Dr. Ingeborg Schmidt-Krey
School of Chemistry and Biochemistry
Georgia Institute of Technology

Dr. Zhong Lin Wang
School of Material Science and Engineering
Georgia Institute of Technology

Dr. Ronghu Wu
School of Chemistry and Biochemistry
Georgia Institute of Technology

Date Approved: March 26, 2019

To My Family

ACKNOWLEDGEMENTS

First, I would like to thank my advisor, Prof. Mostafa A. El-Sayed, for his guidance, encouragement, support, sharing with me his life-long enthusiasm and dedication towards scientific research, and the opportunity he provided me to move into the nanotechnology and nanomedicine field. His optimistic, positive, modest, and humorous personality is always inspiring me. I would also like to acknowledge the professors during my PhD time, including Prof. Ning Fang, for his guidance of optical imaging and great support for my research, Prof. Todd Sulchek for his help with cell mechanical measurement, Profs. Ronghu Wu, Fangjun Wang, and Facundo Fernandez for their help with mass spectrometry based proteomics and metabolomics, Profs. Ivan El-Sayed and Dong Shin for their guidance on animal work or clinical applications, and Prof. Michelle Dawson for her guidance on cytoskeleton and cell migration. I would like to express gratitude to my thesis committee members — Profs. Ingeborg Schmidt-Krey, Ronghu Wu, Robert Dickson, and Zhong Lin Wang — your encouragement, support, and valuable discussions are very much appreciated.

Second, I am very grateful to have the chance to work with some really talented postdocs and students during the past several years. I would like to especially acknowledge Dr. Moustafa Ali, for his great knowledge and skills that he shared with me and his continuous guidance and support. I am very grateful to have worked with him throughout my entire Ph.D. program. I also would like to thank Dr. Kuangcai Chen for his help with differential interference contrast microscopy, Dr. Bin Dong for his help with Stochastic Optical Reconstruction Microscopy (STORM), Drs. Tiegang Han and Yan Tang for their help in bioinformatics analysis, Drs. Haopeng Xiao, Jin Chen, and Xiaoling Zang for their help with mass spectrometry

measurements, Dr. Deepraj Ghosh for his help with cell migration assays, Mr. Brian Do for atomic force measurement, Ms. Sommer Durham for flow cytometry trainings, and Dr. Eric Snider for his help in Western-blot analysis. In addition, I would like to thank all the undergraduate research assistants that were working with me in time order— Kamillah Kassam, Savita Chapman, Sarah Ghalayini, Tessneem Belhadj Yahya, Mostafa Ayman Riad Nasser, Cassidy Tobin, Cecily Ritch, Arusha Siddiqa, Tsion Assaye, Sreenath Raparti, Ahmed Amer, Samuel Nelson, Shreyas Krishnapura, Hashem Mohilldean, Kamaria Dansby, Ziyan Wu, Paige Warner, and Arfa UI-Haque, etc — it has been a pleasure working with you and I wish you all the best moving forward. My labmates, Dr. Sajanlal R. Panikkanvalappil, Mr. Mohammadreza Nazemi, Dr. Xiongwu Kang, Dr. Nasrin Hooshmand, Dr. Cheng Xu, Dr. Hongje Jang, *etc* — thanks for your support and help. I'd also like to thank Ms. Michele Yager, Dr. Kenyatta Johnson, Ms. Tracy Johns, and Mr. Mike Riley for their help for administration, fund applications, and guidance in my PhD program.

Lastly, I would also like to give my special acknowledgements to my family. Mom and Dad, thank you for raising me and Hao, teaching us to work hard and help people, inspiring me to realize my potential and encouraging me to achieve my dreams. My husband, Xiao, thank you for your great understanding, love, patience, and support for my life and work. I feel very lucky to have met you in Georgia Tech. I also thank all my friends. Without your great help and support over the years, none of this would ever have happened.

TABLE OF CONTENTS

LIST OF TABLES

LIST OF FIGURES

LIST OF SYMBOLS AND ABBREVIATIONS

3D: three-dimensional

AFM: Atomic force microscopy

ANOVA: analysis of variance

AuNCs: gold nanoclusters

AuNCSs: gold silica nano core-shells

AuNPs: Gold nanoparticles

AuNRs: Gold nanorods

AuNSs: Gold nanospheres

BAX: Bcl-2-associated X protein

BRIGHTs: bi-layered Raman-intense gold nanostructures with hidden tags

BSA: bovine serum albumin

CAFs: cancer-associated fibroblasts

CSCs: cancer stem cells

CTAB: cetyl trimethylammonium bromide

CW: continuous-wave

DF: dark field

DIC: differential interference contrast microscopy

DMEM: Dulbecco's modified Eagle's medium

DNA-PAINT: DNA points accumulation for imaging in nanoscale topography

E-cadherin: epithelial cadherin

ECM: extracellular matrix

FAK: focal adhesion kinase

FBS: fetal bovine serum

FCM: Flow cytometry

FCS: fluorescence correlation spectroscopy

FSC: Forward scattering channel

HEPES: 4-(2- hydroxyethyl)-1-piperazineethanesulfonic acid

HSC-3: human oral squamous cell carcinoma cells

ICP: inductively coupled plasma

iLSRM: integrated light sheet super-resolution microscopy

iSCAT: interferometric scattering

LSPR: localized surface plasmon resonance

MOONs: modulated optical nanoprobes

mPEG-SH: methoxypolyethylene glycol thiol

MS: Mass spectrometry

MT: microtubule

N-Cadherin: neural-cadherin

NIR: near infrared

NLS: nuclear localization signal

OCT: optical coherence tomography

ODLM: orientation-dependent localization microscopy

PA: photoacoustic imaging

PBS: phosphate buffer saline

PDT: photodynamic therapy

PEF: plasmon enhanced fluorescence

PI: propidium iodide

PPTT: plasmonic photothermal therapy

PRET: plasmon resonance energy transfer

QDs: quantum dots

RGD: Arg-Gly-Asp peptides

RPLC: reversed-phase liquid chromatography

SERS: surface-enhanced Raman scattering

SLN: sentinel lymph node

SPORT: single particle orientation and rotational tracking

SPR: surface plasmon resonance

SPT: single particle tracking

SSC: Side scattering signals

STORM: stochastic optical reconstruction microscopy

TAM: tumor associated macrophage

TEM: transmission electron microscopy

Ti-IMAC: titanium (IV) based immobilized metal ion affinity chromatography

TIR: total internal reflection

TME: tumor microenvironment

TPI: two-photon imaging

UPLC-MS: ultra-performance liquid chromatography−mass spectrometry

UV−Vis-NIR: ultraviolet-visible-near infrared spectrometer

SUMMARY

Based on statistics from the World Health Organization, cancer is among the top killers in the world. Metastasis, which is the process of cancer cells leaving their primary location and forming secondary tumor(s) in remote places in the body, is responsible for the majority of cancer-related deaths. The current anti-metastasis treatments are rarely effective, therefore, this dissertation aims at developing new techniques of using gold nanoparticles (AuNPs) for cancer treatments and inhibiting metastasis. **Chapter 1** introduces the general background of gold nanoparticles including their synthesis, physical and optical properties, their usage in cancer treatment and their biocompatibility. In **Chapter 2**, we introduce the AuNPs to cancer cells, and use their optical properties as sensing and imaging probes in order to study their impact on cancer cells for diagnosis and treatment. **Chapter 3** focuses on the impact of AuNPs on the mechanical properties of cancer cells for inhibiting cancer cell migration and invasion. **Chapter 4** studies the molecular mechanism of AuNPs treatments in inhibiting cancer cell migration and invasion. After studying the AuNPs impact on cells, the purpose of **Chapter 5** is to check the feasibility of utilizing AuNPs treatments for the inhibition of cancer metastasis in animals. This work differs from the previous studies in two major aspects: **1)** Rational designs of AuNPs to achieve high specificity for inhibiting cancer cell migration and invasion, with a greatly reduced effective AuNP concentration to enhance biocompatibility; **2)** Use of state-to-the-art high resolution microscopy imaging techniques and systematic mass spectrometry-based proteomics to gain deep understanding of the underlying principles involved. Biomechanical properties (such as nuclear stiffness) were also studied for revealing the mechanisms.

INTRODUCTION

Recent advancements in nanomedicine provide new opportunities to avoid some drawbacks of commonly used cancer drugs. Due to their unique properties, nanoparticles can cross biological barriers, enter targeted cells with high selectivity, and function inside cells in a controlled manner. Nanoparticles have shown promise as anti-metastasis drug delivery vehicles targeting invasive or metastatic cancer cells, and they could function as anti-metastatic drugs even without drug loading. The photothermal, optical and mechanical properties of gold nanoparticles (AuNPs), as well as their excellent biocompatibility, make them very useful in cancer treatment. Several groups have studied and observed the AuNPs' effect in attenuating cancer metastasis, however, the development of the AuNPs for effective anti-metastasis effect and the mechanism of how AuNPs treatments inhibit cancer cell migration remains largely unexplored. Therefore, this dissertation is devoted to develop effective therapeutic treatment for cancer and inhibiting metastasis using AuNPs, and to address some fundamental questions of how AuNPs inhibit metastasis.

1.1 Introduction of Gold Nanoparticles

Gold has been a mainstay of science and technology for thousands of years. Gold is a rather non-reactive metal, but when the size is reduced to the nanometer scale, its properties completely change due to the drastic changes in its electron behavior at this length scale [1]. Colloida AuNPs are one of the most stable nanoparticles and present fascinating properties. The use of AuNPs possibly dates back to the 4th or 5th century B.C. in Egypt and China for decoration and medical treatment purposes [2]. One famous example in history is the Roman Lycurgus Cup, which appears green when exposed to reflected light and red to transmitted light

due to the unique properties of AuNPs embedded within the glass. In a well-known lecture by Faraday in1857, a ruby solution of colloidal gold was prepared by reduction of ionic gold in an aqueous solution, and the interaction between AuNPs and light was explored [3]. In the last decade, various methods have been developed for synthesizing AuNPs with different shape and sizes and their optical properties have been extensively explored [4-7]. With the development of gold nanotechnology, AuNPs play important roles in a wide range of fields, from catalysis and energy to biology and medicine [6, 8-10].

The unique properties of AuNPs originate from surface plasmon resonance (SPR). When light is applied to AuNPs at the specific wavelengths, electrons begin to oscillate in resonance with the frequency of light due to the interaction between the electromagnetic field of light and the conduction electrons of AuNPs [11]. The SPR gives AuNPs unique optical properties including their large absorption and scattering cross-sections. The SPR wavelengths of AuNPs are dependent on their size, shape, and local dielectric surroundings. In addition, AuNPs can be easily surface-modified with proteins, peptides, oligonucleotides, and many other compounds, while still maintaining their optical properties. The easy surface modification of AuNPs enables their targeting of specific subcellular locations [12]. Furthermore, one of the greatest attributes of AuNPs that has set them above their metallic particle counterparts is their chemical inertness, and it is because of their low toxicity that AuNPs are often used in biological systems. The above properties, including plasmonic properties, targeting, and bio-compatibility have turned AuNPs into incredibly useful nanomaterials with a wide range of chemical and biological applications [13, 14].

1.1.1 Synthesis of Gold Nanoparticles

AuNPs can be prepared by either “top down” or “bottom up” methods. A “top down” method is a procedure that Au bulk is broke down produce AuNPs with the desired sizes and shapes. On the other hand, a “bottom up” method is a procedure that AuNPs form from individual molecules, by reduction of Au precursor ions. The “bottom up” methods are the most popular methods for AuNPs preparation. In “bottom up” methods, the Turkevich method that prepares citrate-stabilized AuNPs are the most commonly recognized, which was introduced by Turkevich in 1951 [15]. In this reaction, the $HAuCl_4$ solution is boiled, then the sodium citrate solution is quickly added. A wine-red colloidal gold nanosphere suspension is obtained after few minutes. By tuning the ratio of $HAuCl_4$ and sodium citrate, different sizes of gold nanospheres can be prepared (15-150 nm) [16].

To prepare non-spherical (shape controlled, anisotropic) AuNPs, selective growth on specific facets are required. The most common strategy of synthesizing shape controlled AuNPs is based on “seed-mediated growth” [17] through a two-step process. In the first step, small Au seeds (1-5 nm) are generated in a condition of high chemical supersaturation, which leads to fastest nucleation rate to ensure the growth of all crystal facets. In the second step, the reaction conditions are altered to ensure the specific growth in certain facets, with templating molecules and much milder reduction condition, therefore the seeds can grow to large anisotropic AuNPs.

Gold nanorods (AuNRs) draw increasing attention due to their tunable plasmonic propertities, which make them ideal candidates for multiple applications such as solar harvesting, spectroscopy and microscopes, sensing and therapies. AuNRs synthesis is one of the most mature and established protocol among all of the anisotropic AuNPs. The most successful strategy is using a seed-mediated , wet chemical synthesis method (firstly developed by Murphy lab [18]), with the presence of cetyl trimethylammonium bromide (CTAB) which forms the rod-

shaped micelles [19] and Ag^+ that leads to an increase of AuNRs yield and improves upon the control of the aspect ratio [17]. This method has been modified by our lab for extremely high yield of AuNRs (can reach 99%) by using CTAB-capped Au seeds, with the addition of $AgNO_3$ [4]. In addition, we have developed a synthetic route for small AuNRs, a method that produces efficacy in heat conversion and photothermal effect [7].

1.1.2 Physical and Optical Properties of AuNPs

In a metal, such as gold, the electrons are highly delocalized over the space, giving the metal the property of conductivity. When we decrease the size of a noble metal below the free electron path, the movement of the electrons are confined. In the presence of light (which is an oscillating electromagnetic field), the free elections of the metal nanoparticles will oscillate. This process is resonant at a particular wavelength of the light, which is termed from surface plasmon resonance (SPR, **Figure 1.1**). The surface plasmon oscillation decays through radiating ways by scattering light or non- radiating ways such as conversion to heat. Therefore, the AuNPs can act as excellent optical probes or an effective heat generator.

The SPR of AuNPs can be tuned by changing the size, shape, composition and the dielectric constant of the environment. Spherical Au NPs have their SPR peak at about 520-540 nm. The gold nanorods possess two SPR peaks, the transverse and the longitudinal. The transverse SPR peak locates at around 520 nm (**Figure 1.1**). The longitudinal SPR of gold nanorods changes from visible to near infrared (NIR) due to the change of aspect ratio (length of a rod divide by its width), as shown in **Figure 1.2**.

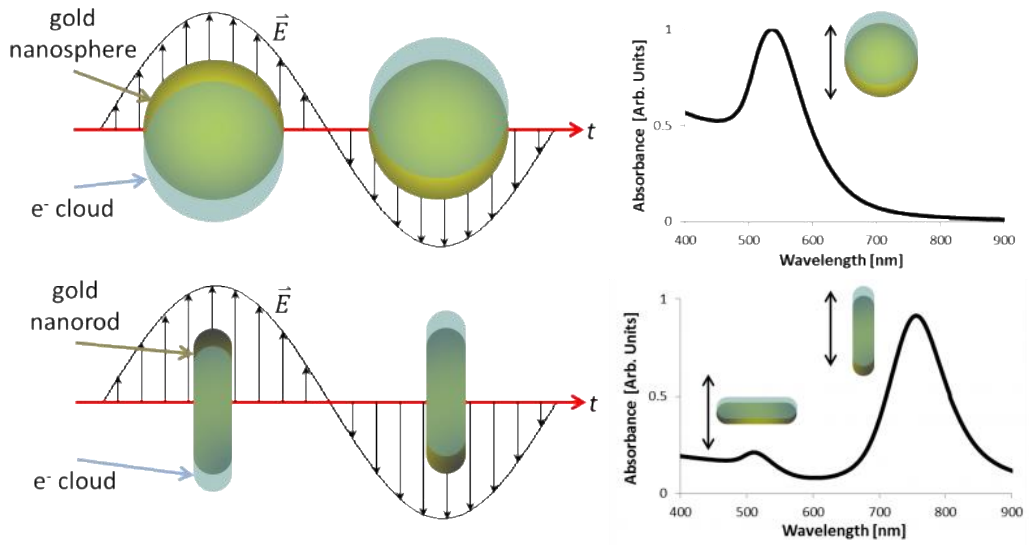

FIGURE 1.1. Gold nanoparticle and light interacting: surface plasmon resonance (SPR). Adapt from Website: https://scholar.harvard.edu/ndurr/pages/multiphoton-luminescence-imaging.

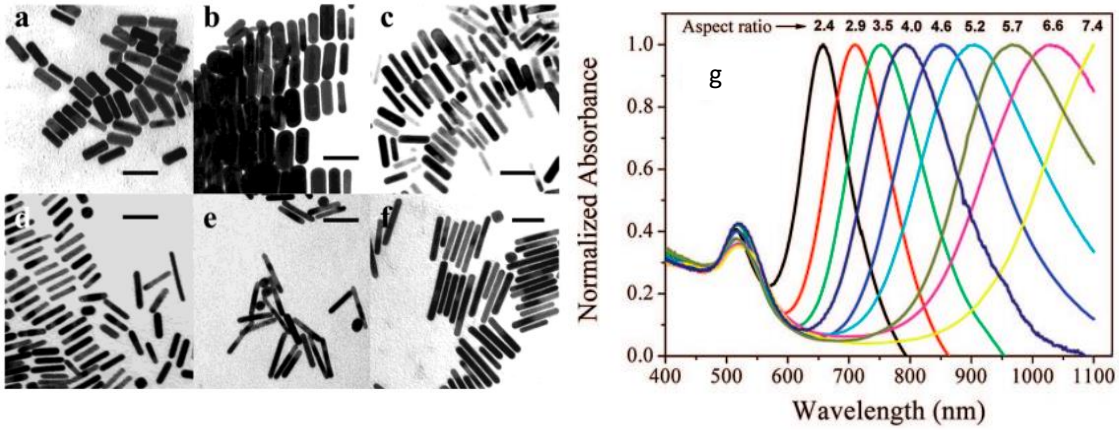

FIGURE 1.2 Tunability of the SPR of AuNRs. (a-f) TEM images of AuNRs with different aspect ratios (length of a rod divide by its width). Reprinted with permission from [4]. Copyright 2006 American Chemical Society. (g) Tuning longitudinal SPR by synthetically controlling aspect ratio. Reprinted with permission from [20]. Copyright 2006 American Chemical Society

AuNPs can act as excellent optical probes. AuNPs can be readily used to enhance optical imaging based on their absorption, scattering, fluorescence, Raman scattering, etc. The scattering

signal from AuNPs is usually much stronger than the scattering background from cells and tissues, making dark field (DF) microscopy a viable choice for reporting the existence of AuNPs within biological systems. A useful by-product of AuNP light scattering is the enhanced Raman signals for molecules [21]. AuNPs can greatly enhance the Raman signal of a molecule. The surface-enhanced Raman scattering (SERS) obtains more than 10 orders of signal enhancement, allowing for ultra-sensitive single molecule level detection (down to 10^{-15} M).

In addition, the non-radiative properties of AuNPs have shown great potential in plasmonic photothermal cancer therapy. It is reported that gold nanospheres about 40 nm size absorb light 10^5 times stronger than most strongly light-absorbing dye molecules [1]. The light absorbed by nanoparticles with specific shape and size can be converted into non-radiative heat with very high efficiency and speed [22]. A previous study done by our lab regarding the photothermal process has revealed that photoexcitation of metal nanostructures can generate a heated electron gas that can quickly cool within ~1 ps via transfer energy to the nanoparticle lattice, which could then exchange energy with the surroundings on a time scale of ~100 ps [23, 24]. The SPR greatly enhanced the photothermal effect of AuNPs, by a few orders of magnitude in a short time. Therefore, if AuNPs are attached to or inside cancer cells and exposed to light, intensive heat can be generated to destroy the cells. Compared with conventional dyes absorbers, the AuNPs are more effective and stable without exposing them to photobleaching.

1.2 Gold Nanoparticles for Cancer Treatment

1.2.1 Plasmonic Photothermal Therapy

The fact that gold is chemically inert, relatively resistant to bacteria, and biocompatible has made it a prime candidate in this quest to improve the human condition by finding more

effective ways to treat patients. There is evidence that gold was used in dental repairs over 4000 years ago[25]. Throughout history, gold has been added to medicine to treat diseases, a practice demonstrated by the use of gold cordial that was used for treating ailments caused by a decrease in the vital spirits (melancholy, fainting, fevers, *etc*), by the application of or a mixture of gold chloride and sodium chloride to treating syphilis [26]. More recently, Robert Koch, a German bacteriologist, discovered that the presence of gold in compounds, specifically gold cyanide, inhibited the growth of tuberculosis causing bacteria in 1890, and a French scientist Jacques Forestier, is credited with the discovery of the anti-inflammatory properties of gold compounds and the manipulation those properties using them in drugs to treat rheumatoid arthritis in 1929. [27] Also, the qualities of gold have deemed it a great choice of metal for surgical implants and for wires in pacemakers or stents.

Since its ancient usage in 1700 BC, heat has demonstrated its ability for tumor therapy when the glowing tip of a fire was used for treating breast cancer [28]. Photothermal therapy is a minimally-invasive therapeutic strategy in which photon energy from light is converted into heat in order to destroy cancer cells. It could avoid the severe infection complications commonly encountered after surgery [29], and circumvent the side effects from using toxic drugs in chemotherapy. Heating sources including NIR or visible light, the magnetic field, radiofrequency waves, microwaves, and ultrasound waves are used to induce a moderate temperature rise, clinically termed as hyperthermia, in a specific target region to destroy the cancer cells [30]. Due to the low absorption efficiency of natural tissue absorbents, photo sensitizers such as synthetic organic dye molecules indocyanine green and porphyrins coordinated with transition metals are externally injected into the tumor sites to enhance the photothermal effects when NIR light is

used [31]. However, the dye molecules photo bleach quickly, rendering insufficient therapeutic outcomes.

As mentioned in Section 1.1, the non-radiative properties of AuNPs have shown great potential in plasmonic photothermal cancer therapy (PPTT). Currently, AuroLase® therapy, a type of PPTT based on 150 nm silica-gold nanocoreshells (AuNCSs) coated with polyethylene glycol (PEG) that absorbs NIR light, was developed by Nanospectra Biosciences, Inc., and has been under clinical trials (ClinicalTrials.gov Identifiers: NCT00848042 for refractory and/or recurrent tumors of the head and neck (2008-2014), NCT01679470 for metastatic lung tumor (2012-2014), and currently recruiting clinical NCT02680535 for localized prostate cancer (2016 until now)). The clinical trials of AuroLase® is based on intravenous (i.v.) injection of AuNCSs in the blood, and their accumulation inside tumors via the enhanced permeability and retention (EPR) effect due to leaky and poorly organized tumor blood vessels. Prior to human clinical trials, PPTT using AuroLase® was performed in treatment of brain tumors in orthotopic canine model, tumor ablation was observed after PPTT (**Figure 1.3 a and b**)[32].

In addition, studies of gold nanorods (AuNRs) have been applied the treatment of spontaneous tumors in canine and feline patients. Cancer is very common in cats and dogs. It is estimated that 23% of all dogs [33] die of cancer and the percentage of feline deaths due cancer is half of canine [34]. In general, dogs and cats develop similar cancers very analogous to those in humans [34], such as mammary gland tumors [35]. Ali *et al* has performed several studies on treating spontaneous mammary gland tumors on cats and dogs by directly inject AuNRs to solid tumor (intratumoral injection, *i.t.*), followed by NIR irradiation. After three sessions of treatments, efficient tumor regression for all cases was achieved with no recurrence and metastasis without toxicity effects on blood profile, or liver and kidney functioning afterwards

(**Figure 1.3 c**) [9] . Abdoon *et al* also conducted similar studies on dogs and cats with mammary gland tumors. Their results showed that the treated animals had complete remission (62.5% (10/16)), partial remission (25% (4/16)) and no response (and 12.5% (2/16)), respectively (Figure 1 d) [36]. The two groups' difference of the conditions is that Ali *et al* have developed gentle conditions to trigger apoptosis, while Abdoon *et al* relied on heating up the tumor harshly. London and coworkers used AuNRs-PTT and applied it for treating spontaneous neoplasia in dogs (carcinoma, sarcoma or mast cell tumor). The AuNRs were injected intravenously to seven canines 72 hours before using a 30 W 808 nm NIR laser to irradiate the tumor mass. At study end, partial or complete remission of tumors was observed and the overall response rate was 28.6% [37].

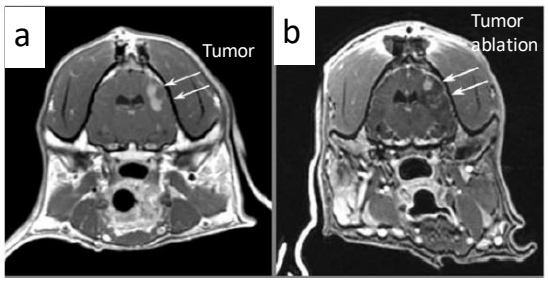

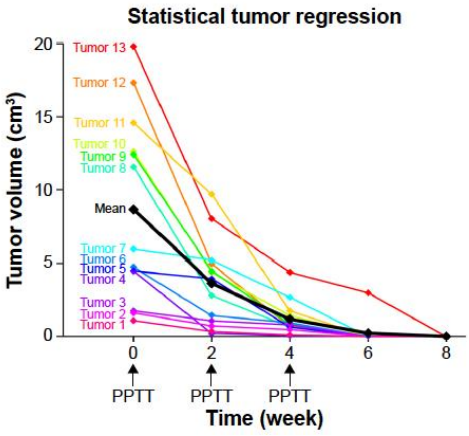

d Effect of GNRs-PPTT on mammary tumor in dogs and cats.

Item	Response		Overall response (%)
	Dogs (%)	Cats (%)	
Complete remission	6/10 (60%)	4/6 (66.7)	62.5
Partial remission	2/10 (20%)	2/6 (33.3)	25
No response	2/10 (20%)	-	12.5
Tumor relapse	2/10 (20%)	2/6 (33.3)	25
Overall survival/days			315.0 ± 20.5

FIGURE 1.3. (a-b) AuroLase® treatment of canine transmissible venereal tumor in brain of a dog. MR-DCE axial images of dog brain showing contrast enhancement of bilobed tumor (a) before and (b) ablation of tumor after treatment. Reprinted with permission from ref [32]. Copyright 2009 American Association for Cancer Research. (c) Our study showed the tumor regression curves from 13 mammary gland tumors in cats and dogs with variable volumes under multiple PPTT treatments using gold nanorods. Reprinted with permission from ref [9]. Copyright 2016 Dove Medical Press. (d) Abdoon et al's study showing the efficacy of PPTT on 16 dogs and cats with mammary tumors using gold nanorods. Reprinted with permission from ref [36]. Copyright 2016 Elsevier.

Advantages and disadvantages of PPTT and types of cancer PPTT has been performed

AuNP-assisted PPTT offers obvious advantages over many other types of cancer treatments. First, AuNPs-assisted PPTT avoids the systemic side effects associated with traditional cancer therapies, such as chemotherapy. The treatment is mainly designed for localized solid tumors, with almost no damage to healthy tissues. Second, since PPTT is a physical treatment, there is no restriction on the types of tumors to be treated. As usually different cancer types have their specific chemotherapy drugs, and many cancers develop resistance to particular drugs after a certain time period, however, PPTT could be a "universal" treatment for many types of cancer.

In spite of the many advantages stated above, AuNP-assisted PPTT presents its unique challenges. The first issue is the biological fate of AuNPs, especially in the long-term. The potential applications for AuNPs are endless, but their applications in nanomedicine are dependent upon their toxicity level. Despite the evidence that AuNPs are biocompatible and chemically inert, there have also been studies with contradictory results[38]. However, for many cases, the toxicity does not come from the AuNPs, but from the non-biocompatible surface ligands [39], the high power of laser [40], or the high treatment dose of AuNPs [41, 42]. AuNPs accumulate mainly in liver and spleen. Many studies, however, have shown that their negative effect is negligible in the aforementioned organs [40, 43]. The second issue is the inconsistency of the treatments due to different laboratory variables such as lab personnel, types of AuNPs, surface modifications, laser dosage, different handling, *etc*. These inconsistencies will result in different results, which are sometimes account for high variations of PPTT. The third issue is that PPTT is largely limited to treating localized solid tumors. For cancers that are not localized, or advanced metastatic cancers, the effectiveness of PPTT might be greatly impaired. Despite

this, the recent advances of PPTT show the feasibility of it preventing and inhibiting cancer recurrence and metastasis [44].

Types of tumors for PPTT treatment. Due to the nature of the PPTT, localized solid tumors are more suitable for treatment. The PPTT has been performed in various cancer types, including breast[45, 46], head and neck[40, 47], [48], melanoma[49, 50], lung (ClinicalTrials.gov Identifiers NCT01679470), prostate (ClinicalTrials.gov Identifiers NCT02680535), liver[51], *etc*.

Gold nanoparticle types for photothermal therapy. The AuNPs that enable the photothermal effect generated with NIR light are more often used in photothermal therapy. NIR light exhibits wavelengths between 750- 1700 nm (first window NIR-I, 750-1000 nm; NIR-II, 1000-1700 nm [52]), where the water absorption is minimal and light can deeply penetrate the tissues in order to reach the tumor area (several cm of tissue). Spherical Au NPs have their show a SPR peak at about 520-540 nm. Several Au nanostructures that absorb NIR light have been reported, with structure including Au nanorods [20], Au nanoshell [53] , Au nanocages [54] and Au nanostars [55]. It has be recently found that, other shapes of AuNPs also exhibit photothermal capability, such as Au bipyramids[46], Au nanoprisms [56], Au nanorings[57], and AuNP assemblies that are caterpillar-like in nature[58]. The useage of different shapes of AuNPs are shown in **Figure 1.4.**

	Nanoshells	Nanorods	Nanocages	Nanostars
Schematic				
SEM	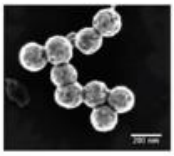	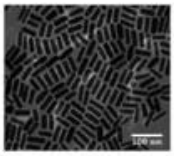	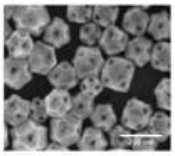	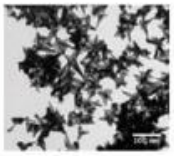
Size for PTT	~150 nm diameter	~10 nm x 40 nm	~40-60 nm length	~45-120 nm
Stage of development	Clinical trials: lung, head & neck, and prostate cancer	Preclinical	Preclinical	Preclinical
Unique features	Core:shell structure	Two resonance peaks	Drug loading capabilities	Large surface area for bioconjugation

FIGURE 1.4. The most frequently used Au nanoparticles in photothermal therapy. Reprinted with permission from [59]. Copyright 2017 Wiley.

1.2.2 AuNPs in Inhibiting Cancer Metastasis

Metastasis enables cancer cells to migrate to distant secondary sites, which is responsible for 90% cancer-related deaths [60-62]. Metastasis is a multi-step process where the primary cancer cells migrate and invade locally, the intravasate and circulate in blood or lymphatic vessels, and extravasate and colonize in the secondary sites, as shown in steps A-F described in **Figure 1.5**.

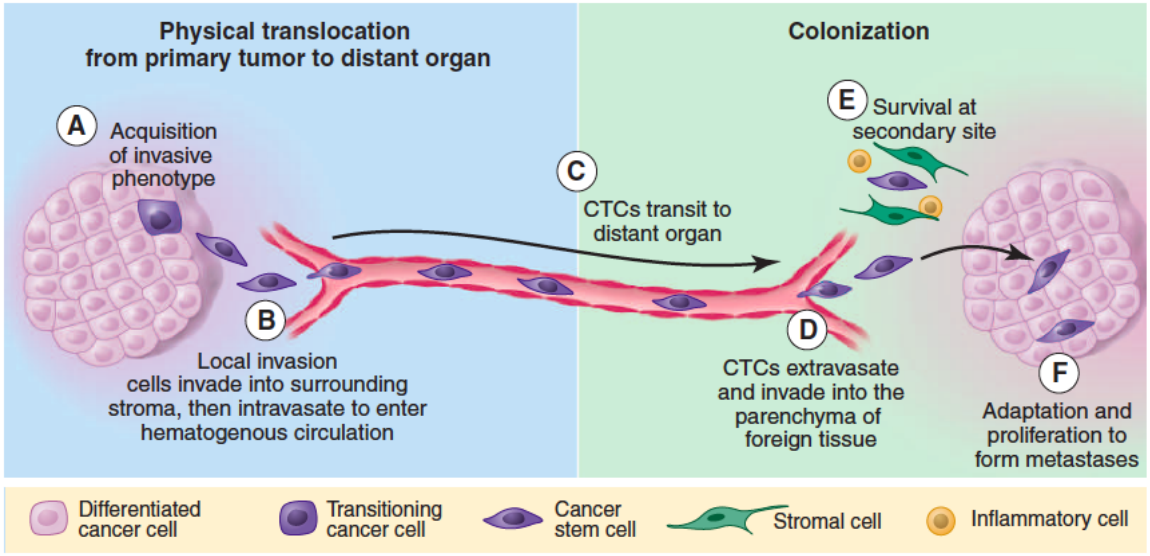

FIGURE 1.5. A scheme of the metastatic cascade. A to F describes the process of metastasis. Cancer cells inside the primary tumor adopted an invasive phenotype, then locally invade into the surrounding stroma and reach blood vessels, enter the blood circulation (the cancer cells traveling in the circulation are called circulating tumor cell (CTCs), and finally reach the secondary site and colonize there Reprint from reference [63]. Copyright 2011 American Association for the Advancement of Science.

The migration of cancer cells from one site to another requires dramatic remodeling of the cellular cytoskeleton[61, 62, 64, 65]. The process of cell migration can be described by four steps: protrusion, adhesion, contraction and retraction (**Figure 1.6**). The cell migration is initiated by polarization and extension of actin protrusions. To stabilize the protrusions, the cells generate adhesions which link the actin cytoskeleton to the extracellular matrix (ECM). The adhesions at the rear of the cell then disassembly and allow the retraction of the cell body forward [66]. Studies on the changes of cytoskeletal components could provide novel therapeutic approaches to prevent cancer cell migration and metastasis [64].

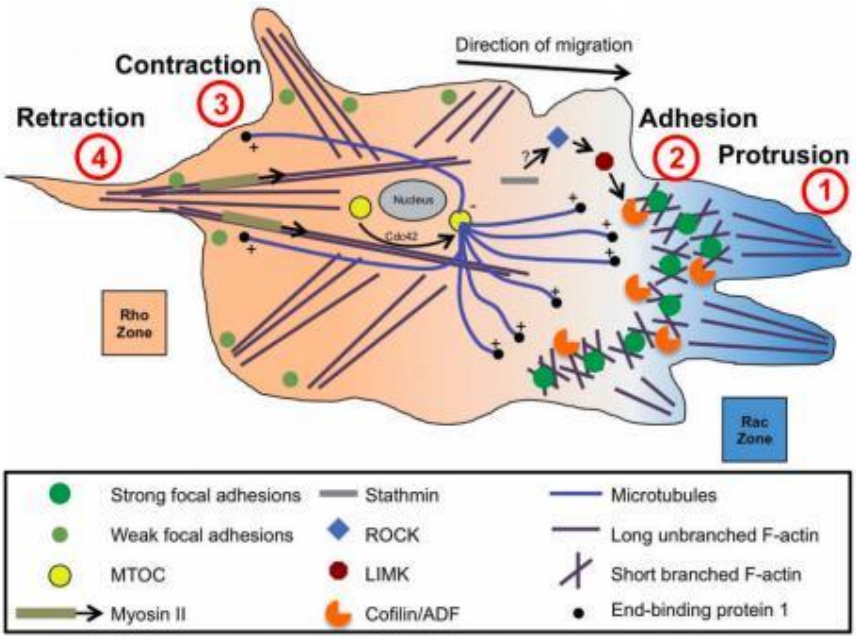

FIGURE 1.6. The cell cytoskeleton and four steps of cell migration: protrusion, adhesion, contraction, retraction. Reprint from reference [66]. Copyright 2014 Wiley.

Past attempts to develop anti-metastasis drugs have not been efficacious in clinical trials [67]. Moreover, in many cases, the anti-cancer drugs that target specific proteins might lose their efficacy after several months of treatment due to mutations of the proteins that result in the rise of drug resistance in cancer cells [68]. Recent advances in nano-medicine provide us with great opportunities to avoid the drawbacks of commonly used drugs [69, 70]. Nanoparticles are able to target tumors selectively [71], a lot of studies showed that nanoparticles are helpful for cancer diagnosis , therapy [72], and recent discovery of their effect on inhibiting cancer cell migration and/or metastasis [73-76] . AuNPs, especially, have been widely used in these studies, due to their unique physical, chemical properties, easy surface modification and good biocompatibility. **Figure 1.7** shows the numbers of publications and citations related to AuNPs inhibiting metastasis, an area of research that started to emerge in the last decade (reach nearly 85 publications in 2018) and still in its preliminary stages.

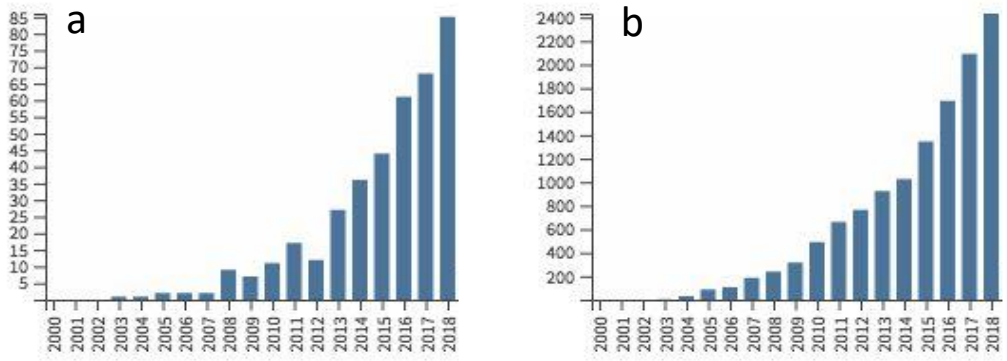

FIGURE 1.7. Total publications (left) and citations (right) per year till the end of 2018, of the topic "AuNPs inhibit metastasis". The figure reference to Web of Science search key words "gold nanoparticles" and "metastasis".

Generally, there are mainly three strategies for using AuNPs for inhibiting metastasis: 1) AuNP-based drug delivery system which delivers chemo-drugs, antibodies or siRNA to invasive cancer cells, cancer stem cells and tumor microenvironment (TME, since metastasis only occurs in a "supportive" TME, the perturbation of TME could be a good strategy for inhibiting metastasis), 2) the using of AuNPs itself without any drugs to inhibit metastasis, and 3) the combining AuNPs with near infra-red light to generate the photothermal effect in order to inhibit metastasis. In the first strategy, AuNPs are usually conjugated with drugs used for targeting and treating invasive or metastatic cancer cells. Peptides have been used for targeting of metastatic breast cancer; including RGD peptides (for targeting integrin), [77] and tumor metastasis targeting (TMT) peptide have been used for targeting of metastatic breast cancer [78]. Beside targeting and treat invasive cancer cells, targeting cancer stem cell [79, 80], inducing angiogenesis [81, 82], and altering the tumor microenvironment [83] could also achieve inhibiting effects on metastasis.

In the second strategy, AuNPs have recently shown their own ability to inhibit metastasis even without drug loading. AuNPs could inhibit the motility of cancer cells [84-86],

induce anti-cancer immune response for effective cancer therapy [87], or modulate the tumor microenvironment and blood vessel components [88, 89]. In 2013, Arvizo *et al*. reported that non-specifically targeted AuNPs could inhibit tumor growth and metastasis by abrogating MAPK signaling and reversing the epithelial-mesenchymal transition. Murphy *et al.* reported that AuNPs with different surface charges and sizes can affect cancer cell migration [73]. In the same year, Zhou *et al*. showed that AuNRs coated with bovine serum albumin (BSA) exhibited reduced cell migration and invasion by impairing ATP synthesis, which subsequently inhibits F-actin cytoskeletal assembly and decreases the metastatic ability of the tumor [76]. However, for most of the previously mentioned works, non-specific targeted nanoparticles were used. For instance, Zhou *et al*.[76] used BSA coated AuNRs that showed inhibitory effects on cancer cell migration, but the high concentration of AuNRs (50-200 μM) used might be an obstacle for clinical usage. Our lab recently discovered that nucleus-targeting of gold nanoparticles (AuNPs) could stimulate the overexpression of Lamin A/C, thus increasing nuclear stiffness, and greatly decreasing cancer cell motility (**Figure 1.8**). The nucleus-targeting AuNPs decrease the dose to 1000 x less [90].

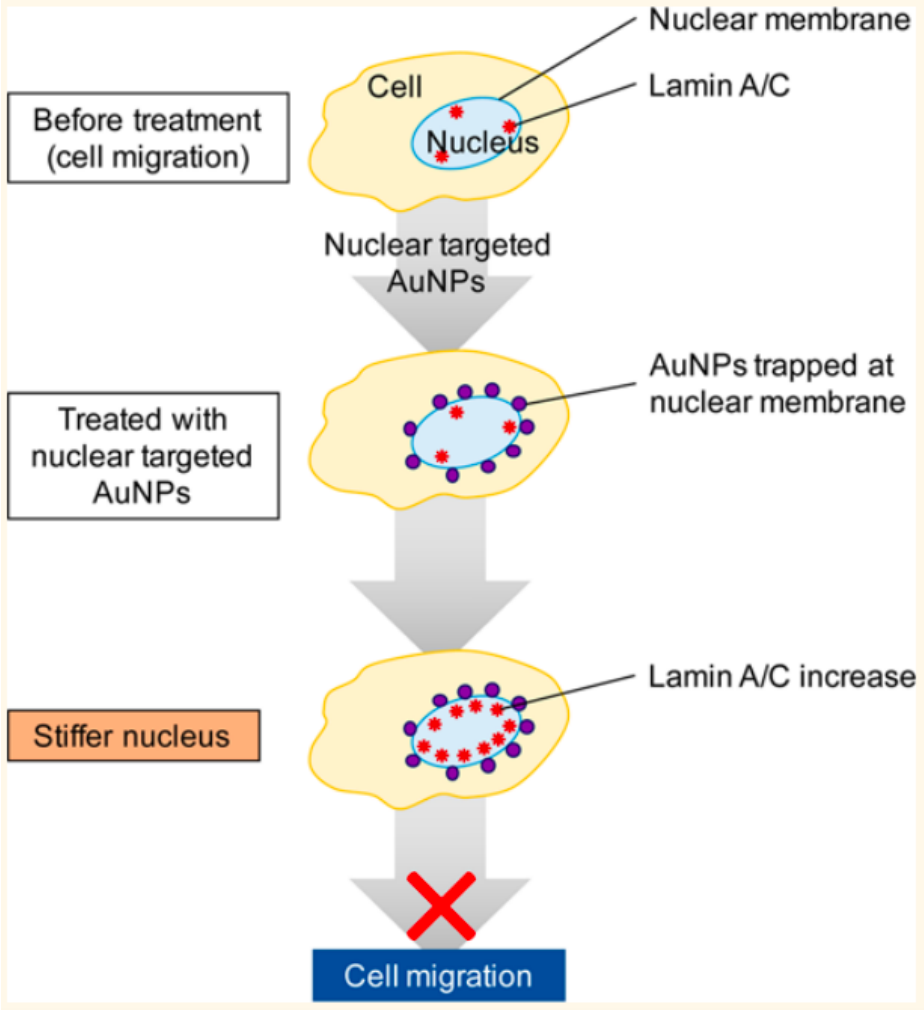

FIGURE 1.8. Nuclear targeting AuNPs increase nuclear stiffness and Lamin A/C formation, and inhibit the ovarian cancer cell migration and invasion. Reprinted with permission from ref [90]. Copyright 2017 American Chemical Society.

The third strategy is using AuNP-assisted plasmonic photothermal effect to inhibit metastasis. PPTT has been reported by many studies for its ability to inhibit metastasis. During our previous studies, we observed animals with induced or spontaneous tumors were effectively cured, interestingly, with no metastasis [9]. PPTT can be used to eliminate primary cancer cells and treat the local metastasis in lymph node [91]. Burke *et al* reported that the breast cancer stem cells, which are persist to many chemo treatment and drive tumor recurrence and metastasis, are sensitive to NPs-mediated PTT and lost their long-term proliferative ability[92]. Li and coworkers

fabricated deep tumor-penetrating polymer nanotherapeutics that loads a NIR probe for photothermal therapy. Although AuNPs they didn't use AuNPs in their study, their platform showed inhibition of tumor growth and metastasis of breast cancer by photothermal therapy, as the metastasized cells decreased greatly in the lung[93].

Although the phenomena that PPTT could inhibit metastasis is starting to uncovered by many animal studies, the mechanism is barely understood. Our results showed that integrin-targeting AuNP-PPTT can cause cytoskeleton remodeling by affecting Rho GTPase and other pathways, causing the decreasing of cancer cell motility [10]. In addition, we also studied the effect of the same treatment on collective cell migration by phosphoproteomics and high-resolution imaging, which reveals impaired cell junctions and actin cytoskeleton[94].

Besides using this strategy alone, PPTT can also be combined with other therapies such as chemotherapy and radiotherapy in order to inhibit metastasis. One reports that combining chemotherapy and photothermal ablation using doxorubicin-loaded DNA wrapped AuNRs , which suppresses lung metastasis in an orthotropic 4T1 mammary tumor model[95]. In addition, the same group developed gold-coated nanocages, which loaded DOX, and used hyperthermia to trigger drug release for anti-metastasis purpose. This caused an obvious decrease in the number of pulmonary metastatic nodules [96]. In addition, Atkinson *et al* reported that gold nanoshells and PPTT could sensitize breast cancer stem cells to radiation therapy [97].

Combination of photothermal therapy with immunotherapy for combating cancer and metastasis.

Immunotherapy emerges as a breakthrough recently for cancer treatment. Although it shows a great success in several clinical cases, when giving systemically, this strategy might lead to many unintended side effects. Nanomedicines, due to the specific properties of nanoparticles such as targeting specific cells, control-release of the drug loaded, *etc*., are promising to avoid the side effects, decrease the toxicity of conventional immunotherapy[98], and stimulate the anti-cancer immunity [99]. The cargos include tumor antigens that induce response to the effective cells (such as CD8+ T cells and CD4+ T cells), inhibitors of immunosuppression (i.e., CTLA-4, PD-1, PD-L1), *etc*. In addition, NPs enables targeted immunotherapies when pharmacologically incompatible. Nanoparticles can recognize specific surface receptors and then enter DCs [100]. After targeting DCs, Rosalia *et al*. observed a further boost of tumor-specific CD8+ T cells [101]. Therefore, the resulting cancer cell membrane-coated NPs can be used to deliver tumor-associated antigens to antigen presenting cells [102], offering a platform for cancer immunotherapy.

Multiple evidences suggest that AuNP-PPTT could be well engaged into cancer immunotherapy. Zhou et al prepared AuNRs conjugated with immunoadjuvant imiquimod (R837) [49]. Under NIR irradiation, tumors ablation and immune responses triggering was observed in metastatic melanoma in mice (**Figure 1.9**). In addition, lung metastasis and tumor recurrence was prevented due to the inducing of a strong long-term antitumor immunity. Liu and coworkers used photothermal therapy that heated tumors and stimulate DC maturation locally. It was synergize with anti-CTLA-4 therapy for effective inhibition of cancer metastasis in mice [103]. In addition, the same group adopted a nanocomposite with R837 that showed the photothermal ablation could generate a "vaccine-like" immune response, inflame the tumour microenvironment, increase pro-inflammatory cytokine and T cell infiltration. This effect can be

synergized with checkpoint blockades for tumor control for achieving effective treatment for metastatic cancer (**Figure 1.10**) [104]. Zhou et al combined local phototherapy and immunotherapy that induces a systemic immune response against primary tumors and metastases in pancreatic tumor model [105]. Although some studies mentioned above used other types of nanoparticles than gold, the concept that photothermal therapy could effectively promote immunotherapy are shown.

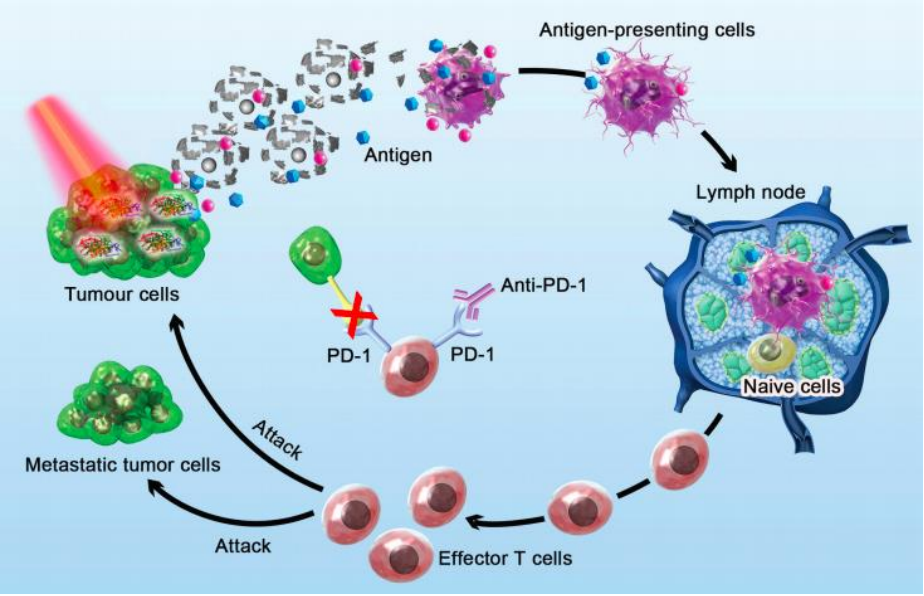

FIGURE 1.9. Schematic figure of photothermal therapy using gold nanorods loaded with immune-adjuvant and the mechanism of antitumor immune responses in the treatment of melanoma. Reprinted with permission from ref [49]. Copyright 2018 The Royal Society of Chemistry.

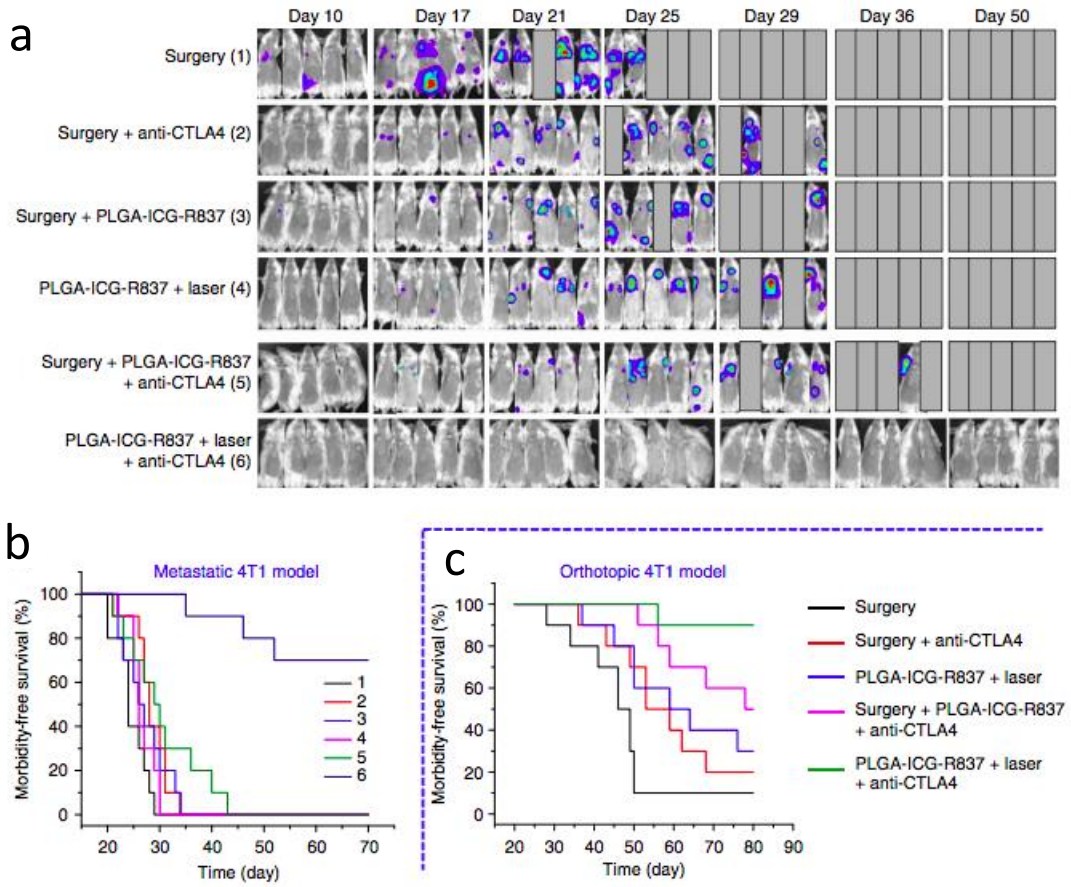

Figure 1.10. (a) Bioluminescence images for tracking breast tumor and metastasis in 4T1 mice after various treatments (conditions # 1-6). (b) Morbidity-free survival of mice with metastatic 4T1 tumors after various treatments. (c) Morbidity-free survival of mice with orthotopic 4T1 tumors with spontaneous metastases after various (10 mice per group). Reprinted with permission from ref [104]. Copyright 2018 Springer Nature.

1.2.3 Biodistribution, pharmacokinetics and toxicity of gold nanoparticles

For PPTT to be successful, ideally the AuNPs need to accumulate in the tumor. However, the distribution and the pharmacokinetics of AuNPs in body are largely dependent on several factors: **size, surface coatings, and administration routes of AuNPs**.

In general, for nanoparticles that are i.v. injected, the main pathway of clearance is through the reticuloendothelial system (RES) via macrophages in the liver and spleen [106]. The

diminished interaction between nanoparticles and the RES lengthens the blood circulation time, which is often associated with higher intratumoral penetration [42]. Nanoparticles show tumor accumulation due to the enhanced permeation and retention (EPR) effect, a phenomenon directly related to immature and leaky tumor blood vessels. In addition, in order for nanoparticles to get inside the tumor, they must first cross a barrier of high interstitial fluid pressure and dense stromal tissues. Smaller AuNP sizes might be more beneficial for overcoming these barriers. The effects of size factor on toxicity, clearance routes, heat generation efficiency, blood circulation time and intratumoral penetration ability are summarized in **Figure 1.11**. The smaller AuNPs (> 20 nm) might be beneficial.

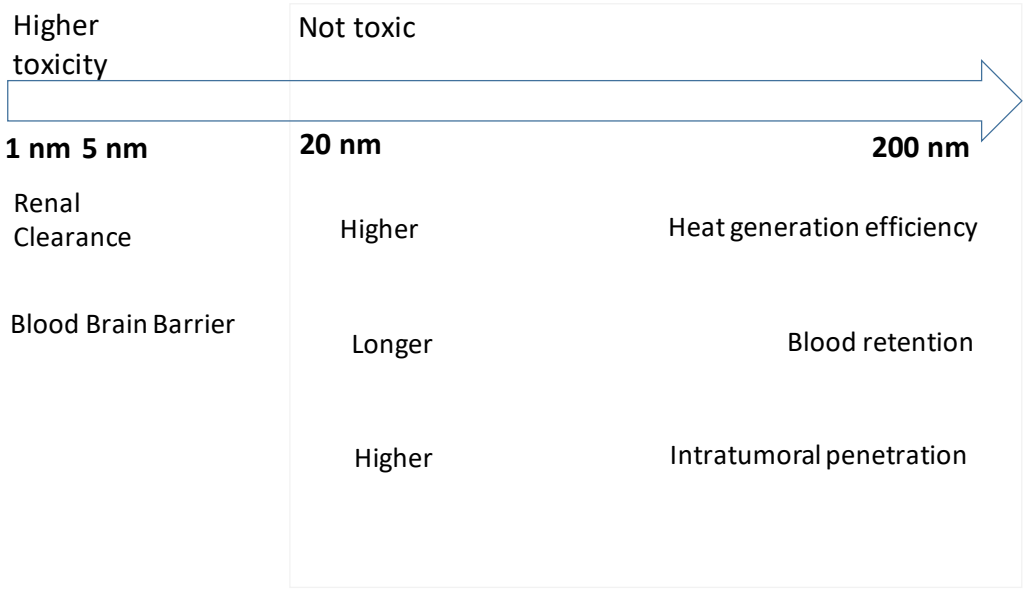

FIGURE 1.11. The sizes of the AuNPs in PTT affect their biological behaviors, concluded from ref [1, 107-111].

Effect of Size and Shape on Cellular Toxicity, pharmacokinetics and Biodistribution.

Nanoparticles display distinctive biological behavior in the body compared to small molecules. Smaller size enables the AuNPs to pass through the blood brain barrier (BBB, <20

nm) and AuNPs with sizes below 5 nm are able to clear from kidney [108]. Fraga *et al.*'s study that utilized 20 nm AuNPs showed a lack of particles in the brain at both assessed time points, 30 min and 28 days, indicating that the AuNPs did not cross the BBB [109]. Most of the AuNPs for PPTT are larger AuNPs (> 20 nm) which are usually unable to pass BBB or achieve renal clearance, showing accumulation mainly in the liver and spleen. There is evidence that smaller nanoparticles are more toxic than larger ones possibly due to their higher chance in interacting with their surroundings and inducing greater immune responses as a result of their high surface area relative to their mass[112]. Pan Y *et al.* reported that AuNPs with a diameter of 1.4 nm are much more cytotoxic than 15 nm AuNPs of similar chemical composition [113]. In another study, Coradeghini *et al.* assess the colony forming efficiency of Balb/3T3 mouse fibroblast cells incubated with 5 and 15 nm AuNPs for 72 hours. The results indicated that the 5 nm AuNPs at a concentration higher than 50 μM shows cytotoxicity, while there was no cytotoxicity found for the 15 nm AuNPs [114]. Low cytotoxicity was observed in 15-20 nm AuNPs despite the differences in cell lines and treatment time. Pattanayak *et al.* studied AuNPs between 15-20 nm in diameter in the L929 mouse cell line for 15-16 hours of treatment, and reported that there was no toxicity observed [115]. Murphy et al shows 18 nm AuNPs do not cause acute cytotoxicity [116]. Khan *et al.* treated HeLa cells with 18 nm AuNPs before incubation for 3 and 6 hours. The AuNPs were not observed to enter the nuclei of the cells, as they were found to be localized within the cytoplasmic membranes. They generated the transcriptional profiles of HeLa cells and found the expression level of most of the genes remained unaltered [117].

Li and co-workers studied the size effect on the biodistribution and pharmacokinetics of intravenously injected AuNPs (20, 40, and 80-nm, all coated with PEG) in mice [111]. The 20-nm AuNPs exhibited slowest clearance from the body and longest blood circulation time (half-life

clearance of particles 30-40 h), followed by the 40-nm AuNPs (half-life 10 h). The 80-nm AuNPs exhibited the fastest clearance (half-life < 1 h), as shown in **Figure 1.12**. In addition, the 20-nm AuNPs had lower accumulation in liver and spleen than the 80-nm AuNPs, but they exhibited higher accumulation in the tumor due to the longer blood circulation time. Similar observations were reported by Cho *et al.*, who also performed studies regarding pharmacokinetics and biodistribution of different sized PEG coated AuNPs (4, 13, and 100 nm) when injected intravenously into mice[118]. Both of the smaller AuNPs, 4 nm or 13 nm, revealed longer blood circulation intervals, peaked at 24 h and cleared by day 7, while the large 100 nm AuNPs were cleared by 24 h. In contrast, 100 nm AuNPs rapidly accumulated (~30 min) in the liver, spleen, and mesenteric lymph nodes, while small AuNPs accumulated more slowly in the organs (peaks at 7 days in liver and spleen; 1 month in mesenteric lymph nodes). TEM showed AuNPs existing in cytoplasmic vesicles and lysosomes of liver Kupffer cells in addition to macrophages in the spleen and mesenteric lymph node.

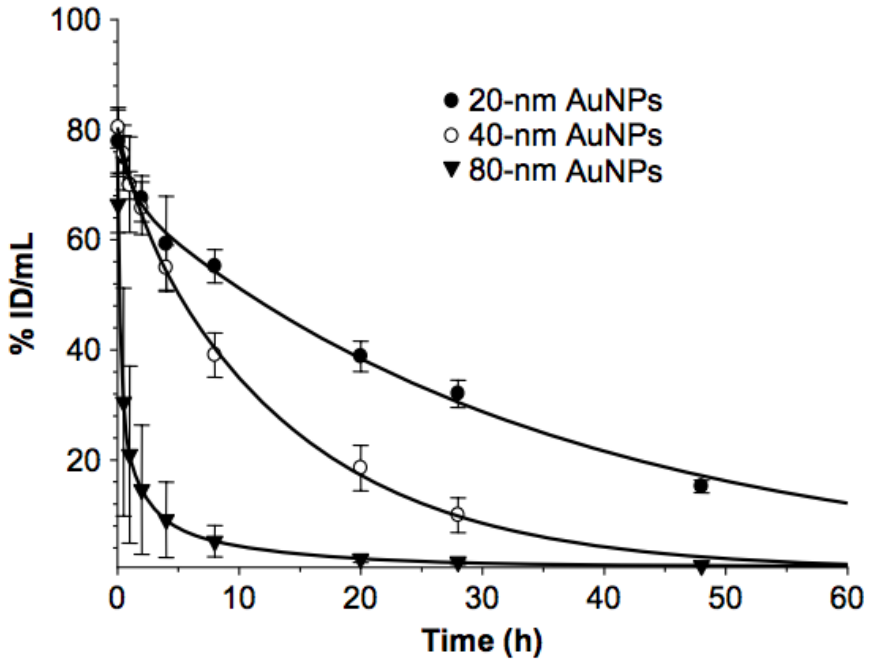

FIGURE 1.12. Pharmacokinetics (of 20, 40, and 80-nm AuNPs) expressed as the percentage of the injected dose per gram of tissue in mice (%ID/g). Reprinted with permission from ref [111]. Copyright 2009 Elsevier.

Effect of Surface Modifications on Toxicity and Bio distribution. Surface modifications have been observed to have drastic effects on the interactions between AuNPs and biological systems. The structures, functional groups, and charges of the surface modifications result in different cellular responses to the conjugated AuNPs. It is noteworthy to mention that the aforementioned debate over the perceived toxicity of AuNRs stems primarily from the surfactants of the AuNRs. Cetyltrimethylammonium bromide (CTAB) is one of the surfactants central to this debate since, there have been studies that confirmed that the incomplete purification of AuNRs during synthesis results in free CTAB molecules that induce the observed cytotoxicity[39, 69, 119].

In order to assess the toxicity of AuNPs with different surface charges, Goodman *et al.* synthesized cationic and anionic particles, and found that the toxicity of the AuNPs was related to their interactions with the cell membrane. The cationic AuNPs were found to be more strongly attracted to the negatively charged membrane than the anionic AuNPs were, as is expected given their electrostatic complementarity relative to the negatively charged bilayer of cell membrane [120]. In another work demonstrating the cellular behavior of positively charged, negatively charged, and neutral AuNPs, Schaeublin *et al.* found that charged AuNPs displayed toxicity at relatively low dosages (10 mg/mL), while the neutral AuNPs displayed significant levels of toxicity at a higher dosage of 25 mg/mL. The final results illustrated that both the positively and negatively charged AuNPs were toxic, with the negatively charged AuNPs having a magnified response resulting in necrosis being the primary mechanism of cell death [121]. It is also worth noting that the physiochemical surface properties of AuNRs change after contacting with

biological media, which needs to be considered when examining the biological impact of AuNRs[122].

The FDA-approved PEG-modification was achieved by adding mPEG-SH in the gold nanoparticles to form a nearly neutral surface, which showed little cytotoxicity *in vitro* and is currently becoming one of the most favorable surface modifications of AuNPs for *in vivo* usage. PEG-modification creates a nonspecific barrier which reduces unspecific bindings in blood components such as proteins and cells[123], which could greatly decrease the interaction between AuNPs and RES, leading to extended blood retention and increased uptake in the tumor [106].

Gold nanoparticle administration strategies, intravenous vs intratumoral. In PPTT treatment, since the intravenous injection relies on the EPR effect, it might face challenges regarding the transportation of adequate amounts of AuNCSs to the tumor site. Several studies have showed less than 10% ID/g delivered to the tumor when administrated by intravenous injection[106, 124]. On the other hand, several other groups, including our lab, have been using intratumoral administration of AuNPs [9, 40]. The intratumoral administration showed a successful result when a reasonable dose was applied. The intratumoral injection could directly introduce AuNPs into the tumor site and therefore, provide a more favorable AuNPs concentration inside the tumor while decreasing the injection dose. However, *i.v.* injection could be more helpful in some cases, especially for tumors that are not accessible by direct injection of AuNPs.

AuNRs, AuNCSs and AuNCs are separately discussed in the following contents.

The PEG-coated AuNRs (Length x width) (65 x 11 nm) completely changed the *in vivo* pharmacokinetics of the initially CTAB coated ones, according to the report from Niidome *et al*. when using a mouse model [123]. PEG-coated AuNRs exhibited stable and an extended circulation

in the blood (half-life of ~ 1 h), with no accumulation in major organs (except for the liver) at least for 72 h. For the CTAB-coated AuNRs, fast clearance in blood and accumulation around 0.5 h was observed, as shown in **Figure 1.13**. The majority of the AuNRs accumulation occurred in the liver. Similar observations in rats comparing CTAB and PEG coated AuNRs (55.3 × 18.5 nm) were reported Lankveld by *et al*, with the conclusion that the PEGylation of AuNRs resulted in a prolongation of blood clearance after intravenous administration[125], and an accumulation of AuNRs mainly inside liver and spleen.

Although most of the studies involving AuNRs biodistribution are performed using ICP-MS to measure the Au content in organs, live animal imaging methods are also used. Su et al. used 3 dimensionnel optoacoustic tomography imaging to map the biodistributoion of AuNRs coated with PEG in live mice [126]. The optoacoustic imaging was equipped with two lasers: one sensitive to both the AuNRs and blood (765 nm, close to the SPR of AuNRs) and the other only sensitive to blood (1064 nm). Maximum levels of blood AuNRs brightness were observed 24 h post-injection, followed by a slow clearance during the next six to seven days.

Our study have reported a 15-month toxicity study of AuNRs@PEG (25 x 5 nm) in mice [40]. To asses the toxicity, we examined the histopathology of liver, spleen, lung, and kidney tissues of mice 1 and 15 months after single *i.v.* injection of AuNRs@PEG. No histopathological abnormalities in the preceding organes were observed (**Figure 1.14 A**). No clinical signs of toxicity, including impeded movement, ruffled fur, signs of abnormal constitution, aberrant behavior, ocular or nasal discharge, loss of weight, respiratory distress, inability to walk, or diarrhea, were observed during the 15 months. The AuNRs were found without morphology changes in the liver and spleen for up to 15 months (**Figure 1.14 B**). Unlike the previous studies by Niidome et al, our *results* showed a higher AuNRs accumulation in spleen than liver (**Figure**

1.14 C and D). Slow AuNRs clearance was observed after 30 days to 15 months, but still Au content exists at 15 months (**Figure 1.14 C-F**).

Furthermore, for the clinical cases of canines and felines (with mammary gland tumors that have been treated with AuNR-assisted PPTT), no evidence of negative impact was shown on their liver and spleen functions[9].

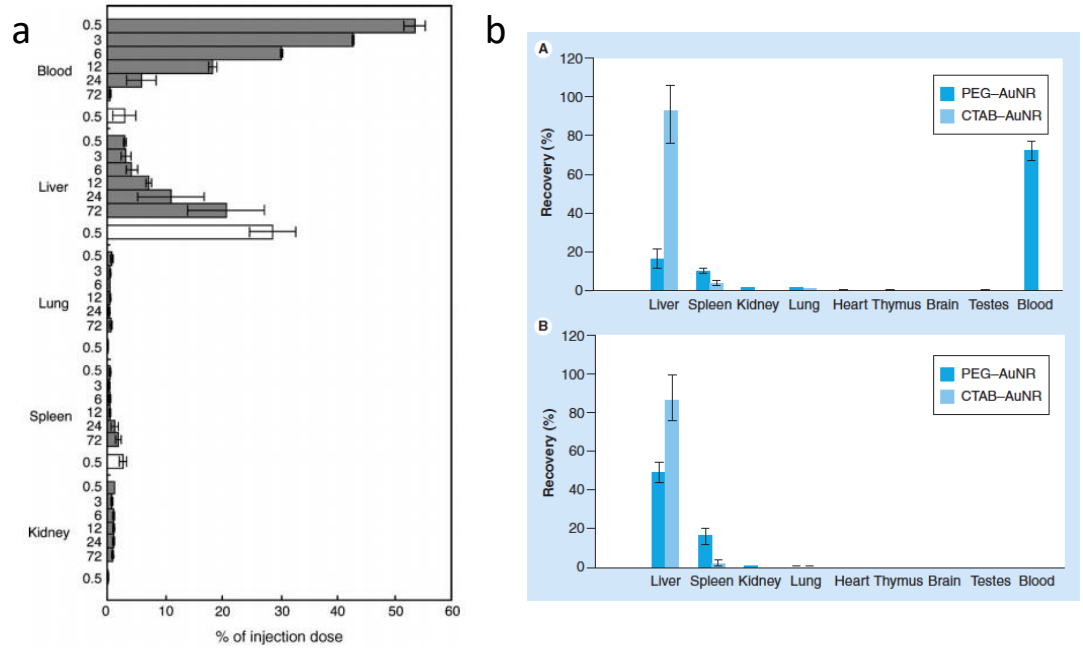

FIGURE 1.13. (a) Blood clearance and Biodistribution of AuNRs in mice after intravenous injection. Black bars show PEG-coated AuNRs at 0.5, 3, 6, 12, 24, and 72 h after injection, and white bars show CTAB-coated AuNRs at 0.5 h. The CTAB-coated AuNRs were washed once with water to reduce toxicity to mice. Reprinted with permission from ref [123]. Copyright 2006 Elsevier. (b) Percentage recovery of gold in different organs at day 1 (top panel) and day 6 (bottom panel). Reprinted with permission from ref [125]. Copyright 2011 Future Medicine.

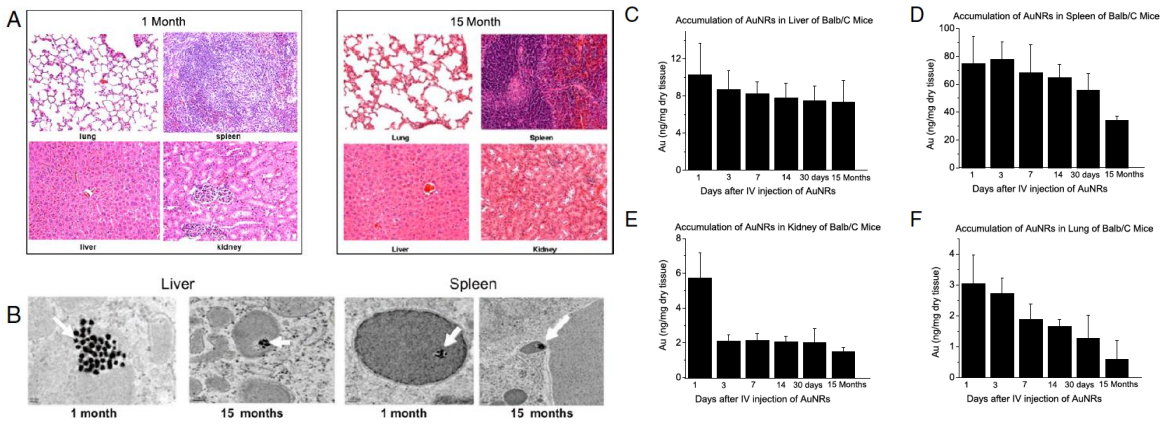

FIGURE 1.14. 15-month toxicity study of AuNRs@PEG in mice. Reprinted with permission from ref [40]. Copyright 2017 National Academy of Sciences.

Gad *et al* conducted a series of studies to evaluate the toxicity of PEG-coated AuNCSs when injected intravenously based on the ISO-10993 standard[43]. In addition, they studied the biodistribution/clearance in mice, acute toxicity in rats, and acute and chronic toxicity in Beagle dogs for time durations of up to 404 days. This study provides an extensive description of the biological fate and safety of AuNCSs. Results shows that the AuNCSs were well tolerated and did not exhibit any toxicities. AuNCSs mainly accumulate in liver and spleen, which account for over 85% of the total gold measured (**Figure 1.15 a).** Furthermore, no variations in the mean body weights was reported for dogs treated with AuNCSs compared to the control in the 10-month long-term study (**Figure 1.15 b**). Stern *et al* evaluated the safety of AuNCSs safety in 22 patients with human prostate cancer that were treated using AuNCSs based PTT[127]. Results of this study indicate no toxicity, lack of tolerance, and a lack of immunological effects 6 months (**Figure 1.16**).

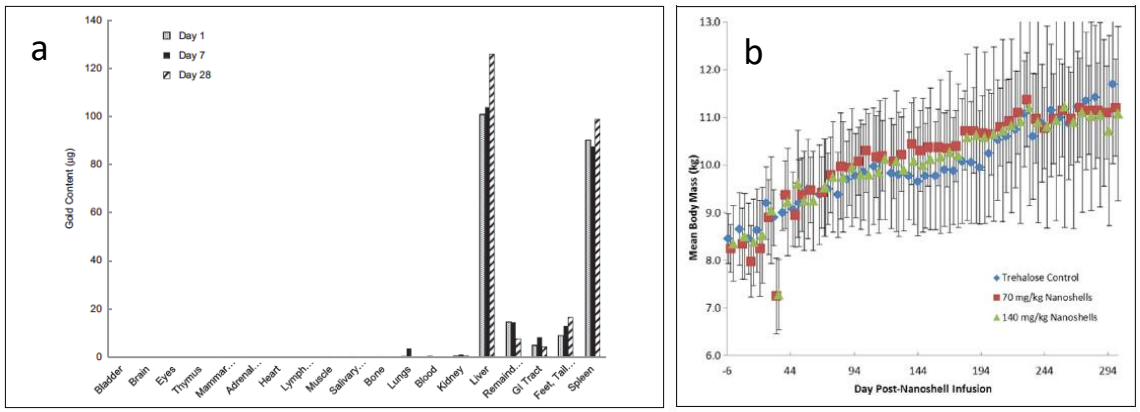

FIGURE 1.15. (a) Gold content in major organs after i.v. injection of PEG coated AuNCSs in Balb/c mice. (b) Mean body mass for dogs in a 10-month study, no variations in body mass were observed for the test groups (with i.v. injection of PEG coated AuNCSs) compared to the control. Reprinted with permission from ref [43]. Copyright 2012 Sage journals.

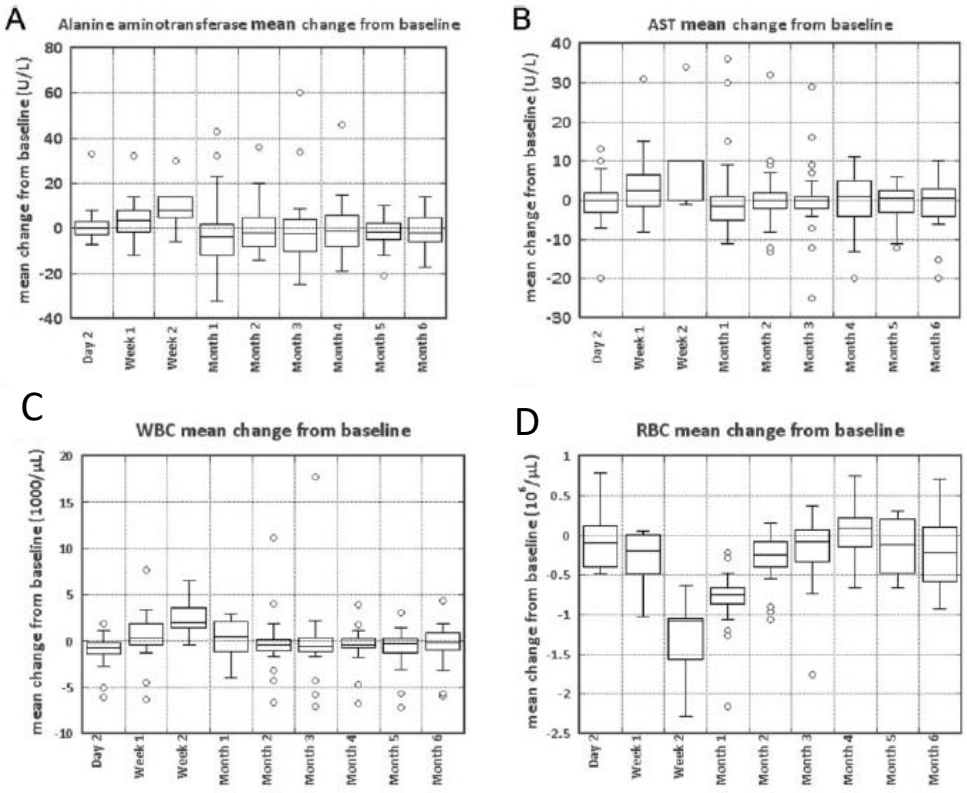

FIGURE 1.16. Blood chemistry and Hematology. Only ALT, AST, WBC, and RBC are shown here. Reprinted with permission from ref [127]. Copyright 2016 Sage journals.

There is less data on the pharmacokinetics and biodistribution of gold nanocages. Xia and co-workers evaluate the pharmacokinetics and tumor targeting ability of PEG-coated AuNCs with different sizes (30 *vs* 55 nm) in an EMT-6 mouse mammary tumor model [110]. Their results suggest that AuNCs of 30 nm in size had more blood retention than AuNCs of 55 nm in size, along with higher uptakes in tumor.

1.3 Motivation of the Work

Metastasis is responsible for over 90% of cancer-related deaths [62]. In order to initiate metastasis, cancer cells must be equipped with the ability to migrate and invade the surrounding tissues, then intravasate to the microvasculature of the lymph and blood stream, and finally translocate to distant tissues and adapt in the microenvironment [62]. However, past attempts to develop anti-metastasis drugs have not been very efficacious in clinical trials [128]. Recent advancements in nanomedicine provide new opportunities to avoid some drawbacks of commonly used cancer drugs, as nanoparticles can cross biological barriers, enter target cells with high selectivity, and function inside cell in a controlled manner [14, 129, 130]. Nanoparticles have shown promise as anti-metastasis drug delivery vehicles targeting invasive or metastasized cancer cells [79, 88, 131], and they could even function as anti-metastasis drugs without drug loading [85, 86, 132, 133].

The recent discovery of nanoparticles's effect on inhibiting cancer cell migration or metastasis has drawn the attention of many researchers [73-76]. The optical and mechanical properties, such as plasmonic photothermal effect and high mechanical strength, as well as excellent biocompatibility of gold nanoparticles (AuNPs) make them very useful in attenuating cancer metastasis [134]. However, non-specific targeting AuNPs was used in nearly all the

previous studies for the self-therapeutic effect of AuNPs in inhibiting cancer metastasis. To develop AuNPs for metastasis treatment, there are several challenges: 1) an optimized therapeutic method needs to be developed; 2) the mechanism of how AuNPs treatments inhibit cancer cell migration remains largely unexplored.

This work differs from the previous studies in two major aspects: 1) Rational designs of AuNPs to high specifically inhibit cancer cell migration, with a greatly reduced effective concentration to enhance biocompatibility. 2) Use of the state-to-the-art high resolution microscopy imaging techniques and systematic mass spectrometry-based proteomics to gain deep understanding of the underlying principles involved. Biomechanical properties (such as cell stiffness) was also used for revealing the mechanisms of how AuNPs inhibit cancer metastasis. With optimized AuNPs-based therapy or its derived therapies, it has great potential to revolutionize treatment regimens by replacing them with ones that are more effective and less toxic, and could potentially eliminate drug resistance effects on cancer cells. The selectivity of optimized delivery of AuNPs to the cancer cells could minimize the side effects on healthy cells. Successful optimization of AuNPs-based therapy and the detailed molecular mechanism study will provide a unique and novel candidate for cancer treatment for the next-phase of translational study in the elimination of the mortality associated with metastatic cancer.

GOLD NANOPARTICLES FOR BIOLOGICAL DIAGNOSIS AND IMAGING

Summary. Due to the SPR effect, AuNPs exhibit excellent optical properties, which can be used for biological imaging and sensing (as shown in **Figure 2.1**). In general, the optical properties of AuNPs adds to their capacity as therapeutic agents for disease treatment (i.e. as theranostics agents). In this chapter, we have **1)** discussed the recent advance of gold nanoparticles in biological optical imaging and sensing, especially using their enhanced Rayleigh scattering and surface-enhanced Raman scattering (SERS) properties; **2)** explored the application of AuNPs in probing dynamic philological behaviors of cancer cell apoptosis using SERS; and **3)** based on the strong Rayleigh scattering of AuNPs to light, we developed a new flow cytometry-based method for the AuNP uptake by cancer cells for fast detection purpose.

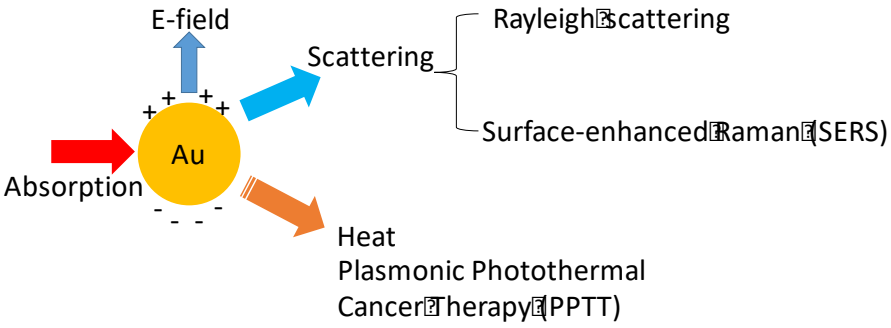

FIGURE 2.1. Simple scheme of some of the properties of AuNPs. Due to the unique optical properties of gold nanoparticles (AuNPs), i.e., the surface plasmon resonance, AuNPs can be readily used to enhance optical imaging based on their absorption, scattering, surface-enhanced Raman scattering, etc. The heat that generated after absorbing photon energy can be convert to heat.

1.4 Current Advance of Using Gold Nanoparticles in Biological Optical Imaging and Sensing [135]

Summary. Optical imaging represents one of the most essential tools in biological studies. Although with great advances, bio-optical imaging still suffers from problems such as resolution, sensitivity, speed, and penetration depth. Due to the unique optical properties of gold nanoparticles (AuNPs), i.e., surface plasmon resonance, AuNPs can be readily used to enhance optical imaging based on their absorption, scattering, fluorescence, Raman scattering, etc. Here, as an introduction part, we include the most recent achievements and challenges associated with using AuNPs to improve resolution and sensitivity in biological imaging *in vitro* and *in vivo*. The application of AuNPs in the following three aspects were discussed: 1) Direct visualization of AuNPs inside the biosystems using i) dark field (DF) microscopy, ii) differential interference contrast (DIC) microscopy, and iii) other techniques, such as interferometric scattering (iSCAT) microscopy and photothermal imaging. 2) Monitoring of biomolecular events and physiological processes using surface-enhanced Raman spectroscopy (SERS). In conclusion, based on our literature study, AuNPs-assisted bioimaging acts as a promising tool in exploring fundamental biological questions and early diagnosis of diseases.

1.4.1 Introduction

Using a microscope, Robert Hooke (in 1665) and Anton van Leeuwenhoek (in 1674) observed the images of “cell”, opening the door of cell biology. The development of optical microscopes during the last 350 years enables us to see more microscale details in the biological system. One recent noteworthy progression is the development of optical super-resolution microscopy, which allows the observation of macromolecules in live cells down to nanoscale

level and was awarded the 2014 Nobel Prize in Chemistry. Although with great advances, bio-optical imaging always has coupled strengths and weaknesses regarding resolution, sensitivity, speed, and penetration depth.

Recently, there has been a great deal of research concerning the advancement of optical imaging using AuNPs due to their unique plasmonic properties [136]. The first question that arises is how to clearly "visualize" the AuNP probes inside cells [137]. The scattering signal from AuNPs is usually much stronger than the scattering background from cells and tissues, making dark field (DF) microscopy a viable choice for reporting the existence of AuNPs within biological systems. Differential interference contrast (DIC) microscopy uses two interference light beams to generate contrast for optical path differences, allowing for the simultaneous imaging of nanoparticles and cellular components, such as nuclei, vesicles, and microtubules. Interferometric scattering microscopy (iSCAT) relies on the interference between a reference light and light scattered by the specimen in the medium to produce a high interferometric contrast image that can be obtained after the removal of static imaging background, allows sensitive and precise imaging of AuNPs with improved spatiotemporal resolution. In addition, the light absorbance by AuNPs could be converted to heat, which can be used for photothermal imaging.

In addition to visualizing the AuNPs inside the cells, a second question that comes to mind is how AuNPs could improve the detection of biological events. A useful by-product of AuNP light scattering is the enhanced Raman signals for molecules [21]. Raman spectroscopy is a powerful tool for analyzing the species within a biosystem as it provides the chemical fingerprint of the molecule [138]. AuNPs can greatly enhance the Raman signal of a molecule. The surface-enhanced Raman scattering (SERS) obtains more than 10 orders of signal enhancement, allowing

for ultra-sensitive single molecule level detection (down to 10^{-15} M). Additionally, compared to other imaging methods, SERS can provide more chemical bond/structure information. As the SERS peaks appear sharper compared to other detection methods such as fluorescence, higher accuracy in detection can be accomplished. *In vivo* SERS imaging for tumor diagnosis and therapy is a recent trendy development, which is bringing SERS into many clinical imaging applications.

1.4.2 Direct Visualization of Gold nanoparticles in Biological Systems

Recent innovations in optical imaging, including DF, bright field, DIC microscopies, photothermal and photoluminescence detection methods, etc., enable the visualization of single AuNPs interacting with the biological systems. The development of these methods has enhanced our ability to detect, localize, and track the dynamics of individual AuNPs and/or their aggregates and has broadened the understanding of bio-nano interactions in terms of the protein corona formation, membrane binding and diffusion, internalization, and trafficking of nanoparticles within cells [139, 140]. Furthermore, AuNPs can be used as both diagnostic and therapeutic agents. In this section, we will mainly focus on the recent advances in DF, DIC, iSCAT, and photothermal microscopies as well as their applications in the study of bio-nano interactions.

1.4.2.1 Dark Field (DF) Microscopy

AuNRs with DF microscopy, a scattering-based technique, produces a bright image of the specimen on a dark background. The strong scattering signal of AuNPs is attributed to their high scattering coefficients (~5 orders of magnitude higher than conventional fluorescent dyes) [141].

Imaging gold nanoparticles inside cells

Extensive work has been conducted regarding the use of DF microscopy to track the intracellular locations and behavior of AuNPs inside cells, such as the examination of AuNP uptake [142], the evolution of AuNP clusters in live cells (based on their color change [143, 144], corresponding to different cluster sizes and cellular locations, as shown in **Figure 2.2 A**), the endocytosis and subsequent transport along the microtubules [144-146]. Rosman *et al.* reported a study regarding the intracellular behaviors of nanoparticles by quantifying the number of AuNPs within cells and the degree of aggregation using both optical DF microscopy and high-resolution TEM. They were able to employ the combined techniques to analyze the uptake of AuNPs with different shapes and surface coatings into epithelial cells [142].

AuNPs trafficking along microtubules. Nan *et al.* developed a novel strategy for the tracking of AuNPs in 2D with **~ 1.5 nm spatial precision and 25 μs time** resolution by utilizing a quadrant photodiode to record the positions of the AuNPs [145]. This technique is able to clearly resolve the 8 nm individual steps of cargoes that are carried by kinesin, as well as the 12, 16, and 20 nm steps by dynein with high localization precision and high time resolution (**Figure 2.2 B**) [145]. Schneider *et al.* visualized the AuNP-loaded motor proteins traveling along the microtubule using a parabolically-shaped quartz prism-based widefield total internal reflection (TIR) illumination design that allows the detection of single-molecule fluorescence and single-particle scattering with the same setup and high S/N ratios. Their results demonstrated sub-nanometer localization accuracy for the scattering of 40 nm AuNPs, and they imaged the characteristic 8-nm walking step distance of individual kinesin-1 motor proteins along the microtubules [146].

Imaging biological processes. Additionally, DF microscopy incorporating AuNPs can be used for understanding biological processes. El-Sayed and co-workers have reported Au nanospheres functioning as DF probes for cell division [147]. AuNPs localized in the nuclear region were tracked in real time during the mitosis of a HSC-3 cancer cell (**Figure 2.2 C**). In addition, real-time tracking of virus-cell interactions was assisted by AuNPs in order to understand the respiratory syncytial virus infection of HEp-2 cells (**Figure 2.2 D**). Streptavidin (SA)-biotin binding chemistry, a study where AuNPs and virus particles are respectively modified with SA and biotin, allows for the stable binding of AuNPs to viruses without affecting their virulence [148]. A possible concern regarding this type of study is the endocytosis of free AuNPs (unbound to virus) that will complicate the detection.

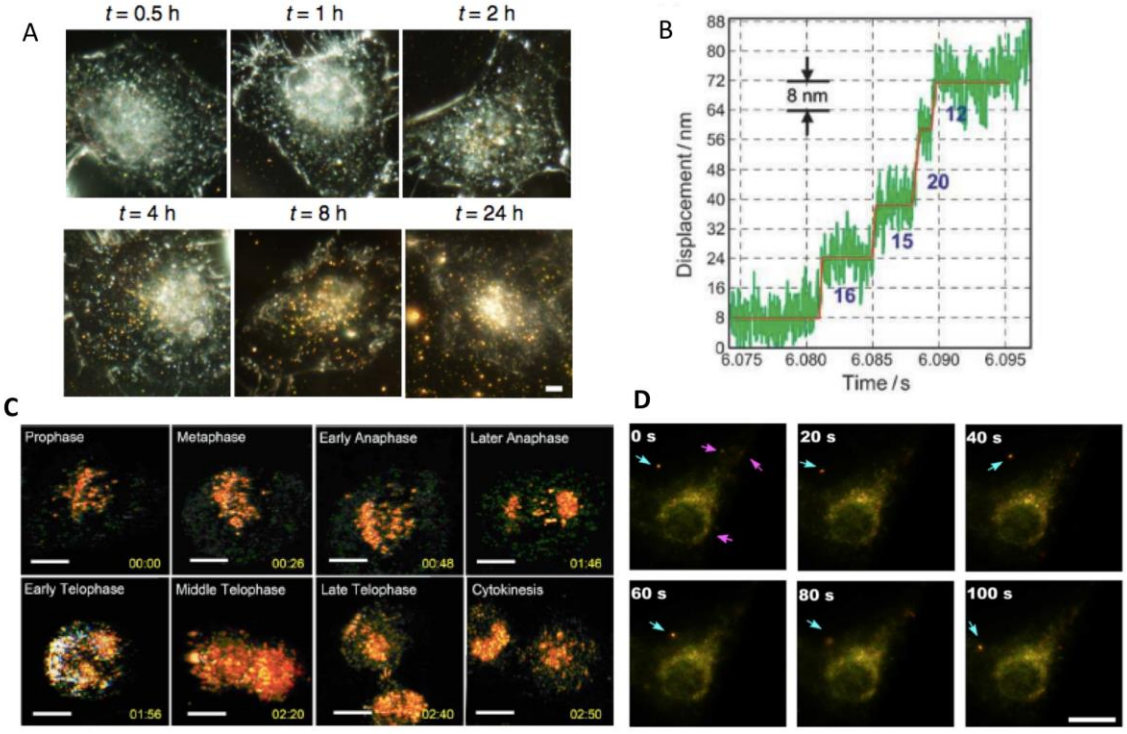

FIGURE 2.2. (A) Dark field (DF) microscopy showing the evolution of AuNP color in HeLa cells at the different durations (0.5-24 h) of incubation. Printed with permission from Springer Nature [144]. (B) The walking steps of cargoes detected that are carried by dynein with ~ 1.5 nm spatial precision and 25 μs time resolution. Printed with permission from

John Wiley and Sons [145]. (C) Human oral squamous cell carcinoma (HSC-3) cell division process (prophase to cytokinesis) visualized by the AuNPs. Printed with permission from SPIE [147]. (D) Real-time tracking (0-100 s) of AuNPs labeled respiratory syncytial virus (indicated by blue and red arrows) infecting HEp-2 cells. Printed with permission from Springer Nature [148].

Measuring biomolecular dynamics and mechanics.

While the location of an individual, isolated nanoparticle can be determined by DF microscopy with nanometer spatial precision due to the strong scattering signal, the resolution for determining the distances between two identical particles is low (limited by the diffraction limit to ~250 nm). Thanks to the SPR shift with the change of inter-particle distances, the detection of close distances between AuNPs is possible. Using this method, the nanometer-level distance between two proteins inside cells was able to be measured, as reported by Rong *et al.* [149]. As shown in **Figure 2.3 A**, in the top case, AuNP-labeled fibronectin-integrin protein complexes are largely separated (separation distance Δ' is larger than AuNP diameter D), and the SPR of the AuNPs are same as individual particles (530 nm). However, in the bottom case, the proteins are close to each other (separation distance Δ'' is smaller than AuNPs diameter D), and the plasmon coupling between individual AuNPs causes a red shift of the SPR to 580 nm. This method can improve the resolution of optical imaging by more than one order of magnitude, where the detection threshold of 15 nm can be obtained with the chosen 530 nm/580 nm filter [149]. However, a possible concern regarding this type of study in general is the aggregation of AuNPs inside cells, which will cause a similar red-shift, and it is difficult to differentiate if this shift is from the small distance of the separated proteins or the AuNPs aggregation. Aside from measuring protein distances inside the cells, Yeung and co-workers recently measured the cell mechanical force using AuNPs and DF microscopy according to the color change [150]. Mechanical force plays important roles in cell signaling for various physiological functions [151],

and AuNP-based optical fluorescence imaging was previously developed to measure small forces in cells [152]. As shown in **Figure 2.3 B**, by using a single plasmonic nanospring that attaches to the cell surface integrins and DF microscopy, the force applied on the spring can result in an SPR alteration, which can be used for real-time measure of forces in live biological systems. In addition, based on the distance-related color change, AuNRs and DF microscopy also enables quantitative imaging of mRNA splice variants in live cells. The probes that Lee et al. developed consist of 40 nm AuNPs functionalized with two oligonucleotides that can match to specific mRNA sequences (BRCA1 mRNA). As shown in **Figure 2.3 C**, the formation of a dimer could cause the SPR color to be red-shifted and intensity to be greatly enhanced. The location and number of dimers can thus be determined and quantified using the signal intensity and spectral peak shift by DF microscopy [153].

AuNRs have also been used to detect the dynamic behavior of proteins. Lambertz *et al.* monitored the oscillations of the MinDE protein wave propagation on from *Escherichia coli* (*E. coli*) membranes [154]. As shown in **Figure 2.3 D,** the attachment of proteins MinD and MinE to the membrane can be detected by the shifting of the AuNRs SPR ($\Delta\lambda$), which exhibits four phases. Enzymatic reactions in live cells can also be indicated by the SPR shift. A single AuNP was used by Zhang *et al.* as a real-time probe for the detection of the NADH-dependent intracellular metabolic enzymatic pathways [155]. The NADH-mediated reduction of Cu^{2+} onto AuNPs that form Au@Cu core-shell nanoparticles causes a red-shift of the SPR spectra of AuNPs (**Figure 2.3 E**). The higher red-shift of the peak indicates the higher NADH concentration.

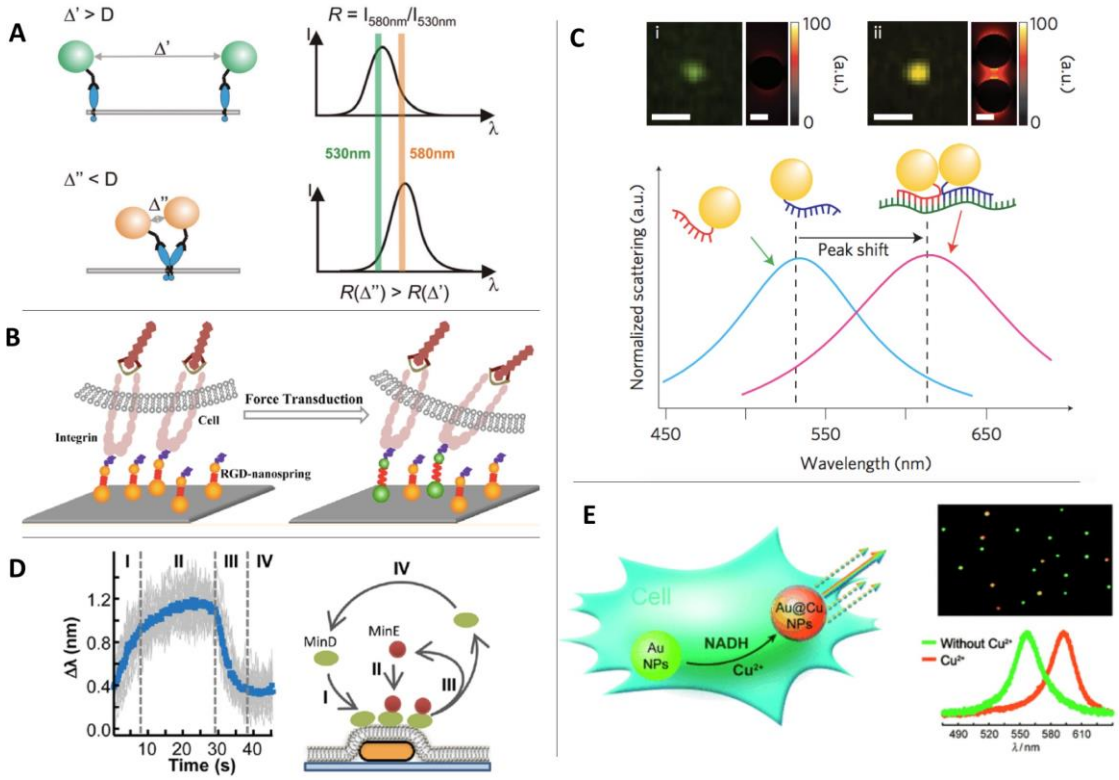

FIGURE 2.3. (A) Schematic of using surface plasmon resonance (SPR) wavelength shift to determine the distance of proteins (labeled by AuNPs) in live cells. If the separation distance (Δ') is larger than AuNP diameter D, the SPR band is at about 530 nm. If separation distance (Δ'') is smaller than D, the SPR band is at 580 nm. Printed with permission from American Chemical Society [149]. (B) Schematic of using SPR shift to determine the cellular mechanical forces. Printed with permission from American Chemical Society [150]. (C) AuNRs enables quantitative imaging of mRNA splice variants in live cells. The real-color images (top) and spectra of monomer and dimer from mRNA splice variants. Printed with permission from Springer Nature [153]. (D) AuNR and dark field microscopy for monitoring protein dynamic behavior on membranes (reflected on the AuNR SPR shift, Δλ, in stage I, II, III and IV during a cycle). Printed with permission from American Chemical Society [154]. (E) AuNPs with Cu^{2+} detection of NADH-dependent intracellular metabolic enzymatic pathways. The deposition of Cu^{2+} on AuNPs causes red shift of SPR. Printed with permission from John Wiley and Sons [155].

***In vivo* dark field imaging.**

Although widely used in single cell imaging, the DF technique has several obstacles that inhibit its application on animal imaging. Light scattering from surrounding tissue is a widely noted drawback of DF microscopy, and it limits the use of this imaging method within deep

tissue. The current *in vivo* DF imaging still exclusively works on the tissue slides sections, such as for observing the AuNPs distribution in tumors, the tumor's vasculature and organs [156, 157]. To characterize the biodistribution profiles of AuNPs, SoRelle *et al.* developed adaptive algorithms for the analysis of hyperspectral DF images that achieve improved sensitivity and specificity with the capability of identifying single nanoparticles in *ex vivo* mouse tissue sections [157]. The dependence on size for the optimal uptake of nanoparticles into brain tissue was highlighted by Betzel *et al.* who used DF images to display the enhanced internalization of glucose-coated 5 nm AuNPs into exosomes in comparison to 20 nm nanoparticles in brain slide sections. AuNPs were then used as tracking probes to map the movement of intranasally administered exosomes through mice focal brain ischemic-like damage, confirming their valuable use as contrast agents in DF microscopy applied to exosome labeling and exosome-based treatment [158].

Plasmon helps improve spatial resolution

DF imaging is yet another method that suffers from the optical diffraction limit, and as such, improving the resolution has been a huge subject of research in recent years [14, 159]. **Figure 2.4 A** shows a traditional working principle of DF microscopy. For selective illumination and decreasing background, Noji and his coworkers developed a simple DF microscope that employed perforated mirror and objective-based TIR. Due to the TIR illumination applied on a thin layer, a low background was achieved (**Figure 2.4 B-D**). The system was applied to visualize the rotation of F_1-ATPase attached to 40 nm AuNPs at 1-2 nm spatial resolution and 9.1 μs temporal resolution with 120º steps and short catalytic dwells on μs-to-ms timescales [160]. Another study established a super-resolution imaging of AuNPs with enhanced DF imaging based on wavelength modulation [161]. Individual bandpass filters were used to reduce the

interference and to differentiate the adjacent AuNP, AuNR and silver nanoparticle at specific SPR wavelengths. The 2D Gaussian fitting algorithm was used to localize the nanoparticles with nanoscale precision.

While such techniques only reduced the interference of overlapping scattering in two dimensions, a very recent study has seen the development of DF imaging that accurately shows the 3D distribution of AuNPs within cells through the reduction of all background interference. This technology, known as orientation-dependent localization microscopy (ODLM), relies on the principle of cross-polarization microscopy to isolate the scattering of polarization-sensitive AuNRs, while intracellular structures incapable of depolarizing light are largely eliminated (**Figure 2.4 E**). Not only does this type of imaging allow for greater accuracy in pinpointing the localization of AuNPs within cells, but it also shows their specific orientation on an individual particle level without the interference of scattering from 3D subcellular structures [162].

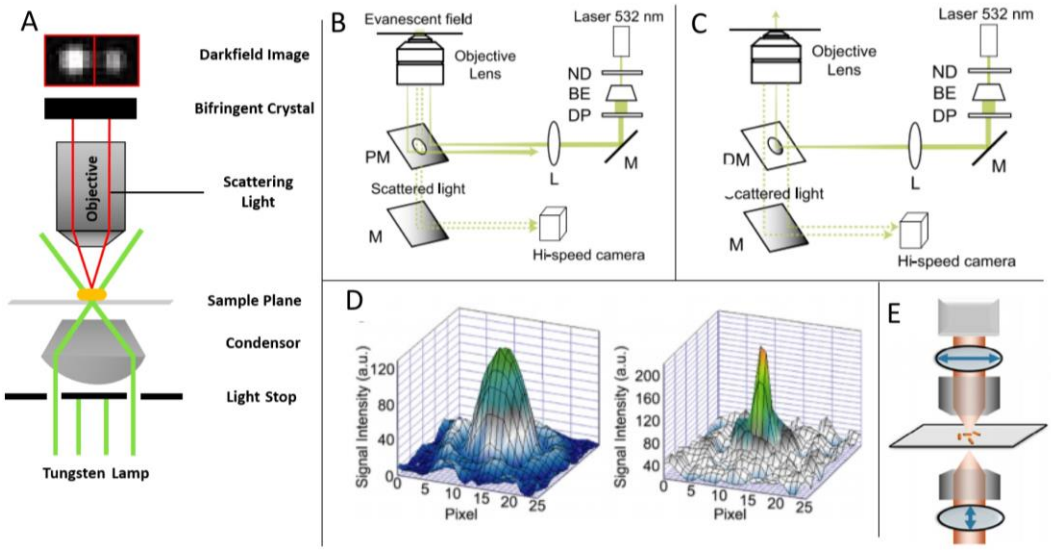

FIGURE 2.4. (A) The working principle of dark field (DF) microscopy. Printed with permission from Iowa State University [163]. (B) Schematic illustrations of objective-type total internal reflection dark-field microscopy (TIRDFM) with a perforated mirror (PM) and (C) vertical illumination dark-field microscopy (VIDFM) with a dot mirror (DM). (ND) neutral density filter, (BE) laser beam expander, (DP) diaphragm, (M) mirror, (L) lens. (D)

Intensity profiles of 40-nm gold nanoparticles by TIRDFM (left) and VIDFM (right). Pixel size = 88.5 nm. The profile was fitted by 2D-Gaussian. FWHM of PSF were 672 ± 36 and 623 ± 41 nm (n = 15), and 259 ± 48 and 212 ± 34 nm (n = 15) in the x- and y directions, for TIRDFM and VIDFM, respectively. Values are means ± SD. B-D are printed with permission from Elsevier [160]. (E) Setup for orientation-dependent localization microscopy (ODLM) for background free 3D imaging. Printed with permission from Springer Nature [162].

1.4.2.2 Differential Interference Contrast (DIC) Microscopy

DIC microscopy utilizes two-beam interferometry in which objects cause a phase shift of the light beams, producing a pseudo-3D, shadowcast image (**Figure 2.5 A**). DIC microscopy allow for the direct observation of many subcellular organelles, such as microtubules, in unstained living cells with sufficiently high contrast. DIC microscopy has been extensively used in cell biology to study microtubule assembly/disassembly dynamics, motor protein-microtubules binding, organelle trafficking in axon, cell division, and even intact organisms such as embryos [164, 165]. AuNPs used as contrast agents in DIC microscopy allows for the imaging of nanoparticles and cellular features simultaneously [166]. Thanks to the high absorption and scattering cross-sections arising from the SPR as well as the excellent photostability of the AuNPs, relatively low illumination light intensity (standard halogen lamp is commonly used) is sufficient for DIC imaging of AuNPs in the cellular environment. This enables the continuous observation of dynamic bio-nano interactions for long periods of time with minimal disruption.

Three-dimensional selective imaging of gold nanoparticles

The challenge of differentiating AuNPs probes from small subcellular features, especially small intracellular spherical vesicles, in DIC images can be relatively easily circumvented by wavelength-dependent DIC microscopy to selectively image AuNP probes in live cells [167]. This method can turn "on/off" the AuNP signals by simply applying two bandpass filters in the light

path. AuNP probes generate high contrast in the SPR wavelength channel, while the non-SPR wavelength channel that "turns off" the AuNP probes, is used as a control (**Figure 2.5 B**).

The use of full NA objective and condenser affords the shallower depth of field and thus better achievable axial (z) resolution than the conventional bright field and DF microscopes for optical sectioning of the samples. It was proven to provide good resolution both laterally and vertically for 3D imaging, which can be conveniently realized with a vertical scan of the focal plane through the specimen to acquire a series of z-stacked images and 3D image reconstructions using software [164]. When combined with AuNP imaging, full NA objective and condenser can be used to characterize the 3D localization and distribution of AuNPs as well as the aggregations of the AuNPs within cells [85, 140, 168]. For example, when the efficiency of different nuclear localization peptides that aid in the nuclear uptake of AuNPs was tested, video-enhanced color DIC microscopy allowed for localization of nanoparticles within HeLa and HepG2 cells [140]. Chithrani *et al.* used the combination of DIC and confocal microscopes to measure the uptake of transferrin-coated AuNPs into cells, where DIC was used to determine the z-positions of the nanoparticles [168]. Similarly, we utilized the optical sectioning ability of DIC microscopy to determine the subcellular location of nuclear targeting AuNPs, which were shown to be trapped and congregated at the outer nuclear membrane (**Figure 2.5 C-F**) [85].

Improving localization, precision, and resolution

It is important to obtain positions of the targeted single nanoparticle probes with high localization accuracy and precision in order to resolve the dynamic motions and interactions. Yet, the intrinsic diffraction limit of light prevents DIC microscopy from resolving nanoparticles that are separated by less than roughly half of the wavelength. The asymmetric point spread functions

(PSF) further complicated the localization in DIC microscopy as they cannot fit into a simple mathematical equation like the common localization strategies used in other imaging techniques [169]. Despite such limitations, recent advancements in both instrumentation and methodology allow researchers to achieve improved resolution and localization of AuNPs in DIC microscopy [169-171]. Chen *et al.* reported the use of a structured illumination DIC (SI-DIC) microscope in the attempt of increasing the lateral resolution of DIC microscopy [170]. A lateral resolution of approximately 190 nm, a value that is double the wavelength found in conventional DIC microscopy, was achieved in the imaging of 53 nm polystyrene beads. This method can be adopted for sub-diffraction-limited imaging of AuNPs. Gu *et al.* reported a model-based correlation mapping method for precise 3D localization of spherical AuNPs and successfully applied the technique to localize 40 nm AuNPs inside fixed HeLa cells as well as to track the AuNPs in live A549 cells [171]. However, the model-based correlation mapping method does not work well for the localization of AuNRs as the DIC image pattern changes with respect to the orientation of the AuNRs. Three different methods have been developed to solve this dilemma [169, 172, 173]. A dual-channel imaging system was developed by Gu *et al.* to localize AuNRs in the bright-field channel using transverse SPR with high accuracy as well as to track the rotational motions of the AuNRs in the DIC channel at the longitudinal SPR wavelength [172]. Zhao *et al.* presented a new localization strategy by combining computer simulated DIC images with the experimentally measured lateral shear distance in order to improve the localization accuracy of AuNRs [169].

Additionally, DIC microscopy has been used to study the interactions between nanoparticles and biomolecules using plasmon resonance energy transfer (PRET) to reveal cellular process within live HeLa cells [174]. This technique relies on the energy transfer from

AuNPs to cytochrome c, a cellular protein involved in several signal transduction pathways, the most notable being the apoptosis signaling pathway. It is quantified by dips in the intensity of nanoparticle emissions that are measured by the change in the AuNPs' DIC contrast upon the interaction with endogenic cytochrome c protein during ethanol-induced apoptosis.

Coupling DIC with other imaging techniques will definitely be a trend in future development. Integrated DIC microscopy will be able to provide more comprehensive molecular and structural information of the biological system and will help to decipher more complex interactions of nanoparticles and biological surroundings in dynamic cellular processes.

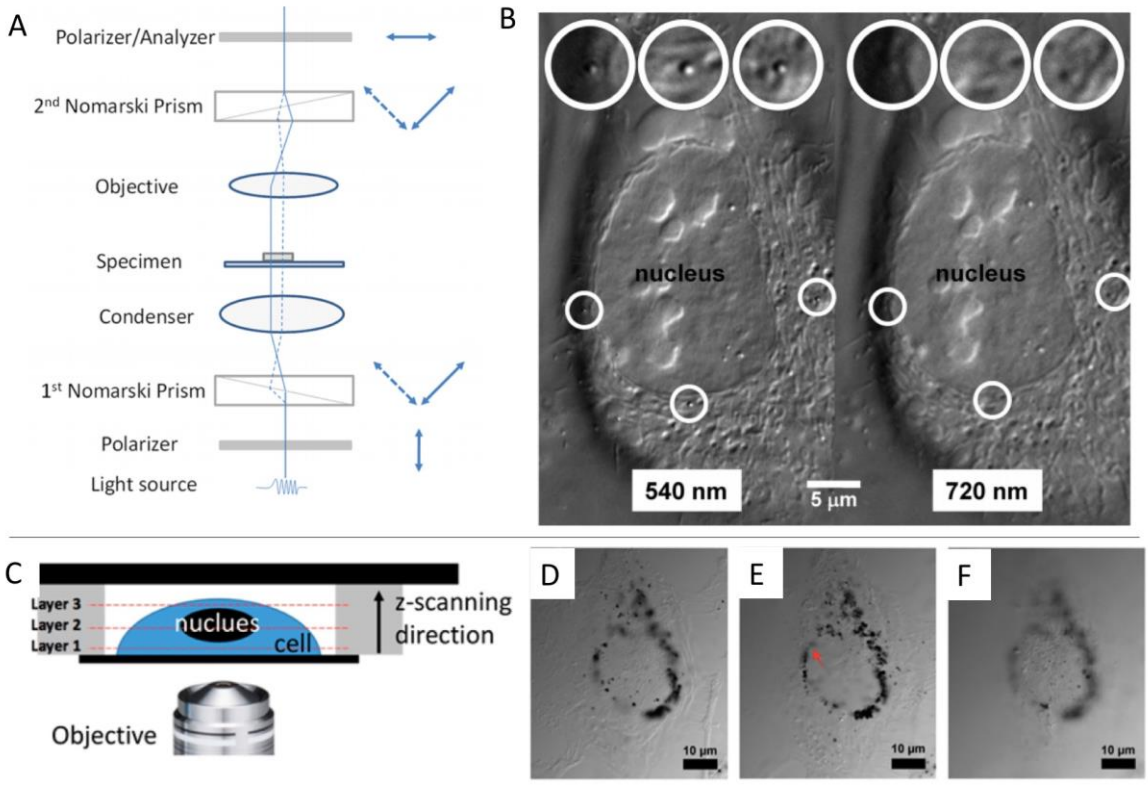

FIGURE 2.5. (A) Differential interference contrast (DIC) microscopy working principle. Printed with permission from American Chemical Society [166]. (B) AuNP probes "turn on" in the surface plasmon resonance (SPR) wavelength channel, while they "turns off" in the non-SPR wavelength channel in HeLa cells. Printed with permission from American Chemical Society [167]. (C) Scheme of optical section for nucleus targeted AuNPs' 3

dimensional cellular distributions, in ovarian cancer cell HEY A8. (D-F) the DIC images from layer 1-3 in C. Printed with permission from American Chemical Society [85].

1.4.2.3 Other Techniques for Visualizing AuNPs.

Interferometric scattering (iSCAT) microscopy

iSCAT is another label-free imaging method for visualizing AuNPs with high spatial resolution and sensitivity. In iSCAT microscopy, the samples are illuminated, and the reflected and scattered lights are collected and interfere at the detector [175]. It is composed of three main parts: (1) reflected light, (2) scattered light, and (3) the interference of the reflected and scattered light [176]. iSCAT collects the scattered light, which is the main signal in a DF image. Different from the DF microscope, the iSCAT has dominated reflected light that is avoided, however, in DF microscopy. The instrumentation set up and the operating principle are shown in **Figure 2.6 A and B**. An iSCAT image of a 30 nm AuNP moving along the microtubule is shown in **Figure 2.6 C** [177].

Using AuNPs as probes, iSCAT is applicable in resolving protein conformational changes down to 2 nm with millisecond temporal resolution [177]. By attaching an AuNP as small as 20-30 nm on targeted motor proteins (such as myosin-5, kinesin-1, and dynein as examples), iSCAT was able to directly observe the structural transitions and protein dynamics [178]. High-resolution tracking of kinesin showed that it uses a two-step powerstroke mechanism for maximum velocity [177]. Hancock group reported direct observation of the binding of individual tubulin dimers to growing microtubules [179]. iSCAT is also used for studying the behavior of lipids. Hsieh et al. achieved 1.9 nm spatial precision at 1 ms temporal resolution for tracking

single particles on supported lipid membranes [180]. To resolve the dynamic molecular interaction between lipid rafts at the nanoscale, iSCAT is employed to record the motion of individual lipids and uses AuNPs as labels [181].

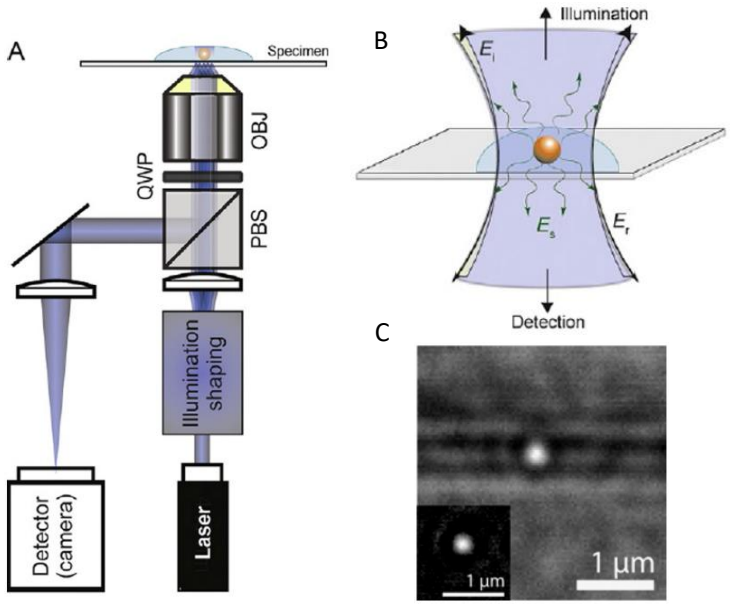

FIGURE 2.6. (A) Optical setup for interferometric scattering (iSCAT) microscopy. OBJ: microscope objective; PBS: polarizing beam splitter; QWP: quarter-wave plate. (B) Operating principle of iSCAT. A and B are printed with permission from Elsevier [178]. (C) Raw iSCAT image of a 30 nm AuNP walking along a microtubule. (Inset) The image after background subtraction. Printed with permission from National Academy of Sciences [177].

Photothermal imaging.

For many of the existing imaging methods that based on AuNPs' Rayleigh scattering, their signal needs to be differentiated from the background. In practice, the minimum size of AuNPs is well above 30-40 nm. Consequently, the detection of smaller AuNPs is challenging. However, for smaller AuNPs, their strong absorbance could be converted to heat that warms up the environment surrounding the AuNPs. The temperature change of the medium will result in a reflection index change that shifts the phase of a transmitted light beam. By using this

"photothermal" imaging, **we can see the AuNPs scale down to ~1 nm in size** [182]. As shown in **Figure 2.7 A**, a green heating laser is focused on the sample and is absorbed by AuNPs as it generates a heat wave. The other red laser is split by a Wollaston prism into two orthogonally polarized beams, one of which coincides with the heating spot of the green laser. The two beams are recombined and the relative phase difference can be identified by the detector. The photothermal imaging is capable of differentiating very small Au nanospheres, which are nearly invisible in DIC microscopy (**Figure 2.7 B-D**) [183]. Recently, Zharov *et al.* demonstrated a super-resolution photothermal microscopy utilizing the non-linear dependence of signal on laser energy, with resolution down to 50 nm [182].

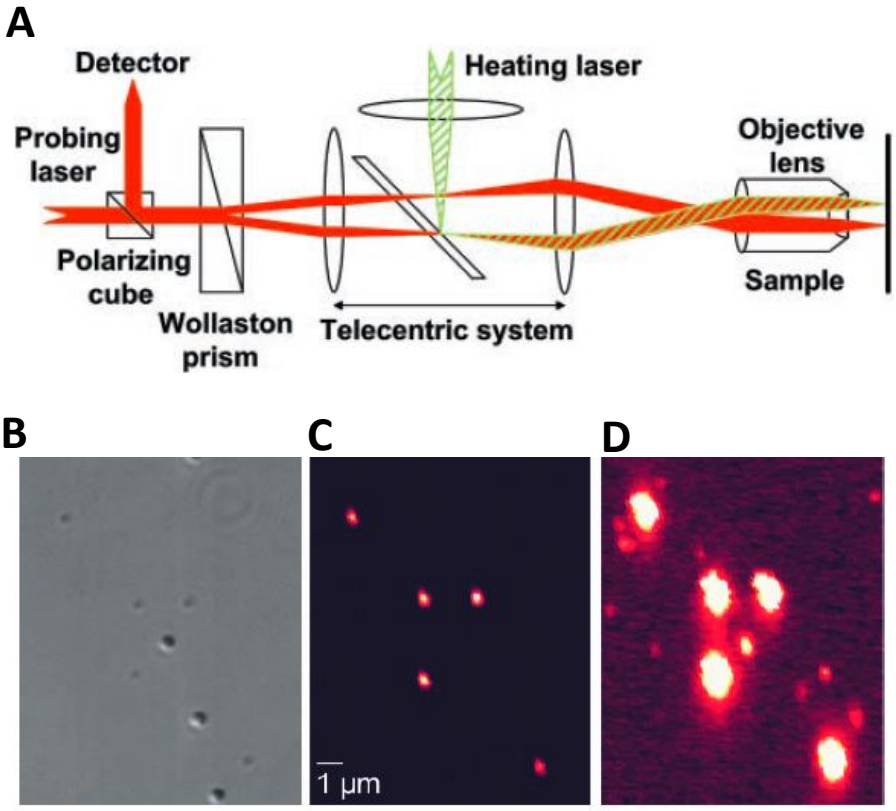

FIGURE 2.7. (A) Optical setup of photothermal optical microscope. (B) Differential interference contrast (DIC) imaging and (C-D) photothermal images of a sample containing 300 nm latex spheres, 80 nm Au nanospheres, and 10 nm Au nanospheres. DIC image shows the 80 nm Au nanospheres and 300 nm latex spheres, while the 10 nm Au

nanospheres are invisible. (C) The photothermal image with lower laser heating intensity showing the 80 nm Au nanospheres. (D) The photothermal image with higher laser heating intensity enables clear visualization of 10 nm Au nanospheres with 80 nm AuNPs reaching saturated detection. Printed with permission from American Association for the Advancement of Science [183].

1.4.3 Molecular Fingerprinting by Surface-enhanced Raman Scattering (SERS)

Compared with other imaging and sensing techniques, SERS can provide highly sensitive and abundant structural information (**Figure 2.8 A**). SERS can detect biomolecules of interest that surround the nanoparticles by a factor of over 10 orders of magnitude compared to normal Raman signals [21]. Furthermore, SERS signals increase in sensitivity when the distance between the Raman reporters and the AuNPs decreases – the shorter the distance, the stronger the SERS signal [184], making it ideal for studying bio-nano interactions. The powerful targeting of nanoparticles through ligand conjugation creates high specificity on the locations of the biomolecules conjugated nanoparticles. The surface plasmon of AuNPs is stable and provides consistent signals for long-term imaging. The range of accessible wavelengths for SERS detection extends from the whole visible spectrum to NIR [185], the latter accounting for the maximum penetration depth within biological samples.

1.4.3.1 Single Molecule SERS

Ultrasensitive detection at extremely low concentrations (femto- or attomole) is limited by diffusion; therefore, the time needed to find and detect a molecule could be unrealistically long. To solve this problem, de Angelis and co-workers developed a method that combines super-hydrophobic artificial surfaces and nanoplasmonic structures to detect a few molecules (10^{-18} mol L^{-1}). By loading a drop of solution that contains the molecules onto a super-hydrophobic surface (periodical silicon micropillar arrays with plasmonic nanostructures on the

top of the pillars), the droplet gradually evaporates to increase the concentration of the molecules inside and shorten the detection time with SERS or surface-enhanced fluorescence (**Figure 2.8 B and C**) [186]. A similar but more practical strategy has been reported by Yang *et al.* for the quantitative detection of rhodamine 6G (R6G) down to 10^{-15} mol·L^{-1} using a platform named slippery liquid infused porous surface-enhanced Raman scattering (SLIPSERS), in which a drop of the analytes and SERS substrates (e.g., AuNPs) were added onto a slippery surface, and the resulting evaporation of the liquid droplet allows for nearly 100% analyte collection efficiency (**Figure 2.8 D and E**) [187].

DNA origami has been recently utilized for directed formation of Au nanostructure for single-molecule SERS due to its ability to exert precise control over the geometrical configuration such as fabricating the Au nanodimers with a hot spot. Sen *et al.* prepared Au nanostar dimers on dimerized rectangular origami structures, with 7 and 13 interparticle gaps and achieved 2×10^{10} and 8×10^{9} enhancement, respectively [188]. Ding's group constructed 80 nm plasmonic bowtie nanostructures via a DNA origami-based bottom-up assembly strategy that have an approximate 5 nm gap and obtain SERS enhancement about 10^{9} [189]. The DNA origami technique is very promising for revolutionizing the SERS detection, providing accurate fabrication methods for SERS probes with a high degree of customization.

1.4.3.2 SERS in Studying the Bio-nano Interaction

Researchers have tracked the nanoparticle motion inside living cells and have provided the molecular maps of organelle transport and liposomal accumulation of the AuNPs, indicating the different types of transport pathways [190, 191]. The SERS spectra changes in space and time during AuNP endocytosis provide the change in the cellular environment (**Figure 2.8 F**).

Consequently, the SERS spectra provide molecular maps dynamics during organelle transport and lysosomal accumulation of AuNP [190]. In addition, SERS was used to monitor the real-time photothermal ablation of cancer cells, for "seeing-and-treating". When exposed to light, AuNPs can convert light energy to heat, which can be used to kill cancer cells (otherwise known as the photothermal effect). Ali *et al*. used SERS to study the molecular mechanism of AuNR-assisted photothermal ablation and observed an increase in specific Raman bands during the process [192]. A similar method for SERS-guided photothermal therapy has been used by Sun *et al.* [193]. SERS has also been employed to image and explore the biosynthetic mechanism of AuNPs. As shown in the study by Lahr *et al*. the intracellular and extracellular AuNP biosynthesis process by green algae was revealed by SERS by identifying the surface-associated biomolecules. The SERS peaks indicate the participation of identified molecules in elucidating the mechanism of the biosynthetic process [194].

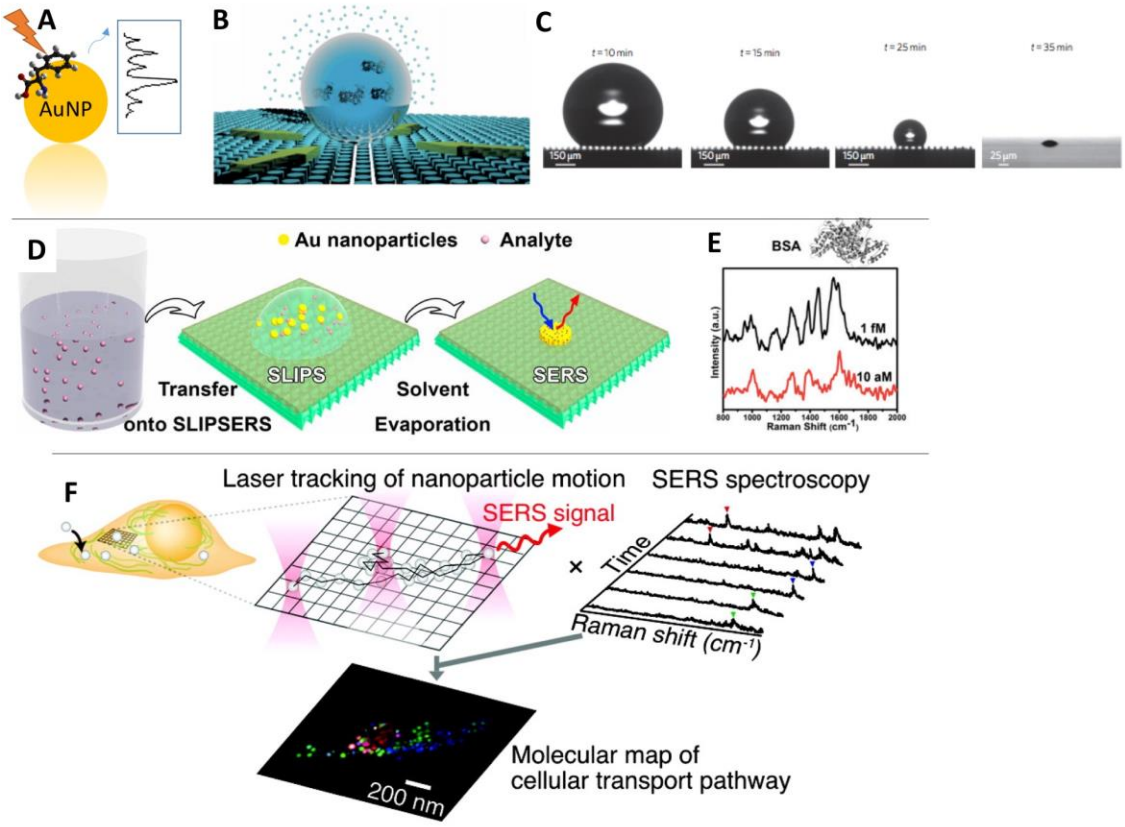

FIGURE 2.8. (A) Principle of surface-enhanced Raman scattering (SERS). (B) Sing-molecule detection by super-hydrophobic surface (periodical silicon micropillar arrays with plasmonic nanostructures on the top of the pillars). (C) The optical images of the analyte drop evaporating at four different times. The B and C are Printed with permission from Springer Nature [186]. (D) Single-molecule detection platform named slippery liquid infused porous surface-enhanced Raman scattering (SLIPSERS). (E) Ultra-sensitive detection of BSA protein using the platform of D. D and E are printed with permission from National Academy of Sciences [187]. (F) SERS spectra changes during AuNP endocytosis. Printed with permission from American Chemical Society [190].

1.4.3.3 *In vivo* SERS Imaging for Tumor Diagnosis and Therapy

In 2008, one of the pioneer studies demonstrated the ability to collect the SERS spectra from tumor-bearing mice that were injected with AuNP probes [195]. Recently, several studies reported the use of SERS *in vivo* that mainly focus on tumor detection and imaging. SERS has been applied to *ex vivo* analysis of tissue slides. It could assist in cancer surgery to ensure complete removal of tumors, with fast speed and high sensitivity. Wang *et al.* developed probes that targeted and visualized a multiplexed panel of cancer biomarkers. The AuNP probes were then put onto freshly excised tissues to determine the presence of cancer cells. This technique could achieve in fast detection (less than 15 minutes) for potential intraoperative use in guiding breast-conserving surgeries (**Figure 2.9 A**) [196]. A dual probe approach that consists of two types of SERS probes (one EGFR-specific and one non-specific) was applied to fresh tissue for measuring the EGFR concentration with the subtraction of the background signal [197]. Kircher *et al.* showed a triple-modality magnetic resonance imaging (MRI)–photoacoustic imaging–Raman imaging (MPR) nanoparticle (**Figure 2.9 B**), where SERS was used to accurately delineate the margins of brain tumors in living mice due to its ultrahigh sensitivity and spatial resolution. Raman imaging allowed clear signal from particles down to 50 pM, which is very low for *in vivo* imaging [198]. Although working well in glioblastoma mouse models, this method has not been very successful in other extracranial tumor models, a result possibly due to the lower enhanced permeability and retention EPR effect, as mentioned by the one of the group's recent paper [199].

1.4.3.4 Recent Improvements of Gold Nanoparticle-based SERS.

Although the SERS probes have high sensitivity, the Raman intensity is greatly attenuated as it travels through tissue due to scattering. To increase the tissue penetration, a combination of the deep Raman spectroscopy with surface-enhanced, spatially offset Raman spectroscopy (SESORS) was developed and greatly improved the penetration depth from less than 5.5 mm to 25 mm thickness [200]. As mentioned earlier, the Raman reporter in the NIR range could reduce the tissue scattering greatly. Gold nanostructures such as AuNRs could assist in this purpose. Maltzahn *et al*. used nanorods coated with SERS active molecules that could be uniquely distinguished *in vivo*, over a spectral sharp bandwidth of 6 nm in the NIR (is much smaller than that of semiconductor quantum dots (QDs) (~30 nm FWHM), organic fluorochromes, and Raleigh scattering nanoparticles). This platform has been used for both SERS imaging and plasmonic photothermal therapy in mice [201]. Qian *et al*. used functionalized AuNRs (conjugated with Raman markers), for sentinel lymph node (SLN) mapping and tumor targeting of mice, as well as for the observation of the distribution and excretion of intravenously injected AuNRs in deep tissues through purely optical imaging *in vivo* [202].

The studies that use SERS as an imaging tool are greatly limited by resolution and speed. Kang *et al.* developed a method to achieve high-speed and high-resolution live cell SERS imaging, using NIR excitation (785 nm) and high-speed galvano mirror-equipped confocal Raman microscopy system. This system leads to accomplish the high resolution (50 × 50 pixels) single live cell imaging within 30 s (10 ms/pixel) and with subcellular resolution of cytoplasm, mitochondria, and nucleus [203]. The SERS-sensitive AuNPs have a highly narrow intra-nanogap (1.2 nm) and Raman markers embedded, allowing for high-sensitive imaging.

To improve the SERS probes for high-sensitive bioimaging, bi-layered Raman-intense gold nanostructures with hidden tags (BRIGHTs) were developed in 2013. The Raman reporters are trapped between the core and shell of the gold nanostructure. This design exhibited great stability and demonstrated more than two orders of magnitude in the enhancement of the SERS signal compared with conventional AuNP SERS probes [204].

SERS presents its own problems for spectroscopy, such as the complex and overlapping Raman bands that are sometimes difficult to understand. In many cases, the SERS bands are a mixture of all types of molecules in the environment of AuNPs. The method used in El-Sayed's lab utilized mass spectrometry along with SERS to improve the understanding of the cellular process in plasmonic photothermal therapy (PPTT). By using metabolomics and proteomics, the changes in SERS bands can be assigned to specific chemical compounds within the cells with an improved degree of confidence (**Figure 2.9 C**) [192].

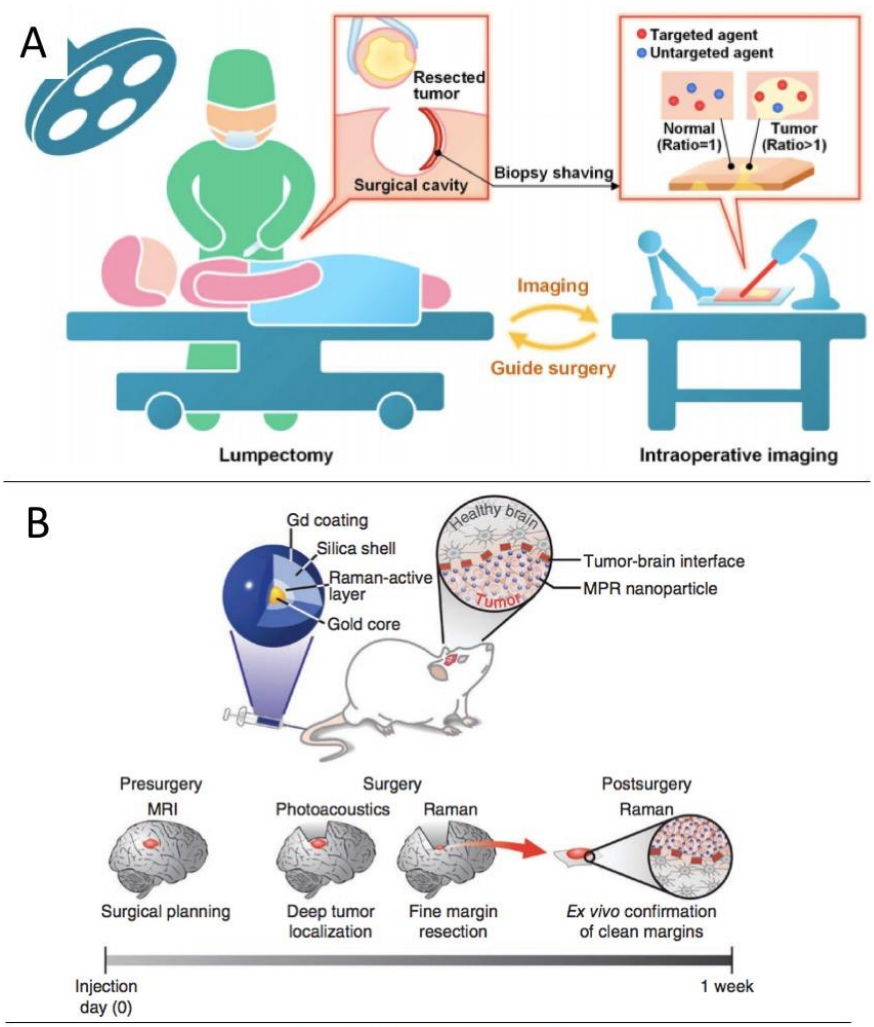
A
Resected tumor
Surgical cavity
Biopsy shaving
Targeted agent
Untargeted agent
Normal (Ratio=1)
Tumor (Ratio>1)
Imaging
Guide surgery
Lumpectomy
Intraoperative imaging
B
Gd coating
Silica shell
Raman-active layer
Gold core
Healthy brain
Tumor
Tumor-brain interface
MPR nanoparticle
Presurgery
MRI
Surgery
Photoacoustics
Raman
Postsurgery
Raman
Surgical planning
Deep tumor localization
Fine margin resection
Ex vivo confirmation of clean margins
Injection day (0)
1 week
C
Raman Spectroscopy
750
1000
1207
1580
Intensity (a.u.)
2 min
1 min
Ctrl
Raman Shift (cm -1)
Phenylalanine Raman Peaks
Laser
PPTT
NPs
HSC-3 Cell
Metabolomics
Phenylalanine
Phenylalanine Derivatives
Phenylalanine Containing Peptides
Proteomics
Phenylalanine Metabolism Pathway
Apoptosis

FIGURE 2.9. (A) Surface-enhanced Raman scattering (SERS) aids cancer surgery. Printed with permission from Springer Nature [196]. (B) Schematic of SERS probes for confirming the brain tumor margins. Printed with permission from Springer Nature [198]. (C) SERS and mass spectrometry-based proteomics and metabolomics for understanding the cell death mechanism after plasmonic photothermal therapy. Printed with permission from American Chemical Society [192].

1.4.4 Conclusions and future outlook

Here we provide a survey of the recent advances regarding the use of AuNPs and optical imaging together for application in biological and clinical studies. After the massive development in the synthesis and surface modification of AuNPs for decades, we now have gained great knowledge of this type of nanoparticle. Various types of AuNPs have been experimentally and theoretically studied for their optical properties and biological applications. Nonetheless, there are still many challenges, issues and opportunities for further exploration in this field. On the technological development side, the following improvements are desirable.

(1) While 2D single particle tracking (SPT) techniques are well established, 3D SPT remains challenging. However, in most occasions, 3D information is much needed in order to recover the bio-nano interaction accurately. In general, 3D SPT techniques rely on simultaneously recording multiple images or manipulating the point spread function. Significant amounts of effort have been dedicated towards the development of 3D SPT for bio-nano interaction [173, 205]. Future development is still needed to provide the multi-particle 3D tracking ability with expanded tracking range (from a few micrometers in depth to the whole cell thickness) and sub-diffraction-limited resolution.

(2) The spatial-temporal distribution of nanoparticles in cells can be monitored with several microscopic methods with high resolution. However, due to the plasmon

coupling effect, it is difficult to discern the small distances between adjacent AuNPs [206], resulting in large uncertainties in the localization of AuNPs. To measure the inter-particle distances, one strategy involves using "plasmon rulers" with high sensitivity. The plasmon ruler is based on the spectra-shift of the SPR when two plasmonic AuNPs approach each other with sensitive color changes under the microscope. Although the SPR shifting is regarded as a sensitive detection of molecules in live cells, concerns arise since the stability and the aggregation of AuNPs can also affect the SPR peak. For example, the red-shift of the SPR peak could also result from AuNPs aggregation, thus complicating the detection of biomolecules.

(3) Traditional methods of AuNP fabrication are usually based on seed growth methods or lithography. Recently, new breakthroughs such as the usage of DNA self-assembly for synthesizing plasmonic gold structures in literally any size and shape [207] provide new possibilities for fabricating ultra-sensitive hot-spots for single-molecule imaging by SERS and PEF.

(4) Advanced scattering or fluorescence-based imaging techniques with increased signal-to-noise ratios and resolution can be coupled with other technological innovations to further improve imaging capabilities of AuNPs *in vivo*. However, the practical application of *in vivo* imaging is still difficult due to the low penetration depth of the scattered light in tissue samples. To lower the scattering background and improve the detection depth, AuNPs that scatter NIR light (such as AuNRs, core-shell AuNPs, *etc.*), especially in the NIR II window (1000–1700 nm), should be developed and used [208].

On the application side, there are also major challenges: First, it is difficult to acquire the fundamental understanding of bio-nano interactions in complex biological environments. While most of the past and current studies focus on observing the nanoparticles' behaviors in internalization, transport and bio-distribution, the detailed mechanism of how the nanoparticles interact with different biomacromolecules, such as proteins, and how they trigger the subsequent biological response is still unknown. The advancement of the super-resolution microscopic techniques is promising in shining a light on the basic understanding of this process in real time. Second, the clinical application is still lacking, which requires more information on the long-term toxicity of AuNPs *in vivo*. The safety of AuNPs in clinical use is still questionable. However, several recent reports estimated the toxicity of AuNPs in mice that seems to accumulate in the liver and spleen, but no obvious toxicity effect is observable [40].

After summarizing current advance of using gold nanoparticles in optical imaging and biological sensing, we are introducing our recent developments for using the SERS and Rayleigh scattering properties for detecting biological processes and studying bio-nano interation, in Section 2.2 and 2.3.

1.5 Simultaneous Time Dependent Surface-Enhanced Raman Spectroscopy Reveals Cancer Death Mechanisms Associated With Gold Nanorod Photothermal Therapy[192]

Note: Yue Wu and Moustafa Ali have equally contributed to designing, performing, analyzing, and writing the research in the 2.2 section.

Summary. In cancer plasmonic photothermal therapy (PPTT), plasmonic nanoparticles are used to convert light into localized heat, leading to cancer cell death. Among plasmonic nanoparticles, gold nanorods (AuNRs) with specific dimensions enabling them to absorb near-infrared laser light have been widely used. The detailed mechanism of PPTT therapy, however, still remains poorly understood. Typically, surface-enhanced Raman spectroscopy (SERS) has been used to detect time-dependent changes in the intensity of the vibration frequencies of molecules that appear or disappear during diff erent cellular processes. A complete proven assignment of the molecular identity of these vibrations and their biological importance has not yet been accomplished. Mass spectrometry (MS) is a powerful technique that is able to accurately identify molecules in chemical mixtures by observing their m/z values and fragmentation patterns. Here, we complemented the study of changes in SERS spectra with MS-based metabolomics and proteomics to identify the chemical species responsible for the observed changes in SERS band intensities during PPTT. We observed an increase in intensity of the bands at around 1000, 1207, and 1580 cm^{-1},

which were assigned in the literature to phenylalanine, albeit with dispute. Our metabolomics results showed increased levels of phenylalanine, its derivatives, and phenylalanine-containing peptides, providing evidence for more confidence in the SERS peak assignments. To better understand the mechanism of phenylalanine increase upon PPTT, we combined metabolomics and proteomics results through network analysis, which proved that phenylalanine metabolism was perturbed. Furthermore, several apoptosis pathways were activated via key proteins (e.g., HADHA and ACAT1), consistent with the proposed role of altered phenylalanine metabolism in inducing apoptosis. Our study shows that the integration of the SERS with MS-based metabolomics and proteomics can assist the assignment of signals in SERS spectra and further characterize the related molecular mechanisms of the cellular processes involved in PPTT.

1.5.1 Introduction

Plasmonic nanoparticles offer a powerful means to follow dynamic changes associated with intracellular molecular events in real time [209, 210],[211]. Their localized surface plasmon resonance (LSPR) confers these particles unique optical properties. For example, the electromagnetic fields on the surface of plasmonic nanoparticles are greatly increased and exhibit exponential decay patterns following non-radiative (heat) or radiative (e.g., light-scattering) processes [212, 213]. Raman scattering from the molecules localized near the plasmonic nanoparticles' surface is therefore enhanced by orders of magnitude, resulting in the well-known surface-enhanced resonance spectroscopy (SERS) phenomenon [214], [215]. SERS has been successfully applied to single cell analysis, where plasmonic gold nanoparticles are placed inside the cell and the resulting SERS spectrum collected in order to record the intracellular microenvironment changes occurring over

time near the nanoparticles. Our group reported on the spectral changes observed by SERS during the full cell cycle of a single cancer cell [216]. The time required to kill cancer cells, associated with the time taken for the SERS spectrum to stop changing when the cells were given anti-cancer drugs [212],[216] or were heated [217], was also determined. However, the molecular species associated with the observed SERS bands could not be. confidently assigned, preventing elucidation of the molecular mechanisms involved in these critical cellular processes. Photothermal therapy has its foundation in the targeted destruction of cancerous cells *via* the heat released by gold nanorods (AuNRs) following near-infrared (NIR) radiation absorption. The so-called "water wavelength window" between 700 and 1200 nm is widely considered to be the optimal spectral region for conducting PPTT[23], [218], as tissue and water absorption are minimized in this range. AuNRs, on the other hand, readily absorb NIR laser light, resulting in effective photothermal generators for both *in vitro* and *in vivo* applications. AuNRs-based PPTT has been successful at inducing cancer cell apoptosis [219], resulting in in vivo tumor removal[220], [221], [222].

Despite the operational success of PPTT, the molecular mechanisms associated with PPTT-induced apoptosis remain largely unknown or under dispute. We observed PPTT-induced apoptosis initiated through heat-shock proteins previously [223], while several reports indicate it is mediated by the mitochondrial apoptotic pathway via Bid activation and caspase 3 activity [56]. Although SERS reports on the real-time biomolecular dynamics in the microenvironment associated with the PPTT process, SERS spectra from cells are incredibly complex, reflecting overlapping signals from a variety of proteins and metabolites that are difficult to assign to individual species. It has

been reported, for example, that the 1000 and 1580 cm^{-1} peaks showed significant increases during cell apoptosis [216], with great debate about their assignment [224]. One report in the published literature assigned the 1000 cm^{-1} signal to phenylalanine[225], while a different report assigned it to tryptophan[225]. Furthermore, it has been argued8 that these SERS signals actually reflect changes in protein structure, a topic that is still being intensively debated. One hypothesis states that the 1000 cm^{-1} signal is indicative of the exposure of protein hydrophobic rings following conformational changes [216], while others report that the protein conformation change induced by adding methanol or sodium dodecyl sulfate (SDS) [226] or increasing temperature [217] does not alter the intensity of the 1000 cm^{-1} peak, contradicting the hypothesis that this signal is associated with alterations in protein conformation.

Herein, we monitored the SERS spectral signature in vitro during apoptosis as a function of PPTT exposure time. We also performed metabolomics and proteomic studies on cell lysates under identical PPTT conditions. Integrative multi-omics network analysis revealed specific alterations that explain the underlying changes in SERS spectral data, demonstrating the power of combining SERS with MS for studying cellular processes following PPTT.

1.5.2 Methods

Materials. Tetrachloroauric acid trihydrate (HAuCl4·3H2O), trisodium citrate, NaBH4, ascorbic acid, CTAB, $AgNO_3$, 4-(2-hydroxyethyl)-1-piperazineethanesulfonic acid (HEPES), NaCl, and sodium deoxycholate (SDC) were purchased from Sigma-Aldrich (USA). Methoxypolyethylene glycol) thiol (mPEG-SH, MW 5000) was

purchased from Laysan Bio, Inc. Cell-penetrating peptide RGD (RGDRGDRGDRGDPGC) and nuclear localization signal NLS (CGGGPKKKRKVGG) peptides were obtained from GenScript, Inc. Dulbecco's phosphate-buffered saline (PBS), Dulbecco's modified Eagle's medium (DMEM), fetal bovine serum (FBS), antibiotic solution, and 0.25% trypsin/2.2 mM EDTA solution were purchased from VWR. Mammalian cell protease inhibitors were purchased from Roche Applied Sciences, sequencing grade trypsin was purchased from Promega, and Lysyl endopeptidase (Lys-C) was from Wako.

Instrumentation. Gold nanoparticles were imaged using a JEOL 100CX-2 transmission electron microscope, and their average size was then measured by ImageJ software. UV−vis spectra were obtained using an Ocean Optics HR4000CG UV−NIR spectrometer. SERS spectra were collected using a Renishaw InVia Raman microscope equipped with a 785 nm diode Raman excitation laser and a Leica optical microscope. Comprehensive metabolomics analyses were performed with ultra-performance liquid chromatography−mass spectrometry (UPLC-MS), using a Waters ACQUITY UPLC H Class system fitted with a Waters ACQUITY UPLC BEH C18 column (2.1 mm × 50 mm, 1.7 μm particle size, Waters Corp., Milford, MA, USA), coupled to a Xevo G2 QTOF mass spectrometer (Waters Corp., Manchester, UK) with an electrospray ionization source. The typical resolving power and mass accuracy of the Xevo G2 QTOF mass spectrometer were 25 000 (fwhm) and 1.8 ppm at m/z 554.2615, respectively. Proteomics analysis was done on a hybrid dual-cell quadrupole linear ion trap−orbitrap mass spectrometer (LTQ Orbitrap Elite, Thermo Fisher) with Xcalibur 3.0.63 software. Flow cytometry experiments were conducted on a BD LSR II flow cytometer (BD Biosciences).

Synthesis, Conjugation, and Characterization of AuNSs and AuNRs. Gold nanospheres with an average diameter of 30−40 nm were synthesized using the citrate reduction method. Briefly, 200 mL of 0.254 mM HAuCl4·3H2O solution was heated until boiling and then reduced by adding 5 mL of 0.35% of trisodium citrate. The solution was then left heating until it turned wine red, followed by cooling under water flow. The citrate-stabilized AuNSs were first centrifuged at 5000g for 10 min and then redispersed in deionized (DI) water to remove extra citrate for the next step of conjugation. AuNRs with an average size of 25 nm × 6 nm (length × width) were synthesized using a seedless growth method. Briefly, 5 mL of 1.0 mM HAuCl4 was added to a mixture of 5 mL of 0.20 M CTAB, 250 μL of 4.0 mM $AgNO_3$, and 8 μL of 37% HCl. Next, 70 μL of 78.8 mM ascorbic acid was added, and then 15 μL of 0.01 M of ice-cold NaBH4 was immediate injected. The solution was left undisturbed for 12 h, followed by centrifugation at 21000g for 50 min. It was redispersed in DI water, and a second centrifugation at 19000g for 40 min removed the extra CTAB. TEM was used to measure the sizes and homogeneity of the nanoparticles. AuNSs and AuNRs were then conjugated according to previous work.8 First, mPEG-SH (1 mM) was added to the nanoparticles overnight to achieve about 1000 ligands on each particle. The PEGylated nanoparticles (1 nM) were then treated with RGD (1 mM) and NLS (1 mM) to achieve 10^4 and 10^5 molar excess, respectively. The number of the ligands bound to the AuNPs was about 25% of the added ligands, evaluated on the basis of Ellman's protocol [227]. The solution was then shaken overnight at room temperature. Excess ligands were removed by centrifugation. A UV−vis spectrometer and zetasizer were used to test the conjugation. Surface

modification causes a red shift of the UV−vis spectra due to the change in the dielectric constant of the surrounding environment of AuNSs.

Cell Culture, AuNPs Incubation, and Plasmonic Photothermal Therapy. Human oral squamous cell carcinoma (HSC-3) cells were grown in DMEM medium containing 10% (v/v) FBS and 1% (v/v) antibiotic solution. Cells were kept at 37 °C in a humidified incubator under 5% CO2. HSC-3 cells were incubated overnight with 2.5 nM AuNRs in complete media and then were exposed to a CW laser (808 nm 5.8 W/cm^2) for different times. The concentration of nanoparticles was carefully chosen to avoid cytotoxicity or perturbation of the cell cycle.

In Vitro SERS Measurement. Time-dependent SERS spectra were collected throughout the NIR laser exposure period to monitor molecular changes in the plasmonic nanoparticle microenvironment during photothermal heating of the AuNRs. The Raman laser was directed into a microscope and, after focusing on the sample by a 50×/0.75 N.A. objective, formed a 1−2 μm spot size. Spectra of molecules in the single cell were measured with a 1200 lines/mm grating and collected by a CCD detector in the range of 400−1800 cm^{-1} using a Renishaw InVia Raman spectrometer. Spectrum baseline was removed using R Package Baseline (version 1.2-1). Dark-field images were taken by a Lumenera Infinity2 CCD camera. For SERS studies, the cells were seeded on glass coverslips in complete growth medium for 24 h to achieve a 40% final confluence before SERS study. The cells were then incubated with 0.05 nM PEG/RGD/NLS-functionalized AuNSs in supplemented DMEM cell culture medium for 24 h. Six hours before the SERS examination, the cell media (with AuNSs) were removed, and a 2.5 nM concentration of AuNRs suspended in supplemented medium was added to the cells to perform PPTT.

Apoptosis/Necrosis Assay. HSC-3 cells were cultured in 12-well plates for 24 h and then treated with a 2.5 nM concentration of AuNRs@NLS for 24 h. After AuNRs incubation, PPTT was applied for different time periods. Before the apoptosis/necrosis assay, the cell culture medium was removed, and cells were collected after trypsinization, followed by washing with cold PBS twice. The cells were the dispersed in 493 mL of Annexin V binding buffer, and 5 μL of Annexin V FITC (BioLegend) and 2 μL of PI (BioLegend, 100 μg/mL) were added to the cell suspension and incubated for 15 min at room temperature. The cells were then filtered and subjected to flow cytometry analysis using a BSR LSR II flow cytometer (BD Biosciences). A 488 nm laser was applied for excitation, and FITC was detected in FL-1 using a 525/30 BP filter, while PI was detected in FL-2 using a 575/30 BP filter. Standard compensation using unstained and single-stained cells was done before performing actual experiments. FlowJo software (Tree Star Inc.) was used for analysis of the viable, apoptotic, and necrotic cells from at least 10 000 events.

Sample Preparation for Metabolomics Experiments. Cells were cultured in 60 mm Petri dishes. The culture media was removed, and cells were washed three times with PBS, followed by a wash with DI water for 2 s and immediate removal of the wash solution. Immediately, 7 mL of metabolite extraction solvents (HPLC-grade methanol:acetonitrile (ACN):0.5 M formic acid (FA), 2:2:1 v/v/v, −20 °C) was added for quenching and lysing the cells.65 Cells were then scraped down, and the cell suspension was transferred to centrifuge tubes, followed by vortexing and sonication in an ice−water bath and incubation on ice for 15 min for metabolite extraction. The cell suspension was then centrifuged at 20400g at 4 °C for 15 min. Solvent in the sample was evaporated

using a CentriVap vacuum concentrator until dryness. The dried samples were kept at −80 °C until analysis.

Sample Preparation for Proteomics Experiments. Cells were cultured in 60 mm Petri dishes. Ice-cold lysis buffer (50 mM HEPES, pH 7.8, 150 mM NaCl, 0.1% SDS (optional), 0.5% SDC, 1% Triton X 100 or NP-40, phosphatase inhibitors) was added directly to the cells after they were washed twice with PBS. The cells were then scraped down and the obtained mixtures homogenized with sonication and vortexing. Cell debris was then removed by centrifugation at 18000g for 20 min at 4 °C. Four volumes of ice-cold acetone:ethanol:acetic acid (50:50:0.1 v/v/v) was added to the supernatant to precipitate the proteins at −20 °C overnight. After centrifugation, the protein pellet was redissolved in denaturing buffer (pH 8.0) containing 8 M urea and 50 mM HEPES, and the protein concentration was tested using a Bradford assay. The disulfide bonds in the protein solution were reduced by 2 mM dithiothreitol at 37 °C for 2 h and subsequently alkylated by addition of 6 mM iodoacetamide. The solution was kept in darkness at room temperature for 40 min.

Ultra-Performance Liquid Chromatography (UPLC)-MS Metabolomics Analysis. Before analysis, ultra-pure water was added to each dried sample to obtain a final biomass concentration of ~50 000 cells/μL. Samples were further vortexed and then centrifuged at 15 000 rpm for 10 min at 4 °C. The supernatant of each biological sample was transferred to auto-sampler vials for UPLCMS analysis. Gradient elution was employed in the chromatographic separation method using 0.1% acetic acid in water (mobile phase A) and ACN (mobile phase B), with the following program: 0−1 min, 98%

A, 1−3 min 98%−70% A, 3−8 min 70%−50% A, 8−10 min 50%−5% A, 10−15 min 5% A. The flow rate was constant at 0.3 mL min^{-1}. After each sample run, the column was re-equilibrated to the initial conditions in 6 min. The injection volume was 5 μL. The column and auto-sampler tray temperatures were set at 35 and 5 °C, respectively. The mass spectrometer was operated in negative ion mode with a probe capillary voltage of 2.2 kV and a sampling cone voltage of 45.0 V. The source and desolvation gas temperatures were set to 120 and 350 °C, respectively. The nitrogen gas desolvation flow rate was 650 L h^{-1}. The mass spectrometer was calibrated across the range of m/z 50−1200 using a 0.5 mM sodium formate solution prepared in 2-propanol:water (90:10 v/v). Data were drift-corrected during acquisition using a leucine enkephalin (m/z 554.2615) reference spray (Lock Spray) infused at 3 μL min^{-1}. Data were acquired in the range of m/z 50−1200, and the scan time was set to 1 s. Technical duplicates were acquired in all cases. Tandem MS experiments were carried out by fast data-dependent acquisition (fast DDA) or MS/MS in negative polarity and resolution mode. Targeted ions for MS/MS were entered in an include list. A 0.2 s continuum MS survey scan was collected from 50 to 650 Da until the intensity of an individual precursor ion rose above 5000, and then we switched to MS/MS acquisition, in which a 0.1s continuum scan was collected from 30 to 650 Da. The MS/MS scan switched off once the accumulated total ion current reached 100 000 or after 0.25 s. A collision energy profile of 15, 25, and 35 V was applied to the trap cell for ion fragmentation. For the MS/MS method, the scan time was 1 s, and collision voltages between 8 and 30 V were applied to the trap cell. Data acquisition and processing were performed with Masslynx v4.1 software.

LC-MS/MS Analysis for Proteomic Experiments. Purified and dried peptide samples were dissolved in a 10 μL solution containing 5% ACN and 4% FA, and 3 μL was loaded onto a microcapillary column packed with C18 beads (Magic C18AQ, 3 μm, 200 Å, 100 μm × 16 cm, Michrom Bioresources) by a Dionex WPS-3000T PLUS auto-sampler (UltiMate 3000 thermostated Rapid Separation Pulled Loop Well Plate Sampler). Peptides were separated by reverse-phase chromatography using an UltraMate 3000 binary pump with a 110 min gradient of 8−38% ACN (with 0.125% FA) for the triplicates. Peptides were detected with a data-dependent Top 20 method (the 20 most abundant ions were selected for MS2) in a hybrid dual-cell quadrupole linear ion trap−Orbitrap mass spectrometer (LTQ Orbitrap Elite, Thermo Fisher, with Xcalibur 3.0.63 software). For each cycle, each full MS scan (resolution: 60 000) in the Orbitrap at 10^6 AGC target was followed by up to 20 MS/MS for the most intense ions in the LTQ. The selected ions were excluded from further analysis for 90 s. Ions with singly or unassigned charge were not sequenced. For each full MS scan, the maximum ion accumulation time was 1000 ms, and that for MS/MS scans was 50 ms. Mass spectra Raw files were converted into mzXML format and then searched using the SEQUEST algorithm (version 28).68 Spectra were matched against a database containing sequences of all proteins in the UniProt Human (Homo sapiens) database (downloaded in February 2014). The search was performed using following parameters: fully digested with trypsin; up to 3 missed cleavages; fixed modifcations: carbamidomethylation of cysteine (+57.0214); variable modifcations: oxidation of methionine (+15.9949). False discovery rates (FDRs) of peptide and protein identifications were controlled by the target-decoy method. Linear discriminant analysis was used to control the quality of peptide

identifications using parameters such as Xcorr, precursor mass error, and charge state. Peptides less than seven amino acid residues in length were deleted. Furthermore, peptide spectral matches were filtered to <1% FDR.

Data Analysis. For metabolomics, spectral features (tR, m/z pairs) were extracted from UPLC-MS data using Progenesis QI version 2.0 (Nonlinear Dynamics, Waters Corp.). The data preprocessing procedures included retention time alignment, peak picking, integration, and deconvolution to group the adducts derived from the same compound. Raw data from metabolomics were normalized using supervised normalization of the microarray (SNM).[73] In the SNM procedure, variances due to biological and technical replicates were adjusted by setting them as variables in the model. A variance explained by different experimental treatments (control, AuNRs@NLS, and AuNRs@NLS/PPTT) was fitted as a biological variable in the model. Clustering analysis on the similarity matrix of metabolomics data was carried out to verify the reproducibility of metabolomics experiments. Hierarchical clustering was done with JMP software (version 9, SAS Institute Inc., Cary, NC). Metabolomics data were log2 transformed before analysis of variance (ANOVA), which was used to detect differential levels of metabolites between control and treatment groups. We fitted models with treatment conditions as fixed effects. A Benjamini−Hochberg 5% FDR correction was used to select differential metabolites. For identified differential metabolites perturbed by PPTT, we used the Mummichog program for network-level metabolites annotation. The MS mode considered in Mummichog was negative ion in order to compute isotopic and adduct species. The metabolites identified as being affected by PPTT were subjected to pathway analysis using the MetaCore pathway analysis software

(from Thomson Reuters). For proteomics, raw data were also normalized using SNM. Clustering analysis on the similarity matrix of data was also carried out to show the reproducibility of the experiments. Hierarchical clustering was done with JMP software. The identified proteins were subjected to pathway analysis using the MetaCore software to study the effect of PPTT.

1.5.3 Results

1.5.3.1 Formulation of AuNRs and cell uptake

To perform PPTT inside human oral squamous cell carcinoma (HSC-3) cells, AuNRs were used in order to efficiently convert NIR light into heat. The AuNRs were synthesized using a seedless method [228] with an average size of 25 nm × 6 nm, as shown in **Figure 2.10 b** (transmission electron microscopy (TEM) image), and an absorption maximum at about 800 nm (as shown in the UV−vis spectrum in **Figure 2.10 c**). This particle size is favorable in conducting PPTT, as it has better efficiency for conversion of light into heat [229].

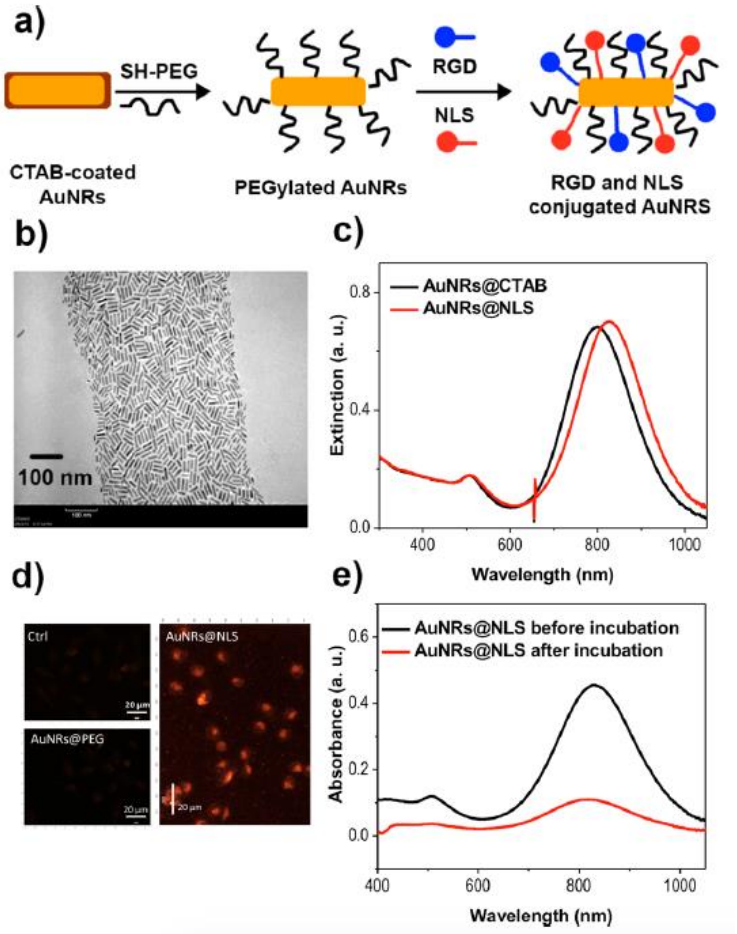

FIGURE 2.10. Characterization of conjugated AuNRs and measurement of HSC-3 (human squamous carcinoma) cell endocytosis with AuNRs. (a) Schematic showing the surface conjugation of the AuNRs with PEG, followed by RGD and NLS. (b) Transmission electron microscopy (TEM) image of conjugated AuNRs. Scale bar = 100 nm. (c) UV−vis absorption spectra of the unconjugated AuNRs (black spectrum) and AuNRs conjugated with NLS (red spectrum). (d) Dark-field images of control HSC-3 cells (not exposed to AuNRs), cells exposed to AuNRs@PEG, and cells exposed to AuNRs@NLS for 24 h. Scale bar = 20 μm. (e) UV−vis absorption spectra of the AuNRs@NLS dispersed in culture media before (black spectrum) and after (red spectrum) incubation with cells.

For formulation of AuNRs@NLS, we first used methoxypolyethylene glycol thiol (mPEG-SH) to modify the surface of AuNRs to gain better biocompatibility [230]. The PEGylated particles were then functionalized with Arg-Gly-Asp (RGD) peptides (known to bind to Rvβ6 integrin on the surface of cancer cells to enhance the receptor-mediated endocytosis of the nanoparticles [231]) and nuclear localization signal (NLS) peptides

(peptide sequences that are recognized by importin and translocate near the nucleus [232]), as shown in **Figure 2.10 a.** Successful surface modification of AuNRs@NLS is evident in the red-shift of the plasmon peak of AuNRs, from 800 nm for the as-synthesized AuNRs to 825 nm for AuNRs@NLS (**Figure 2.10 c).** The zeta potentials of the AuNRs at different stages were measured (**Table 2.1**) to confirm surface modifications. The as-synthesized cetyltrimethylammonium bromide (CTAB)-coated AuNRs had highly positive surface charges, as imparted by the CTAB cationic surfactant. Following PEG modification, the AuNRs became negatively charged (−10.2 ± 6.73 mV). The zeta potential of the AuNRs became positive again after further modification of the RGD and the NLS peptides.

Table 2.1. Zeta potential results for AuNRs with different surface modifications

Nanoparticles	Zeta potential value/ mV
CTAB-coated AuNRs	22.9±15.1
AuNRs@PEG	-10.2±6.73
AuNRs@PEG@RGD/NLS	35.7± 8.96

The uptake of AuNRs was first monitored by dark-field (DF) microscopy. The HSC cells were incubated with a 2.5 nM concentration of AuNRs for 24 h. For AuNRs@NLS, as shown in the DF image (**Figure 2.10 d**), clear internalization was observed compared with cells not exposed to AuNRs and cells exposed to AuNRs without targeting agents. The DF image shows that AuNRs@NLS accumulated in nuclear regions. In addition, the UV−vis spectra of culture media with AuNRs before and

after incubation with cells were also collected (**Figure 2.10 e**), which showed a decrease of the peak intensity that reflects the portion of AuNRs being uptaken by the cells. Differential interference contrast (DIC) microscopy also confirmed the cellular internalization of AuNRs@NLS (**Figure 2.11**). In summary, AuNRs were successfully formulated and then introduced into cells with good cell uptake. The cell viability and apoptosis were tested under different concentrations of AuNRs. The results indicate that the concentration of the AuNRs utilized in this study is much lower than that affecting cell viability or inducing apoptosis (**Figure 2.12**).

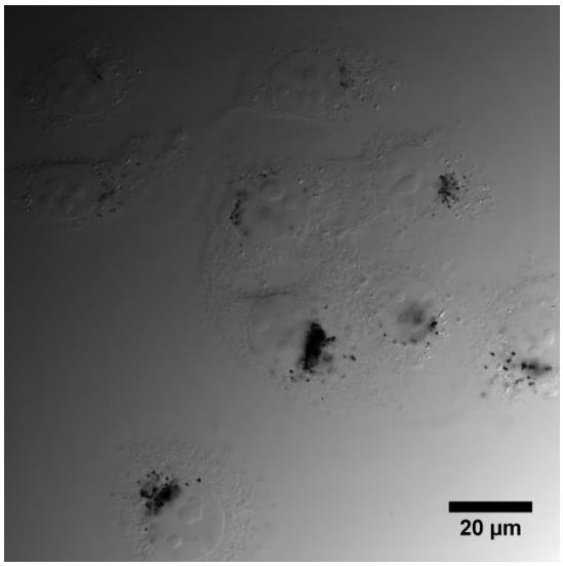

FIGURE 2.11. Differential interference contrast (DIC) microscopy image of the AuNRs@NLS after incubation with the HSC-3 cells for 24 hours.

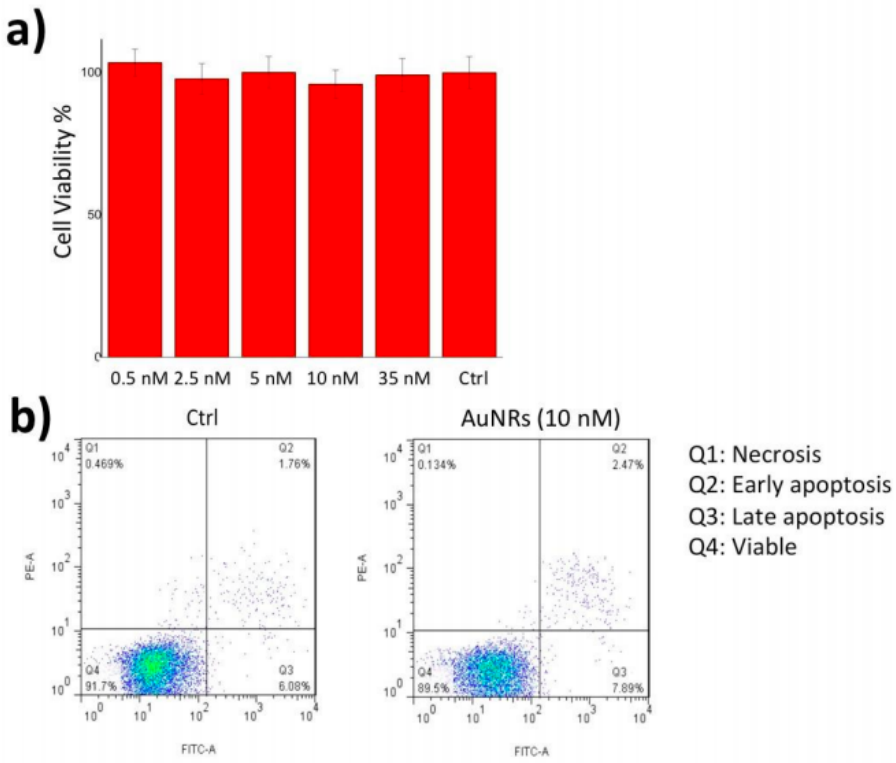

FIGURE 2.12. Cell viability (XTT assay) (a) and flow cytometry (apoptosis/necrosis assay) (b) results for HSC cells incubated with AuNRs.

1.5.3.2 SERS of cancer cells undergoing AuNRs-based photothermal therapy

The AuNRs with dimensions 25 nm × 6 nm and concentration 2.5 nM were selected for use for heat generation. After incubation with AuNRs for 24 h, a continuous-wave (CW) 808 nm NIR laser with power of 5.8 W/cm^2 [229, 233, 234] was used for irradiation of the cells for different time intervals. The laser wavelength overlapped with the longitudinal SPR peaks of the AuNRs. The temperature rose to 45 °C after 2 min of laser exposure. The effect of PPTT was confirmed using a cell viability assay and an apoptosis/necrosis assay. The cell viability results showed a significant decrease in the percentage of viability (~40%) for the HSC cells incubated with AuNRs (2.5 nM) after exposure to the 808 nm NIR laser for 3 min (**Figure 2.13**). In the apoptosis/necrosis

assay, cells were labeled with Annexin V and propidium iodide (PI), and the fluorescent signals were examined by flow cytometry. As shown in **Figure 2.13,** the number of apoptotic cells significantly increased after PPTT was applied. The decrease of cell viability and increase of apoptosis indicated the efficacy of PPTT.

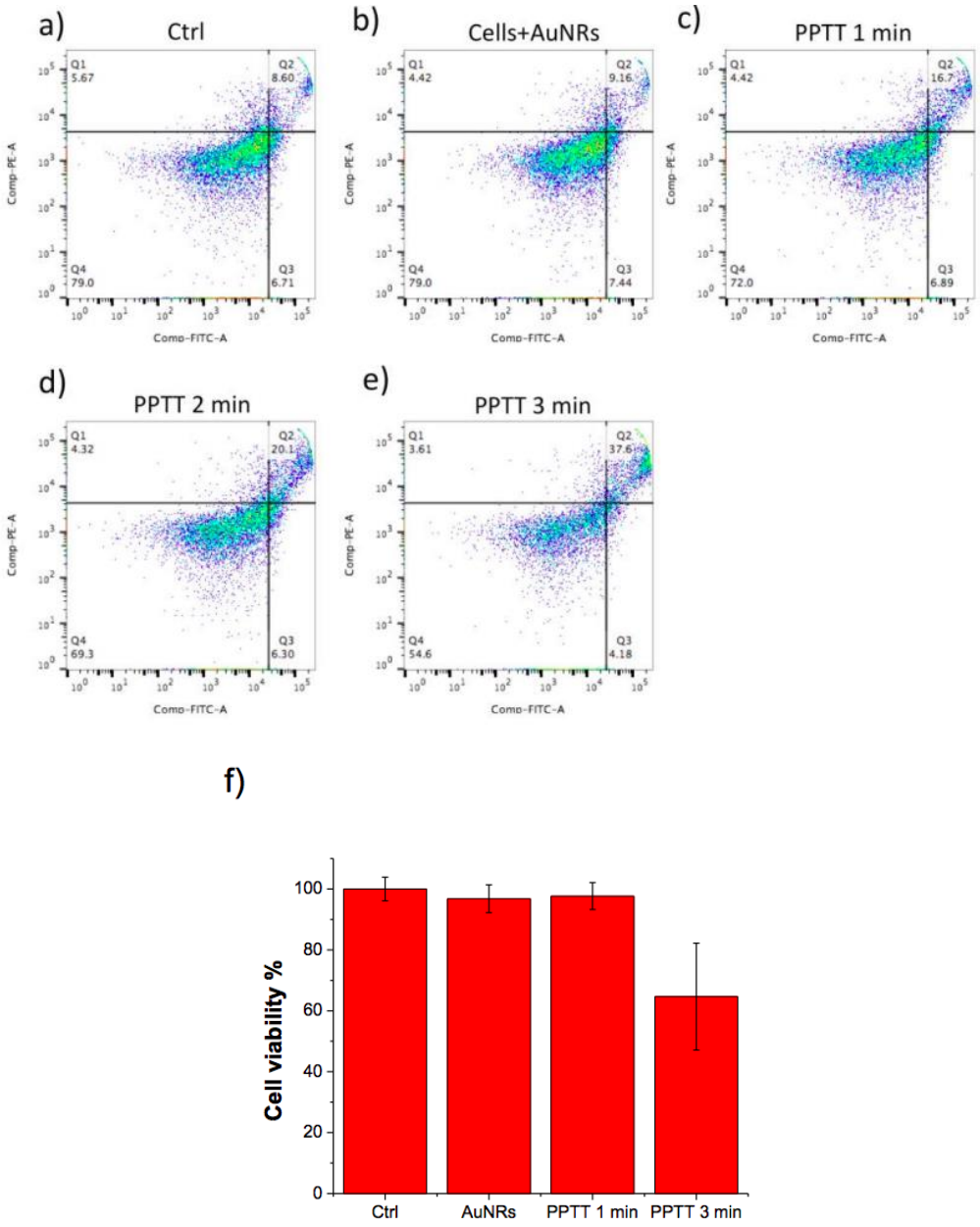

FIGURE 2.13. Apoptosis/necrosis assay (a to e) and cell viability assay (f) for the HSC-3 samples treated with PPTT at different time; Q1 (necrosis), Q2 (apoptosis), Q3 (early apoptosis) and Q4 (early apoptosis).

For real-time SERS measurement, spectra were collected at a single spot of cells to avoid variations due to changing location. A 785 nm laser was focused on a single cell, and spectra were recorded. As our AuNRs have weak SERS signals (due to their small size), in order to enhance the signals, 40 nm gold nanospheres (AuNSs) with the same

surface modification as AuNRs were used to assist the detection [235]. Detailed information about AuNSs@NLS characterization and cellular uptake is given in **Figure 2.14.** The introduction of AuNSs does not affect AuNRs uptake or SERS spectra shapes during the PPTT process due to their small amount and the fact that they do not absorb NIR light (**Figure 2.15**). SERS spectra of HSC cells without PPTT were comparable with our previous publications[216], [224],[236]; possible assignments for each peak are given in **Table 2.2**. Upon NIR laser exposure, the band around 1000 cm^{-1} increased in intensity, due mainly to the benzene ring breathing of phenylalanine as mentioned before [237]. Though in most publications this band is assigned to phenylalanine, some debate is still going on regarding its assignment [226], [238]. Further, we observed that the enhancement of the 1000 cm^{-1} peak was accompanied by the enhancement of the 1207 and 1580 cm^{-1} bands (**Figure 2.16 a**), which are attributed to the in-plane CH stretching vibration and sidechain vibration coupled with the in-phase motion corresponding to phenylalanine [216, 239]. The same experiment was repeated three times, and the same trend of peak intensity changes of 1000, 1207, and 1580 cm^{-1} was obtained (**Figure 2.16 b and 2.17**). SERS of cells 12 h after PPTT has also been performed to confirm that the signal remains altered (**Figure 2.18**). On the other hand, a control experiment was conducted on cells without laser exposure. No obvious SERS spectral change was observed during NIR laser irradiation of the control (**Figure 2.19**). This gave us more evidence of the phenylalanine increase after the PPTT process.

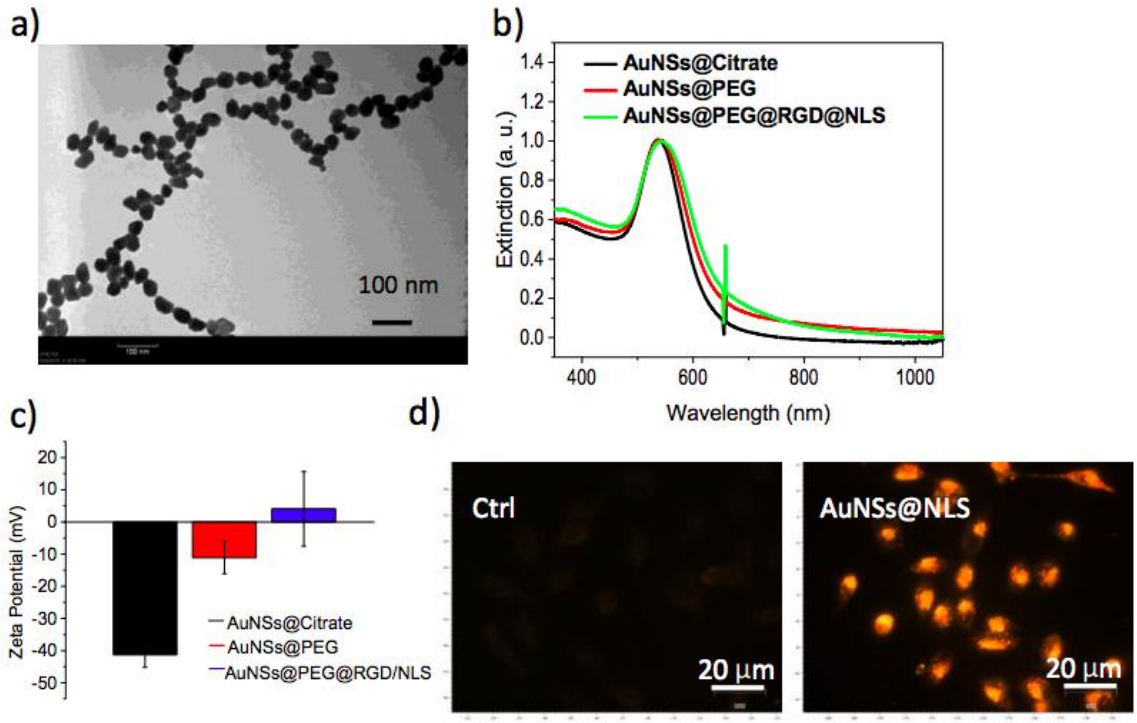

FIGURE 2.14. Characterization of AuNSs@PEG@RGD@NLS. (a) Transmission electron microscope (TEM) image of conjugated gold nanospheres (AuNSs). Scale bar = 100 nm. (b) UV-Vis absorption spectra of the unconjugated AuNSs (black spectrum), PEG conjugated AuNSs (red spectrum) and AuNSs conjugated with NLS (green spectrum). (c) Zeta potential of AuNSs with different conjugations. (d) The dark field images of HSC-3 cells with or without AuNRs@NLS incubation for 24 hours. Scale bar = 20 μm.

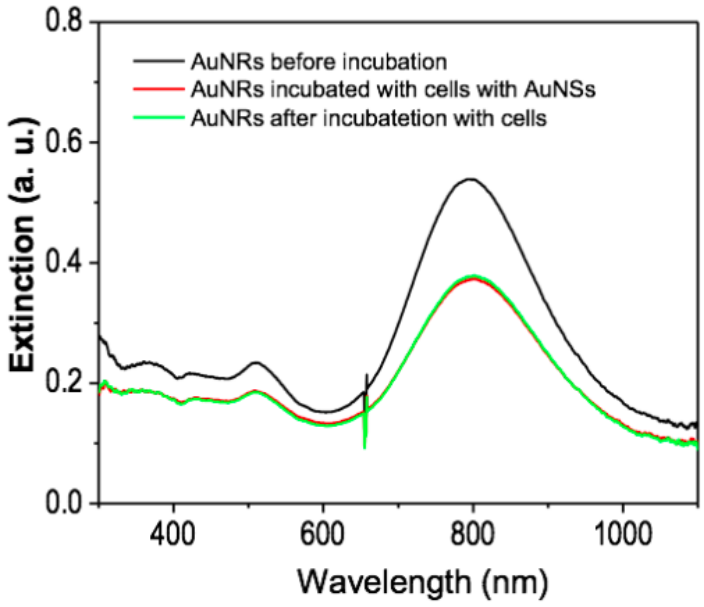

FIGURE 2.15. The uptake of AuNRs by HSC-3 cells before and after 24 h incubation. The pre-existence of AuNSs does not affect the further internalization of AuNRs.

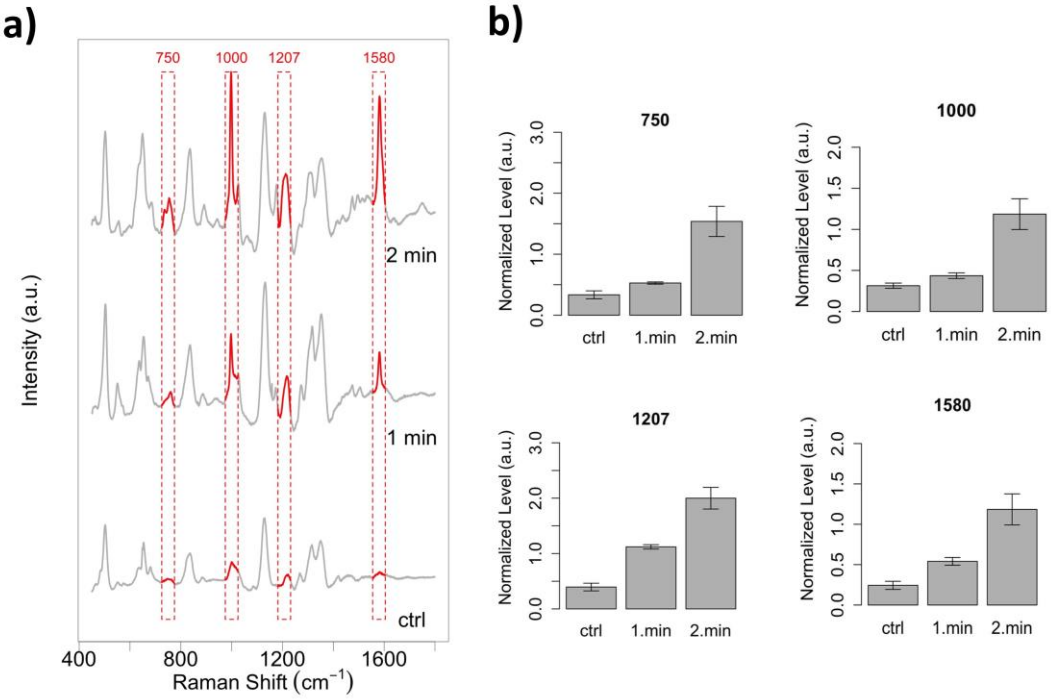

FIGURE 2.16. (a) SERS spectra collected from a single HSC-3 cell under NIR laser exposure (808 nm diode laser, 5.8 W/cm^2) at 1 and 2 min delays. The 750, 1000, 1207, and 1580 cm^{-1} bands are shown in red and placed in red boxes. (b) Bar graphs of

the Raman bands associated with biomolecules located within the AuNP plasmonic field.

Table 2.2. Tentative assignment of Raman bands in the SERS spectra collected from HSC cells [236, 240].

Wavenumber (cm-1)	Tentative assignments of SERS bands
495-510	-S-S-
640−660	-C-S-
820−850	Tyr and lipids O−C−C−N symmetric stretches
990-1010	Phe ring breathing
748-758	pyrrole breathing mode ν15 in cytochrome c
1012−1030	In-plane bending mode of Phe and ring breathing of Trp
1200−1210	C6H5−C stretch of Phe and Tyr
1584−1592	Phe

Generally, we can rule out the possibility of tryptophan contributing to the 1000 cm^{-1} signal since side-chain vibrations in its SERS spectrum appear at 758, 869, 1011, 1357, 1410, 1546, and 1602 cm^{-1}, corresponding to the counterparts at 756, 874, 1009, 1358, 1423,1558, and 1619 cm^{-1} in the solid Raman spectrum [241]. However, our SERS data did not show obvious increases of these peaks. Therefore, our SERS results support the conclusion that the phenylalanine increases in the microenvironment around the nanoparticles during PPTT.

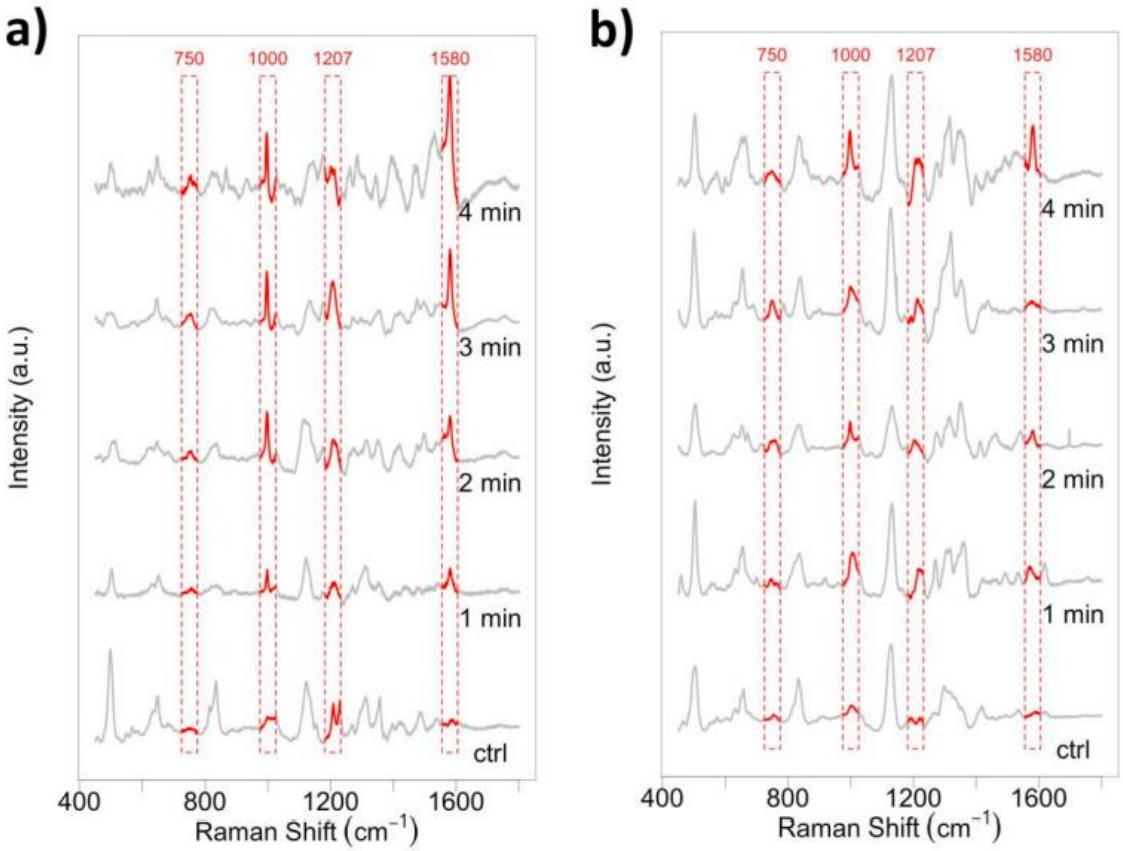

FIGURE 2.17. Additional SERS spectra collected from single HSC-3 cell (incubated with AuNRs 24 h prior to PPTT) under NIR laser exposure of (808 nm diode laser 5.8 w/cm^2) at different times (1 and 2 minutes).

In addition to the phenylalanine bands, we also observed a 750 cm^{-1} band whose intensity increases during PPTT (**Figure 2.16**), which has been assigned to the pyrrole breathing mode ν15 in cytochrome c [242],[243]. This result suggested the increase of apoptotic cells during thermal heating through cytochrome cmediated apoptosis. This result is in agreement with our flow cytometry data (**Figure 2.13**), indicating that PPTT triggered apoptosis.

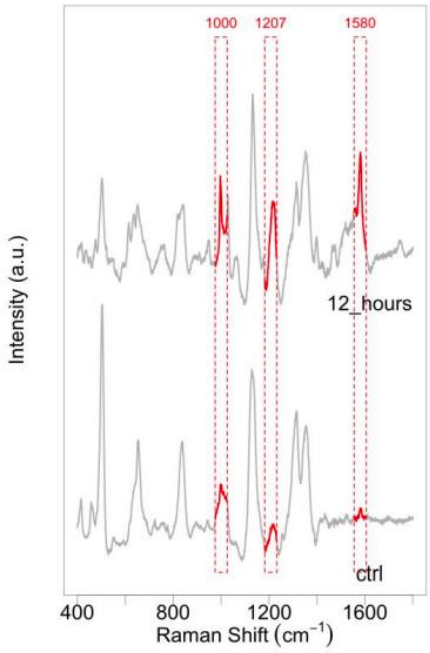

FIGURE 2.18. SERS spectra collected from single HSC-3 cell 12 hours after PPTT (incubated with AuNRs 24 h prior to PPTT, under NIR laser exposure of 808 nm diode laser 5.8 w/cm^2).

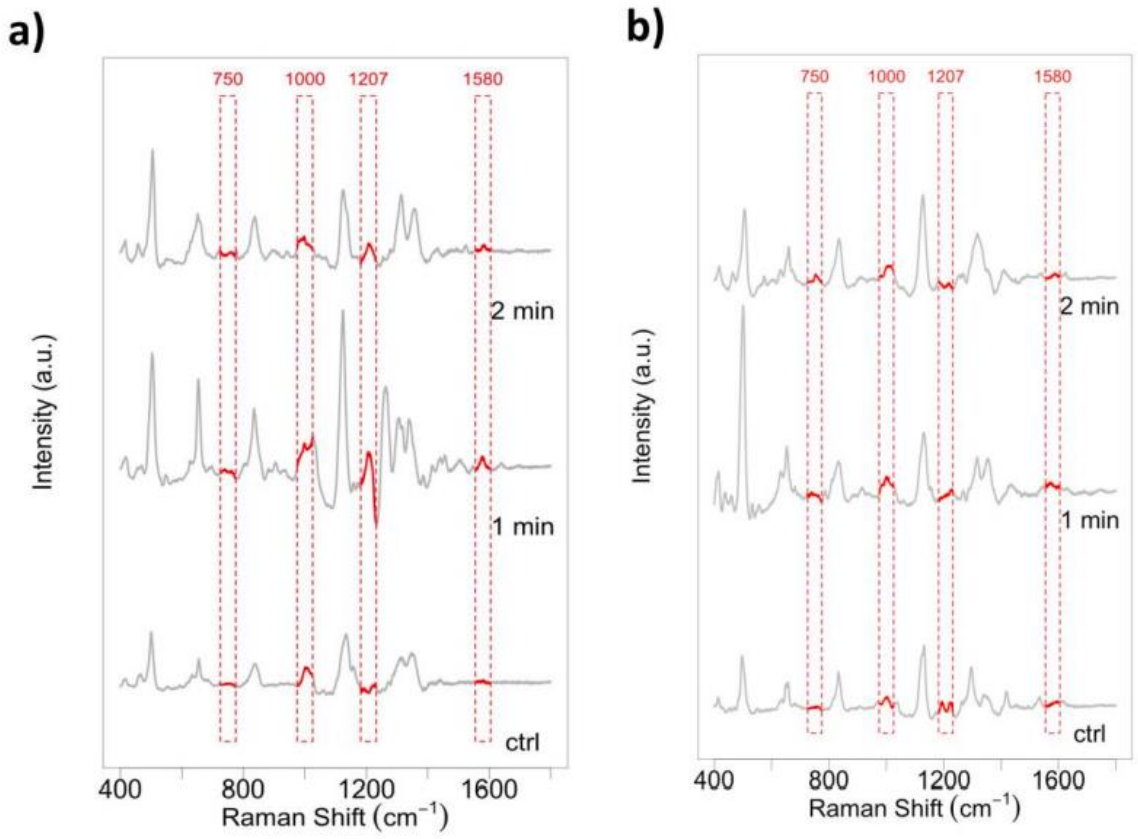

FIGURE 2.19. SERS spectra of a) PPTT on cells with AuNSs alone (without AuNRs) and b) cell incubated with AuNRs but no laser exposure.

1.5.3.3 Metabolomics and Proteomics Experiments Confirming Perturbation of Phenylalanine Metabolism during gold nanorod-based photothermal therapy

For metabolomics experiments, we analyzed the metabolites of cells using liquid chromatography−mass spectrometry (LC-MS). Two biological replicates and two technical replicates were conducted. A total of 1122 tentative features (retention time (tR), m/z pairs) were detected in metabolite extracts, corresponding to 152 metabolites with detectable ([M − H]−) primary ion. Hierarchical clustering analysis on the similarity matrix of metabolomics data was carried out to verify the reproducibility of the experiments (**Figure 2.20 b**). Among these, 238 metabolomics features were

differentially expressed in the AuNR@NLS-treated group when compared to the control group (FDR = 0.05, corresponding to p = 0.015) (**Figure 2.20 e**); 483 metabolomics features were differentially expressed in the AuNR@NLS/PPTT group when compared to the control group (FDR = 0.05, corresponding to p = 0.015) (**Figure 2.20 f**). Specifically, many of these features corresponded to an increase in the relative amount of phenylalanine (**Figure 2.21 a**) and related species after PPTT (**Figure 2.21 b−d and 2.22**). Phenylalanine derivatives and phenylalanine-containing short peptides, such as glutamylphenylalanine (**Figure 2.21 b**), asparaginyl-phenylalanine (**Figure 2.21 c**), and histidinyl-phenylalanine (**Figure 2.21 d**), were among those altered, explaining the trends observed in the SERS data. Tandem MS experiments confirmed the identity of the species detected by MS with excellent accuracy (**Figure 2.21 e**).

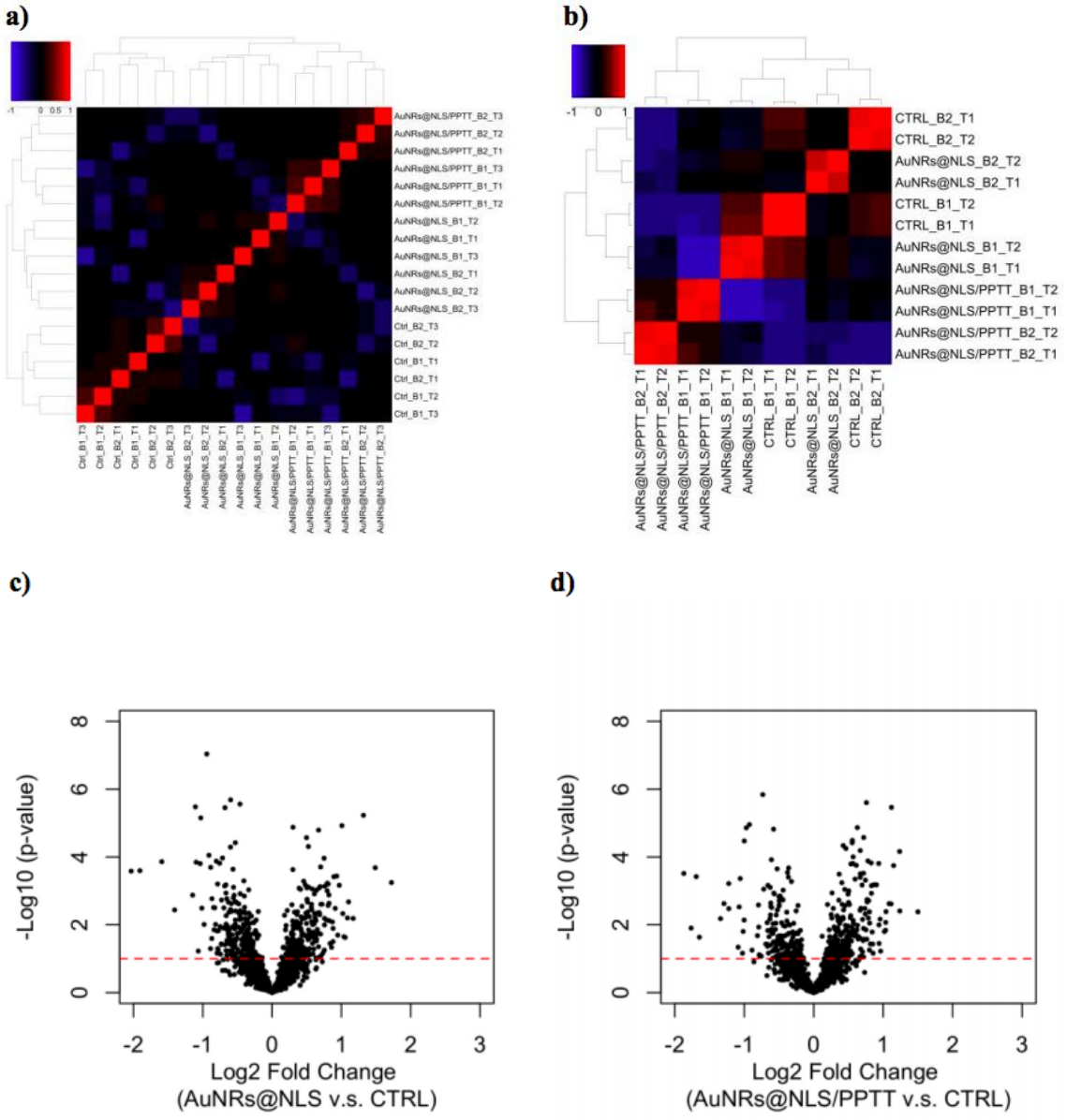
a)
b)
c)
d)
AuNRs@NLS/PPTT_B2_T3
AuNRs@NLS/PPTT_B2_T2
AuNRs@NLS/PPTT_B2_T1
AuNRs@NLS/PPTT_B1_T3
AuNRs@NLS/PPTT_B1_T1
AuNRs@NLS/PPTT_B1_T2
AuNRs@NLS_B1_T2
AuNRs@NLS_B1_T1
AuNRs@NLS_B1_T3
AuNRs@NLS_B2_T1
AuNRs@NLS_B2_T2
AuNRs@NLS_B2_T3
Ctrl_B2_T3
Ctrl_B2_T2
Ctrl_B1_T1
Ctrl_B2_T1
Ctrl_B1_T2
Ctrl_B1_T3
CTRL_B2_T1
CTRL_B2_T2
AuNRs@NLS_B2_T2
AuNRs@NLS_B2_T1
CTRL_B1_T2
CTRL_B1_T1
AuNRs@NLS_B1_T2
AuNRs@NLS_B1_T1
AuNRs@NLS/PPTT_B1_T2
AuNRs@NLS/PPTT_B1_T1
AuNRs@NLS/PPTT_B2_T2
AuNRs@NLS/PPTT_B2_T1
-Log10 (p-value)
Log2 Fold Change
(AuNRs@NLS v.s. CTRL)
Log2 Fold Change
(AuNRs@NLS/PPTT v.s. CTRL)

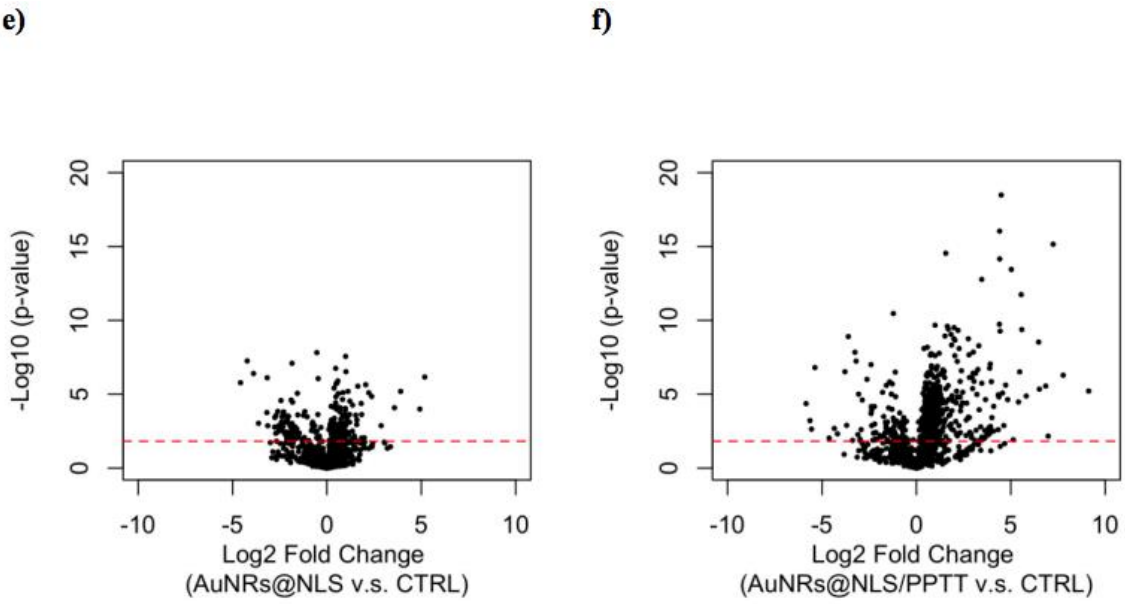

FIGURE 2.20. Clustering analysis and differential analysis of proteomics and metabolomics data. (a) Clustering analysis of proteomics data. Two biological replicates (labeled as B1 and B2) and three MS technical replicates (labeled as T1, T2, and T3) were conducted. Clustering analysis indicated good reproducibility for the proteomics experiments. (b) Clustering analysis of metabolomics data. Two biological replicates (labeled as B1 and B2) and two MS technical replicates (labeled as T1 and T2) were conducted. Clustering analysis indicated good reproducibility for the metabolomics experiments. (c) Volcano plot showing that 434 proteins were differentially expressed in AuNR@NLS group compared to control group (p=0.1). In total, 1341 proteins are identified. (d) Volcano plot showing that 402 proteins were differentially expressed in AuNR@NLS/PPTT group in contrast to control group (p=0.1). (e) Volcano plot showing that 238 metabolomics features were differentially expressed in AuNR@NLS group compared to control group (FDR=0.05, corresponding to p=0.015). A total of 1122 metabolomics features were detected in metabolite extracts, corresponding to 152 metabolites with primary ion ([M-H]-). (f) Volcano plot showing that 483 metabolomics features were differentially expressed in AuNR@NLS/PPTT group in contrast to control group (FDR=0.05, corresponding to p=0.015).

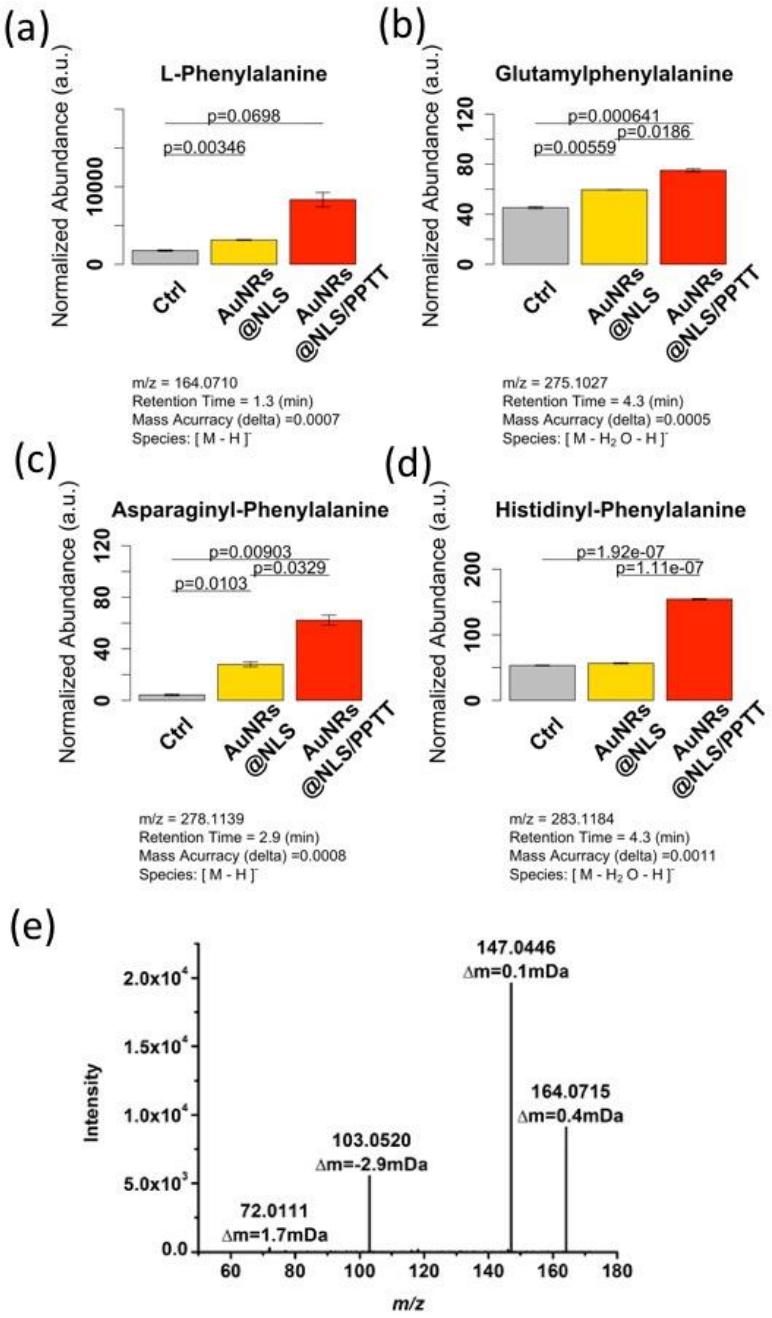

FIGURE 2.21. Metabolite perturbations observed in HSC-3 cells treated with AuNRs-PPTT (NLS conjugated particles). (a−d) Bar graphs showing the normalized abundance of phenylalanine-related metabolites altered following PPTT: (a) L-phenylalanine (the result was confirmed by MS/MS, shown in panel e); (b) glutamyl-phenylalanine; (c) asparaginyl-phenylalanine; and (d) histidinyl-phenylalanine. Normalized abundances of metabolites following AuNRs@NLS without PPTT are also given for comparison. (e) Product ion spectrum obtained under data-dependent acquisition conditions for the precursor ion at m/z 164.0710. Matching of this mass spectrum to the Metlin database MS/MS reference spectrum

of phenylalanine (10 V collision energy) is shown, with mass accuracies indicated for each ionic species detected.

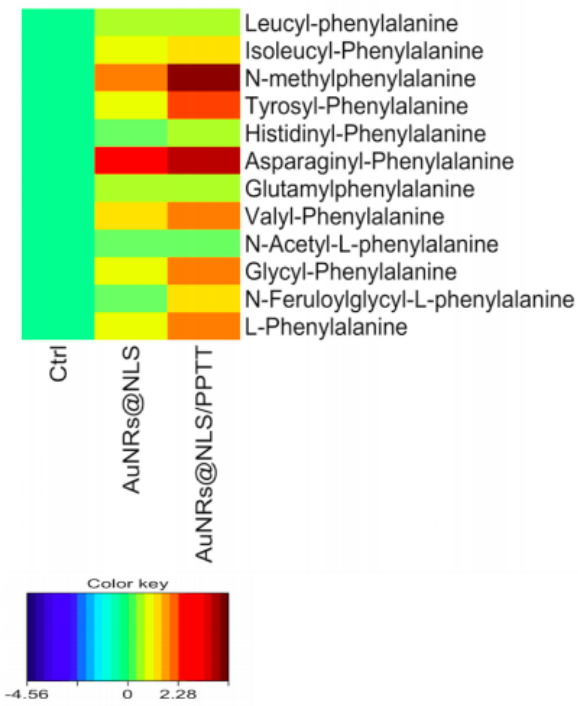

FIGURE 2.22. Heat map showing fold change (log2) of key metabolites related to phenylalanine metabolism in treatment experiments (AuNRs@NLS, AuNRs@NLS/PPTT) compared to control group.

Furthermore, we also conducted a label-free quantitative proteomics experiment for studying alterations in protein abundances and seeking possible evidence for, and understanding of the mechanisms responsible for the phenylalanine concentration increase. A test experiment was done to measure the accuracy of our proteomics workflow using the reported method [244], where 99% of the proteins have shown accurate quantification (**Figure 2.23**). Mitochondrial acetyl-CoA acetyltransferase (ACAT1) has been shown to be involved in the development of doxorubicin resistance to decrease cell apoptosis [245]. Another mitochondrial protein, hydroxyl-coenzyme A dehydrogenase/3-ketoacyl-coenzyme A thiolase/enoylcoenzyme (HADHA), has been shown to prevent chemically induced apoptosis in cancer treatment [246] [247]. In our experiments, both

proteins were observed to be down-regulated following PPTT treatment, suggesting that the anti-apoptotic protection was turned off resulting in enhanced vulnerability to apoptosis (**Figure 2.24 b,c**).

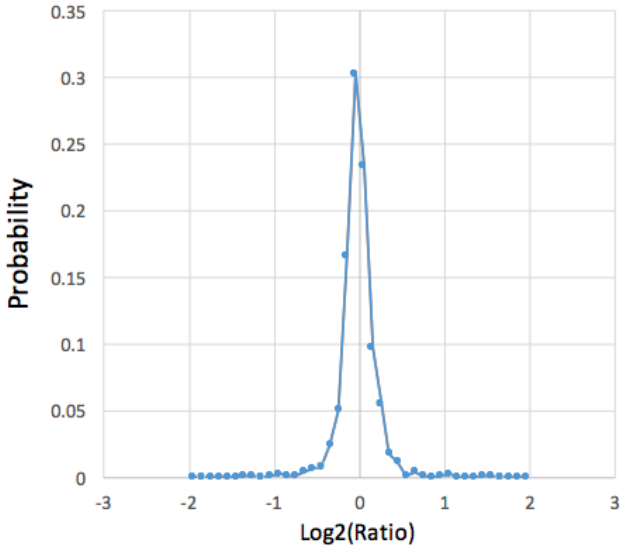

FIGURE 2.23. Quantification accuracy examination of proteomics workflow: Log2 ratio distributions of quantified peptides from 2 identical test samples (yeast whole proteome sample), each sample having 3 technical replicates.

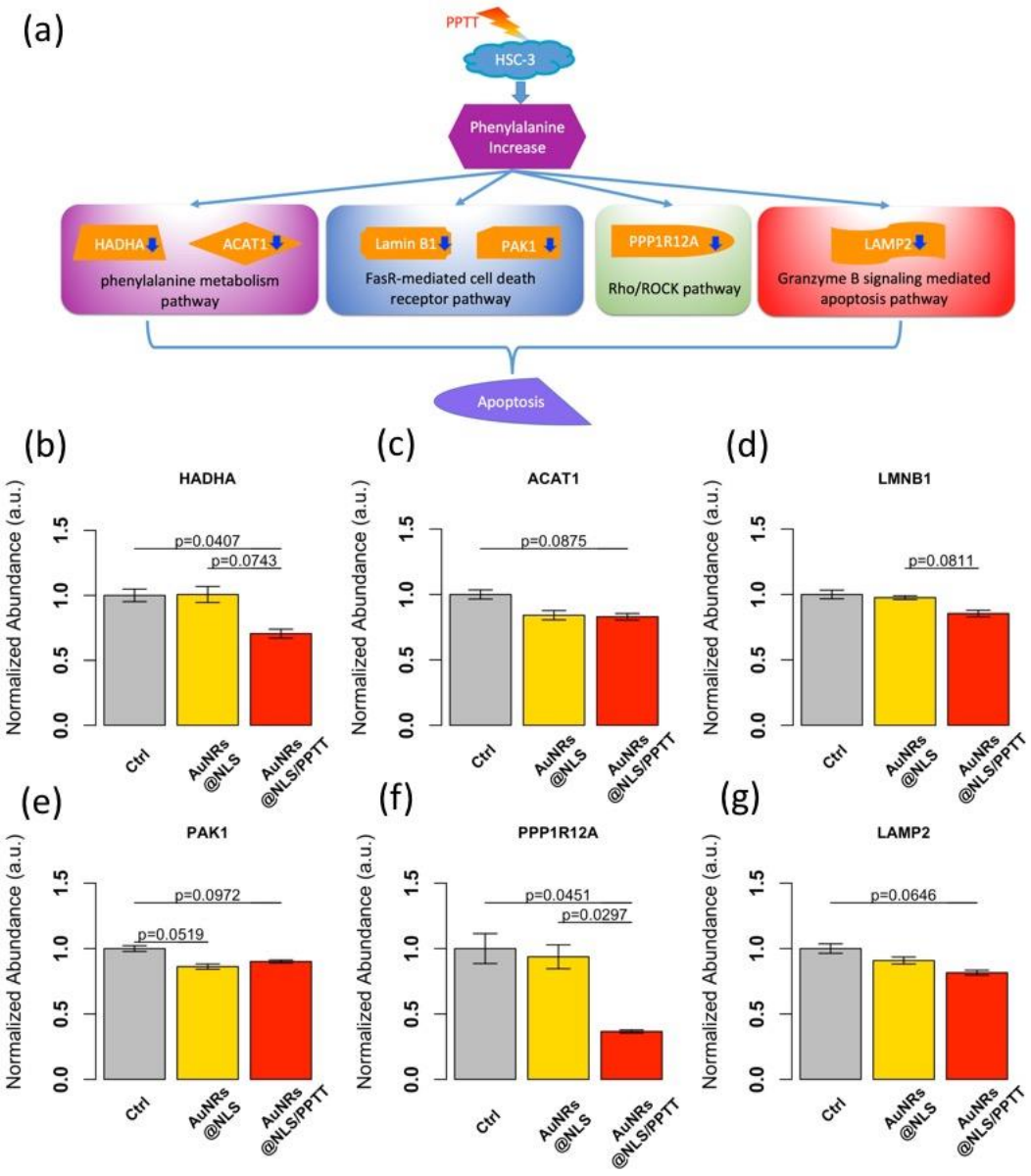

FIGURE 2.24. (a) Schematic diagram explaining the molecular apoptosis mechanisms involved in altering phenylalanine metabolism as induced by PPTT. (b−g) Bar graphs showing the normalized abundance of key proteins contributing to apoptosis involved in altering phenylalanine metabolism following PPTT: (b) HADHA, (c) ACAT1, (d) Lamin B1 (LMNB1), (e) PAK1, (f) PPP1R12A, and (g) LAMP2. Normalized abundances of key proteins following AuNRs@NLS without PPTT are also given for comparison.

In addition to the phenylalanine metabolism pathway, three possible mechanisms of phenylalanine-induced apoptosis were suggested by the results. First, increased phenylalanine was shown to induce apoptosis by involvement of the Fas receptor (FasR)-

mediated cell death receptor pathway [248]. In this study, two proteins (Lamin B1 and PAK1) in the Fas/Fas ligand death receptor pathway were identified. These two proteins have been previously demonstrated to be associated with apoptosis. Lamin B1, as the major component of the nuclear lamina underlying the nuclear membrane, plays an important role in maintaining nuclear membrane integrity. Destruction of nuclear membrane integrity being a hallmark of apoptosis. During apoptosis, Lamin B1 mRNA level have been shown to decrease [249], which could result from induction of either p53 or pRB tumor suppressor pathways [250] [251]. Literature results also show that the Fas/Fas ligand complex downstream effector PAK1 is required to prevent apoptosis by limiting the expression of pro-apoptotic proteins or modulating posttranslational modifications on effectors [252]. In this study, both of these proteins were down-regulated, suggesting a cellular shift toward apoptosis, and reduced anti-apoptotic protection (**Figure 2.24 d,e**).

Phenylalanine has also been shown to activate mitochondriamediated apoptosis through the Rho/ROCK pathway [36,47.] In this study, we identified down-regulation of the myosin phosphatase targeting subunit 1 (PPP1R12A) in PPTT-treated cells, this being a downstream effector of ROCK (**Figure 2.24 f**) that would contribute to the apoptotic phenotype following PPTT. In apoptotic cells, PPP1R12A is cleaved, with the cleaved PPP1R12A inhibiting myosin II binding, which results in membrane blebbing and apoptosis [253].

A third mechanism of phenylalanine-induced cell death involves a component in Granzyme B signaling-mediated apoptosis, known as lysosome-associated membrane protein 2 (LAMP2). This protein was down-regulated following PPTT treatment (**Figure 2.24 g**). LAMP2 is critical to maintain lysosome integrity and normal cellular function,

and lower levels of LAMP proteins have been positively associated with apoptosis [254]. It is not yet conclusively established, however, whether decreased LAMP2 levels are alsodirectly associated with phenylalanine-induced apoptosis.

1.5.4 Discussion.

Time-dependent SERS has recently enabled researchers to probe molecular changes in single (cancer) cells over time during the full cell cycle, or as the cell dies from exposure to drugs or from heat treatment. SERS accurately follows changes in cellular and subcellular environments during the onset and progression of processes such as apoptosis and mitosis [216, 236] in real time and at a single-cell level. Cells present several active molecular Raman bands associated with biomolecules located within the AuNP plasmonic field.

Herein, we coupled SERS measurements with metabolomics and proteomics experiments performed on the same set of samples, aiming to study the change of the subcellular microenvironment around AuNRs during the PPTT process. Our SERS data showed that the 1000, 1207, and 1580 cm^{-1} bands increased during PPTT, which suggested an increase of phenylalanine and its derivatives. These findings were confirmed with whole cell metabolomics experiments using high-resolution mass spectrometry. We observed an increase of free phenylalanine, together with an increase of its derivatives and phenylalanine-containing peptides. Integrative analysis of proteomics and metabolomics data also showed that the proteins and metabolites in the phenylalanine metabolism pathway related to apoptosis were perturbed in apoptosis direction. Elevated levels of phenylalanine have been implicated in mitochondria-

mediated apoptosis through Rho/ROCK pathway and Fas/Fas ligand mediated apoptosis [248, 255]. In this study, both pathways were changed in favor of apoptosis in PPTT, where the level of phenylalanine was increased. In addition, the results suggested that, during phenylalanine induced apoptosis, lysosome integrity may have been perturbed, which may further contribute to cell death. This hypothesis was further strengthened by the observation of an increasing pattern of pyrrole breathing mode ν15 in cytochrome c shown in the SERS spectra (750 cm^{-1}), which suggests the increase of apoptotic cells during thermal heating through cytochrome c-mediated apoptosis, which is in agreement with flow cytometry data **(Figure 2.13.).** Meanwhile, some other apoptosis pathways were revealed by proteomics, shown in **Figure 2.25.**

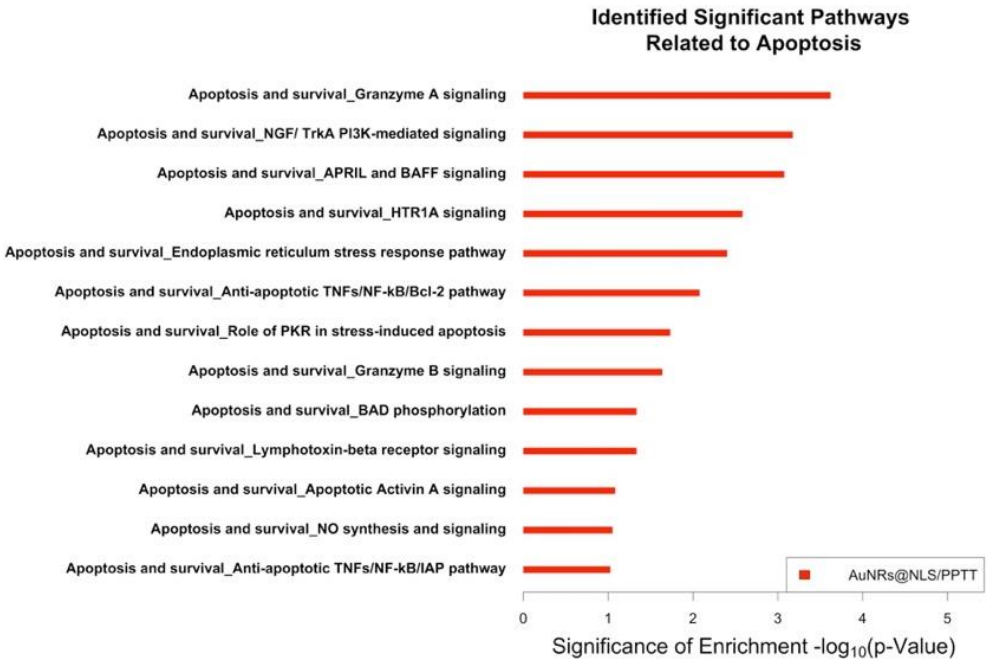

FIGURE 2.25. Other apoptosis pathways revealed by proteomics results.

Further investigations into the mechanism of how PPTT treatment increases phenylalanine levels in cells focused on the fact that phenylalanine can be converted to L-

tyrosine [256]. Metabolomics data indicated that, after PPTT treatment, the level of L-tyrosine was actually decreased (**Figure 2.26**). Based on our results, the channel allowing for the conversion from phenylalanine to L-tyrosine could have contributed to the accumulation of phenylalanine, which further induced mitochondria-mediated apoptosis.

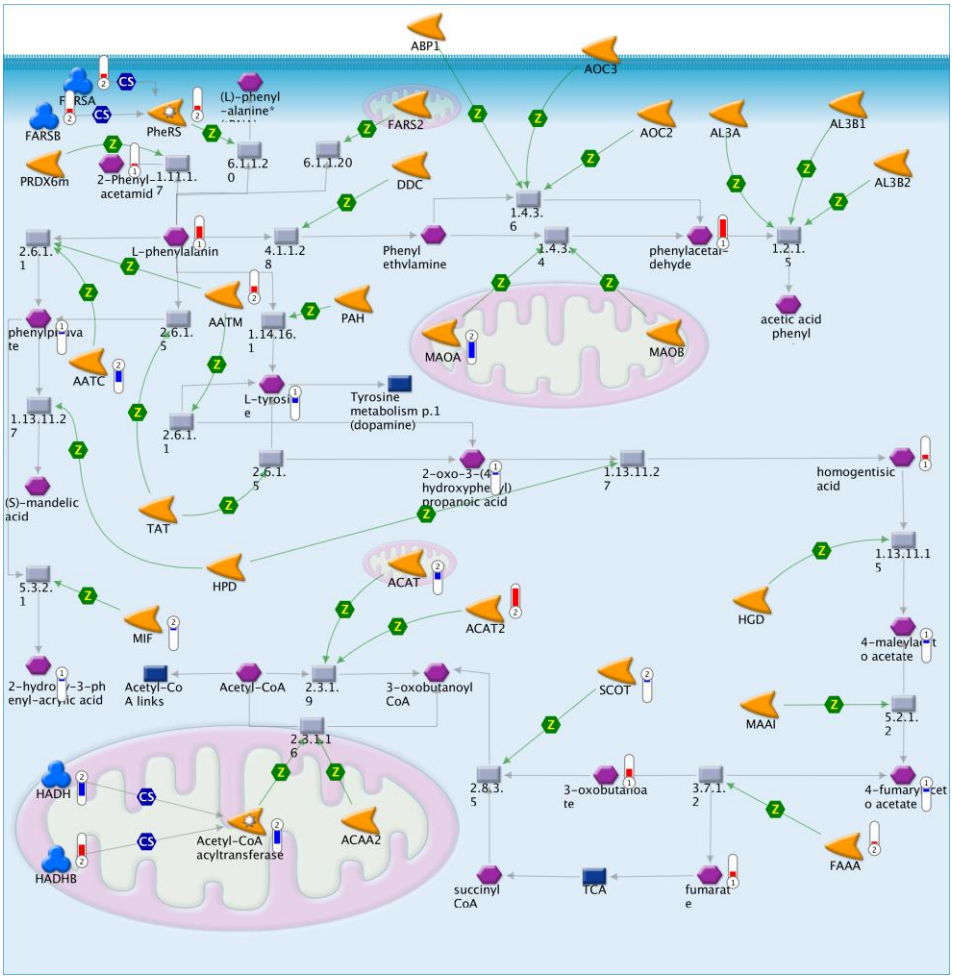

FIGURE 2.26. Pathway map showing that the phenylalanine metabolism pathway was perturbed after PPTT and key proteins (HADHA, ACAT1) were down-regulated, which triggers apoptosis. (Red) means upregulation after PPTT, (blue) means down-regulation after PPTT. In the thermometer sign, 1 refers to metabolomics results, 2 refers to proteomics results. The thermometers are filled to various degrees, corresponding to the amount by which the markers were up-regulated or down-regulated.

Note: in the figure, “Acetyl-CoA acyltransferase” represents “hydroxyacyl-CoA dehydrogenase/3-ketoacylCoA thiolase/enoyl-CoA hydratase (trifunctional protein), alpha subunit”, which is a protein complex catalyzing the 3-hydroxyacyl-CoA dehydrogenase and enoyl-CoA hydratase activities. HADHA and HADHB are both subunits of this protein complex. HADHA is down-regulated, while the HADHB is upregulated. However, the down-regulation of HADHA is the rate limiting step forming the effective protein complex. Therefore, the activity of protein complex Acetyl-CoA acyltransferase is down-regulated, contributing to the mitochondria mediated apoptosis process. ACAT1 is acetyl-CoA acetyltransferase 1, which is a mitochondrially localized enzyme that catalyzes the reversible formation of acetoacetyl-CoA from two molecules of acetyl-CoA. ACAT2 is cytosolic localized acetyl-CoA acetyltransferase 2, which involved in lipid metabolism. The mitochondrial isoform ACAT1 is down-regulated hints its perturbation contributes to mitochondria mediated apoptosis processes, while the cytosolic isoform ACAT2 is not related to this process.

We observed in our results (**Figure 2.21, 2.22 and 2.24**) that several metabolites/proteins change abundance in the presence of AuNRs even without light exposure, possibly due to the gold nanoparticles alone which could perturb apoptosis pathways of the biological system, as has been reported previously [257]. This effect, however, compared to the effect of PPTT treatment on apoptosis pathways, occurs to a much smaller extent and did not cause actual apoptosis (**Figure 2.12**).

Besides the phenylalanine-dependent process, we further identified significantly perturbed pathways by integrative analysis of proteomics and metabolomics (**Figure 2.27**). Other amino acid metabolism pathways are enriched, including methionine-

cysteine-glutamate and lysine metabolism, both of which are very essential for the basic survival of the cells. Interestingly, we also found clues on the perturbation of pathways related to lipid metabolism and ketone body metabolism.

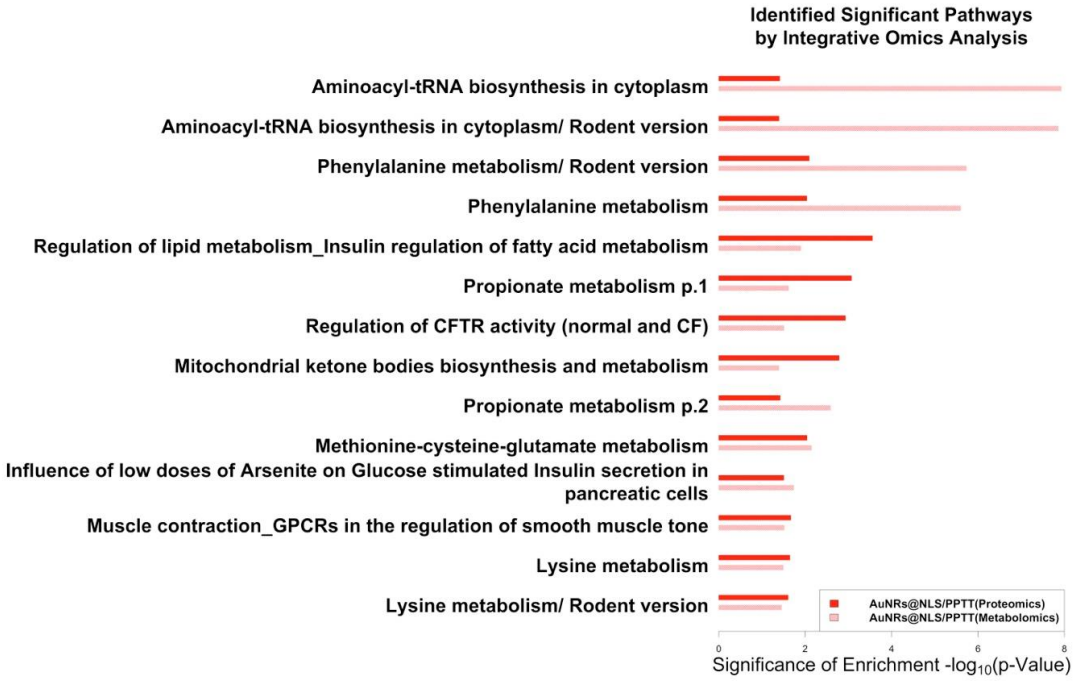

FIGURE 2.27. Significant pathways identified from proteomics (red bars) and metabolomics (light pink bars) that perturbed by photothermal therapy.

In conclusion, by integrative analysis of Raman spectroscopy profiles, metabolomics, and proteomics mass spectrometric data, we discovered that free phenylalanine and associated metabolites are significantly perturbed by PPTT, leading to cell apoptosis. We therefore propose that phenylalanine measurements by SERS can be developed as a sensitive and convenient readout for non-invasive direct apoptosis characterization.

1.6 Improving the Flow Cytometry-based Detection of Gold Nanoparticle Cellular Uptake

Summary. Due to the considerable amount of applications of gold nanoparticles (AuNPs) in biological systems, there is a great need for an improved methodology to quantitatively measure the uptake of AuNPs in cells. Flow cytometry has the ability to measure intracellular AuNPs by collecting the light scattering from a large population of live cells through efficient single cell analysis. Traditionally, the side scattering setting of the flow cytometer which is associated with a 488 nm excitation laser (SSC channel) is used to detect nanoparticle uptake. This method is limited as AuNPs do not have the optimized response when excited with this laser (for Au nanospheres, AuNSs, the SPR peak is around 520-540 nm, for Au nanorods, AuNRs, the SPR peak will be in higher wavelength to infrared range). Here, we reported that the use of more red-shifted excitation lasers, will greatly enhance the optical signal needed for the flow-cytometry based detection of AuNSs (25 nm) and AuNRs (40 x 80 nm, width x length) uptake in triple negative breast cancer cells (MDA-MB-231).

1.6.1 Introduction.

Gold nanoparticles (AuNPs) emerges to be a key branch of materials that are widely used in diverse scientific fields such as chemistry, biology, medicine and engineering [13, 14]. AuNPs have great and unique optical properties due to their interaction with light. When AuNPs are excited by light at specific wavelengths, the interaction between the electromagnetic field of light and the conduction electrons of AuNPs causes the electrons to oscillate in resonance with the frequency of light [11],

which is termed the surface plasmon resonance (SPR). The SPR gives AuNPs unique optical properties which include their large scattering cross-sections, that are 5 orders of magnitude higher (from the 80 nm gold nanospheres) than the light emission from fluorescent molecules such as fluorescein [1]. The strong scattering of AuNPs allow them to be easily detected by scattering based detection methods. Additionally , AuNPs can be easily surface-modified with many types of functional groups, such as proteins, peptides, oligonucleotides, *etc*, while still maintaining their optical properties [12].

The amount of intracellular AuNPs can be positively correlated to their possible effects at cellular levels. Currently, several methods can be used for measuring intracellular AuNPs. **Element analysis techniques** such as inductively coupled plasma (ICP)-based spectroscopic methods (including optical emission spectrometry (ICP-OES), and mass spectrometry (ICP-MS)) are commonly regarded as the most accurate AuNP quantification methods. However, an obvious drawback of this type of method is that it only provides the average amount of AuNP intracellular content, with little to no information regarding the distribution within the cell population or spatial location [258]. In addition, **spectroscopic methods** that use UV-Vis and Beer-Lambert's law which correlate the AuNP concentration with the absorbance at their SPR peak could also be regarded as a fast detection of average AuNP uptake [259], though the accuracy might not be comparable to other methods. On the other hand, many **microscopic methods** that provide the distribution and spatial location of AuNPs are used in quantifying AuNPs as well. These methods include transmission electron microscopy (TEM) and optical microscopies such as dark-field microscopy (DFM) that is based on light scattering [142, 258]. Although TEM provides much higher resolution (Ångstrom to nanometer) when

compared to DFM (>250 nm) for measuring intracellular spatial distribution, it requires complex and laborious sample section preparation. In addition, the number of measured cells are always limited. Flow cytometry (FCM) is a cell sorting method that can detect the fluorescence or scattering from cells. AuNPs uptake can be quantified from the side scattering signal (SSC) as the existence of AuNPs increases the SSC response from the flow cytometer. A recent article measured the SSC signal from intracellular AuNPs and compared this data with similar data from the ICP-MS, which showed a perceptible agreement between the two methods [260]. The FCM method is beneficial as it is quick and without labor-intensive and complicated sample preparation. It is very effective for measuring not only the average amount of AuNP intracellular content, but it also provides information regarding AuNP distribution within the cell population. In addition, we can sort portion of cells using FCM based on specific AuNP content which is useful for further studies, such as proteomics and gene sequencing.

Traditionally, the side scattering mode with 488 nm laser illumination (SSC channel) was used for measuring the intracellular AuNP amount[260], but AuNP scattering detection is not optimized under this illumination laser due to the SPR phenomenon. For most of the spherical AuNPs (AuNSs), the SPR peak is around 510-550 nm, while for Au nanorods (AuNRs), the SPR peak will be a higher wavelength ranging from the visible range of the electromagnetic spectrum to the infrared region. In addition, the aggregation of AuNPs inside cells will cause a red shift of the SPR peak [144]. Therefore, we hypothesized that the use of an incident light with a higher wavelength is a promising approach to improving the flow cytometry-based detection of intracellular AuNPs by way of SSC signals.

Herein, we measured the FCM side scattering of intracellular AuNSs (25 nm) and AuNRs (40 x 80 nm, width x length) using incident lasers with different wavelength. Our results show that by red-shifting the illuminating laser wavelength, the signal will be greatly enhanced for detecting both AuNSs and AuNRs cellular uptake using FCM.

1.6.2 Methods.

Materials. Tetrachloroauric acid trihydrate ($HAuCl_4 \cdot 3H_2O$), trisodium citrate, silver nitrate ($AgNO_3$), sodium borohydride ($NaBH_4$), ascorbic acid, cetyltrimethylammonium bromide (CTAB), paraformaldehyde, glutaraldehyde, ethylenediaminetetraacetic acid (EDTA), HEPES, bovine serum albumin (BSA), were purchased from Sigma (St. Louis, MO). Dulbecco's modified Eagle's medium (DMEM), fetal bovine serum (FBS), antibiotic/antimycotic solution, phosphate buffered saline (PBS), and 0.25% trypsin/2.2 mM EDTA solution were purchased from VWR. Methoxypolyethylene glycol thiol (mPEG-SH, MW 5000) was purchased from Laysan Bio, Inc. Cell-penetrating peptide RGD (RGDRGDRGDRGDPGC) and Nuclear localization sequence NLS (CGGGPKKKRKVGG) peptides were purchased from GenScript, Inc. All the water used in experiments was purified with a Milli-Q system from Millipore (Milford, MA).

Instrumentation. Gold nanoparticles were imaged under a JEOL 100CX-2 transmission electron microscope (TEM). The average sizes of AuNPs were measured by ImageJ software based on the TEM images. The spectra of AuNPs were obtained using an Ocean Optics HR4000CG ultraviolet-visible-near infrared (UV−Vis-NIR) spectrometer. The surface charge of AuNPs (zeta potential) was determined by use of a

ZetaSizer 3000 (Malvern Instruments). Flow cytometry experiments were performed on BD LSR Fortessa supplied with 405 nm, 488 nm, 561 nm, and 640 nm excitation lasers. The BioTek Synergy H4 Hybrid plate reader was used for reading the XTT cell viability assay results. Dark field microscopy is equipped with Lumenera Infinity2 CCD camera.

Gold Nanoparticle Synthesis, Conjugation, Characterization. Gold nanospheres (AuNSs) with an average diameter of 40 nm were synthesized using the citrate reduction method. 500 mL of 0.254 mM $HAuCl_4$. $3H_2O$ solution was heated until boiling and reduced by adding 9 mL of 0.35% citrate solution quickly to the precursor solution. Solution was left under heat and an observable color change occurred from light yellow to burgandy upon reaction completion. Solution was then removed from the heating apparatus and cooled with a water bath. Newly synthesized AuNSs were purified via centrifugation with initial conditions being 1,500 g for 5 minutes and adding DI H_2O to the pellets.

Gold nanorods were synthesized using a seed growth method that developed by our lab [4]. Briefly, to prepare Au seed, CTAB solution (5 mL, 0.20 M) and $HAuCl_4$ (5.0 mL of 0.00050 M) was mixed with stirring. Then, 0.60 mL of ice-cold $NaBH_4$ (0.010 M) was added. The mixture was vigorously stirred of generate Au seed for 2 min. A brownish yellow solution was formed. Next, to prepare the growth solution, 5.0 mL of $HAuCl_4$ (1.0 mM), 270 μL of $AgNO_3$ (4.0 mM), 5.0 mL of CTAB (0.2 M) and 70 μL of ascorbic acid (78.8 mM) was gently mixed. The prepared Au seed (12.0 μL) was then added to the growth solution and allowed to react with no disturbance for hours. The as-synthesized AuNRs were washed by DI H_2O via centrifugation twice with initial

conditions being 10,000 g for 30 minutes and 5,000 g for 10 min. TEM was used for imaging the sizes and the homogeneity of the AuNPs prepared.

For surface modification, the purified nanoparticles were treated with polyethylene glycol (PEG, 1 mM) as an initial conjugation step and left on a shaker overnight with 1:1,000 (AuNP: PEG). RGD (1 mM) and NLS (1 mM) were added concurrently, with 1:10,000 (AuNP: RGD) and 1:100,000 (AuNP: NLS) after initial conjugation step and shaken overnight. Conjugated AuNPs were then centrifuged and re-dispersed in DI water. To test the surface modification, UV−Vis-NIR spectrometer and zetasizer were used. The AuNPs' spectra red shift due to the changes in the dielectric constant of the surrounding environment of AuNPs offers verifiable evidence of conjugation success.

The molar concentrations (C) of the AuNPs (AuNSs and AuNRs) are calculated based on Beer's law $A=\varepsilon \times b\times C$, where A is the extinction of AuNPs (O.D.), ε is the molar extinction (L mol^{-1} cm^{-1}), b is the path length of the sample (1 cm). Both of the AuNSs and AuNRs have $\varepsilon\sim 3\times 10^{9}$ L mol^{-1} cm^{-1} according to literatures[7, 261], due to their specific sizes and/or aspect ratios.

Cell culture and incubation with AuNPs. Human breast adenocarcinoma MDA-MB-231 cells were cultured in Dulbecco's Modified Eagle Media (DMEM) (without Phenol red) with 1% antibiotic and 10% Fetal Bovine Serum under standard incubation conditions (5% CO_2, 37℃). Cells were treated with differing concentrations of AuNSs and AuNRs (C0, control no AuNPs; C1, 0.033 nM; C2, 0.083 nM; C3, 0.17 nM; C4, 0.33 nM and C5, 0.5 nM) for 24 h. UV-Vis-NIR spectra was taken of media solutions with

varying concentrations of AuNSs and AuNRs before and after a 24 h incubation period. The difference of the absorbance peaks corresponds to a quantification of cellular uptake. The cellular uptake of AuNPs can also be measured by dark field imaging. The cellular uptake of AuNPs were also measured by dark field microscopy. For dark field imaging, the cells were fixed with paraformaldehyde and glutaraldehyde and subsequently imaged with a Lumenera Infinity2 CCD camera.

Cell Viability Assay. To examine the toxicity effect of the AuNPs, XTT cell viability assays were performed according to the Biotium ™ experimental protocol, in which the XTT activation reagent was mixed with the XTT solution and added to cells. After a 24 h incubation time with AuNPs, absorbance signals from cells were obtained via a plate reader. Background absorbance was subtracted from signal absorbance to collect normalized absorbance values.

Flow Cytometry Measurements. Following AuNP treatment, cells were trypsinized, centrifuged at 1500 x g for 5 mins, and re-suspended with FBS sorting buffer composed of phosphate buffer saline (PBS), 1mM EDTA, and 25 mM HEPES. The samples were then washed with PBS three times, and fixed with paraformaldehyde. Samples were analyzed using a flow cytometer supplied with 488 nm, 561 nm, and 687 nm excitation lasers. Side scattering signals (SSC) from cell samples were collected from varying excitation laser sources and detected with corresponding detection channels. Data output was analyzed utilizing the FlowJo ™ software. Signals were transformed into histogram plots to visualize the comparisons among detection channels and excitation laser combinations.

Data Analysis. A Two Tailed T-Test was performed to determine the statistical significance. The analyses were performed with the alpha type error set at 0.05.

1.6.3 Results

Two types of gold nanoparticles (spheres and rods) are synthesized and surfaced modified with PEG, RGD, and NLS according to our previous methods discussed in Section 2.2. No obvious toxicity effect was observed after incubation with MDA-MB-231 triple negative breast cancer cells with different doses of AuNPs (**Figure 2.28**).

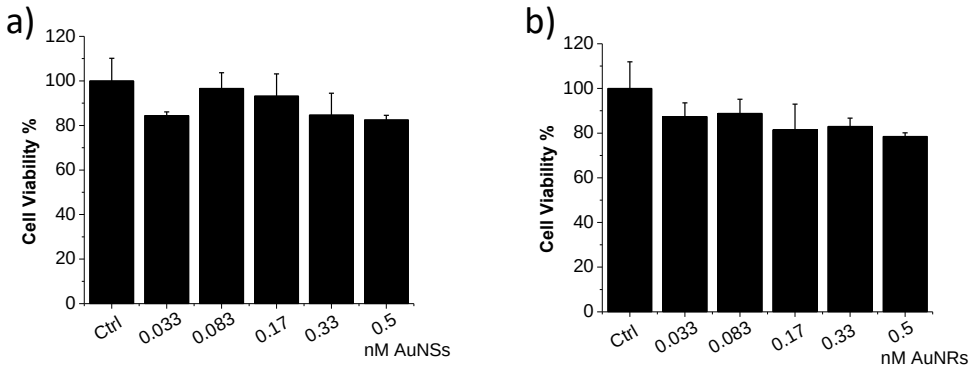

FIGURE 2.28. MDA-MB-231 cell viability when incubated with different concentrations of gold nanoparticles (a) AuNSs, (b) AuNRs.

1.6.3.1 Flow Cytometry Method Development for Measuring Cellular Uptake of Gold Nanoparticles

In flow cytometry, there are two modes of scattering measurements, t side scattering and forward scattering. The forward scattering channel (FSC) intensities of the MDA-MB-231 cells incubated with AuNPs were similar to those of the controls **(Figure 2.29)**, which is in agreeance with previous reports [260, 262]. The side scattering channel (SSC) usually indicates the scattered light collected at the perpendicular direction (90^{o}) of

the incident laser (usually 488 nm), which is commonly used as an indication of the cell's internal complexity or granularity. When nanoparticles are internalized into the cells, they increase the complexity of cells which could be attributed to the increased SSC intensity. Several studies have indicated that when cells uptake gold, TiO_2, ZnO nanoparticles, *etc*, the SSC intensity increases [260, 263, 264]. Due to the high scattering coefficients of AuNPs (~5 orders of magnitude greater than conventional fluorescent dyes), SSC could be especially beneficial for detecting signals from AuNPs. The SSC supplied with a 488 nm laser illumination is a commonly used setting for flow cytometry based detection of intracellular AuNPs, but is not optimized for detecting AuNPs. For most of spherical AuNPs, their SPR peaks are located between 510-550 nm; while for Au nanorods (AuNRs), the SPR peak will be tuned to higher wavelength from visible range to infrared. In addition, the aggregation of AuNPs inside cells will cause red shift on the SPR peak [144]. Therefore, herein, we used an incident light with higher wavelength, which is promising to improve the flow cytometry detection for AuNPs using the SSC signal.

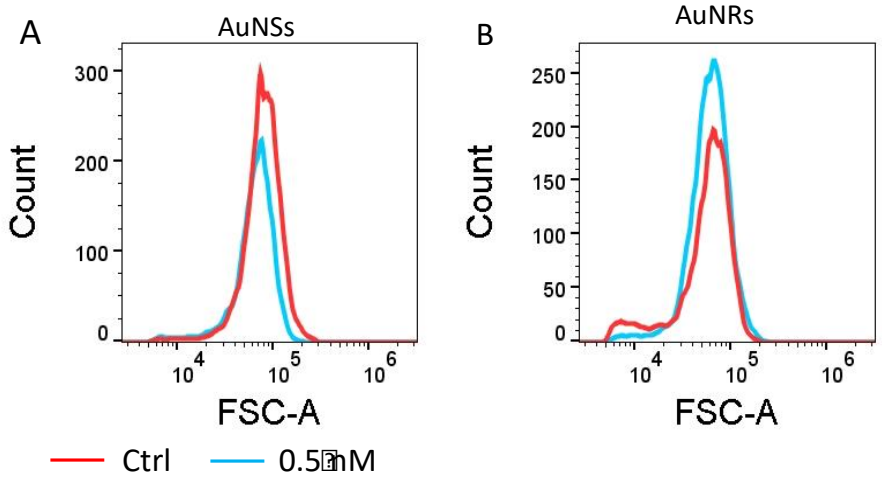

FIGURE 2.29. FSC signals of MDA-MB-231 cells without (Ctrl, blue) or with AuNPs (0.5 nM, red).

The conventional 488-SSC was examined first, and the result is shown in **Figure 2.30**. The cells incubated with 0.17 nM AuNPs showed only a very minor increase in the 488-SSC channel as compared with the control. Therefore, to optimize the incident laser, three different incident lasers (488, 561, 687 nm) were used. The scattering intensities were collected for different samples (C0-C5). As shown in **Figure 2.31** (for AuNSs) and **Figure 2.32** (for AuNRs), the SSC intensities increase when the intracellular AuNPs increase. The 687 nm incident laser gives the most significant change when measuring cells with varying intracellular AuNPs concentration (**Figure 2.31 m-r, 2.32 m-r**), while 488 nm, which is the default SSC channel laser, gives the worst performance (**Figure 2.31 a-f, 2.32 m-r**). Therefore, optimizing the incident laser could greatly assist the detection of intracellular plasmonic nanoparticles using flow cytometry. This can also be seen from the histograms in **Figure 2.33**.

The quantitative relationship between the scattering intensities and the amount of AuNPs from UV-Vis measurements were examined. The relation between flow cytometry and UV-Vis data was fitted with a linear function, as shown in Figure **2.34**. The 687 nm incident laser gives the largest slope of fitting and a much improved R^2 values compared with the other two lasers.

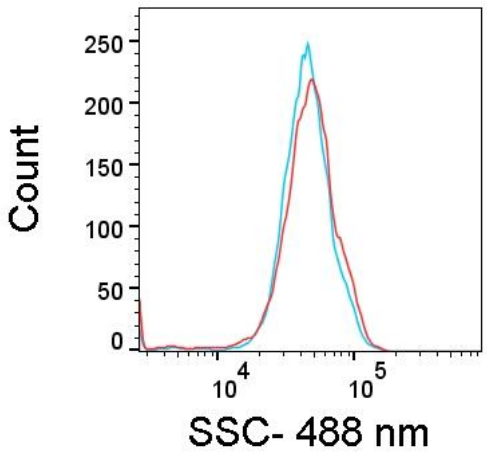

FIGURE 2.30. SSC signals of MDA-MB-231 cells with 488 nm incident laser is not sufficient for resolving cells or with AuNPs (0.33 nM, blue) and cells without AuNPs (Ctrl, red).

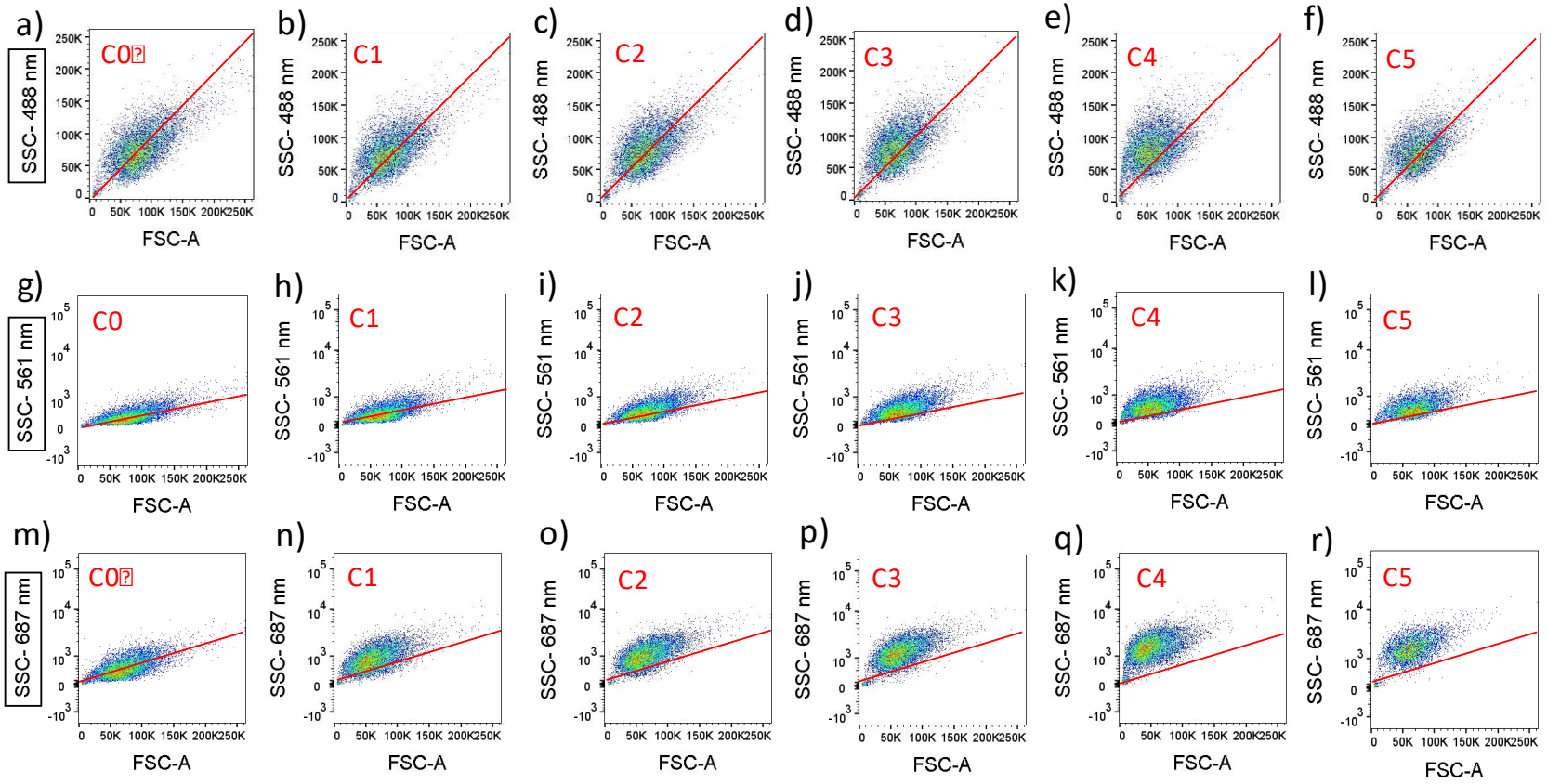

FIGURE 2.31. Flow cytometry scatter plots of MDA-MB-231 cells incubated with different concentrations of AuNSs in DMEM media (sample C0, control no AuNPs; C1, 0.033 nM; C2, 0.083 nM; C3, 0.17 nM; C4, 0.33 nM and C5, 0.5 nM). The plots are side scattering (SSC-A) versus forward scattering (FSC-A) under different incident lights (a-f, 488 nm; g-i, 561 nm; m-r, 687 nm).

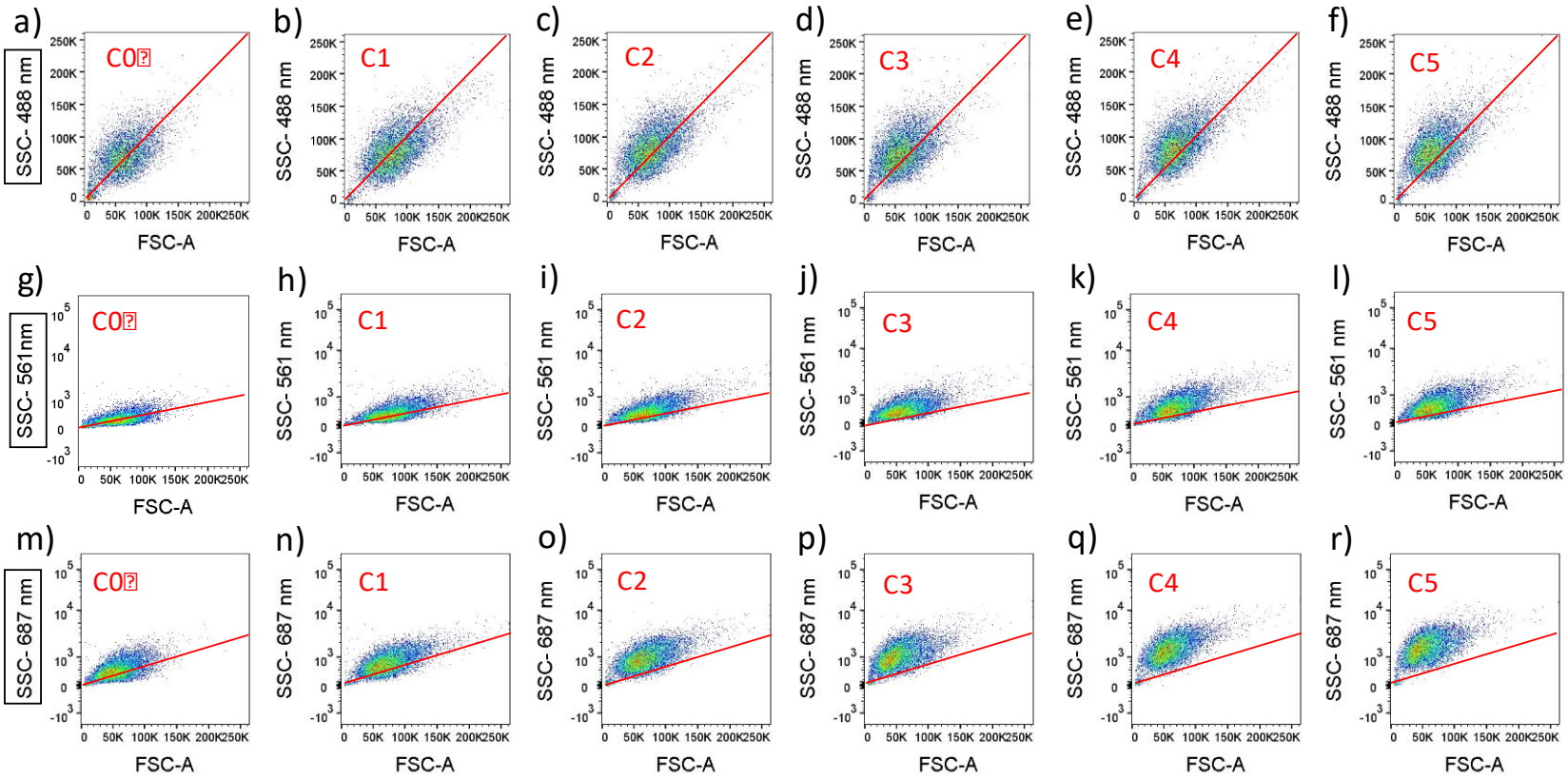

FIGURE 2.32. Flow cytometry scatter plots of MDA-MB-231 cells incubated with different concentrations of AuNRs in DMEM media (sample C0, control no AuNPs; C1, 0.033 nM; C2, 0.083 nM; C3, 0.17 nM; C4, 0.33 nM and C5, 0.5 nM). The plots are side scattering (SSC-A) versus forward scattering (FSC-A) under different incident lights (a-f, 488 nm; g-i, 561 nm; m-r, 687 nm).

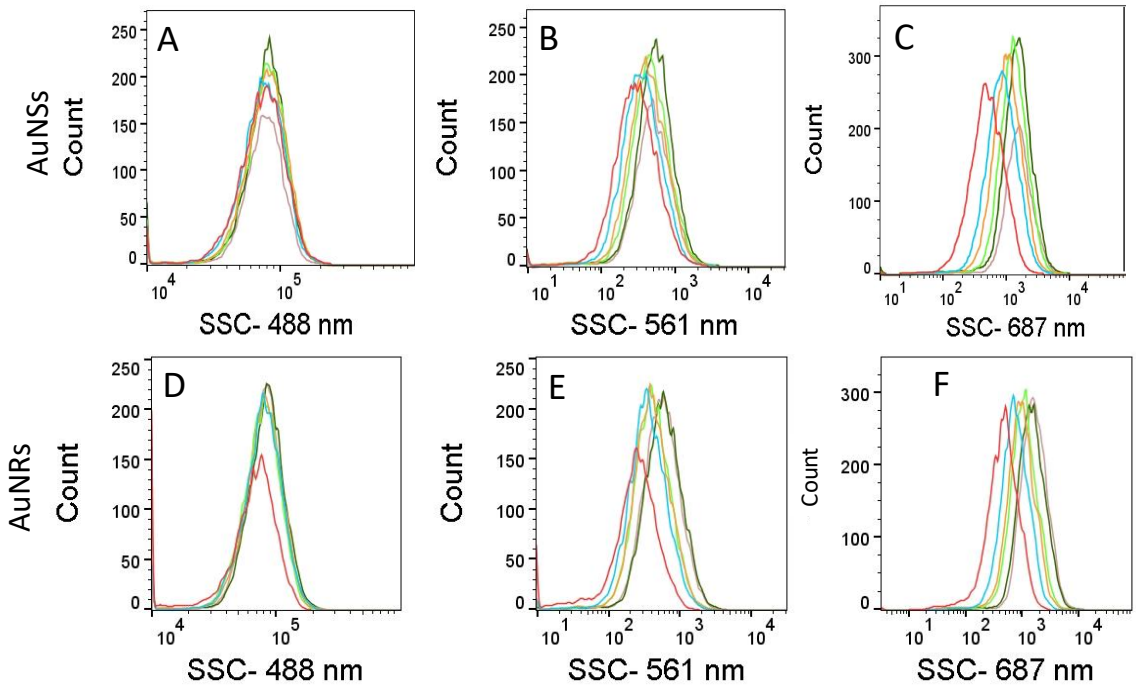

FIGURE 2.33. Side scattering intensity (SSC-A) histograms of MDA-MB-231 cells with different incident light wavelengths (488 nm, A for AuNSs and D for AuNRs; 561 nm, B for AuNSs and C for AuNRs; 687 nm, C for AuNSs and F for AuNRs). Cells with different intracellular concentrations were measured. Red, blue, orange, light green, dark green and tan lines represent samples C0-C5 (C0, Ctrl; C1, 0.033 nM; C2, 0.083 nM; C3, 0.17 nM; C4, 0.33 nM and C5, 0.5 nM) for 24 h.

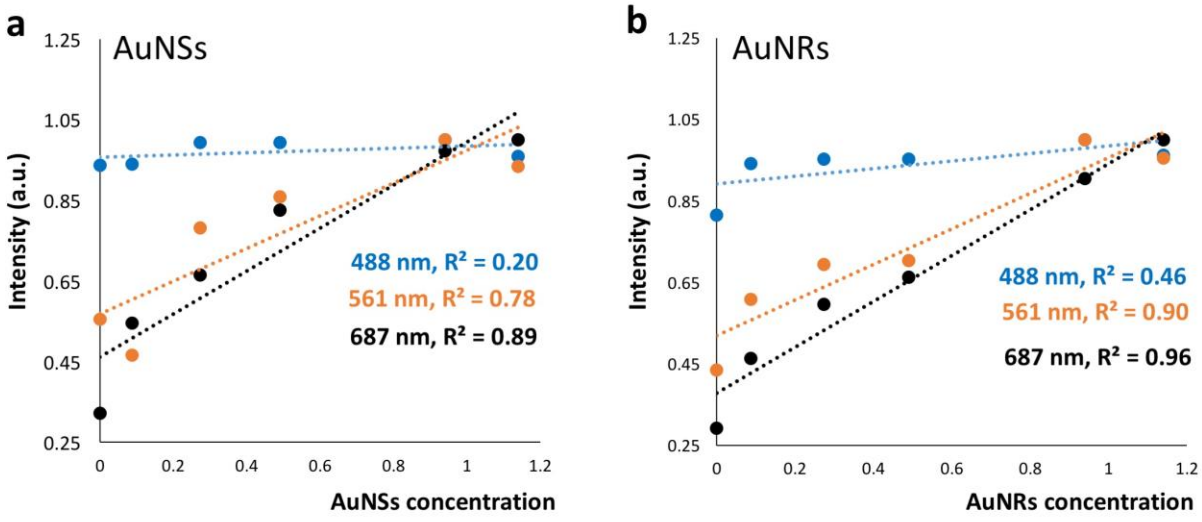

FIGURE 2.34. Cellular AuNPs versus scattering intensities, including linear regression lines: (a) gold nanospheres (AuNSs) and (b) gold nanorods (AuNRs). Blue: 488 nm incident laser; orange: 561 nm incident laser; black: 687 nm incident laser.

1.6.4 Discussion

Gold nanoparticles are widely studied as intracellular imaging probes or as therapeutic reagents. To study the AuNPs amount in cells, the ICP-MS, spectroscopic method or imaging are used. Some of these methods are labor-intensive due to complicated sample preparation procedures, destructive to the cells because of biological incompatibilities, and lacking in the information provided as they only provide the average intracellular particle amount. Flow cytometry can act as an easy and efficient method for not only measuring average cellular uptake, but also providing information regarding the AuNPs distribution within the cell population. Herein, by improving the sensitivity of the flow cytometry- based detection of intracellular AuNPs, through simply increasing the incident laser wavelength and collecting the scattering signals, we are able to distinctly differentiate cells with different AuNPs amount.

The objects (cells or particles with size range of 1-40 μm[264]) in flow cytometry detection usually requires fluorescent labels. Several types of nanoparticles present high scattering cross sections, which enables sensitive scattering detection for their existence in cells. TiO_2 nanoparticles, which are used as ingredients in sunscreen and paints, can absorb UV light. As the default, flow cytometry side scattering channel (488 nm) are close to the extinction range of TiO_2, good resolution has been reported to differentiate cell samples with and without TiO_2, using the default setting of SSC channel in flow cytometry [262, 263]. Zucker et al claimed that by using flow cytometry, they were able to

detect as low as 5-10 TiO_2 nanoparticles per cell, which is very sensitive[263]. Ag nanoparticles, which presents the SPR at around 400-500 nm, have strong scattering at this range, are also suitable for the default 488 nm SSC channel [265]. In addition, for the internalization of other types of nanoparticles, such as CuO[266], superparamagnetic iron oxide nanoparticles (SPIONs) [267], ZnO_2 [264], this method might also apply according to previous reports.The same method using 488 nm laser was also been used in the case of AuNPs [260]. However, the response of AuNPs scattering under 488 nm is not optimized. In our results, we demonstrated that by using a higher-wavelength incident laser, we are able to achieve much better signals of intracellular AuNPs.

It is widely recognized that when cells undergo apoptosis, the shrinkage of the cell body will cause a decrease of the FSC signal, and an increase of the cell granularity (due to the apoptotic body that is produced inside the cells) which will cause a subsequent increase of the SSC signal [264]. Therefore, it is always beneficial to know the cause of an increased SSC signal which could be due to the apoptosis process or nanoparticle uptake. A fast way to distinguish between these two causes is to reference the change or lack thereof in the FSC, as many studies reports no change of FSC when NPs internalized [260, 264], including this work. Another way is to add a cell apoptosis analysis to see if there is apoptosis process happening.

1.6.5 Conclusion.

By increasing the incident laser wavelength, the scattering signal of cells with different AuNPs (AuNSs and AuNRs) concentrations can be much better differentiated. This simple method will be very useful in detecting cellular gold nanoparticles combining

with sorting cells with specific gold nanoparticle amount. The greatest advantage of using flow cytometry is its ability for subsequent studies, such as proteomics, gene sequencing, Western blot, *etc*.

GOLD NANOPARTICLES CHANGES THE MECHANICAL PROPERTIES OF CANCER CELLS IN INHIBITING THE CANCER CELL MIGRATION AND INVASION

Previously, the optical properties of AuNPs has been explored for developing theranostics agents for cancer. In this section, we studied the impact of AuNPs on the mechanical properties of cancer cells for inhibiting cancer cell migration and invasion.

Note: Yue Wu and Moustafa Ali have equally contributed to designing, performing, analyzing, and writing the research in this section.

1.7 Nuclear Membrane-targeted Gold Nanoparticles Inhibit Cancer Cell Migration and Invation [85]

Summary. Most cancer patients die from metastasis. Recent studies have shown that gold nanoparticles (AuNPs) can slow down the migration/invasion speed of cancer cells and suppress metastasis. Since nuclear stiffness of the cell largely decreases cell migration, our hypothesis is that targeting AuNPs to the cell nucleus region could enhance nuclear stiffness, and therefore inhibit cell migration and invasion. Our results showed that upon nuclear targeting of AuNPs, the ovarian cancer cell motilities decrease significantly, compared with non-targeted AuNPs. Furthermore, using atomic force microscopy, we observed an enhanced cell nuclear stiffness. In order to understand the mechanism of cancer cell migration/invasion inhibition, the exact locations of the targeted AuNPs were clearly imaged using a high-resolution three-dimensional imaging microscope, which showed that the AuNPs were trapped at the nuclear membrane. In

addition, we observed a greatly increased expression level of lamin A/C protein, which is located in the inner nuclear membrane and functions as a structural component of the nuclear lamina to enhance nuclear stiffness (**Figure 3.1**). We propose that the AuNPs that are trapped at the nuclear membrane both: 1) add to the mechanical stiffness of the nucleus and 2) stimulate the overexpression of lamin A/C located around the nuclear membrane, thus increasing nuclear stiffness and slowing cancer cell migration and invasion.

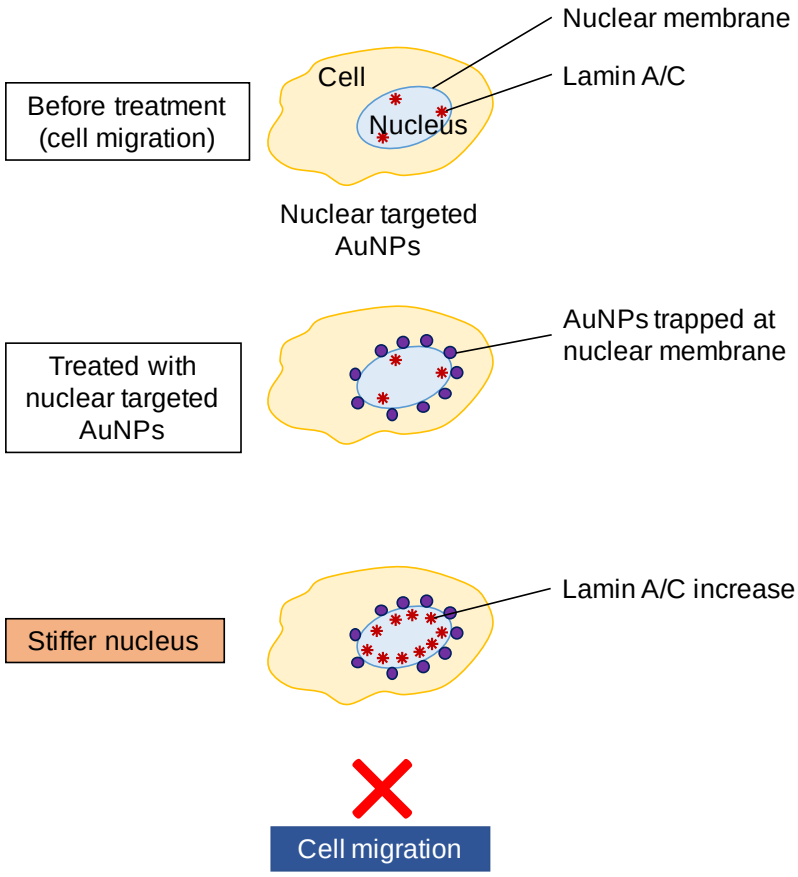

FIGURE 3.1. Figure abstract that shows (top) before the gold nanoparticle (AuNPs) treatment, the ovarian cancer cell (HEYA8) migration ability was high. However, upon nuclear targeting AuNPs treatment, the AuNPs were trapped at the nuclear membrane (middle). The trapped AuNPs in the membrane enhanced the nuclear stiffness of the cell (Bottom). Meanwhile, we observed that Lamin A/C protein expression increased, which is a protein located in the inner nuclear membrane that plays a key role in nuclear stiffness and thus slows down the cell migration.

1.8 Introduction

Metastasis, a process in which cancer cells migrate to other locations of the human body, is responsible for most cancer-related mortality. It usually begins with local invasion to the surrounding tissues, followed by intravasation into the lymph and blood microvasculature before the cancer cells finally colonize within the microenvironment of other locations in the patient's body [65, 268]. Many treatments for inhibiting metastasis are based on drugs that target specific proteins that promote the cell migration or invasion process; however, past attempts to develop anti-metastasis drugs have not been efficacious in clinical trials [67]. In many cases, the anti-cancer drugs that target specific proteins on the cancer cells might lose their efficacy after several months of treatment due to protein mutations thus conferring drug resistance to cancer cells [269]. Moreover, the anti-cancer drugs could cause side effects to appear in healthy tissues [270].

Recent advances in nanomedicine provide us with a great opportunity to avoid the drawbacks of current drugs [69, 269, 271], [130], [272, 273]. Nanoparticles have been widely used in cancer diagnosis and cancer therapy thanks to their intrinsic chemical, physical and optical properties [272, 274]. Nanoparticles with proper surface modifications can target tumors selectively [233, 234, 271, 275], and their effects on cancer cell migration or metastasis have drawn attention from many researchers [73], [132, 276], [76]. In 201, Murphy et al. reported that gold nanoparticles (AuNPs) with different surface charges and sizes can affect cancer cell migration [73]. In 2014, Chor Yong Tay et al.20 found that after incubation with nano-ceramics, such as titania, silica, and hydroxyapatite, cells showed significantly impaired wound healing capability because of the disruption of the intracellular microtubule assembly. In the same year, Zhou et al. [76] showed that gold nanorods (AuNRs) coated with bovine serum albumin (BSA) exhibited reduced cell

migration and invasion by impairing ATP synthesis, which subsequently inhibits the F-actin cytoskeletal assembly and decreases metastatic ability of tumor [76]. Arvizo et al. used non-specific targeted gold nanospheres (AuNSs) to inhibit tumor growth and metastasis by abrogating MAPK signaling and reversing the epithelial-mesenchymal transition [84]. For most of the related works, non-specific targeted nanoparticles have been used. For instance, Zhou et al. [76] used BSA coated AuNRs that showed inhibitory effects on cancer cell migration, but the high concentration of AuNRs (50-200 μM) used might be an obstacle for clinical usage. To maintain the nanoparticle effect on slowing the cancer cell migration and invasion with a minimized amount of nanoparticles, the intracellular locations of nanoparticles could be an important factor to consider. It is thus promising to design nanoparticles that can target specific intracellular regions to enhance the inhibition of cancer cell migration and invasion.

Mechanical stiffness of cancer cells has been shown to grade metastatic potential in patient tumor cells [277], as well as in cultured cancer cell lines [278]. Lower stiffness is related to more invasive cells [279]. In eukaryotic cells, the nucleus contains most of the cell's genetic material and controls cell activities by transcriptional regulation. It is the largest and stiffest organelle in most cells and largely determines the cell migration ability[280]. Lamin A/C (LMNA) proteins are an important factor in nuclear stiffness. They form a dense protein network that connects the nuclear membrane and chromatin structures on the interior of the nuclear membrane. Recent studies have shown that nuclear lamin A protein scales with tissue stiffness [281] and generates a barrier to cells migrating through three-dimensional (3D) environments [282]. It is shown that lamin A/C deficiency hampers cell mechanics, polarization, migration and invasion [283] [284].

Here, targeted AuNPs were used to locate the AuNPs to the cells, because of their specific physical and chemical properties and better biocompatibility than other nanomaterials such as nano-ceramics or silver nanoparticles [234, 285]. By targeting and locating the AuNPs to the cell in a manner to modulate the stiffness of its nucleus, we could improve the inhibition effect on cell migration and invasion. In our experiment, we used three ligands, methoxy-polyethylene glycol thiol (PEG) for increasing the biocompatibility of AuNPs, RGD (RGDRGDRGDRGDPGC) peptides for binding to the surface integrin of cancer cells and enhancing endocytosis, and nuclear localization signal (NLS, CGGGPKKKRKVGG) peptides for targeting the AuNPs to the nucleus. Cell migration or invasion abilities have been measured, and the results show a clear decrease in these functions after the nuclear targeting of the nanoparticles. For studying the cell mechanical response, atomic force microscope (AFM) showed that the two types of AuNPs (i.e. AuNRs and AuNSs) both significantly enhanced the nuclear stiffness. A high-resolution 3D optical imaging system showed the exact location of the nanoparticles, which were trapped at the nuclear membrane. The levels of lamin A/C were found to be elevated upon nanoparticle incubation, which could be an explanation for the observed enhanced nuclear stiffness causing inhibition of cell motility upon gold nanoparticle treatment.

1.9 Methods

Materials: Tetrachloroauric acid trihydrate ($HAuCl_4.3H_2O$), trisodium citrate, $NaBH_4$, ascorbic acid, cetyltrimethylammonium bromide (CTAB), $AgNO_3$, and bovine serum albumin (BSA) were purchased from Sigma-Aldrich (USA). Methoxypoly(ethylene glycol)-thiol (mPEG-SH, MW 5000) was purchased from Laysan

Bio, Inc. Cell penetrating peptide RGD (RGDRGDRGDRGDPGC) and nuclear localization signal (NLS, CGGGPKKKRKVGG) peptides were obtained from GenScript,Inc. Dulbecco's phosphate buffered saline (PBS), RPMI-1640 cell culture media, fetal bovine serum (FBS), antibiotic solution, and 0.25% trypsin/2.2 mM EDTA solution were purchased from VWR. 8.0 μm polycarbonate membrane inserts were bought from Costar. Hoechst 33342 solution was purchased from Thermo Fisher Scientific (20 mM solution)

Instrumentation: Gold nanoparticles were imaged using a JEOL 100CX-2 transmission electron microscope (TEM) microscope and their average size was then measured by ImageJ software. UV−vis spectra were obtained using an Ocean Optics HR4000CG UV-NIR spectrometer. Cell stiffness was obtained using a MFP-3D AFM (Asylum Research, Santa Barbara, CA) with a combined Nikon Ti inverted optical microscope (Nikon, Melville, NY) for optically aligning the probe (MCST-AUHW, Bruker, Camarillo, CA) with a nominal spring constant of 0.03 N/m) to the cells. Confocal images were taken with a Zeiss LSM 700-405 confocal microscope.

Gold nanoparticle synthesis, conjugation and characterization: Gold nanospheres (AuNSs) with an average diameter of 35 nm were synthesized using the citrate reduction method [15]. Briefly, 100 mL of 0.254 mM $HAuCl_4.3H_2O$ solution was heated till boiling, and then reduced by adding 2.5 mL of 0.35% of trisodium citrate. The solution was then left heating until it turned wine red, followed by cooling under water flow. The citrate stabilized AuNSs were centrifuged under 5000 g for 10 min and redispersed in deionized (DI) water to remove extra citrate and be ready for conjugation.

Gold nanorods (AuNRs) with an average size of 25 x 6 nm (length x width) were synthesized using a seedless growth method [228]. Briefly, 5 ml of 1.0 mM $HAuCl_4$ was added to a mixture of 5 mL of 0.20M CTAB, 250 ul of 4.0 mM $AgNO_3$ and 8 μL of 37% HCl. For reduction, 70 μL of 78.8 mM ascorbic acid was added, followed by immediate injection of 15 μL of 0.01M of ice-cold $NaBH_4$. The solution was left undisturbed for 12 hrs, then centrifuged at 21000 rpm for 50 min and redispersed in DI water followed by a second centrifugation at 19000 rpm for 40 min to remove the extra CTAB. TEM was used to measure the sizes and homogeneity of the nanoparticles.

AuNSs and AuNRs were then conjugated according to previous work [286] , [233], to achieve nuclear and cytoplasmic targeting. For nuclear targeting, first, mPEG-SH (1 mM) was added to the nanoparticles for overnight to achieve about 1000 ligands on each particle. Then, the PEGylated nanoparticles (1 nM) were treated with RGD (1 mM) and NLS (1 mM) to achieve 10^4 and 10^5 molar excess, respectively. The solution was then allowed to shake overnight at room temperature. Excess ligands were removed by centrifugation. For preparing BSA conjugated nanoparticles, BSA (4.5 mM) was added to the nanoparticles and left for 3 h to incubate. UV-vis spectrometer and zetasizer was used to test the conjugation. Surface modification causes red shift of UV-vis spectra due to the change in the dielectric constant of the surrounding environment of Au nanoparticles.

Cell culture and AuNPs incubation: The ovarian cancer HEY A8 cell lines were provided by Dr. G. Mills (MD Anderson Cancer Center, Houston, TX) and were grown in RPMI-1640 media supplemented with 10% FBS and 1% antibiotic-antimycotic solution (R10 medium). Cells were kept in a humidified incubator at 37 ^oC and under 5% CO_2. After achieving 50% confluence, the cells were incubated with functionalized

AuNSs or AuNRs in supplemented DMEM cell culture medium for 24 h. The concentration of nanoparticles was carefully chosen to avoid cytotoxicity or perturbation to the cell cycle [287].

Apoptosis/necrosis assay: The HEY A8 cells were collected by trypsinization and washed with cold PBS twice. Then, cells were the dispersed in 493 mL of Annexin V binding buffer before labeling by 5 μL of Annexin V FITC (BioLegend) and 2 μL of PI (BioLegend, 100 μg/ mL). The mixture was then incubated for 15 min at room temperature. The cells were subjected to flow cytometry analysis using a BSR LSR II flow cytometer (BD Biosciences). For excitation, a 488 nm laser was applied. FITC and PI were detected in FL-1 and FL-2 using 525/30 and 575/30 BP filters, separately. Standard compensation using unstained and single-stained cells was conducted before performing actual experiments. FlowJo software (Tree Star Inc.) was used for data analysis. At least 10 000 events were collected for each experiment [57].

Cell motility assay: HEY A8 cells were seeded on uncoated 24-well plate at a sub-confluent density for 24 hours. Then the cells were treated with nanoparticles of varying shapes and conjugated motifs before returning them to incubator for 12 hours to facilitate particle uptake. After the incubation period, cells were stained with nuclear dye Hoechst 33342 (dilution 1: 10,000) for 30-60 minutes. Cells were maintained at 37°C and 5% carbon dioxide throughout the experiment using an environmental cell chamber (InVivo Scientific). For observation, a Nikon Eclipse Ti inverted epifluorescent microscope was used and both bright field (BF) and DAPI images were taken at multiple xy positions at 12-minute time interval for 6-8 hours at 10x magnification. The locations of cell nuclei, segmented from fluorescent images, were tracked in MATLAB to define

cell traces. The cell migration coefficients and directional velocities were determined by fitting the traces to the persistent random walk model. Briefly, mean square displacements were calculated from the two-dimensional tracking data and was used for fitting the following equation,

$$\langle d^2(\tau)\rangle = 4\mu\{t - P[1 - e^{-t/P}]\} \quad (1)$$

Where P= persistence time and μ=migration coefficient.

Trans-well invasion assay: The Cultured 24 Well BME Cell Invasion Assay kit (Trevigen) was used according to the manufacturer's instructions. For these studies, HEY A8 cells were seeded and grown in a 6 well plate to 60-80% confluency before treating with nanoparticles in serum free media for 24 hours. Cells were then detached, spun down and re-suspended in serum free media. We also counted the cell number at this time to adjust the density to 500,000 cells/mL. Then 50,000 cells (100 μL) were added for each condition to the top surface of transwell inserts with 8 μm membrane pores coated with basement membrane matrix (BME). Cells were allowed to migrate toward the 10% FBS containing media in bottom chamber acting as the chemo attractant for a period of 32 hours. After the desired incubation time, non-migratory cells were gently removed from the top of each transwell using q-tips and the migrated cells at the bottom surface were detached using detaching buffer and incubated with Calcein AM. A plate reader was used to measure the fluorescence intensity, which is positively related to the number of trans-well cells.

Atomic Force Microscopy: AFM mechanical measurements [288], [289] of HEY A8 cells were obtained using an MFP 3-D AFM (Asylum Research, Santa Barbara, CA) on a vibration isolation table (Herzan, Laguna Hills, CA). A silicon nitride cantilever (Bruker, Camarillo, CA) was used for the experiments. The pyramidal tip had a half angle of 35° and the radius of curvature of the point of the tip was 20 nm. Measurements were performed on cells plated to the glass bottom of the Fluorodish and in culture media at room temperature. For eliminating the effect of the overlapping neighboring cells on the stiffness, single cells were measured. Thermal calibration[290] yielded the cantilever spring constant, k=28.01pN/nm. A measurement rate of 0.39 Hz was used. The 5 nN force trigger resulted in indentations of approximately 4 μm for typical cells. Cells were optically located using a Nikon Eclipse Ti microscope (Nikon, Melville, NY). Force-displacement curves were recorded to obtain the Young's modulus of each cell. Two distinct sets of measurements were performed with the AFM. The first investigated changes in mean cell stiffness between populations treated with AuNPs@NLS and an untreated control population. The second set of measurements investigated subcellular elasticity of nucleus. For the first set of measurements, the cantilever probe was positioned over the individual cells for indentation and measurement. For the second set, the probe was positioned over the perinuclear region.

Cell Imaging Using DIC Microscopy: An inverted Nikon Eclipse Ti-E microscope equipped with Perfect Focus System (PFS, 25 nm z-axial resolution) was used for imaging and z-stacks acquisitions under differential interference contrast (DIC) microscopy. The DIC mode utilized a pair of DIC polarizer and analyzer, a high resolution 100×I-R DIC slider, a high numerical aperture (N.A., 1.40) oil immersion

condenser lens, a Nikon CFI Apo TIRF 100× (N.A., 1.49) oil immersion objective, and a 12 V/100 W halogen lamp as light source. Appropriate bandpass filters were placed in the light path. The z-stack movies were taken by a Hamamatsu ORCA-Flash 4.0 V2 CMOS camera (C11440-22CU, pixel size: 6.5 μm × 6.5 μm) with Camera Link interface using Micro-Manager and analyzed using NIH ImageJ and reconstructed in Amira. Fixed HEYA8 cells on 22 mm × 22 mm glass coverslips were rinsed with DPBS at pH 7.4 and fabricated into a sandwiched chamber with two pieces of double-sided tape and a cleaned glass slide. PBS solution was added into the chamber to fill the space and the chamber was then sealed by clear nail polish. The so-formed sample slide was then place under the microscope for observation. Z-stacks were acquired using the Multi-Dimensional Acquisition function in Micro-Manger. More specifically, the DIC optical sectioning through the whole cell thickness was achieved by moving the objective on the motorized nosepiece using PFS at 65 nm/step at 33 ms (30 fps) exposure time.

Scratch assay: The scratch assay has been performed according to former report[291]. Cells were cultured in a 6 well plate to a confluent monolayer. A p200 pipet tip was used to scrape the cell monolayer in a straight line to create an empty gap. The debris was then remove by washing the cells once with culture medium and then replace with 2 ml of fresh medium. Then the cells were imaged shortly after and 12 hours after scratch.

Western blot: Briefly, cells were lysed in RIPA buffer (20 mM Tris pH 7.4, 150 mM NaCl, 2 mM EDTA, 2 mM EGTA, 0.1% Sodium Deoxycholate, 1% Triton X-100, 0.1% SDS) containing protease inhibitors (Sigma-Aldrich). BCA assay (Pierce) was performed to measure the protein concentration and equal amounts of protein were

loaded on a SDS-PAGE gel. After SDS-PAGE, the resulting gels were transferred to PVDF membranes (Millipore) overnight. Afterwards, the gel was blocked with 5% milk in TBS (20 mM Tris, 150 mM NaCl). A rabbit polyclonal antibody to Lamin A/C was used as the primary antibody (Bethyl Laboratories, Inc.) overnight in 4 °C with shaking. A goat anti rabbit HRP labeled antibody was used as the secondary antibody (Jackson Immuno Research Laboratories). Blots were washed 3 times for 20 m in TBS after primary and secondary antibodies. Konica Minolta developer and Hyglo enhanced chemiluminescence (Denville) were used to develop the immunoblots.

Immunofluorescence labeling and confocal microscopy: Cells were cultured on confocal chamber slides (MATECH Co. USA). After gold nanoparticle treatment[234], cells were fixed in 4% Paraformaldehyde/0.1% Glutaraldehyde for 10 min at room temperature the wash with PBS. Cells were then permeabilized with 0.1% Triton X-100 for 5 min at room temperature. Cells were then blocked with 5% BSA and incubated with the primary antibody as stated in the Western-blot method for overnight. Cells were then incubated for 1 h with an Alexa Fluor 488 secondary antibody (Invitrogen) for 1 h before mounting with Prolong Gold (Invitrogen). Lastly images were taken with a Zeiss LSM 700-405 confocal microscope and the fluorescence intensity was quantified in Image J.

Data analysis: To determine the Young's modulus, IGOR Pro software (Wavemetrics, Portland, OR) was used to apply the Hertzian contact model [292],[293] from 10-90% of the maximum indentation of the extension force-displacement curve. Due to the unequal sample size and heteroscedasticity of the AFM data, overall statistical significance of differences in mean cell stiffness and nuclear stiffness between cells treated with AuNPs@NLS was tested using Welch's analysis of variance (ANOVA).

Post-hoc analysis was performed using the Games-Howell test. For the rest of the studies, we used t-test. The analyses were performed with the alpha type error set at 0.05.

1.10 Results and Discussion

1.10.1 Gold Nanoparticle Synthesis, Conjugation, Cellular Uptake and Cytotoxicity Measurements

The AuNRs with an average size of 25 (± 2) x 5 (± 0.5) nm were synthesized using a seedless method, with a surface plasmon resonance (SPR) peak centered ~ 800 nm. The AuNSs with an average size of 35 ± 2 nm that absorb at 535 nm wavelength of light were synthesized using citrate reduction method. Both of the two types of the nanoparticles are widely used in the biological studies [294] [295] [285].

AuNPs were functioned with three ligands, methoxy-polyethylene glycol thiol (PEG), RGD (RGDRGDRGDRGDPGC) peptides and nuclear localization signal (NLS, CGGGPKKKRKVGG) peptides, as shown in schematic **Figure 3.2 a.** First, we conjugated the PEG to the surface of the AuNPs surface in order to enhance the biocompatibility [296]. The second ligand, RGD bound to surface integrins which are highly expressed on the surface of the cancer cells when compared to healthy cells to enhance the receptor-mediated endocytosis of the nanoparticles selectively to the cancer cells [231]. The third ligand, NLS, was recognized by importin and translocate into the nucleus [232]. Successful surface modification of AuNRs@PEG@RGD/NLS (AuNRs@NLS) is evident in the red-shift of the plasmon peak of AuNRs to longer wavelengths (we have previously desctibe this process in **Figure 2.10**). Similarly, the surface plasma peak of AuNSs@PEG@RGD/NLS (AuNSs@NLS) was also red-shifted

(**Figure 3.2 b**), which is in agreement with our former publication [286]. A TEM showing the sizes of AuNSs in **Figure 3.2 c**.

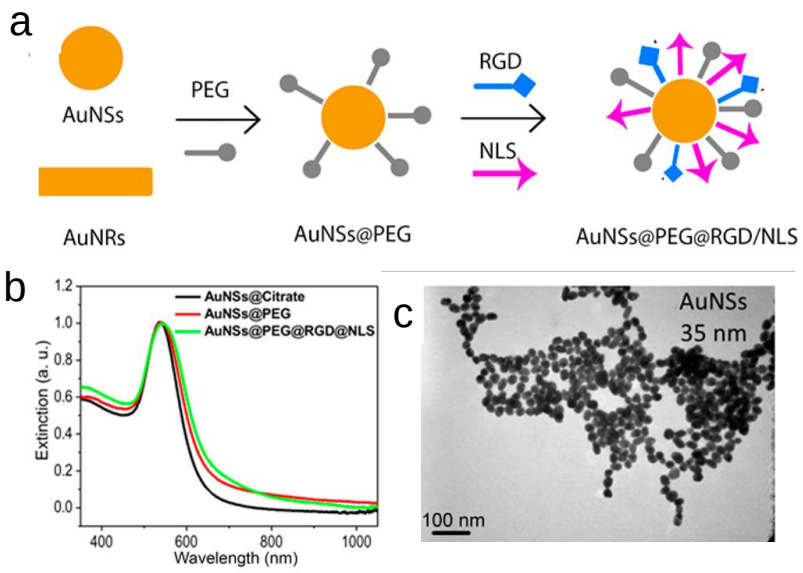

FIGURE 3.2. Characterization of Au nanoparticles. (a) Schematic figure of Au nanoparticle conjugation with PEG, RGD and NLS peptides. (b) UV-Vis extinction spectra of the unconjugated AuNSs (black spectrum), AuNSs@PEG (red spectrum), and AuNSs@PEG@RGD/NLS (green spectrum). (c) Transmission Electron Microscopic (TEM) image of gold nanospheres (AuNSs), Scale bar = 100 nm.

The zeta potential of the AuNRs at the different conjugating stages of the three ligands were measured (**Table 3.1**) to confirm the surface modifications. The as-synthesized CTAB coated AuNRs has a highly positive surface charge (50.9 ± 7.97 mV); this makes sense as CTAB is a highly cationic surfactant. After PEG modification, the AuNRs become negatively charged (-13.6 ± 11.8 mV). The zeta potential of the AuNRs becomes positive again (14.9 ± 3.13 mV) after further modification with RGD and NLS peptides (**Table 3.1**). Also, the zeta potential of the AuNSs@NLS proved their successful surface modification (**Table 3.1**), similar to previous studies [286].

Table 3.1. Zeta potential of AuNPs with different surface ligands

Au nanoparticles with different surface ligands	Zeta potential (mV)
AuNRs@CTAB	50.9 ± 7.97
AuNRs@PEG	-13.6 ± 11.8
AuNRs@PEG@RGD@NLS	14.9 ± 3.13
AuNSs@Citrate	-29.7 ± 4.72
AuNSs@PEG	-12.1 ± 5.79
AuNSs@PEG@ RGD@NLS	18.3 ± 7.55
AuNRs@BSA	-19.6 ± 9.89
AuNSs@BSA	-15.2 ± 12.5

To examine the cytotoxicity of the AuNPs, the XTT cell proliferation assay was conducted and no significant change of the cell viability was observed for nanoparticles at frequently used concentrations 0.5, 2.5 and 5 nM (for AuNRs) [234],[297] (**Figure 3.3 a and b**), and 0.05, 0.1 and 0.2 nM concentrations (for AuNSs) [236, 286]. Apoptosis/necrosis assay was also conducted for 5 nM of the AuNRs or 0.2 nM of the AuNSs (**Figure 3.3 c, d and e**) using flow cytometry. The results indicate that the concentrations of the AuNRs used in this study are lower than those affecting cell viability or inducing apoptosis.

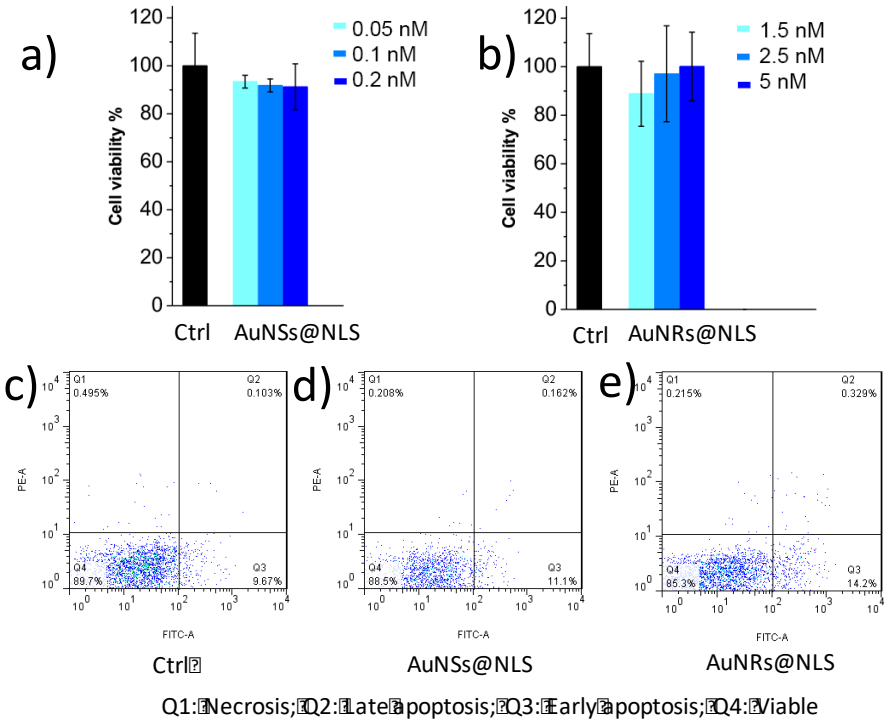

FIGURE 3.3. Au nanoparticles cytotoxicity measurements and cellular uptake. (a) Cell viability measurement (XTT assay, n=3) of HEY A8 cells after 24 h incubation with AuNSs@NLS at concentrations 0.05 nM (light blue), 0.1 nM (medium blue) and 0.2 nM (dark blue). (b) Cell viability (XTT, n=3) assay for cells after 1.5 nM (light blue), 2.5 nM (medium blue) and 5 nM (dark blue) of AuNRs@NLS incubation with HEY-A8 cells for 24h. (c, d, and e) Flow cytometry experiment for apoptosis/necrosis assay (c, Ctrl; d, cells incubated with 0.2 nM of AuNSs@NLS; e, cells incubated with 5 nM of AuNRs@NLS).

The mass concentration (gram /L) of the two types of particles are very similar (SI, Equation 1). The uptake of AuNPs@NLS was monitored using dark-field (DF) microscopy and UV-Vis absorption. The HEY A8 cells, which were previously identified to be highly invasive cell line [298], were incubated with 2.5 nM of AuNRs@NLS or 0.05 nM of AuNSs@NLS for 24 hrs. As shown in the DF image (**Figure 3.4 a and b**), clear internalization of both AuNPs (AuNRs@NLS and AuNSs@NLS) was observed. To evaluate the AuNPs uptake to the HEY A8 cells, UV-Vis spectra were collected for the AuNPs in culture media before incubation with cells and compared with the ones after 24 h cell incubation (**Figure 3.4 c and d**). According to the Beer's law, the concentration of

gold nanoparticles is linearly correlated with the absorbance at their localized surface plasmon resonance (LSPR) wavelength. Therefore, the decrease of the absorbance indicates the portion of AuNRs internalized in cells [299], [300].

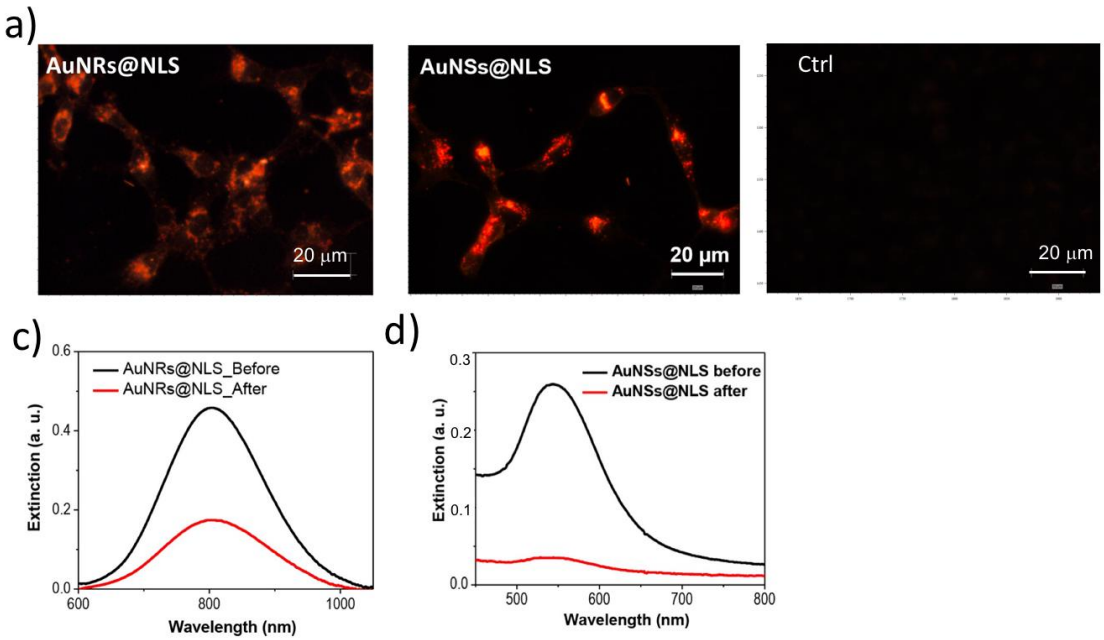

FIGURE 3.4. HEY A8 cell uptake of AuNRs@NLS and AuNSs@NLS. (a) Dark field images of cells without AuNPs incubation (Ctrl), with 2.5 nM of AuNRs@NLS and 0.1 nM of AuNSs@NLS incubation. (c) UV-Vis spectra of 2.5 nM of AuNRs@NLS or 0.1 nM of AuNSs@NLS (d) in culture media before incubation with cells (black spectrum), compared with the ones after 24 h cell incubation (red spectrum).

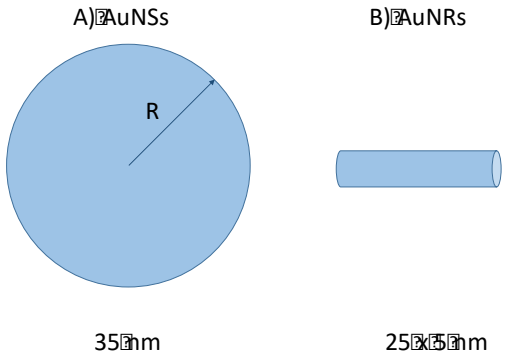

$$\frac{C_{\text{AuNSs (g/L)}}}{C_{\text{AuNRs (g/L)}}} = \frac{M_{w(Au)}\rho_{(Au)}V_{AuNSs}C_{AuNSs}}{M_{w(Au)}\rho_{(Au)}V_{AuNRs}C_{AuNRs}}$$

$$= \frac{V_{AuNSs}C_{AuNSs}}{V_{AuNRs}C_{AuNRs}} = \frac{{}^{4}/_{3}\pi R^{3}C_{AuNSs}}{\pi(\frac{w}{2})^{2}lC_{AuNSs}} = 0.92 \approx 1 \quad (2)$$

where C_{AuNSs}(g/L) or C_{AuNRs}(g/L) is the mass concentration (in gram of gold/L), Mw(Au) is the molar mass of gold, ρ(Au)is the density, V_{AnNSs} or V_{AuNRs} is the volumn of the gold nanoparticles (AuNSs or AuNRs), C_{AuNSs} or C_{AuNRs} is the molar concentration of the gold nanoparticles (AuNSs or AuNRs), R is the average radius of the AuNSs, w and l are the width and length in the AuNRs.

Non-targeted AuNPs with bovine serum albumin (BSA) coating were also fabricated. Successful surface modification of AuNPs@BSA (both AuNRs@BSA and AuNSs@BSA) was evident in the red-shift of the surface plasmon peak of AuNPs to longer wavelengths (**Figure 3.5 a and b**). Zeta potential of AuNRs after BSA modification became negatively charged (-19.6 ± 9.89 mV, Table 3.1) due to the negative charge of BSA, while the as-synthesized CTAB coated AuNRs has highly positive surface charge (50.9 ± 7.97 mV, **Table 3.1**). The AuNSs@BSA also has a negative zeta potential of -15.2 ± 12.5 mV (**Table 3.1**). No toxicity effect of AuNPs@BSA was observed, as shown in **Figure 3.5 c and d.**

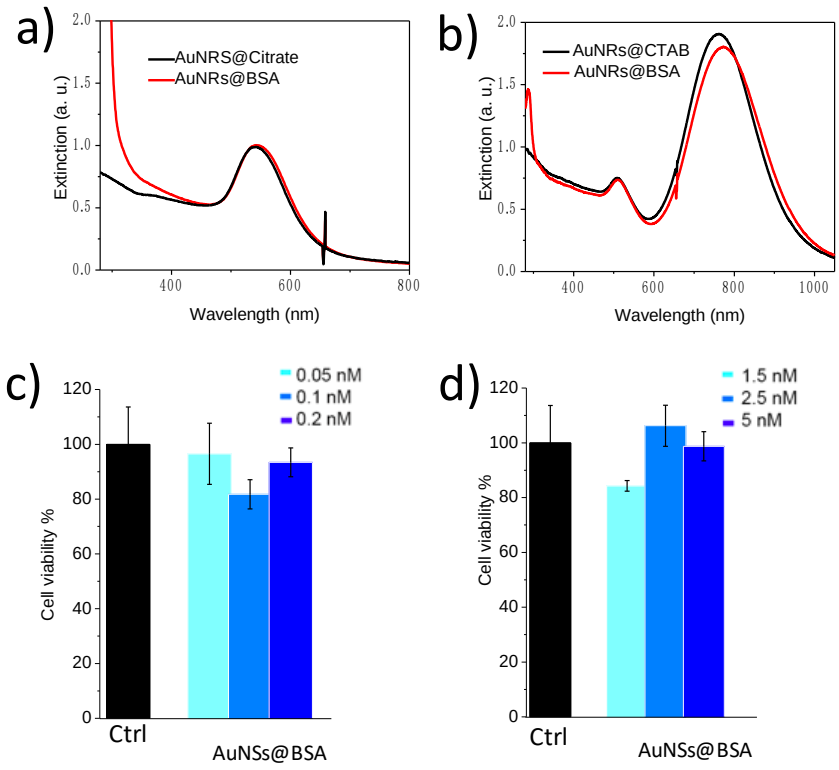

FIGURE 3.5. Characterization for AuNPs@BSA and HEY A8 cell uptake. (a) UV-Vis extinction spectra of the unconjugated AuNSs@Citrate (black spectrum) and AuNRs@BSA (red spectrum). (b) UV-Vis extinction spectra of the unconjugated AuNRs@CTAB (black spectrum) and AuNSs@BSA (red spectrum). (c) XTT assay of HEY-A8 cells after 24 h incubation with AuNSs@BSA at concentrations 0.05 nM (light blue), 0.1 nM (medium blue) and 0.2 nM (dark blue), n=3. (d) XTT assay for cells after 1.5 nM (light blue), 2.5 nM (medium blue) and 5 nM (dark blue) of AuNRs@BSA incubation with HEY-A8 cells for 24h (n=3).

1.10.2 Nuclear Targeting Gold Nanoparticles Inhibit Cancer Cell Migration and Invasion

To test the cell motility, HEYA8 cells were incubated with AuNPs for 12 hours before staining with fluorescent nuclear dye. Cells were then placed on an inverted epi-fluorescent microscope equipped with a cell culture chamber for continuous bright field and fluorescence imaging. The cell migration coefficients were then determined from the images. As shown in **Figure 3.6 a**, both nuclear-targeted AuNRs and AuNSs inhibit the

motility of HEY A8 cells. The average migration coefficient of the cells decreases from 3 x 10^{-10} by a factor of 3-10 (**Figure 3.6 a**). We conducted a control experiment of non-targeted AuNPs coated with BSA, (AuNPs@BSA, **Figure 3.5**). The motility assay shows that there is no apparent inhibition of AuNRs@BSA or AuNSs@BSA on cell migration (**Figure 3.6 b**).

The scratch assay was conducted to evaluate the migration ability. Results (**Figure 3.6 c**) indicate that the control cells had a completely healed "wound" after 24 h following AuNPs incubation, while the ones treated with AuNRs@NLS and AuNSs@NLS were not completely healed after 24 h. No obvious change in cell proliferation rate were observed after 24 hours (**Figure 3.3 a and b**), thus the scratch assay result merely reflects the migration ability of the cells.

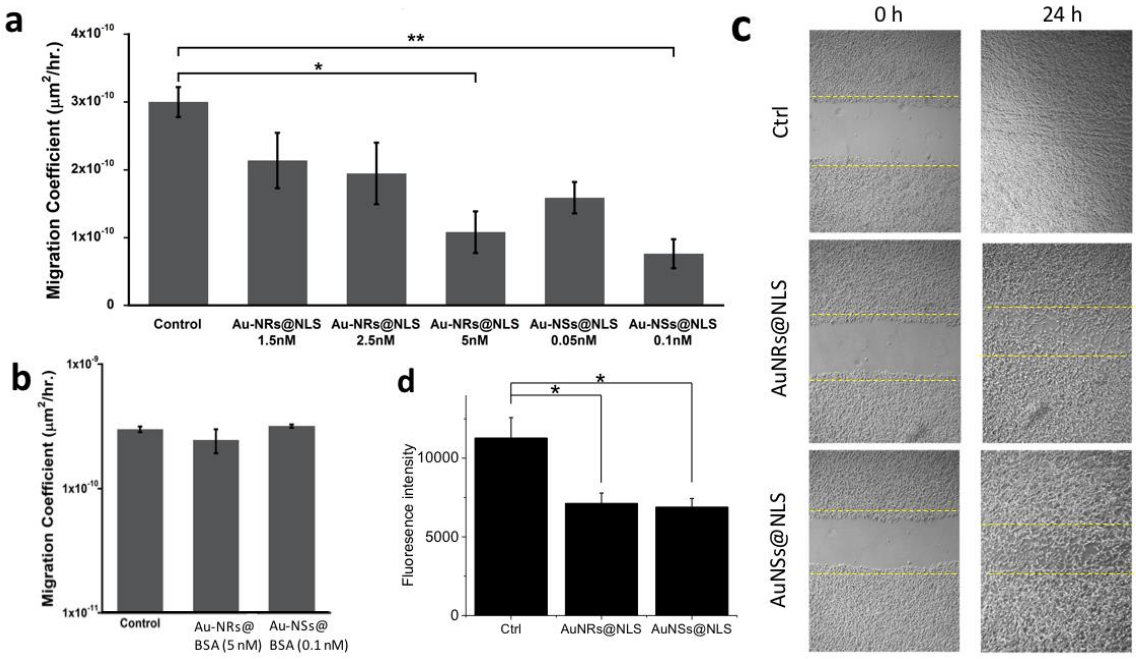

FIGURE 3.6. Effect of AuNPs (2.5 nM AuNRs@NLS and 0.1 nM AuNSs@NLS if not mentioned) on motility and invasion of HEY A8 cells. Cell migration study was performed to determine the effects of both AuNRs@NLS and AuNSs@NLS (a), and AuNRs@BSA (5 nM) and AuNSs@BSA (0.1 nM) (b) on the HEY A8 cells motility (error bar ±SEM, n=2). (c) Scratch assay of cells incubated with AuNRs@NLS and AuNSs@NLS displayed arrested healing/closing of the scratch. (representative pictures from 3 repeated experiments) (d) Invasion assay of cells without AuNPs or

with AuNRs@NLS and AuNSs@NLS treatment (error bar ± SD, n=3). *P < 0.05, **P < 0.01, ***P<0.001.

In order to examine the invasion ability of HEY A8 cells after their treatment with the nuclear membrane-targeted AuNPs, the trans-well invasion assay was performed. The cells that invaded the basement membrane extract (BME) after 32 h were dissociated and stained with Calcein AM, a fluorescent dye that labels living cells. A control experiment has been performed to eliminate the possibility that gold nanoparticles could quench the fluorescence from Calcein AM (**Figure 3.7**). A significant decrease in fluorescence intensity was observed in the AuNPs treated groups, indicating the inhibition of the invasion ability of HEY A8 cells particles (**Figure 3.6 d**).

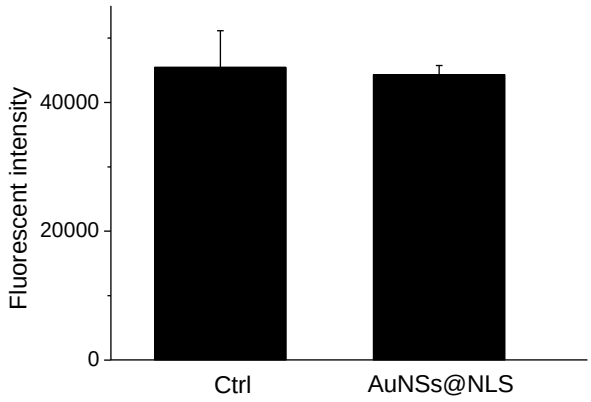

FIGURE 3.7. The introduction of Au nanoparticles in cells does not affect the Fluorescent intensity of Calcein AM (n=3).

In general, the cell migration and invasion abilities of HEY A8 cells were inhibited effectively by both AuNRs@NLS and AuNSs@NLS.

1.10.3 Nuclear Targeting Gold Nanoparticles Enhance Nuclear Stiffness

Next, we tested our hypothesis that the nuclear-targeted AuNPs can enhance nuclear stiffness. Cell stiffness as quantified by the Young's modulus has been used as a

biomarker of the metastatic potential of cancer cells [298]. For AFM measurements (**Figure 3.8 a**), a beaded cantilever was lowered on top of the individual cells, producing an indentation in those cells and corresponding deflection of the AFM cantilever, which allowed for the measurement of cell stiffness. An overhead image of AFM cantilever tip next to HEY A8 cells with nanoparticles was shown in **Figure 3.8 b**. The distribution of Young's moduli of individual cells, as well as that of the cell nucleus, from different nanoparticle treatments and the control is depicted in **Figure 3.8 c and d**. In our study, both AuNSs@NLS and AuNRs@NLS exhibit significant increase in the cell stiffness (**Figure 3.8 c**), which is similar to previous observations that nanoparticles could increase cell stiffness [301]. For the nuclear stiffness, as shown in **Figure 3.8 d**, the mean nuclear Young's modulus of the cells treated with AuNPs (AuNRs and AuNSs) were also significantly higher than the mean nuclear Young's modulus of the untreated cells, in agreement with the results of the overall cell stiffness. In addition, we observed the increase of gold nanoparticle amount could increase the nuclear stiffness, as shown in **Figure 3.9**.

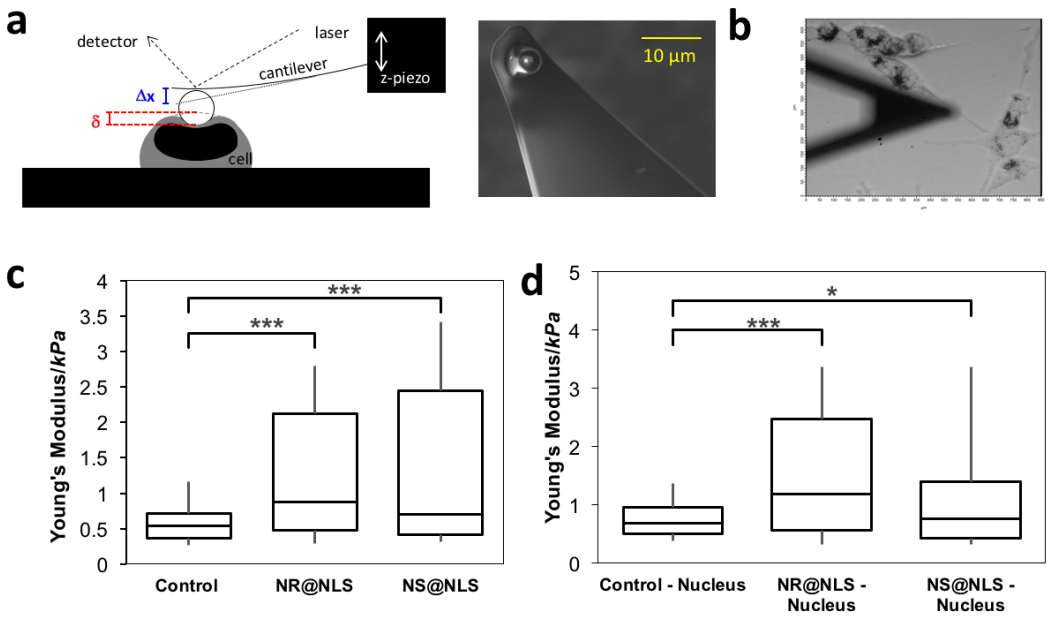

FIGURE 3.8. Stiffness distribution of cells. (a) Schematic of measurements on cells with AFM; δ is indentation, Δx is cantilever deflection. To measure bulk cellular stiffness, a beaded cantilever was used to increase cell-probe surface area. (b) Overhead image of AFM cantilever tip next to HEY A8 cells with nanoparticles (c) Box-and-whisker plots of stiffness of single cells for different nanoparticles treatment, the percentiles are 10%, 25%, 50%, 75%, and 90%. Overall difference between means is significant (p-value calculated from ANOVA); (d) Box-and-whisker plots of nuclear stiffness. *P < 0.05, **P < 0.01, ***P<0.001, n=3, cell counts>20 for each time.

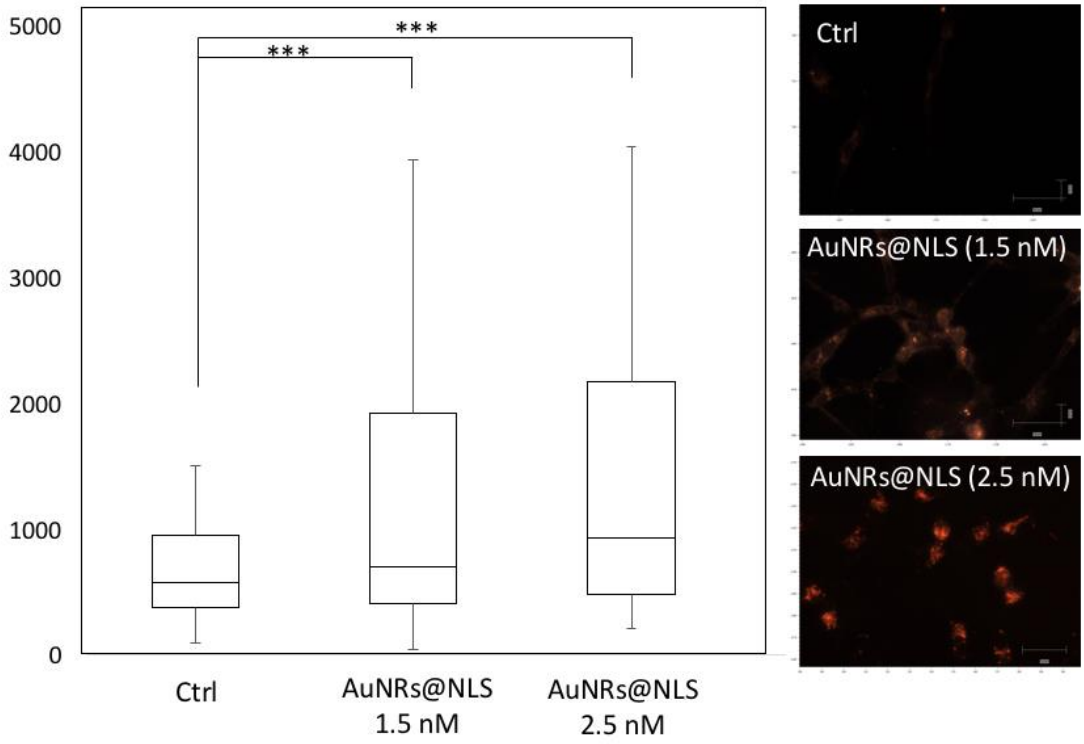

FIGURE 3.9. Nuclear stiffness increase with the increased quantity of AuNRs. AFM result (left) and dark field images (right) show the stiffness and the nanoparticle uptake of AuNRs under different nanoparticle concentrations, respectively. n=3, cell counts>20 for each sample.

1.10.4 AuNPs Accumulate at Nuclear Membrane Resolved by Three Dimensional Microscopy

Resolving the exact localizations of AuNPs with regard to the nuclear membranes [302], [303] is a crucial, yet highly challenging, step in our attempt to understand the effects of AuNPs on the inhibition of cell migration/invasion. Most commonly used optical microscopy methods, such as confocal fluorescence microscopy and dark field (DF) microscopy, do not offer the accurate locations of the nuclear membranes and AuNPs simultaneously, and they usually suffer from high background. On the other hand, TEM, despite its high resolving power, is limited by the high costs and tedious sample

preparation to gain the full 3D distribution of AuNPs inside the cells. To circumvent these challenges, we employed a recently-developed differential interference contrast (DIC) microscopy-based 3D imaging method to visualize and locate plasmonic AuNPs inside the cells [304]. As shown in **Figure 3.10 a**, the cells were placed in a sandwiched chamber. DIC optical sectioning was performed on the whole cell thickness. The arrow indicates the scanning optical sectioning of the cell, directed from layer 1 (close to the surface of the cover glass) to layer 2 (middle of the cell) and to layer 3 (top of the cell) (**Figure 3.10 and 3.11**). The DIC microscope, which was equipped with a set of high numerical aperture (NA = 1.4), oil-immersion condenser and objective, features a shallow depth of field in optical sectioning of a 3D specimen to generate sharply focused images. More importantly, the nuclear membranes are clearly visible under the DIC microscope to allow the determination of the relative positions of the nuclear membranes and AuNPs.

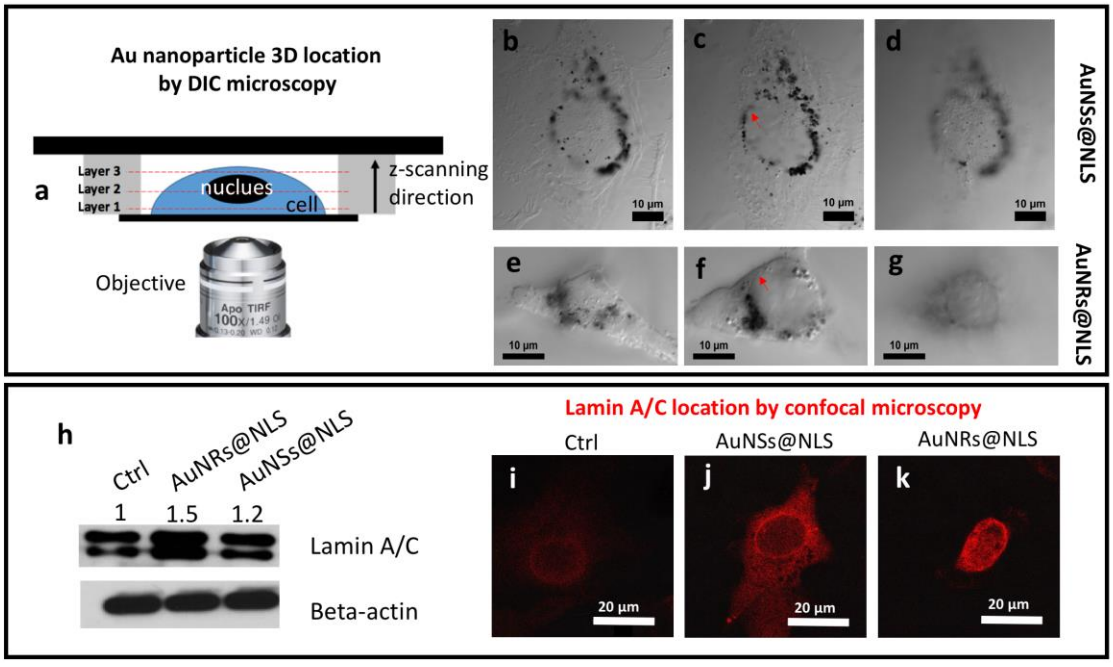

FIGURE 3.10. Locations of AuNPs inside the HEYA8 cell (up) and lamin A/C protein location/expression (down) inside the HEY A8 cell. (a) Scheme of the cell sample in sandwiched chamber for 3 dimensional DIC microscope imaging. Z-axis

scanning step is 65 nm from the bottom (close to the attached glass surface) to the top of the cell. Three layers from the bottom, middle, and the top of the cell, for cells incubated with 0.1 nM of AuNSs@NLS (b-d) and 2.5 nM of AuNRs@NLS (e-g) were imaged, corresponding to frame 75, 235, and 395 (AuNSs@NLS) and frame 49, 179, and 285 (AuNRs@NLS) of the movies in the Supporting Information. (h) Western-blot results of lamin A/C, with beta-actin as reference protein. (i, j and k) Lamin A/C localization by confocal microscope of (i) cells without or (j) with AuNSs@NLS or (k) AuNSs@NLS incubation. The red arrows in (c) and (f) indicate the nuclear membrane of the cells.

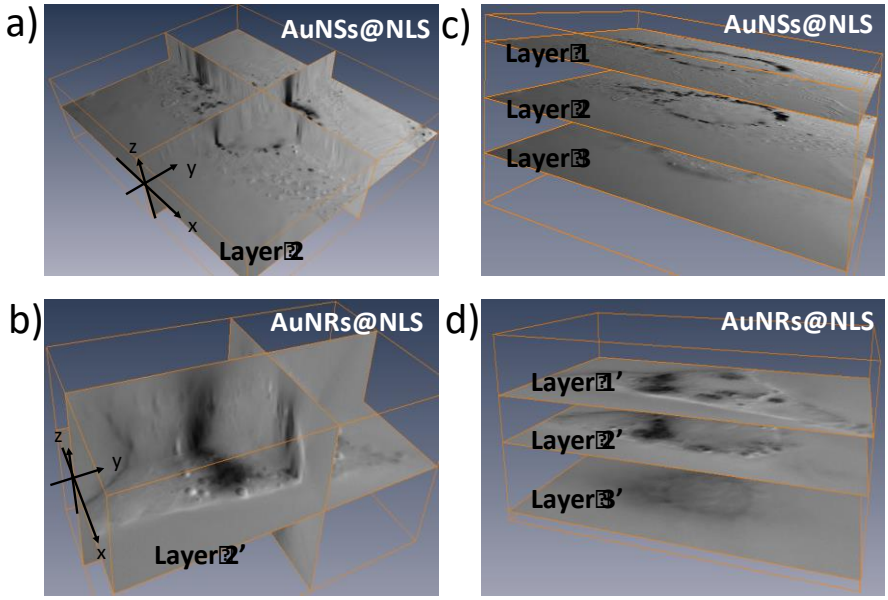

FIGURE 3.11. 3 dimensional (3D) view of HEY A8 cells incubated with AuNPs. (a and b) 3D figures of cells with 2.5 nM of AuNRs@NLS and 0.1 nM of AuNRs@NLS, showing xy, xz and yz planes (c and d) showing the z-stacking of 3 layers from the bottom of the cell (close to the attached glass surface as shown in the scheme), the middle of the cell, and the top of the cell, respectively, for AuNSs@NLS (c) and AuNRs@NLS (d).

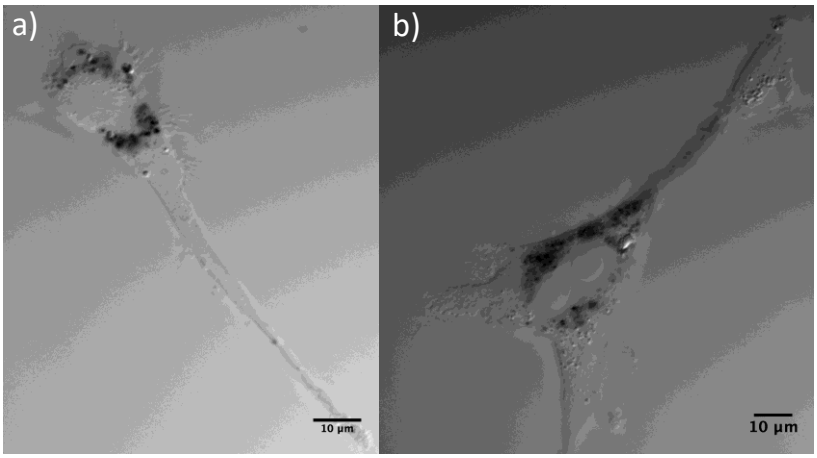

FIGURE 3.12. The nuclear membrane targeting for AuNRs@NLS indicated by differential interference contrast (DIC) images.

Figure 3.10 b to d shows the AuNSs@NLS locations inside the HEY A8 cells. The black spots in the figures are the nanoparticle aggregates, which are shown clearly surrounding the nucleus from difference optical sections. Similarly, **Figure 3.10 e to g** shows a similar distribution of AuNRs@NLS inside HEY A8 cells. Both AuNRs@NLS and AuNSs@NLS aggregates were located predominantly on the nuclear membranes (indicated by the red arrows in **Figure 3.10 c and f**, more evidences in **Figure 3.12**), while the internalization of nanoparticles inside the nucleus was rarely found, which was likely due to the large sizes of the nanoparticles and their aggregates compared to the nuclear pores (around 9~12 nm [305]).

1.10.5 Nuclear Targeting Gold Nanoparticles Cause Lamin A/C Protein Increase.

Lamins, especially lamin A/C, are intermediate filament proteins found at nearly all cell nuclei and contribute to nuclear stiffness and stability [306], [307]. Nuclear lamins interact with the membrane-associated proteins to form the nuclear lamina (30-100 nm thick), which is located in the interior of the nuclear membrane. It has been reported that lamin A/C-deficient cells exhibit severely reduced nuclear stiffness [281], [307]. To further

understand the biological mechanism for why nuclear membrane-targeting AuNPs increase nuclear stiffness and inhibit cancer cell migration/invasion, we measured the expression level of lamin A/C in Western-blots (**Figure 3.10 h**) and confocal microscopy imaging after immuno-staining (**Figure 3.10**). The results indicate a clear overexpression of lamin A/C after incubation with AuNSs@NLS or AuNRs@NLS. As shown in **Figure 3.10 i, j and k**, the fluorescence signal from lamin A/C was increased as a circle-surrounding the nucleus, which is in agreement with the location of nuclear lamina.

AuNPs conjugated with a nuclear localization signal were thought to be able to internalize into the nucleus[302],[308]. In our study we clearly observed most of the NLS conjugated gold nanoparticles aggregated around the nuclear membrane. Without NLS, the nanoparticles (AuNPs@RGD) spread in the cytoplasm, instead of accumulating around the cell nuclear region, which has been discussed in our previous reports) [302]. Western blot experiment showed that the endocytosis and nuclear transportation has been activated upon nanoparticle incubation (**Figure 3.13**), due to the increased expression level of dynamin protein (a GTPase responsible for endocytosis in the eukaryotic cell) and GTP-binding nuclear protein Ran (involved in the transport into and out of the cell nucleus). Since the cellular and nuclear transportation are all activated, the trapping of AuNPs at the nuclear membrane was most likely due to the large size of the gold nanoparticles aggregates compared to the nuclear pores.

It has been widely reported that following the entry of nanoparticles, they traffic through early endosomes to late endosomes and lysosomes (endolysosomal trafficking) [309]. To achieve nuclear membrane targeting, nanoparticles need to escape from the endosome and/or lysosomes. There are several well-established mechanisms explaining the cytosolic release of the NPs from endosomes or lysosomes. One of the most popular mechanism is through the charge interactions. The cationic nanoparticles could interact with the negatively charged phosphor lipid membrane, followed by “proton sponge”

effect, causing endosomal membrane rupturing [310] and nanoparticle escaping. In our study, the positively charged AuNRs@NLS [311] could have the similar mechanism to escape from the endosome. In our results, most of the nanoparticles finally locates surrounding the cell nucleolus after incubation with cells overnight (**Figure 3.10 b to g**), indicating a good efficacy that gold nanoparticles escape from the endosome/lysosomes and target the nuclear membrane. Meanwhile, the above results show that the effect of endosome degradation [312] of the surface conjugated peptides might be very minor.

Coincident with the increased nuclear stiffness by the AuNPs is the aggregation of the AuNPs at the nuclear membrane and the increase of the Lamin A/C expression, which is located at the inner side of nuclear membrane. Lamin A/C is known to maintain the mechanical strength of the nucleus [313], and is thus consistent with an inhibited cell migration or invasion. In our results, a clearly increased expression level of Lamin A/C was observed. Thus, we propose that the increase of nuclear stiffness not only due to the mechanical contribution of the presence of gold nanoparticles, but could also due to the increase of Lamin A/C. How AuNPs increase Lamin A/C is not yet well explored in literature. **Figure 3.10** shows AuNPs closely contact with the nuclear membrane, which could potentially disturb the membrane integrity. Therefore, we propose it could be a cellular defense mechanism as lamin is known to remain the mechanical strength of nucleus. Interestingly, nuclear lamin-associated proteins, such as emerin, which stabilizes nuclear architecture for maintaining the structural integrity [312, 314], are also increased as the AuNPs are added at the nuclear membrane as shown in **Figure 3.13**. To investigate this mechanism, further studies such as proteomics and high-resolution imaging could be fruitful to elucidate the exact role of the AuNPs in inhibiting cell migration and invasion.

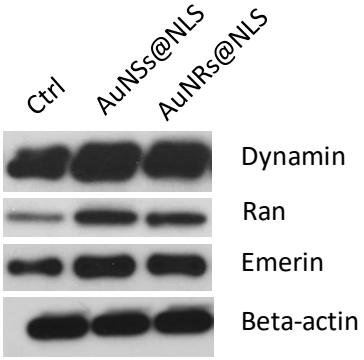

FIGURE 3.13. Western blot of expression levels of Dynamin, Ran, emerin proteins and beta-actin from HEY-A8 cells (without AuNPs), HEY A8 cells with 0.1 nM of AuNSs@NLS and 2.5 nM of AuNRs@NLS treatment for 24 h.

The clearance of nanoparticles from body after treatment has great importance to the evaluation of long-term effect of nanoparticles. While small nanoparticles (hydrodynamic diameter less than 5.5 nm) can be discard rapidly and efficiently through renal/urinary excretion [315]. big nanoparticles (over 18 nm) tend to accumulate in liver and spleen [316]. Such body deposition of metallic NPs over a long time period raises significant concerns regarding their long-term safety. A decrease of the liver content of gold has been reported after 1 month from 0.54% to the 0.07% [317]. The ultimate fate and the body elimination pattern of gold nanoparticles are not well studied. Future work will be focused on studying the effect of gold nanoparticles for preventing and treating the metastasis in animals.

1.11 Conclusions

This study shows that nuclear membrane-targeting AuNPs can increase nuclear stiffness and thereby inhibit cell migration and invasion. Compared with the previous studies with non-targeted AuNPs at relatively high amount (50-200 μM of AuNRs@BSA[76] and 5-20 μg AuNSs@Citrate[276]), the nuclear membrane-targeted AuNPs showed higher inhibition effects at significantly lower concentrations (0.1 nM for

35 nm AuNSs and 2.5 nM for 25 × 5 nm AuNRs). The AuNPs were found to be trapped on the nuclear membranes from mapping the 3D distributions of the AuNPs under a DIC microscope. The trapping of AuNPs at the nuclear membranes could possibly: 1) add to the mechanical stiffness of the nucleus, and, 2) stimulate the overexpression of lamin A/C, which is known to lead to nuclear stiffness and thus slows down cancer cell migration and invasion. This insight takes us one step closer to fully understand the effects on AuNPs on the inhibition of metastasis.

MOLECULAR UNDERSTANDING OF GOLD NANOPARTICLES AND PLASMONIC PHOTOTHERMAL EFFECT IN INHIBITING CANCER CELL MIGRATION

After studying the AuNPs impact on the mechanical properties of cancer cells in Chapter 3, we focused in Chapter 4 to systematically study their molecular mechanism in inhibiting cancer cell migration and invasion using gold nanorods and their photothermal effect. The ability of targeting gold nanorods (AuNRs) to cancer cell surface integrins and the introduction of NIR light to generate mild plamonic photothermal effect are shown to cause a broad regulation on cytoskeletal proteins which thus hamper the cancer cell migration and invasion, and disturb the cell junctions for inhibiting collective cancer cell migration.

1.12 Targeting Cancer Cell Integrins Using Gold Nanorods in Photothermal Therapy Inhibits Migration Through Affecting Cytoskeletal Proteins[10]

Note: Yue Wu and Moustafa Ali have equally contributed to designing, performing, analyzing, and writing the research in Section 4.1 of this chapter.

Summary. Metastasis is responsible for most cancer-related deaths, but the current clinical treatments are not effective. Recently, gold nanoparticles (AuNPs) were discovered to inhibit cancer cell migration and prevent metastasis. Rationally designed AuNPs could greatly benefit their antimigration property, but the molecular mechanisms need to be explored. Cytoskeletons are cell structural proteins that closely relate to migration, and surface receptor integrins play critical roles in controlling the organization

of cytoskeletons. Herein, we developed a strategy to inhibit cancer cell migration by targeting integrins, using Arg–Gly–Asp (RGD) peptide-functionalized gold nanorods. To enhance the effect, AuNRs were further activated with 808-nm near-infrared (NIR) light to generate heat for photothermal therapy (PPTT), where the temperature was adjusted not to affect the cell viability/proliferation. Our results demonstrate changes in cell morphology, observed as cytoskeleton protrusions—i.e., lamellipodia and filopodia—were reduced after treatment. The Western blot analysis indicates the downstream effectors of integrin were attracted toward the antimigration direction. Proteomics results indicated broad perturbations in four signaling pathways, Rho GTPases, actin, microtubule, and kinases-related pathways, which are the downstream regulators of integrins. Due to the dominant role of integrins in controlling cytoskeleton, focal adhesion, actomyosin contraction, and actin and microtubule assembly have been disrupted by targeting integrins. PPTT further enhanced the remodeling of cytoskeletal proteins and decreased migration. In summary, the ability of targeting AuNRs to cancer cell integrins and the introduction of PPTT stimulated broad regulation on the cytoskeleton, which provides the evidence for a potential medical application for controlling cancer metastasis.

1.12.1 Introduction.

Metastasis is a process that enables cancer cells to spread to other sites of the body, and is responsible for most cancer-related deaths [60-62]. The migration of cancer cells from one site to another requires dramatic remodeling of the cellular cytoskeleton [61, 62, 64, 65]. Studies on the changes of cytoskeletal components could provide novel therapeutic approaches to prevent cancer cell migration and metastasis [64]. The targeting

of cytoskeletal components, such as actin or tubulin [318, 319], or regulatory proteins, such as Rho-ROCK or LIM kinases, has been shown to inhibit the invasive and metastatic behavior of cancer cells [320]. However, the pharmacological inhibitors of cytoskeleton have not been very effective in clinical trials due to their non-specific targeting of cytoskeleton in normal cells, which might cause side effects, such as cardiotoxicity [64, 319, 321]. Moreover, in many cases, the anti-cancer drugs that target specific proteins might lose their efficacy after several months of treatment due to mutations of the proteins that result in the rise of drug resistance in cancer cells [68].

Recent advancements in nanomedicine provide us with great opportunities to avoid the drawbacks of commonly used drugs [69, 70]. Due to their small size and surface modifications, nanoparticles, in general, are able to target tumors selectively [71] and have been widely used in cancer diagnosis and therapy [72]. The recent discovery of nanoparticles' effect on inhibiting cancer cell migration or metastasis starts to draw the attention of researchers [73-76, 322]. However, high concentrations of non-targeted nanoparticles (in μM) were used in these previous studies, which might be an obstacle when considering the translation to clinical usage. Additionally, several types of nanoparticles, including TiO_2, SiO_2, iron oxide, *etc*. have been found to exhibit toxicity when used in relatively high concentrations [323]. In our previous work, we designed nuclear membrane targeted gold nanoparticles (AuNPs) for inhibiting cancer cell migration by increasing their nuclear stiffness, which greatly reduced AuNPs dosage and could be favorable for clinical applications [324]. Therefore, to maintain the nanoparticles' effect on impeding cancer cell migration, an intelligent design with a reduced quantity of nanoparticles promises to be crucial in the development of novel and effective anti-

metastasis therapy. In addition, the preliminary observations of several groups have shown that this inhibition effect of nanoparticles are related to some individual cytoskeleton proteins [86, 132, 133], such as microtubule and actin. However, various mechanisms have been proposed. Tay *et al*. found that TiO_2, SiO_2, and hydroxyapatite nanoparticles could slow cancer cell migration by disrupting the intracellular microtubule assembly [74]. Soenen *et al*. reported that iron oxide nanoparticles at high concentrations within cells affect the cellular cytoskeleton and focal adhesion kinase [75]. Zhou *et al*. showed gold nanorods (AuNRs) can inhibit ATP production, thus inhibit F-actin cytoskeletal assembly and decrease cancer cell migration [76]. Therefore, a complete scope of the mechanism of nanoparticles' effect on the cytoskeletal proteins needs to be explored by systematic biological strategy.

In general, it has been reported that heat stress affects the cytoskeleton and induces their rearrangements [325]. Thus, we hypothesized that the use of gold nanorods (AuNRs), allows us to apply near-infrared (NIR) laser to generate heat efficiently through non-radiative processes [69, 219, 326]. AuNRs, due to their unique chemical, physical and optical properties, have been used in drug delivery [273], bio-imaging, and PPTT of cancer [223, 327]. NIR light is a low energetic (safe) light that can deeply penetrate the tissues, which could potentially enhance the AuNRs' effects on cytoskeletal proteins and inhibit migration.

Integrins are major adhesion and signaling receptor proteins that play an important role in regulating cytoskeleton [328], by providing a physical linkage between the cytoskeleton and the extracellular matrix (ECM), and receiving signals from the ECM [329]. They could perturb the down-stream cell adhesion and migration pathways and

modulate the cytoskeleton, thus regulating cell motility and migration [330]. Numerous studies have reported differentially expressed integrins in many cancers. Integrins $\alpha_v\beta_3$, $\alpha_5\beta_1$, and $\alpha_v\beta_6$, are found in very low abundance, even undetectable levels, in most adult epithelial cells, whereas they can be highly overexpressed in many tumors [331]. Integrins are also regulators of metastasis. For instance, inducing the expression of the $\alpha_v\beta_3$ integrin subunit in cancer cell lines increases their metastatic potential [332]. The Arg-Gly-Asp (RGD) peptides are known for specific binding to a wide number of surface integrins, including $\alpha_v\beta_3$, $\alpha_3\beta_1$ and $\alpha_5\beta_1$ integrins [333, 334]. The good selectivity of RGD to cancer cells has been reported by numerous studies for delivering nanoparticles to cancer cells or tumors [335].

To overcome the drawbacks of using nanoparticles, four aspects of the nanoparticle design have been considered to achieve more effective inhibition of cancer cell migration: 1) lowering the concentration of nanoparticles to nM dosage, as a means for lowering toxicity; 2) enhancing the selectivity to the cancerous cells; 3) applying NIR light to enhance the AuNRs' effects on cytoskeletal proteins to inhibit migration; 4) most importantly, enhancing the migration inhibition effect by targeting AuNRs to integrin proteins to remodel the cytoskeleton with systematic understanding of the mechanism behind. In our work, RGD peptides were conjugated on the surface of AuNRs to achieve the selective targeting of integrin. NIR light was applied to the AuNRs to generate mild heat. The concentration of the AuNRs and heat were kept well below the threshold to avoid negative effects on cell viability or proliferation. We compared both non-targeted and integrin-targeted AuNRs (AuNRs@RGD). Results indicated that, while both types of AuNRs decreased the cell migration speed, the targeted ones did so with a greater effect.

After applying NIR light, cell motility was further decreased. We have performed a proteomics study to understand the molecular mechanism, explaining how and why AuNRs have a wide range of effects in perturbing cytoskeletal proteins and cell migration pathways. Compared to the drugs composed of small molecules that target only a single protein, AuNRs exhibit great promise as a novel anti-metastasis strategy for clinical usage.

1.12.2 Methods.

Materials. Tetrachloroauric acid trihydrate (HAuCl4.3H2O), NaBH4, ascorbic acid, cetyltrimethylammonium bromide (CTAB), AgNO3, 4-(2- hydroxyethyl)-1-piperazineethanesulfonic acid (HEPES), NaCl, sodium deoxycholate, sodium dodecyl sulfate (SDS) and Triton X 100 were purchased from Sigma-Aldrich. Methoxypolyethylene glycol-thiol (mPEG-SH, MW 5000) was purchased from Laysan Bio, Inc. Cell penetrating peptide RGD (RGDRGDRGDRGDPGC) was obtained from GenScript, Inc. Dulbecco's phosphate buffered saline (PBS), Dulbecco's modified Eagle's medium (DMEM), fetal bovine serum (FBS), antibiotic solution, and 0.25% trypsin/2.2 mM EDTA solution were purchased from VWR. Mammalian cell protease inhibitors and phosphatase inhibitors were purchased from Roche Applied Sciences, and sequencing grade trypsin was purchased from Promega. Lysyl endopeptidase (Lys-C) was purchased from Wako.

Instrumentation. Gold nanoparticles were imaged using a JEOL 100CX-2 transmission electron microscope (TEM) microscope, and their average size was then measured by ImageJ software. UV−vis spectra were obtained using an Ocean Optics

HR4000CG UV-NIR spectrometer. An inverted Nikon Eclipse Ti-E microscope equipped with Perfect Focus System (PFS, 25 nm z-axial resolution) was used for imaging under a Nikon differential interference contrast (DIC) microscope. Proteomics analysis was performed on a hybrid dual-cell quadrupole linear ion trap − Orbitrap mass spectrometer LTQ Orbitrap Elite (Thermo Fisher) with XCalibur 3.0.63 software. Flow cytometry experiments were conducted on a BD LSR II Flow Cytometer (BD Biosciences).

Synthesis, Conjugation and Characterization of AuNRs. AuNRs with an average size of 25 × 6 nm (length × width) were synthesized using a seedless growth method.[228] 5 ml of 1.0 mM $HAuCl_4$ was added to a solution of 5 mL of 0.2 M CTAB, 250 μL of 4.0 mM $AgNO_3$, and 8 μL of 37% HCl. Then, 70 μL of 78.8 mM ascorbic acid was added, followed by immediate injection of 15 μL of 0.01M of ice-cold $NaBH_4$. The solution was left undisturbed for 12 hours. The particles were centrifuged at 21000 g for 50 min and dispersed in DI water, followed by a second centrifugation at 19000 g for 40 min to remove the extra CTAB. TEM was used to measure the sizes and homogeneity of the nanoparticles.

After rinsing them with water, AuNRs were then conjugated with different surface ligands (PEG and RGD). For AuNRs@PEG, mPEG-SH (1 mM) was added to the nanoparticles overnight to achieve about 5000 ligands on each particle. For preparing AuNRs@RGD, first, mPEG-SH (1 mM) was added to the nanoparticles overnight to achieve about 1000 ligands on each particle. Then, the PEGylated nanoparticles (1 nM) were treated with RGD (1 mM) to achieve 10000 molar excess. The solution was then

allowed to shake overnight at room temperature. Excess of ligands were removed by centrifugation. UV-vis spectrometer and zetasizer were used to test the conjugation.

Cell Culture, AuNR Treatments and PPTT. Cells were grown in Dulbecco's modified Eagles' medium (DMEM, Mediatech) containing 10% (v/v) fetal bovine serum (FBS, Mediatech) and 1% antimycotic solution (Mediatech) at 37 ^{o}C in a humidified incubator under 5% CO_2. Cells were cultured in 60 mm dishes for 24 hours followed by incubation with AuNRs for 24 hours. Then, a CW 808 nm laser (5.8 W/cm^2, spot size 5.6 mm) was applied to the cells for 1 minute. To cover the entire area of the culture dish, the laser was applied spot by spot using scanning with each spot undergoing two minutes of laser exposure time. The cells were then harvested for MS analysis, with a final confluence about 80-90%.

Sample Preparation for Proteomics Experiment. After treatment for 24 hours, cells were washed twice using PBS. Cell lysates were prepared by directly adding the lysis buffer (150 mM NaCl, 50 mM HEPES, pH =7.4, 0.1% SDC, 10 units/ mL benzonase, protease inhibitor cocktail) to the cells followed by scraping and collecting on ice. Lysates were vortexed for 90 s (30 s × 3 times, 2 min pause), sonicated on ice, and centrifuged at 18000 g for 15 min at 4 ^{o}C. The supernatant solutions were saved and proteins were precipitated by adding 4 x excess volumes of ice-cold precipitation solvents (acetone: ethanol: acetic acid=50:50:0.1). After centrifugation, the protein pellet was re-dissolved in an solution with 8 M urea and 50 mM HEPES (pH=8) [336].

Protein disulfide bonds were reduced using 1 mM dithiothreitol (DTT) followed by alkylation with 5.5 mM iodoacetamide. After the lysates were diluted twice (final urea

concentration of 4 M), endoproteinase Lys-C (1:100 w/w) was added to digest proteins for 4 hours. Then, modified sequencing grade trypsin (1:100 w/w) was used for further digestion in a more diluted solution with the final urea concentration of 1 M for overnight [337]. Protein concentration was measured by Bradford assay.

RPLC-MS/MS Analysis for Label-free Quantitative Proteomics. The proteomics analysis was conducted using the previous reported method [338]. Briefly, purified and dried peptide samples from the previous step were dissolved in 10 μL solvent with 5% acetonitrile and 4% FA, and 4 μL of the resulting solutions were loaded onto a microcapillary column packed with C18 beads (Magic C18AQ, 3 μm, 200 Å, 100 μm × 16 cm, Michrom Bioresources) by a Dionex WPS-3000TPLRS autosampler (UltiMate 3000 thermostatted Rapid Separation Pulled Loop Well Plate Sampler). A reversed-phase liquid chromatography (RPLC) was employed for peptides separation with a 110 min gradient of 8-38% ACN (with 0.125% FA). Peptides were detected with a data-dependent Top20 method, *i.e.* for each cycle, one full MS scan (resolution: 60,000) in the Orbitrap was followed by up to 20 MS/MS in the ion trap for the most intense ions. The selected ions were excluded from further analysis for 90 seconds. Ions with singly or unassigned charge were not sequenced. Maximum ion accumulation times were 1000 ms for each full MS scan and 50 ms for MS/MS scans. The sample at each condition was repeated 6 times (2 biological and 3 technique replicates) for label-free quantification.

Apoptosis/Necrosis Assay. After removing the cell culture media, and cells were washed with phosphate-buffered saline (PBS) and collected after trypsinization followed by washing with cold PBS twice again. Then, the cells were dispersed in a mixture of 493 mL of Annexin V binding buffer, 5 μL of Annexin V FITC (BioLegend), and 2 μL of

propidium iodide PI (BioLegend, 100 μg / mL) and incubated for 15 min at room temperature. The cells were then filtered and subjected to flow cytometry analysis using a BSR LSR II flow cytometer (BD Biosciences). A 488 nm laser was applied for excitation, and FITC was detected in FL-1 using a 525/30 BP filter while PI was detected in FL-2 using a 575/30 BP filter. Standard compensation using unstained and single-stained cells was done before running actual experiments. FlowJo software (Tree Star Inc.) was used for analysis of the viable, apoptotic and necrotic cells from at least 10000 events.

Cell Imaging Using DIC Microscopy. The Nikon DIC mode utilized a pair of polarizer and analyzer, a high resolution 100×I-R Nomarski DIC slider, a high numerical aperture (N.A., 1.40) oil immersion condenser lens, a Nikon CFI Apo TIRF 100 × (N.A., 1.49) oil immersion objective, and a 12 V/100 W halogen lamp as light source. Appropriate bandpass filters were placed in the light path. Fixed HEYA8 cells on 22 mm × 22 mm glass coverslips were rinsed with PBS at pH 7.4 and fabricated into a sandwiched chamber with two pieces of double-sided tape and a cleaned glass slide. PBS solution was then added into the chamber to fill the space, and the chamber was then sealed by clear nail polish. The so-formed sample slide was then place under the microscope for observation. Two scientific CMOS cameras were used to capture the DIC images: a Hamamatsu C11440-22CU, ORCA-Flash 4.0 V2 with a 2048 × 2048 pixel array and a pixel size of 6.5 μm × 6.5 μm and a Tucsen Dhyana 95 with a 2048 × 2048 pixel array and a pixel size of 11 μm × 11 μm. These cameras performed similarly in our experiments.

Scratch Assay. The scratch assay has been performed according to a former report [291]. Cells were cultured in a 6-well plate to a confluent monolayer. A p200 pipet

tip was used to scrape the cell monolayer in a straight line to create an empty gap. The debris was then removed by washing the cells once with a culture medium and then replaced with 2 mL of fresh medium. Then, the cells were imaged immediately after scratch and 12 hours after scratch.

Proteomics Data Analysis. Two biological replications and three MS technical replications for each condition (control, AuNRs@PEG, AuNRs@PEG/NIR, AuNRs@RGD, AuNRs@RGD/NIR) were conducted. Raw data from proteomics was normalized using supervised normalization of the microarray (SNM) [339]. In the SNM procedure, variance due to biological and technical replicates were adjusted by setting them as variables in the model. Variance explained by different experimental treatments (control, AuNRs@PEG, and AuNRs@PEG+NIR for PEG-conjugated AuNRs group; control, AuNRs@RGD, and AuNRs@RGD+NIR for RGD-conjugated AuNRs group) was fitted as a biological variable in the model. Hierarchical clustering was done with statistical software R [340]. Proteomics data was log2 transformed before analysis of variance (ANOVA) which was used to detect differential expression of proteins between control and treatment groups, with treatment conditions set as fixed effects. P-value threshold at 0.1 was set to select differential proteins. The proteins identified as being affected were subjected to pathway analysis using the MetaCore pathway analysis software ("MetaCore from Thomson Reuters").

Western-blot Analysis. Briefly, cells were lysed in RIPA buffer (20 mM Tris pH 7.4, 150 mM NaCl, 2 mM EDTA, 2 mM EGTA, 0.1% sodium deoxycholate, 1% Triton X-100, 0.1% SDS) containing protease inhibitors (Sigma-Aldrich). BCA assay (Pierce) was performed to measure the protein concentration, and equal amounts of protein were

loaded on a SDS-PAGE gel. After the protein separation, the resulting gels were transferred to PVDF membranes (Millipore) overnight. Afterwards, the gel was blocked with 5% milk in TBS (20 mM Tris, 150 mM NaCl). The primary antibodies (Bethyl Laboratories, Inc.) was incubated with the membrane overnight in 4 °C with shaking, followed by adding the secondary antibodies (Jackson Immuno Research Laboratories). Blots were washed three times for 20 m in TBS after primary and secondary antibodies.

1.12.3 Results.

1.12.3.1 AuNR Fabrication, Characterization, Cell Uptake and Cytotoxicity Studies.

AuNRs with size of 25 (± 3) × 6 (± 1) nm (length × width) and aspect ratio of 4.2 were synthesized according the seedless method [228], as shown in the transmission electron microscope (TEM) in **Figure 4.1 A**. This size of AuNRs has shown better efficacy in heat generation in PPTT by our previous study [341]. The as-synthesized AuNRs were washed twice with water to remove cetyltrimethylammonium bromide (CTAB) to decrease the cytotoxicity and for the next step of surface modification. The AuNPs were functionalized with polyethylene glycol thiol (PEG) and RGD peptides to increase the biocompatibility [230] and achieve integrin targeting [333], respectively. Surface modification causes a red shift of the longitudinal surface plasmon resonance (SPR) band of AuNRs due to the change in the dielectric constant of the surrounding environment of AuNRs (as shown in the UV-Vis spectra in **Figure 4.1 B**). After PEGylation, the SPR band red-shifts to 785 nm for AuNRs@PEG (initially 771 nm). Further red-shift to 796 nm for AuNRs@RGD was observed, indicating the surface binding of RGD. In addition, the zeta potentials of the AuNRs at different stages were

measured to confirm the surface modifications. As shown in **Figure 4.1 C**, the as-synthesized CTAB coated AuNRs had a positive surface charge of 22.9 ± 15.1 mV as the CTAB is a highly cationic surfactant. After PEG modification, the AuNRs became negatively charged (-10.2 ± 6.73 mV), then became positive again after further modification of the RGD peptides. The characterization results are consistent with those of our and other groups [286, 338], which indicates the successful conjugation of the RGD peptides to the surface of AuNRs.

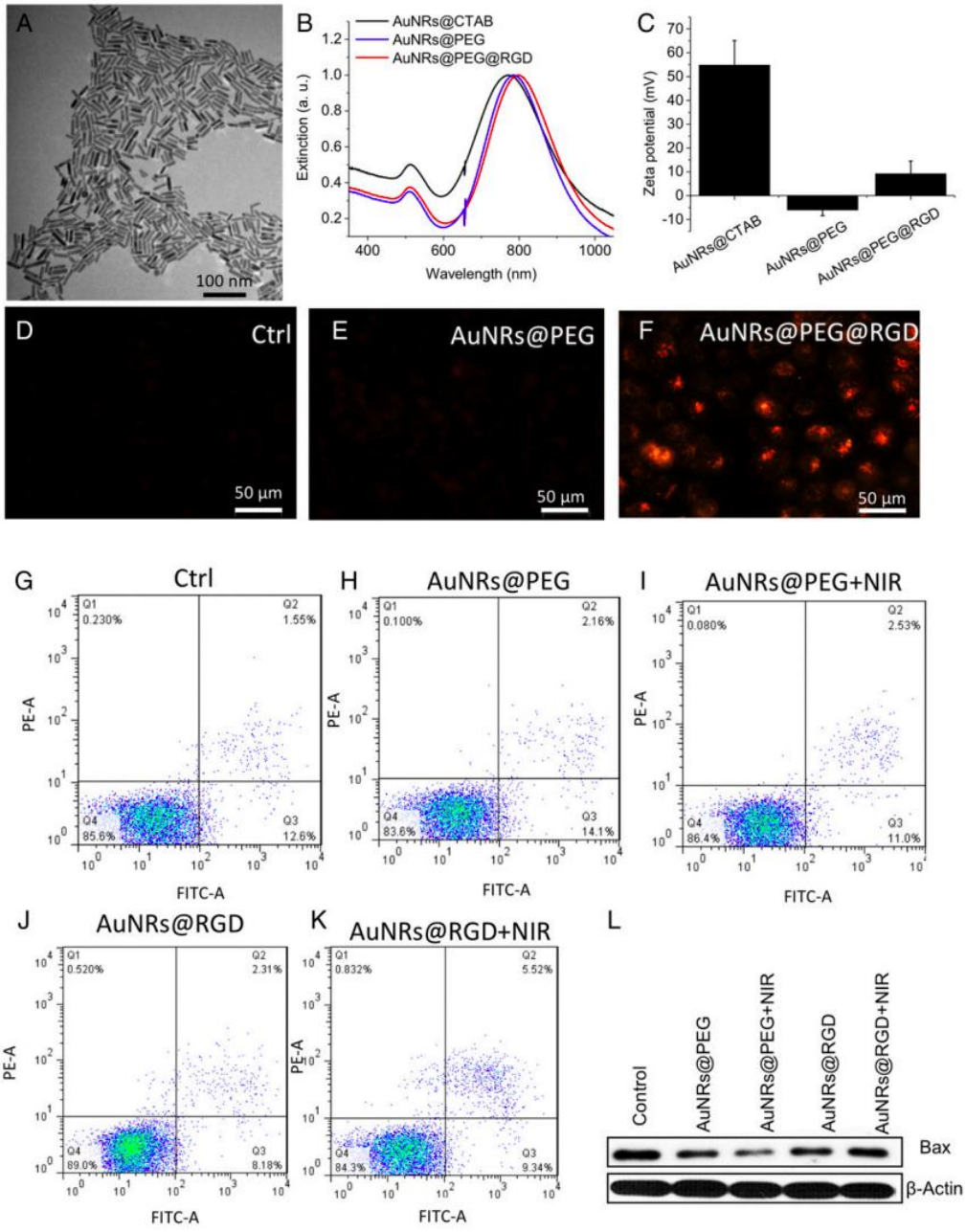

FIGURE 4.1. AuNR synthesis, characterization, HSC-3 cellular uptake, and cytotoxicity study. (A) TEM image of AuNRs. (B) UV-Vis spectrum of AuNRs with different surface ligands. Black, the as-synthesized AuNRs with CTAB on the surface; blue, PEGylated AuNRs; red, AuNRs conjugated with PEG and RGD. (C) Zeta potential shows the surface charge before/after conjugations. (D–F) DF image of cells without AuNRs, incubated with AuNRs@PEG or AuNRs@RGD, respectively (representative of replicated experiments, another two sets of results in FIGURE. 4.2). (G–K) Cell viability/apoptosis/necrosis assay of cells under different treatments, using flow cytometry. Q1, necrotic cells; Q2, late apoptotic cells; Q3, early apoptotic cells; Q4, viable cells (representative of replicated experiments,

statistical results in FIGURE. 4.2). (L) Western blotting for the BAX protein after four groups of treatments.

Successful internalization of AuNRs within the cells was observed as monitored under a dark-field (DF) microscope (**Figure 4.1 D-F and 4.2**), where the brightness of the scattering light from AuNRs indicates the internalized AuNRs amount. The human oral squamous cell carcinoma (HSC-3) cells were incubated with 2.5 nM of AuNRs for 24 hours. For AuNRs@RGD, clear scattering light of AuNRs was observed while AuNRs@PEG did not show high uptake when compared to the AuNRs@RGD. The difference in uptake of these two types of AuNRs is due to the binding of RGD to the surface integrin that enhances the endocytosis of AuNRs [342]. For further confirmation, the internalization of AuNRs was also measured by UV-Vis spectra (**Figure 4.3 A**) and the differential interference contrast (DIC) microscopy (**Figure 4.3 B-D**). In addition, the retaining of the Gaussian-shape peaks in the UV-Vis spectra of AuNRs after incubation with cells indicates the colloidal stability. Flow cytometry was used to measure the cell viability and apoptosis status, and the results indicated the 2.5 nM of AuNRs@PEG and AuNRs@RGD did not affect the cell viability or cause apoptosis (**Figure 4.1 G and 4.4**). This result confirms that the functionalization of AuNRs has been well performed by ligand-ligand exchange to replace the CTAB with PEG and RGD. A 808 nm CW NIR laser was applied for 1 minute to raise the temperature of the culture media to about 42 ± 1 ^{o}C. As the temperature increased, there was no obvious change in the cell viability and no sign of apoptosis/necrosis (**Figure 4.1 G-K and 4.4**). In addition, no cell apoptosis occurred after AuNRs incubation and slight NIR exposure, as confirmed by our Western-blot results (**Figure 4.1 L**). BAX, an important protein that participates in the initiation of apoptotic signaling [343], did not increase.

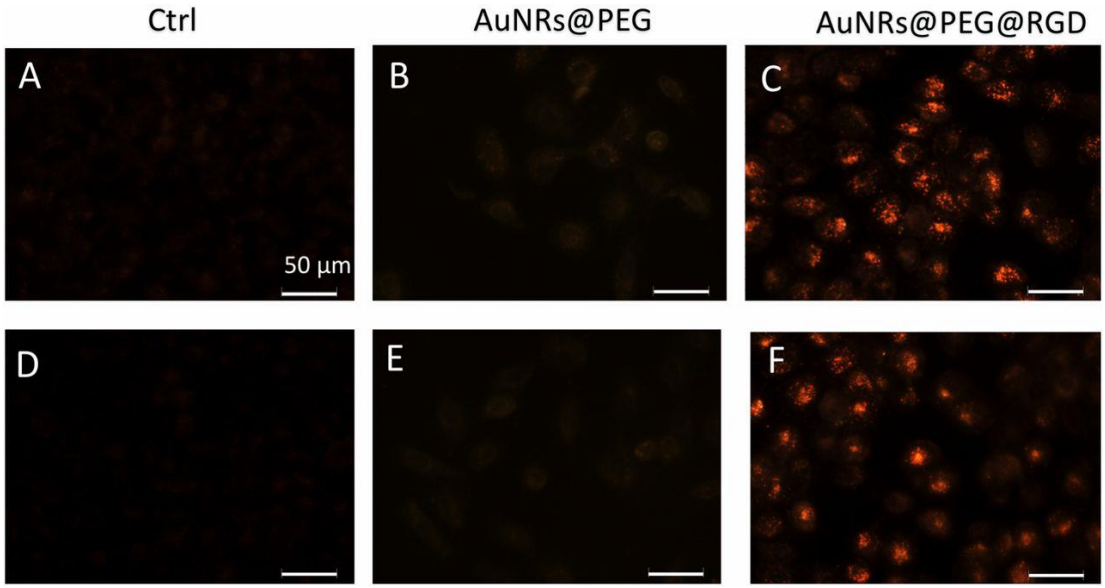

FIGURE 4.2. DF image of cells without AuNRs (A and D), incubated with AuNRs@PEG (B and E), or AuNRs@PEG@RGD (C and F), respectively (replicated experiments of Fig. 1 D–F). (Scale bar, 50 µm.)

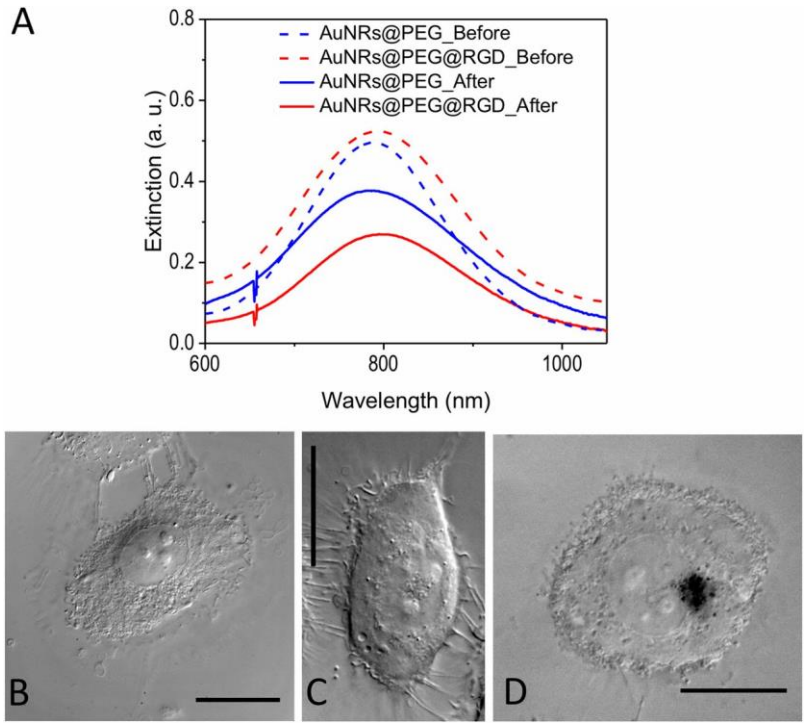

FIGURE 4.3. HSC cell uptake of AuNRs. (A) UV-Vis spectra of AuNRs before and after incubation with cells. (B–D) DIC microscopy images of cells without nanoparticle incubation (B), incubated with AuNRs@PEG (C), and incubated with AuNRs@RGD (D). (Scale bar, 20 µm.)

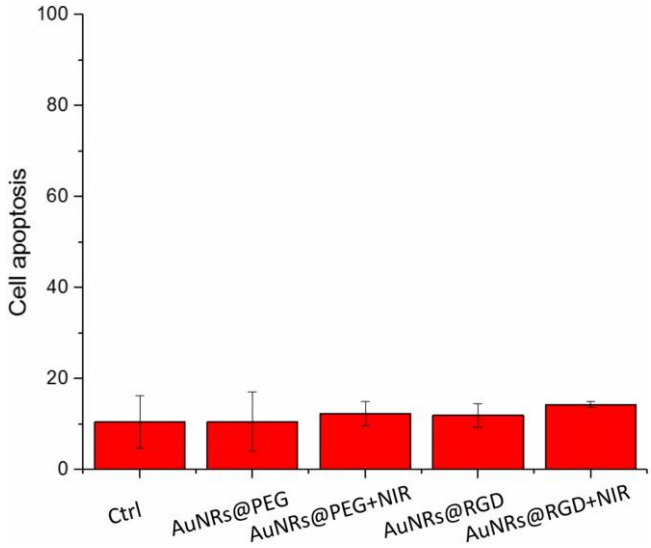

FIGURE 4.4. Apoptosis populations of HSC cells under different treatments, using flow cytometry.

1.12.3.2 AuNR Inhibit Cancer Cell Migration and Invasion Ability

To evaluate the AuNRs' effect on cancer cell migration, we conducted a scratch assay [291] on the monolayers of cells that were incubated with or without AuNRs for 24 hours. After introducing a "scratch" or "wound" into a cell culture, images were captured immediately and 12 hours after the scratch. **Figure 4.5 A and 4.6 A** indicates that cells in the control group had the "wound" completely healed, while cells treated with AuNRs were not completely healed. The integrin-targeting AuNRs (AuNRs@RGD) have a greater inhibition effect than the non-targeted AuNRs (AuNRs@PEG). In addition, NIR light exposure demonstrated an enhanced inhibition effect on cancer cell migration.

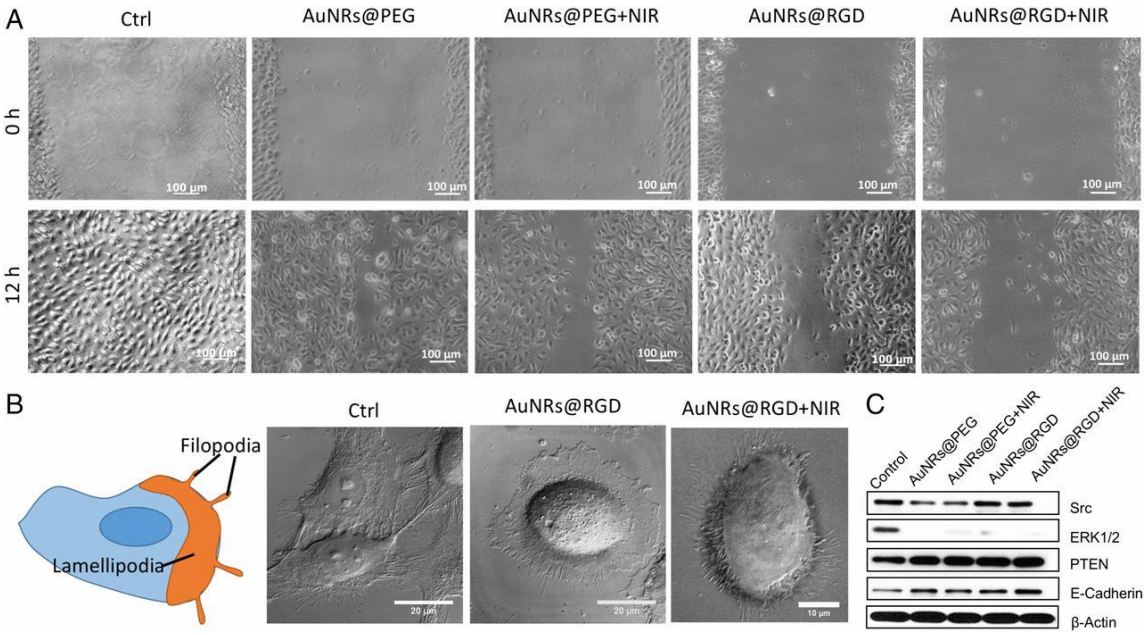

FIGURE 4.5. Changes of cell migration rate and shapes upon AuNRs treatments. (A) Images of HSC cell movement using scratch assay (representative of replicated experiments, another set of results in Figure. 4.6 A). (B) Changes in the cell shape using DIC images before and after AuNR or NIR treatments (representative of replicated experiments, another set of results in Figure. 4.6 B). (C) Western-blot analysis of integrin- and migration-related proteins in AuNRs@PEG and AuNRs@RGD (with or without NIR light).

As mentioned above, the cell motility decreased upon the AuNR treatment. It is well known that changes in cell morphology are closely related to cell motility, which is initiated through two types of membrane protrusions: flat, sheet-like lamellipodia and needle-like actin-based filopodia (**Figure 4.5 B**). Both structures contain a large density of integrins [344] and play major roles in leading cancer cell migration and invasion [345]. To study the cell morphological changes (lamellipodia and filopodia), a differential interference contrast (DIC) microscope was used. The control sample exhibited a normal and extended lamellipodia and filopodia. After treating with AuNRs@RGD alone, the cells tended to have around shape with fewer lamellipodia and filopodia when compared to the control. When we applied AuNRs@RGD and NIR light together, the area of

lamellipodia was further decreased, and many needle-like filopodia appear outside the cell (more information in Figure 4.6 B). The morphological changes of integrin-rich lamellipodia and filopodia indicate that the integrin targeted AuNRs with or without NIR light are effective in changing the cytoskeleton structures, a probable cause for the decrease in cell motility.

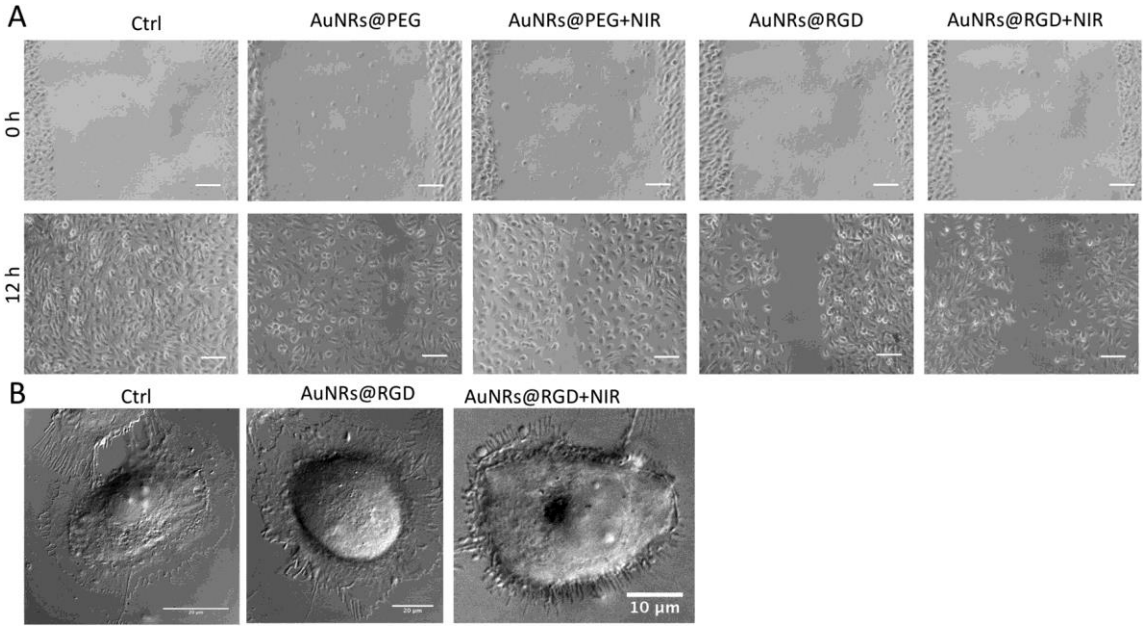

FIGURE 4.6. (A) Images of HSC cell movement under different conditions using scratch assay (replicated experiment). (B) Changes in the cell shape using DIC images before and after gold AuNRs or NIR treatments (replicated experiments).

To study the molecular mechanism, we checked the expression levels of several proteins that are closely associated with integrin and cell migration. Two important down-stream regulators of integrin, Src and ERK1/2 were found to be down-regulated with the AuNRs treatment when compared with the control (**Figure 4.5 C**). Src is a critical protein which bridges between integrin and Rho (a main regulator of cytoskeleton) signaling [346], and ERK1/2 is a mitogen-activated protein kinase [347]. The decrease of Src and ERK1/2 indicates that targeting the surface integrin using AuNRs@RGD could block

the down-stream regulators of integrin signaling [348], which contributes to the inhibition of cell migration by AuNRs. Moreover, in a further investigation of integrin-related proteins, **Figure 4.5 C** showed that epithelial cadherin (E-cadherin) and phosphatase and tensin homolog (PTEN), were up-regulated upon AuNRs treatments. Recent discoveries have shown that E-cadherin have cross-talk with integrin signaling [349] that alter cytoskeletal organization [350]. Loss of E-cadherin is often associated with tumor invasive progressing [351]. In addition, the tumor suppressor protein PTEN has been reported to inhibit integrin-mediated cell migration, spreading, and adhesion and affecting mitogen-activated protein kinase [352]. Our results indicated that the up-regulation of E-cadherins and PTEN contributes to the inhibition of cancer migrations.

1.12.3.3 Proteomics Analysis Reveals the Inhibition of Migration Pathways

To gain a global view of proteome change, label-free quantitative proteomics was conducted to identify and quantify protein expression changes in HSC-3 cells after incubation with AuNRs. Proteomics results indicated a wide range of perturbations of proteins in migration-related pathways after AuNRs treatment. In this experiment, cells were lysed and proteins were then extracted and digested. The purified peptides were analyzed by an on-line liquid chromatography-mass spectrometry (LC-MS) system. Two biological replications and three technical replications for each condition were conducted. In total, over 4000 proteins were identified and about 1800 common proteins were quantified in four treatment groups (AuNRs@PEG, AuNRs@PEG+NIR, AuNRs@RGD, and AuNRs@RGD+NIR) **(Figure 4.7 A)**. The clustering analysis **(Figure 4.8 A and B)** shows that the control group and experimental groups were separately clustered, also indicating a good reproducibility of the proteomics experiments. Differential analysis

identified proteins with significant changes in AuNRs treated groups compared to the control group (**Figure 4.8 C-F**). The numbers of up- and down-regulated proteins in each group are shown in **Figure 4.8 G**. Comparison of differentially expressed proteins identified in the four treatments is shown in the Venn diagram **(Figure 4.8 H)**. Expression levels of key proteins in migration-related pathways are shown in the heatmap (**Figure 4.7 B)**, where a wide range of cytoskeletal proteins were observed to be affected in the four AuNRs treated groups. Pathway analysis using MetaCore (Thomson Reuters) reveals the perturbation of signaling pathways related to cell migration in all groups (**Figure 4.7 C**), including the cytoskeleton remodeling, Rho GTPase signaling, integrin-mediated cell migration and invasion, *etc*. Per the pathway analysis results, AuNRs@RGD+NIR caused the greatest changes to the migration-related pathway and was considered the most effective for inhibiting cancer cell migration, followed by AuNRs@RGD and then AuNRs@PEG.

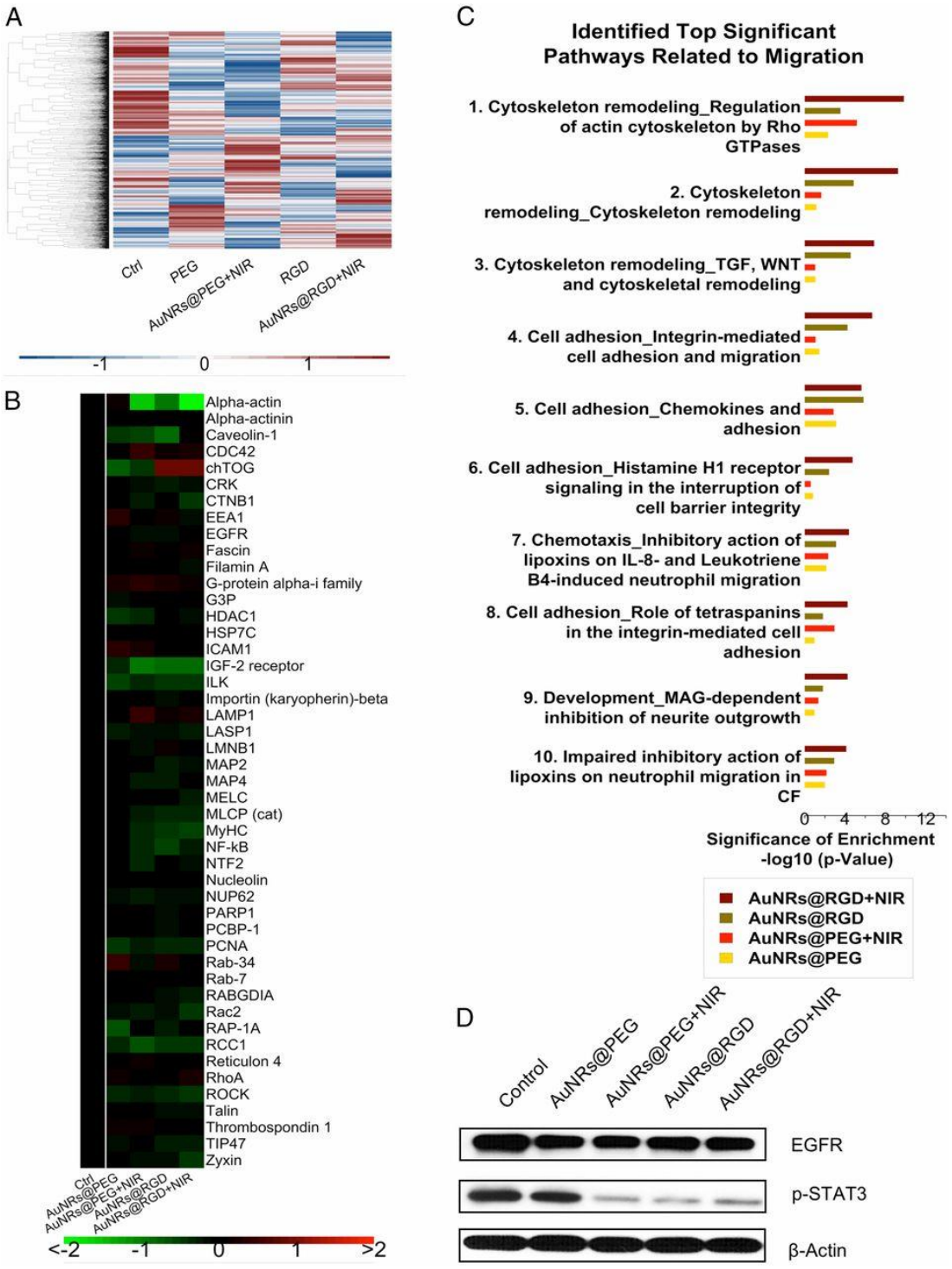

FIGURE 4.7. Experimental results of proteomics in the four treatment groups (AuNRs@PEG, AuNRs@PEG+NIR, AuNRs@RGD, and AuNRs@RGD+NIR). (A) Heatmap showing the expression levels of all of the quantified proteins. (B) Heatmap showing identified proteins contributing to migration inhibition. (C) Bar graph showing identified significant pathways related to migration. (D) Western-blot analysis of some integrin- and migration-related proteins.

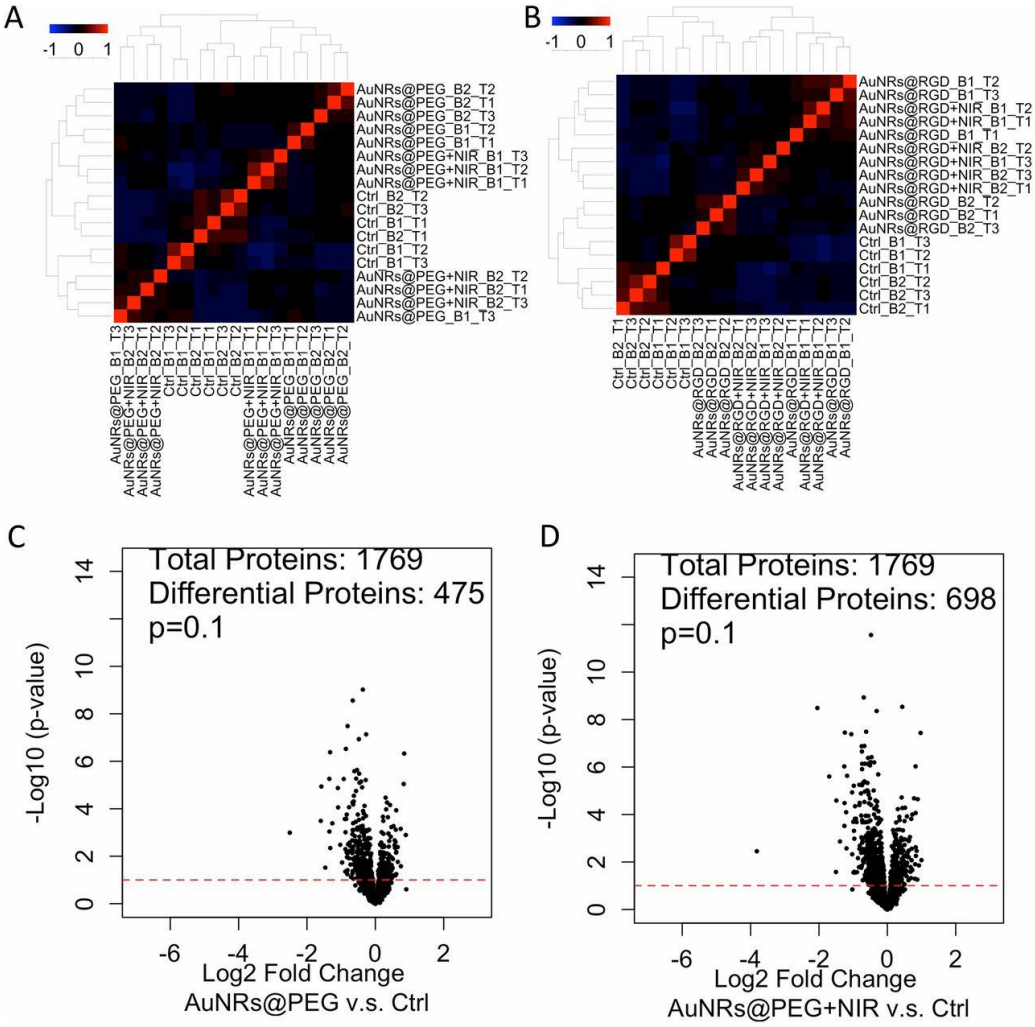
A
-1 0 1
AuNRs@PEG_B2_T2
AuNRs@PEG_B2_T1
AuNRs@PEG_B2_T3
AuNRs@PEG_B1_T2
AuNRs@PEG_B1_T1
AuNRs@PEG+NIR_B1_T3
AuNRs@PEG+NIR_B1_T2
AuNRs@PEG+NIR_B1_T1
Ctrl_B2_T2
Ctrl_B2_T3
Ctrl_B1_T1
Ctrl_B2_T1
Ctrl_B1_T2
Ctrl_B1_T3
AuNRs@PEG+NIR_B2_T2
AuNRs@PEG+NIR_B2_T1
AuNRs@PEG+NIR_B2_T3
AuNRs@PEG_B1_T3
B
-1 0 1
AuNRs@RGD_B1_T2
AuNRs@RGD_B1_T3
AuNRs@RGD+NIR_B1_T2
AuNRs@RGD+NIR_B1_T1
AuNRs@RGD_B1_T1
AuNRs@RGD+NIR_B2_T2
AuNRs@RGD+NIR_B1_T3
AuNRs@RGD+NIR_B2_T3
AuNRs@RGD+NIR_B2_T1
AuNRs@RGD_B2_T2
AuNRs@RGD_B2_T1
AuNRs@RGD_B2_T3
Ctrl_B1_T3
Ctrl_B1_T2
Ctrl_B1_T1
Ctrl_B2_T2
Ctrl_B2_T3
Ctrl_B2_T1
C
Total Proteins: 1769
Differential Proteins: 475
p=0.1
-Log10 (p-value)
0 2 4 6 8 10 14
-6 -4 -2 0 2
Log2 Fold Change
AuNRs@PEG v.s. Ctrl
D
Total Proteins: 1769
Differential Proteins: 698
p=0.1
-Log10 (p-value)
0 2 4 6 8 10 14
-6 -4 -2 0 2
Log2 Fold Change
AuNRs@PEG+NIR v.s. Ctrl

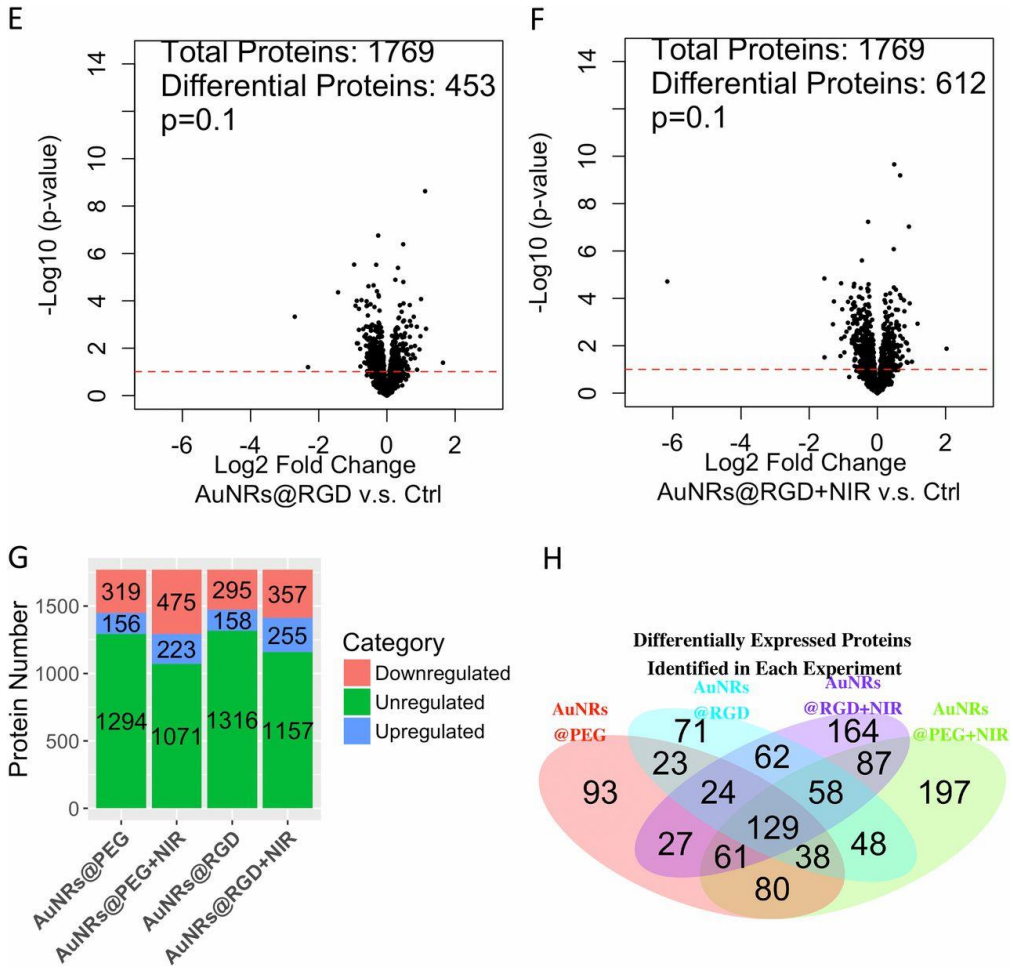

FIGURE 4.8. Experimental results of proteomics and data analysis. (A) Clustering analysis of samples: AuNRs@PEG, AuNRs@PEG+NIR, and control. (B) Clustering analysis of samples: AuNRs@RGD, AuNRs@RGD+NIR, and control. (C–F) Volcano plots of proteins under perturbation by (C) AuNRs@PEG, (D) AuNRs@PEG+NIR, (E) AuNRs@RGD, and (F) AuNRs@RGD+NIR. (G) Numbers of regulated/unregulated proteins identified in each experiment. (H) Venn diagram showing the comparison of differentially expressed proteins identified in each experiment.

A scheme (**Figure 4.9**) was concluded from the pathway maps to illustrate the changes of the key protein players in the migration-related pathways. AuNRs regulate the cell migration by affecting the cytoskeleton in four main ways: 1) Rho GTPases, 2) actin, 3) microtubule, and 4) kinases related signaling pathways.

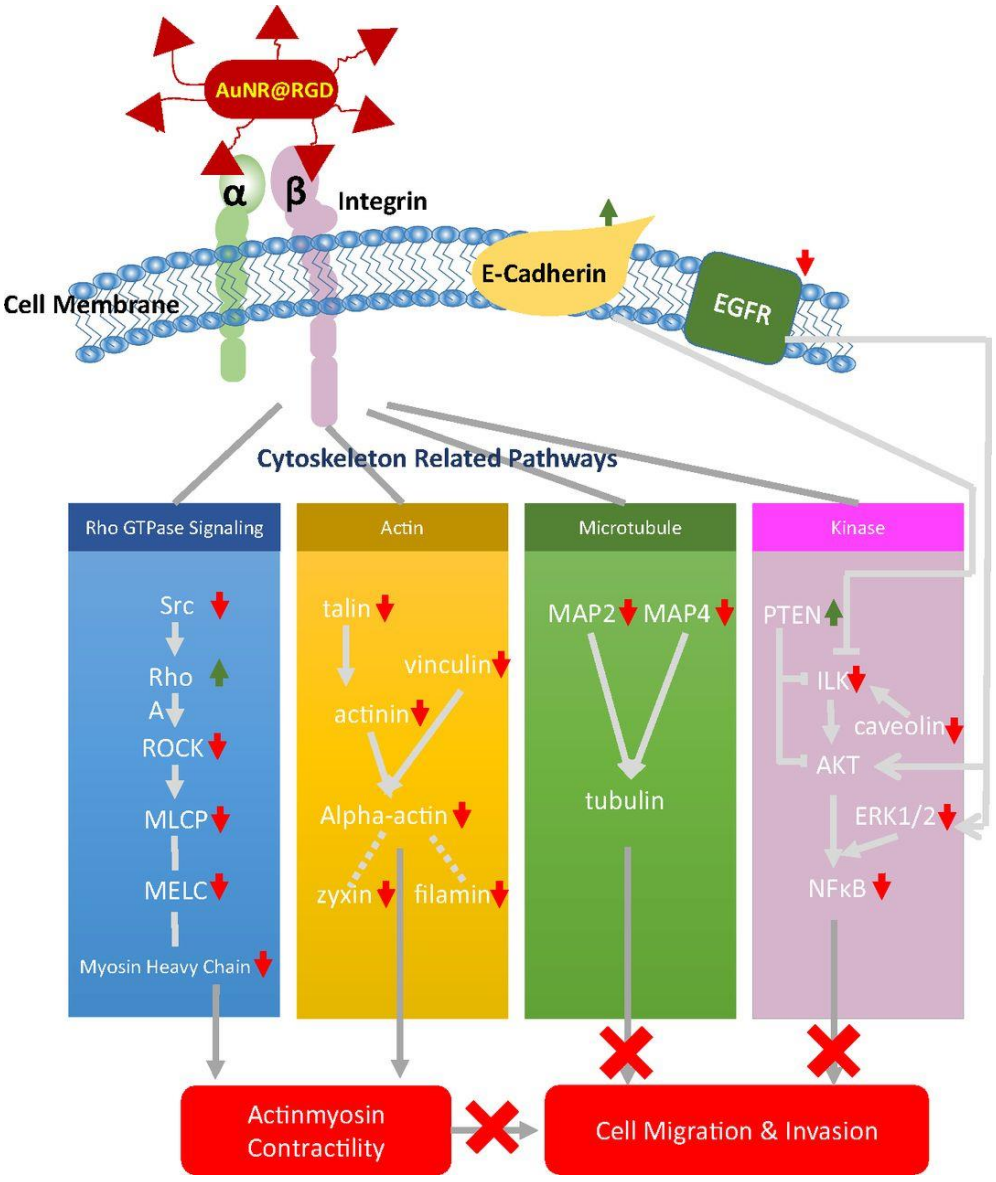

FIGURE 4.9. Scheme representing the mechanisms involved in inhibiting cell migration upon AuNR treatments. When the AuNRs@RGD (in red) target the alpha/beta integrins, four different cytoskeletal proteins pathways are regulated, Rho (blue), Actin (yellow), Microtubule (green), and Kinase (pink), all of which affect the cell contractility and thus inhibit cell migration (shown in red at the bottom of the figure).

1) Rho GTPases regulate the actin cytoskeleton [353], which plays an important role in cellular contractility (actomyosin contraction) by directly controlling the balance between myosin II and actin, and initiates the force needed for cell

migration [354]. Many key proteins in Rho GTPase signaling pathways were perturbed, including serine/threonine kinase ROCK, myosin heavy chain (MyHC), myosin essential light chain (MELC), myosin light-chain phosphorylation (MLCP), RhoA, α-actinin, talin, *etc*., as shown in **Figure 4.7 B** and **4.9**. All four treatments exhibit the regulation of Rho GTPase signaling to different extents. The AuNRs@RGD+NIR group has the highest statistical significance with the lowest p-value (1.5×10^{-10}), reflecting this group's highest efficacy in inhibiting the cancer cell migration-related pathways. Our results indicate the disruption of actomyosin contraction, which might prevent the generation of traction force during the migration process.

2) In addition to disrupting actomyosin contraction, the effect of AuNRs on focal adhesions (or cell-matrix adhesion) was also observed. Focal adhesions are structures that contain integrin and other associated proteins, which form links between intracellular actin cytoskeleton and ECM [355]. The activated integrins couple to the actin cytoskeleton by recruiting actin-binding proteins [356]. Our results show that actin-binding proteins, including alpha-actinin, talin, vinculin, were down-regulated after AuNRs incubation (**Figure 4.7 B** and **4.9**), suggesting the connectivity between integrin and actin cytoskeleton was likely weakened due to the blocking effect of AuNRs on the migration pathways.
3) While the actin cytoskeleton provides contractile forces, microtubules form polarized network throughout the cell. The microtubule-associated proteins (MAPs) were significantly down-regulated (MAP2 and MAP4), indicating the rearrangement of microtubules. MAPs binds directly to the tubulin dimers of

microtubules which often leads to the stabilization and polymerization of microtubules [357]. The disruption of the intracellular microtubule assembly could also limit the cell motility [358].

4) Furthermore, our results show several kinases related to the integrin signaling pathways were perturbed, including integrin linked kinase (ILK), nuclear factor-κB (NF-κB), the epidermal growth factor receptor (EGFR), caveolin, *etc*. These proteins are closely associated with integrin regulation and cell migration [359]. It has been reported that the overexpression of ILK could promote the migration and invasion of colorectal cancer cells via NF-κB signaling [360]. In the current results, the down-regulation of ILK and NF-κB is associated with reduced cancer cell migration ability. In addition, the expression level of EGFR, a surface receptor for epidermal growth factor decreased. The down-regulation of EGFR was also confirmed in the Western-blot results. EGFR is regarded as an important target for anticancer therapeutics [361]. Furthermore, $STAT_3$, which is normally activated by tyrosine phosphorylation in response to the addition of EGFR [362] and can promote cell migration, was also down-regulated in all the AuNRs treated samples (**Figure 4.7 D**).

1.12.4 Discussion.

Current advances of nanoscience and nanomedicine enable us to fabricate "intelligent" nanomaterials that can specifically target cellular and subcellular locations in living animals for treating diseases [209, 295]. While larger nanoparticles (> 18 nm in diameter) can accumulate in organs such as the liver and spleen and be eliminated slowly [317], the long-term effect of AuNRs in mice shows no toxic effect after 15 months [363].

The biocompatibility and special physicochemical properties of AuNRs provide us an effective and safe potential treatment of cancer.

Our previous study has shown success in treating xenograft mice and natural mammary gland tumors in dogs and cats using AuNR-assisted PPTT, where no cancer relapse or metastasis occurred in any of the test subjects [272, 363], implying the potential effect of AuNRs in inhibiting cancer metastasis. We also designed nuclear membrane-targeted AuNPs for inhibiting cancer cell migration and invasion, by mechanically increasing their nuclear stiffness, with greatly reduced AuNPs dosage [324, 363]. Herein, we reported that targeting AuNRs to cancer cell surface integrins could greatly rearrange the cytoskeleton proteins, thus enhance the inhibition effect on cancer cell migration. When compared to non-targeted AuNRs, the integrin-targeted AuNRs are more effective on cell migration inhibition with a nanoparticle concentration at the nM scale (1000× lower than the literature values [74-76], which could be safer for future clinical usage.

Our result shows that cancer cells incubated with integrin-targeted AuNRs (with or without NIR light exposure) exhibited impaired migration abilities. Morphological changes were observed in cytoskeleton protrusions by targeting surface integrins using AuNRs, namely lamellipodia and filopodia, which form the leading edge for cell movement. These cytoskeleton protrusions were reduced after treating the cells with AuNRs@RGD. Furthermore, greater morphological changes were observed after applying NIR light. Integrins are often found in the tips or alone in the shaft of filopodia and lamellipodia, which creates the “sticky fingers” and facilitate the migration and invasion [364]. The reason for this morphological change has been explored in our Western

blot and proteomics analysis, which indicated that the integrin related proteins were obviously affected.

In addition to the morphological change through lamellipodia and filopodia, systematic molecular mechanisms have been studied and many protein pathways exhibit changes after exposing to integrin-targeted AuNRs. This broad change of cytoskeletal proteins is possibly due to the ability of integrin in controlling cytoskeleton through many different ways as an up-stream surface receptor. Results show that by targeting surface integrins, the focal adhesion connecting the cytoskeleton to the extracellular matrix through integrin has been weakened. Moreover, the actomyosin contraction, which creates intracellular tension for migration, has been modulated through the Rho GTPase signaling. Though targeting integrins, both the change of actin and microtubule were observed, as well as several protein kinases that related to cytoskeleton and cancer progression and metastasis. All the above aspects could finally result to the inhibition of cancer cell migration.

In summary, the ability of targeting AuNRs to cancer cell surface integrins and the introduction of PPTT caused wide-range regulation on cytoskeletal proteins, observed as lamellipodia/filopodia morphological changes and four major groups of migration-related protein changes. Applying NIR light to generate mild heat further enhanced this effect. This strategy provides a potential application for controlling cancer metastasis. Future work will be focused on testing the effect of gold nanoparticles on preventing and treating cancer metastasis in animals. The injection method (either active or passive tumor targeting) should be decided and more investigation will be conducted.

1.13 Gold Nanorod-photothermal Theralpy Alters Cell Junctions and Actin Network in Inhibiting Cancer Cell Collective Migration[94]

Summary. Most cancer-related deaths come from metastasis. It was recently discovered that nanoparticles could inhibit cancer cell migration. While most researchers focus on single-cell migration, the effects of nanoparticle treatment on collective cell migration has not been explored. Collective migration occurs commonly in many types of cancer metastasis, where a group of cancer cells move together, which requires the contractility of the cytoskeleton filaments and the connection of neighboring cells by the cell junction proteins. Here, we demonstrate gold nanorods (AuNRs) and the introduction of near-infrared light could inhibit the cancer cell collective migration by altering the actin filaments and cell junctions with significantly triggered phosphorylation changes of essential proteins, using mass spectrometry-based phosphoproteomics. Further observation using super-resolution stochastic optical reconstruction microscopy (STORM) showed the actin cytoskeleton filament bundles were disturbed, which is difficult to differentiate under a normal fluorescence microscope. The decreased expression level of N-Cadherin junctions and morphological changes of tight junction protein ZO-2 were also observed. All these results indicate possible functions of the AuNRs treatments in regulating and remodeling the actin filaments and cell junction proteins, which contribute to decreasing cancer cell collective migration.

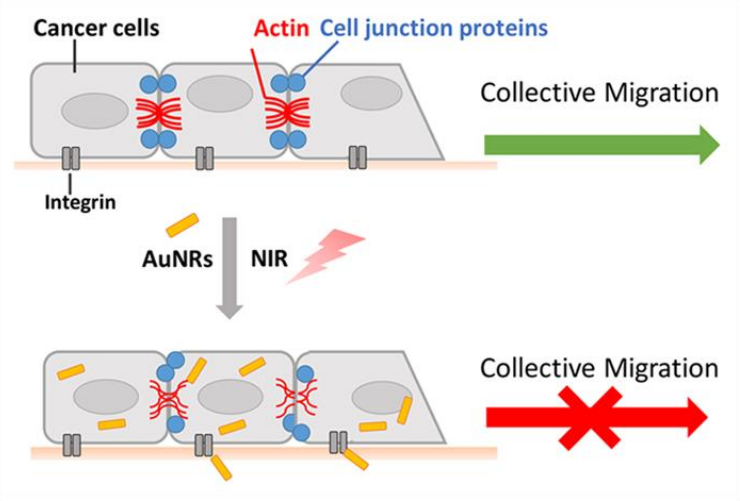

FIGURE 4.10. Schematic of AuNRs and PPTT disturb the actin network and cell junctions.

1.13.1 Introduction.

Metastasis is responsible for over 90% of cancer-related deaths[62]. In order to initiate the metastasis, cancer cells must be equipped with the ability to migrate and invade the surrounding tissues, then intravasate to the microvasculature of the lymph and blood stream, and finally translocate to distant tissues and adapt in the microenvironment [62]. However, past attempts to develop anti-metastasis drugs have not been efficacious in clinical trials [128]. Recent advancements in nanomedicine provide new opportunities to avoid some drawbacks of commonly used cancer drugs, as nanoparticles can cross biological barriers, enter target cells with high selectivity, and function inside cell in a controlled manner [14, 129, 130]. Nanoparticles have shown promise as anti-metastasis drug delivery vehicles targeting invasive or metastasized cancer cells[79, 88, 131], and they could even function as anti-metastasis drugs without drug loading[85, 86, 132, 133]. The optical and mechanical properties, such as plasmonic photothermal effect and high mechanical

strength, as well as excellent biocompatibility of gold nanoparticles (AuNPs) make them very useful in attenuating cancer metastasis[134].

Previously, we have developed cancer treatment using gold nanorods (AuNRs) for plasmonic photothermal therapy (PPTT). In PPTT, AuNRs that absorb the incident near infra-red (NIR) light to induce heat, and thereby could trigger tumor apoptosis [40]. AuNRs-PPTT has been applied successfully on treating tumor bearing mice, cats and dogs. In these studies, we observed that animals with induced or spontaneous tumors were effectively cured with no tumor reoccurrence or metastasis [9, 48, 365]. Our recent *in vitro* studies also revealed AuNPs and PPTT inhibits cancer cell migration and invasion [10, 85]. However, the mechanism of how AuNPs treatments inhibit cancer cell migration remains largely unresolved.

While the mechanism of nanoparticles on inhibiting the migration of single cells have been explored in the previous works, the mechanism regarding collective cell migration has rarely been studied. In collective cancer cell migration, a group of cancer cells migrate together, which might be a more efficient route for metastasis possibly due to a diverse cell population seeding other organs or the multicellular signal integration engaged [366]. Collective cell migration has been widely observed in human cancers, especially in human epithelial cancers such as breast cancer and colon cancer [366, 367]. It requires both the contractility of the cytoskeleton filaments and the active interactions of neighboring cells through the cell-cell junctions that connect the cytoskeleton of the neighboring cells [368]. This process is highly dynamic and regulated by signal transduction through protein phosphorylation [369, 370]. Given their important roles, it is imperative to understand the signals evolved in the cytoskeleton filaments and cell-cell

junctions shortly after AuNRs and PPTT stimulation for the rational design of effective strategies to inhibit cancer metastasis.

In the current study, we hypothesized that the integrin-targeting AuNRs and PPTT treatment could affect the cytoskeleton and cell junctions, due to their interactions and connections as a network, to result in the inhibition of collective cancer cell migration (as shown in Scheme **1** in the Experimental section). To test this hypothesis, quantitative mass spectrometry (MS)-based phosphoproteomics was employed to examine the signaling pathways upon the stimulation of AuNRs and PPTT. A primary signaling pathway map has been constructed to display a large number of identified alterations. Furthermore, super-resolution microscopy imaging techniques were used to visualize the changes of key cytoskeletal and cell junction proteins. Both phosphoproteomics and super-resolution imaging results indicated possible functions of the AuNRs and PPTT in regulating and changing the architecture of the cytoskeletal filaments and cell junctions, contributing to the inhibition of collective cancer cell migration.

1.13.2 Results and Discussion.

1.13.2.1 Gold Nanorods and NIR Light Attenuate the Migration and Invasion of Cancer Cells

The preparation of integrin targeted AuNRs was stated in our previous work [10]. Briefly, AuNRs with a size of 25 (± 3) × 6 (± 2) nm (length × width) and an aspect ratio of 4.2, transmission electron microscopy (TEM) image) were synthesized using the seedless growth method [228]. Optimal heat-generating efficacy in PPTT with these AuNRs has been demonstrated previously [341]. To remove the cytotoxic

cetyltrimethylammonium bromide (CTAB), the as-synthesized AuNRs were washed twice with D.I. water. Then, the AuNRs were functionalized with polyethylene glycol thiol (PEG) and Arg–Gly–Asp (RGD) peptides to increase the biocompatibility [230] and obtain integrin targeting [333], respectively. The surface conjugations were confirmed by the red-shift of the longitudinal surface plasmon resonance (SPR) band and surface charge changes of the AuNRs, consistent with the previous reports [10]. For the details of the AuNRs synthesis, conjugation and characterization, please refer to 4.1 section.

The binding of RGD peptide to the cell surface integrin could enhance the endocytosis of AuNRs [342]. The internalization of AuNRs within the cervical cancer cell line HeLa, was observed under a differential interference contrast (DIC) microscope (**Figures 4.11 A and B**). DIC images indicates the AuNRs@RGD distribute spread the cytoplasm and the cell junction areas (**Figure 4.11 C**). The z-scanning indicates the successful internalization of AuNPs inside cells after 24 h (**Figure 4.13 A-C**). The cell viability (XTT) assay revealed that the cells remained viable and had similar proliferation rates after incubation with AuNRs and after PPTT for 24 h (**Figure 4.11 D**). (AuNRs@PEG was used as a "bare", nonspecifically targeted AuNRs for control, as shown in **Figure 4.12** (no cytotoxicity), **Figure 4.13 B** (cellular uptake not obvious), indicating the importance of RGD peptides to increase cellular uptake). In addition, no observable change of the apoptosis regulator Bcl-2-associated X (BAX) protein indicates no apoptosis after treatment (**Figure 4.11 E**). We performed the same assays with the breast cancer cell line MCF-7, and similar results were obtained (**Figure 4.13**).

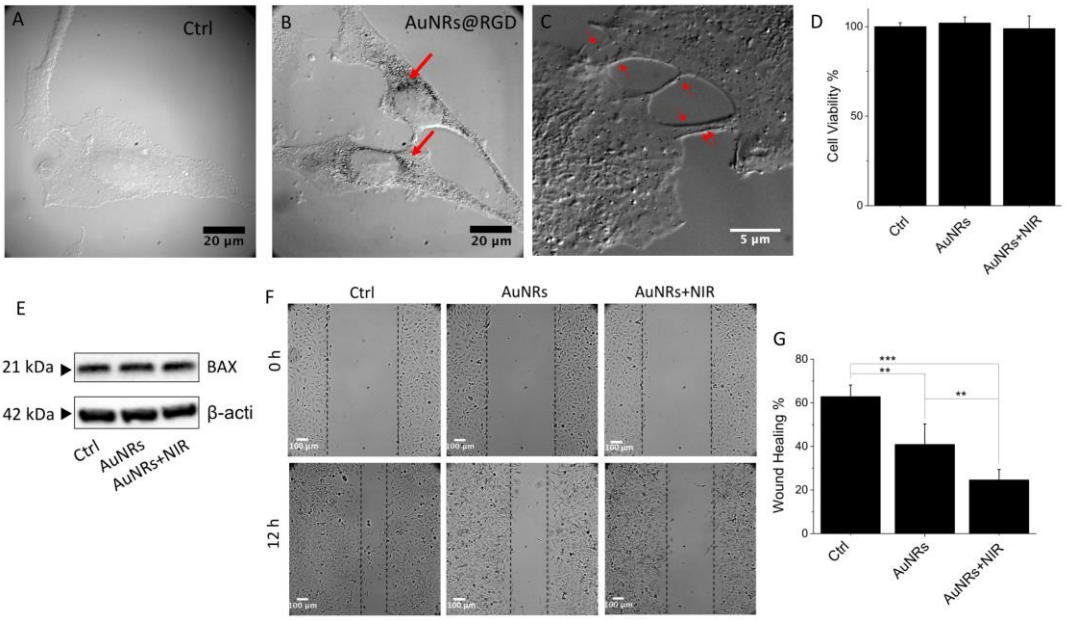

FIGURE 4.11. Cellular uptake, cytotoxicity and motility upon AuNRs treatments (the results of MCF-7 cells are in Figure S2-4). (A-B) Differential interference contrast (DIC) microscopic images of HeLa cells without (A) and with AuNRs@RGD after 24 h incubation (B). (C) DIC image of AuNRs@RGD distribute in the cell junction areas after 24 h incubation. The red arrows identify the locations of AuNRs. (D) Cell viability of HeLa cells after AuNRs and AuNRs+NIR treatments (n=3). (E) Western blotting for the BAX protein upon different treatments. (F and G) Scratch assay of HeLa cells (control, AuNRs treatment, and AuNRs+PPTT treatment) at 0 and 12 h (n=6). Student's t test was used for statistical analysis. All values are expressed as means ± standard errors of the mean (SEM). ***p < 0.001, **p< 0.01, *p<0.05. If not specified otherwise, "AuNRs" in all other figures means "AuNRs conjugated with RGD ligands".

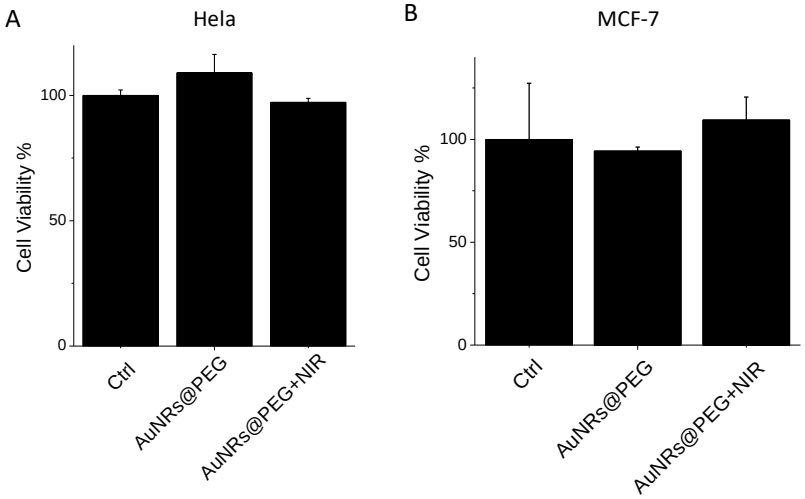

FIGURE 4.12. Cytotoxicity of non-specifically targeted AuNRs (AuNRs@PEG) on HeLa and MCF-7 cells (n=3).

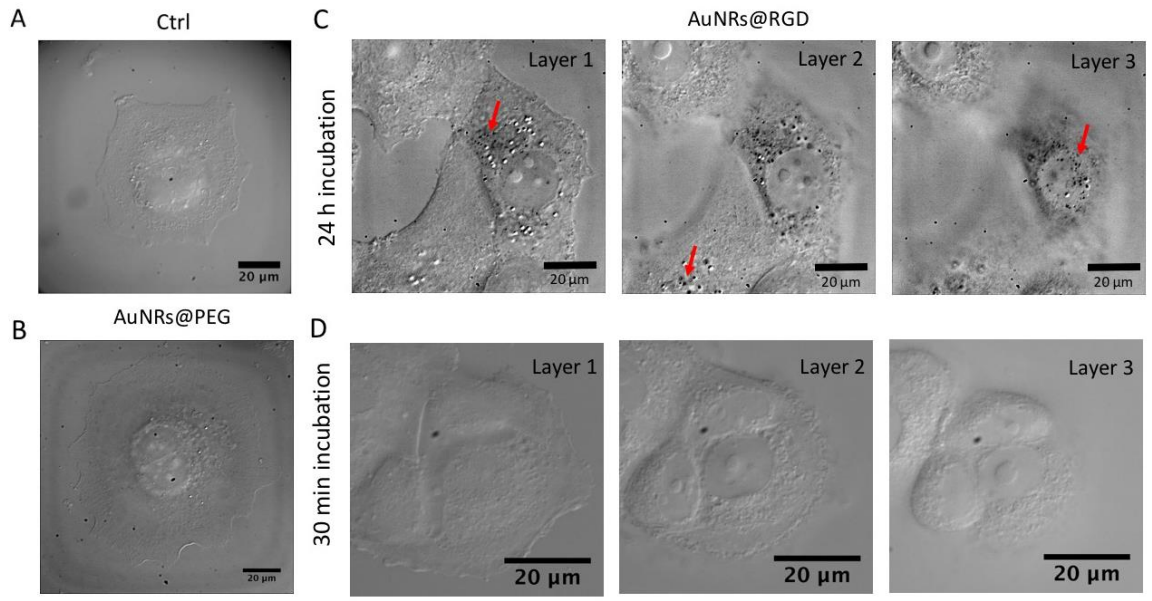

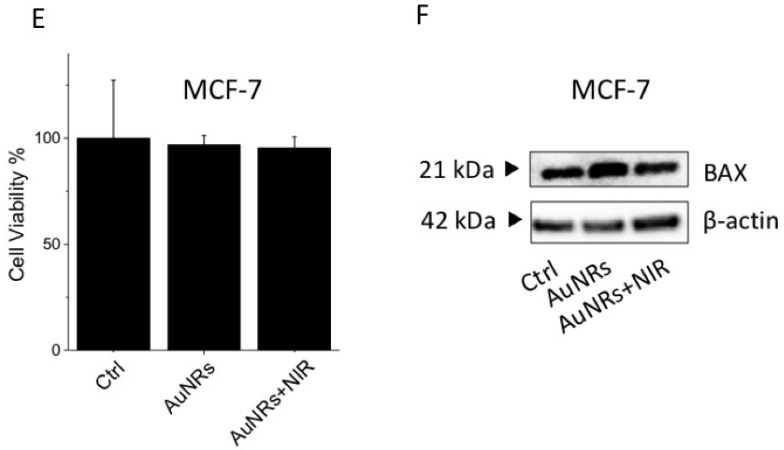

FIGURE 4.13. Cellular uptake and cytotoxicity of AuNRs treatments of MCF-7 cells. (A-D) Differential interference contrast (DIC) microscopic images of MCF-7 cells without AuNRs (A) and with AuNRs@PEG (B), or with AuNRs@RGD for 24 h (C) and 30 min (D) with Z-scanning. The red arrow indicates the locations of AuNRs. Three layers (layer 1 locates close to the bottom (surface), layer 2 locates in the middle of cells, layer 3 locates in the top of cells) indicate clearly the internalization of AuNRs. (E) Cell viability of MCF-7 cells after 24 h AuNRs and AuNRs+NIR treatments (n=3). (F) Western blotting for the BAX protein upon different treatments (after 24 h).

To evaluate the effects of AuNRs on cancer cell collective migration, we conducted a 2D scratch assay [291, 371] on the monolayers of MCF-7 and HeLa cells that were incubated with or without the treatments. After introducing a "scratch" or "wound" into a cell culture, the cancer cells migrate collectively to the empty space, and images were captured immediately and 12 hours after the scratch of HeLa cells in **Figure 4.11 F** (or 24 hours of MCF-7 cells in **Figure 4.14**). The statistics (**Figure 4.11 G**) indicates that cells have exhibited significantly different wound-healing ability in the control groups compared with those treated with AuNRs, while the introduction of NIR light to generate PPTT further decreases the wound-healing ability of cancer cells. If only treated with same dose of NIR light (no AuNRs added), no change in the cell viability and motility was observed (**Figure 4.15**). Our result shows both specific targeted AuNRs (AuNRs@RGD) and nonspecific targeted AuNRs (AuNRs@PEG, **Figure 4.16**) could inhibit collective cell migration to different extents, among which the AuNRs@RGD assisted PPTT is most effective.

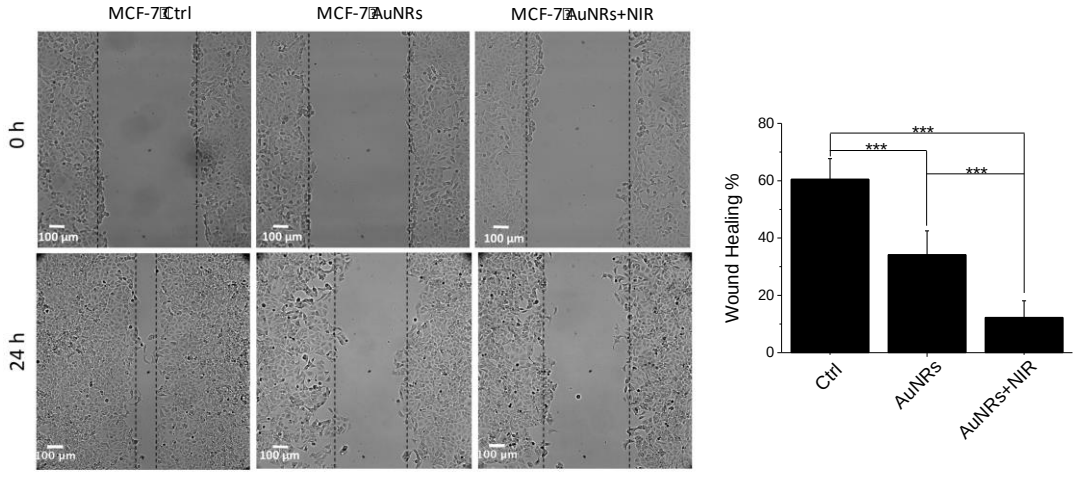

FIGURE 4.14. Scratch assay images of MCF-7 cells (control, AuNRs treatment, and AuNRs/PPTT treatment) at 0 and 24 h (n=6). Student's t test was used for statistical

analysis. All values are expressed as means ± standard errors of the mean (SEM). ***p < 0.001, **p< 0.01, *p<0.05.

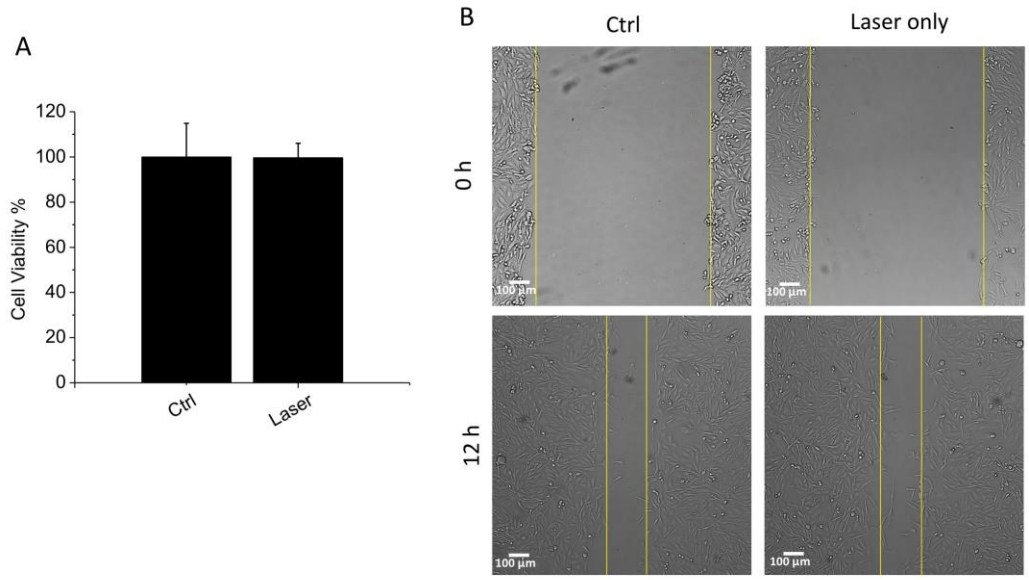

FIGURE 4.15. (A) HeLa cell viability comparing Ctrl (no treatment) and Laser treatment (no AuNRs added, n=3). (B) Scratch assay images of HeLa cells (Ctrl and Laser treatment) at 0 and 12 h.

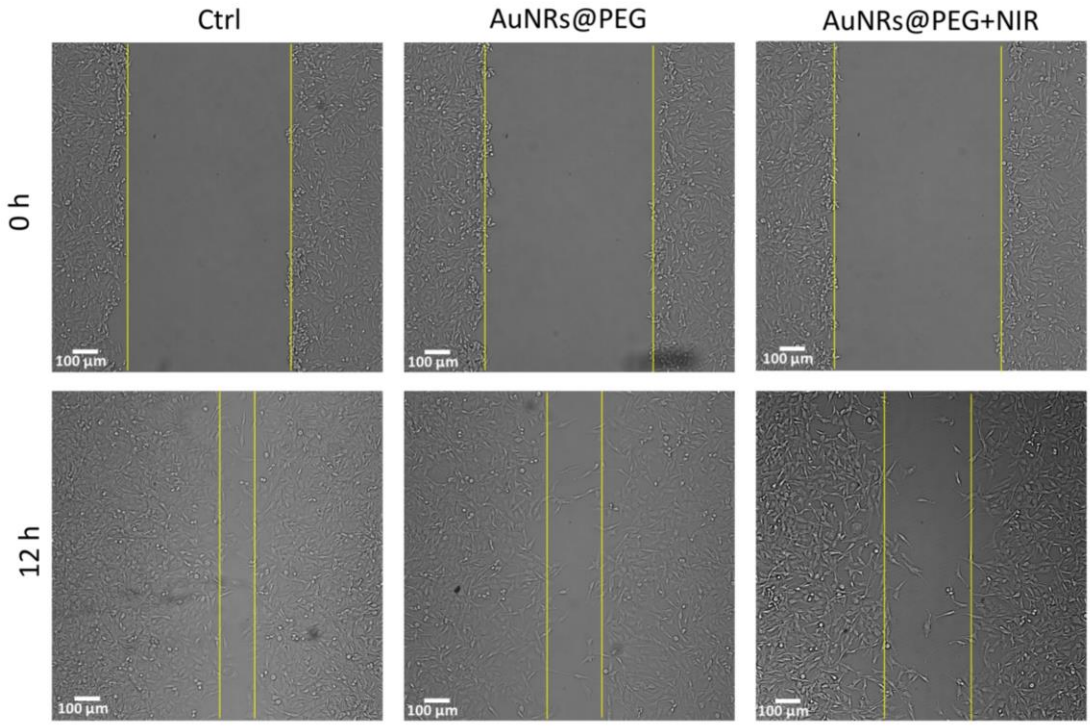

FIGURE 4.16. Scratch assay images of HeLa cells (Ctrl, AuNRs@PEG, AuNRs@PEG+NIR treatments) at 0 and 12 h.

1.13.2.2 Mass Spectrometry-based Phosphoproteomics Analysis Reveals Perturbations of the Signal Transduction of the Actin Network and Junction Proteins

To elucidate the effects of AuNRs and PPTT treatments on cytoskeleton filaments and cell junctions, we examined the phosphoproteomics of cancer cells using quantitative mass spectrometry (MS). A simplified experimental procedure is shown in **Figure 4.17 A** (detailed and complete experimental procedure in the Method section, and **Figure 4.18,** including conditions of non-specific targeting AuNRs@PEG). Protein phosphorylation was identified and quantified in both HeLa and MCF-7 cells after incubation with AuNRs for 30 min or after AuNRs+PPTT treatment for 30 min. Three-plex dimethyl labeling was used for phosphoproteomic quantification, and titanium (IV) based immobilized metal ion affinity chromatography (Ti-IMAC) was used to enrich the phosphorylated peptides from the protein digest of cell lysate. The enriched phosphorylated peptides were analyzed by an on-line liquid chromatography-mass spectrometry (LC-MS) system. Three replications of each condition were conducted and about 1200 common phosphorylation sites (where the phosphorus group binds to the protein) were quantified. The clustering analysis (**Figure 4.19**) shows that the control and experimental groups were separately clustered with good reproducibility. Differential analysis identified proteins with significant changes in AuNRs-treated groups compared to the control group (**Figure 4.20**). The numbers of dysregulated phosphorylation sites of different treatments and their overlap in the Venn diagrams are shown in **Figure 4.21**. For instance, compared with the control group, the phosphorylation levels of 371 and 244 sites are significantly

up- and down-regulated, respectively, for HeLa cells upon AuNRs treatment. Further changes from PPTT were observed, with 73 and 189 phosphorylated sites up- and down-regulated.

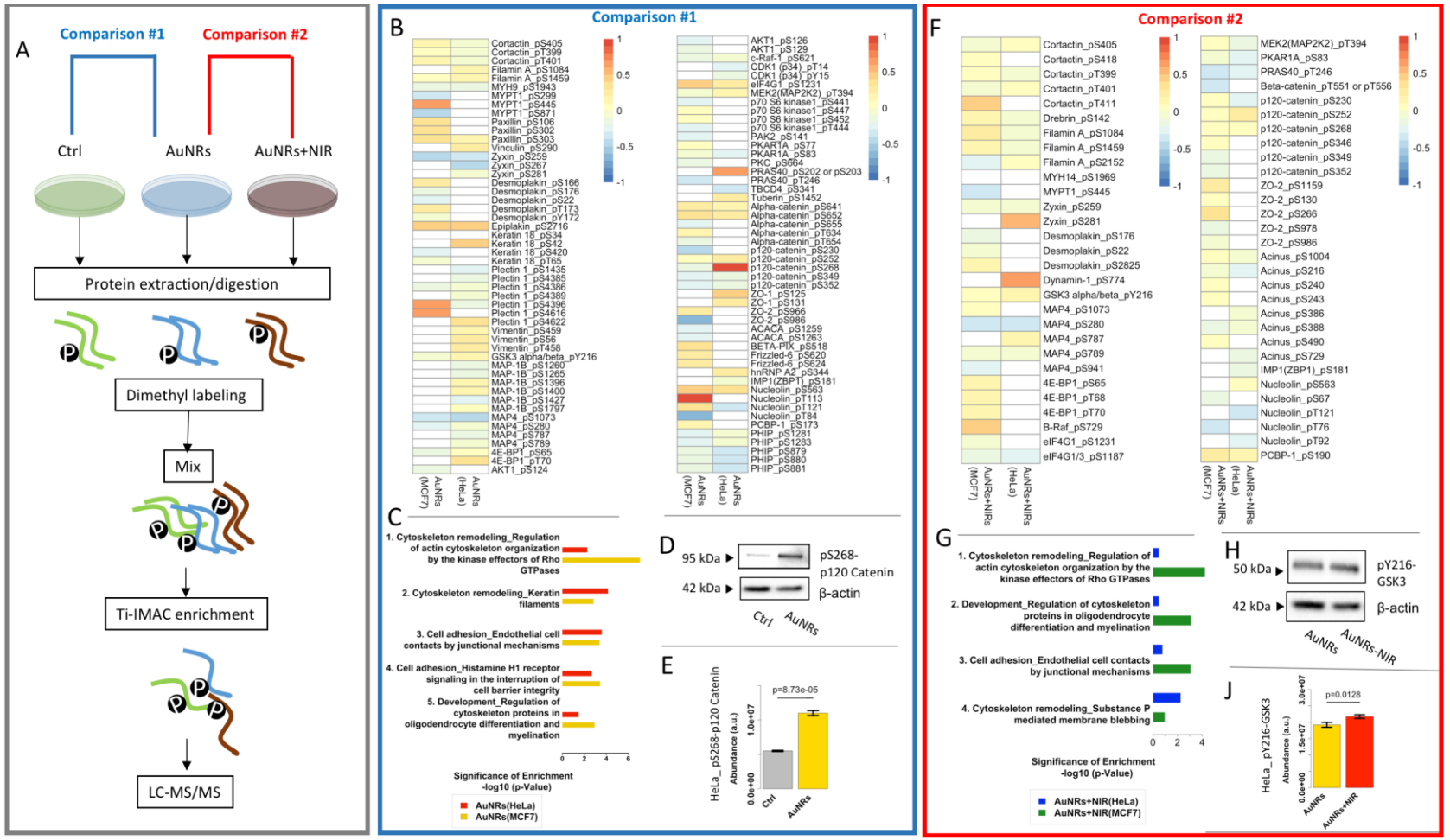

FIGURE 4.17. Phosphoproteomics results. (A) Experimental workflow. Two comparisons were performed in data analysis. Comparison #1 (AuNRs vs. control): (B) Heatmap and (C) pathway analysis after AuNRs treatment. (D) Western blotting showing the altered phosphorylation sited in p120 Catenin (HeLa cells). (E) Altered phosphorylation sited in p120 Catenin

(pS268) indicated by phosphoproteomics (HeLa cells). Comparison #2 (AuNRs + NIR vs. AuNRs): (F) Heatmap and (G) pathway analysis after AuNRs + NIR treatment. (H) Western blotting showing the altered phosphorylation sited in GSK3 (HeLa cells). (I) Altered phosphorylation sites GSK3 (pY216) indicated by phosphoproteomics (HeLa cells). Mean values in are shown in the heatmaps (n=3).

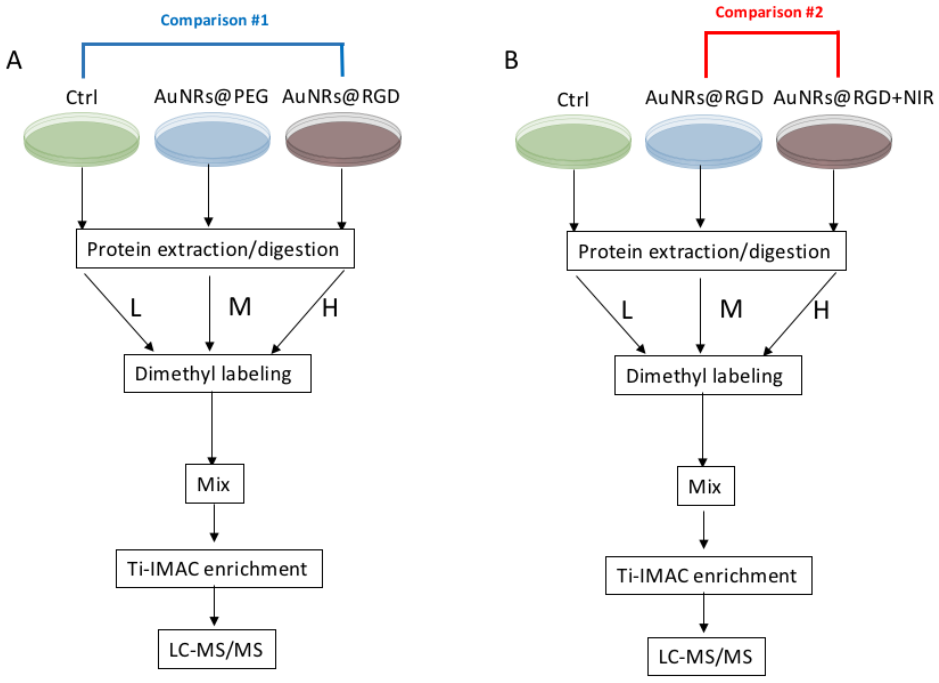

FIGURE 4.18. Experimental design of quantitative phosphoproteomics. Two sets of experiments were performed to examine the AuNRs and the photothermal effects separately. (A) Studying the protein phosphorylation upon treatments of AuNRs@PEG (30 min stimulation) and AuNRs@RGD (30 min stimulation). (B) Studying the protein phosphorylation upon photothermal effects (30 min stimulation) after overnight incubating the cells with AuNRs@RGD. The comparisons #1 and #2 are indicated in.

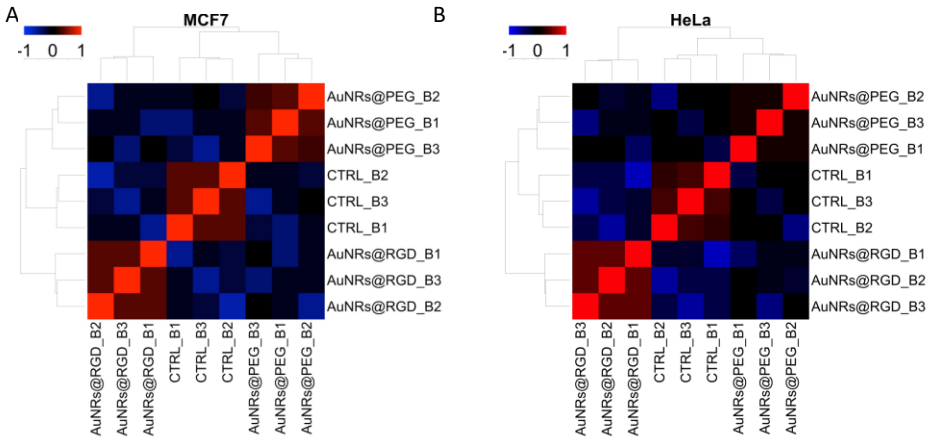

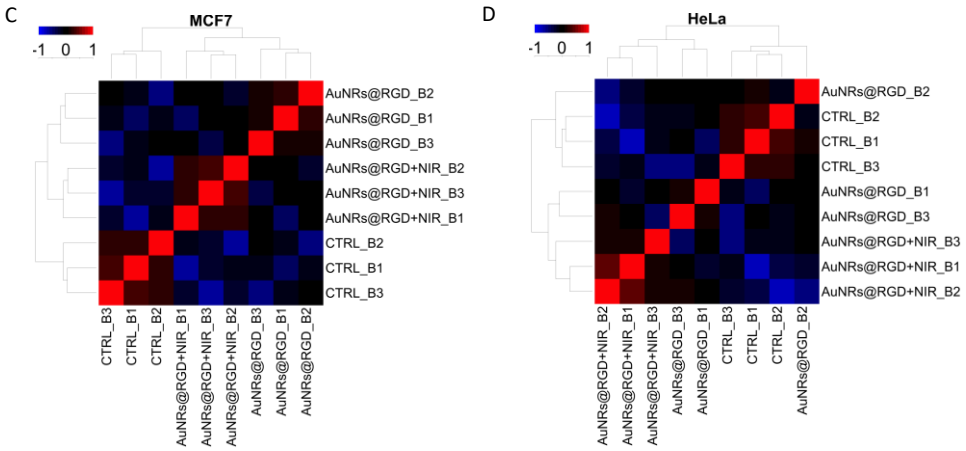

FIGURE 4.19. Clustering analysis of the samples. (A) AuNRs@PEG, AuNRs@RGD and control for MCF-7. (B) AuNRs@PEG, AuNRs@RGD and control for HeLa. (C) AuNRs@RGD, AuNRs@RGD+NIR, and control for MCF-7. (D) AuNRs@RGD, AuNRs@RGD+NIR, and control for HeLa. B1, B2, and B3 in the figures indicate the three biological replications.

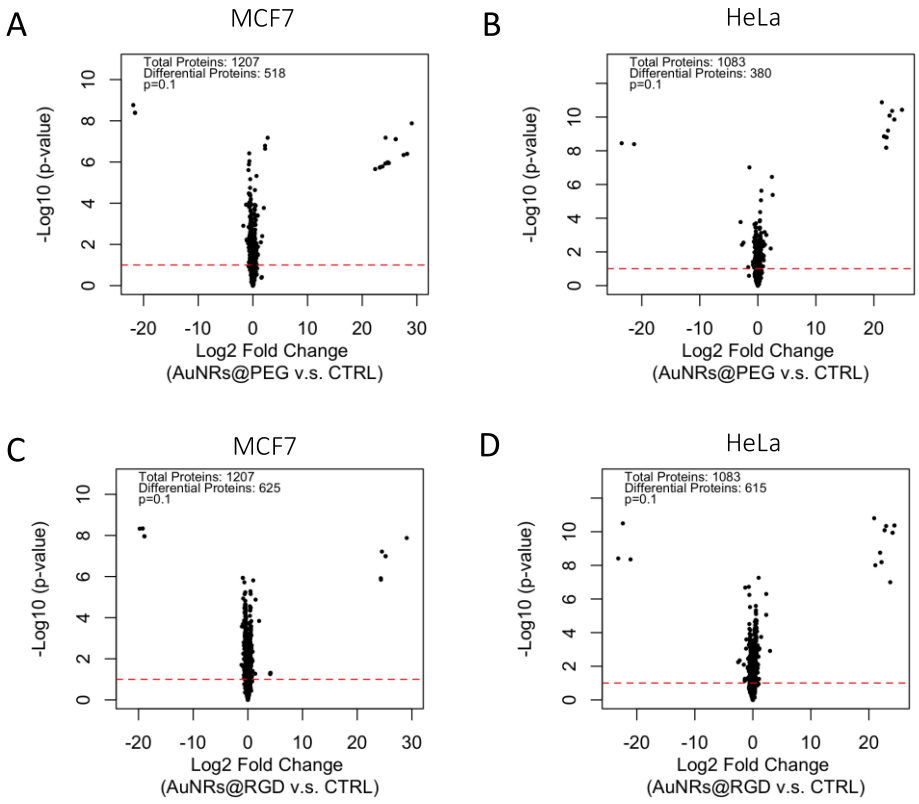

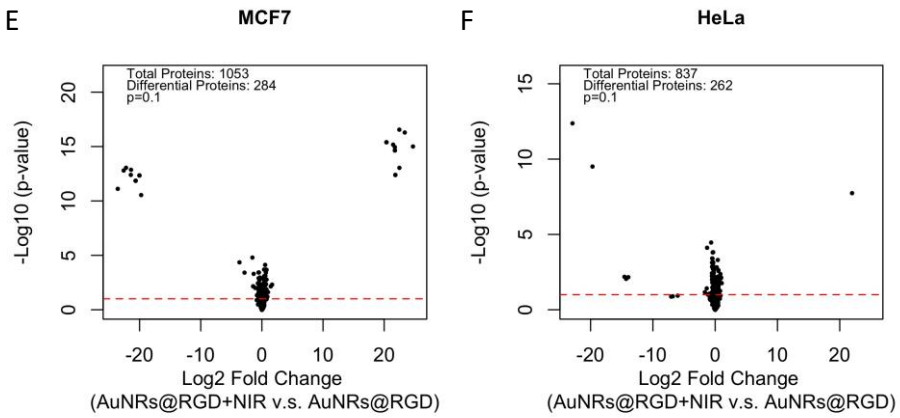

FIGURE 4.20. Volcano plots of proteins under perturbation by (A) AuNRs@PEG for MCF-7, (B) AuNRs@PEG for HeLa, (C) AuNRs@RGD for MCF-7, (D) AuNRs@RGD for HeLa, (E) AuNRs@RGD+NIR for MCF-7 and (F) AuNRs@RGD+NIR for HeLa.

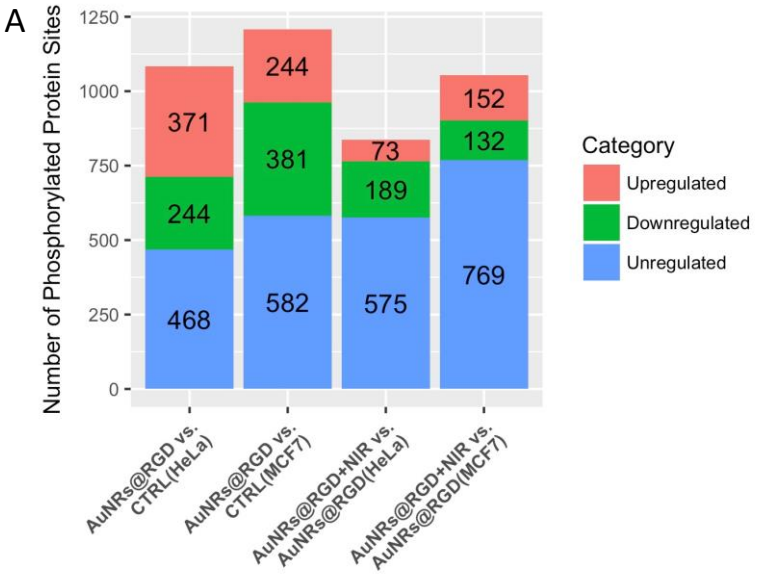

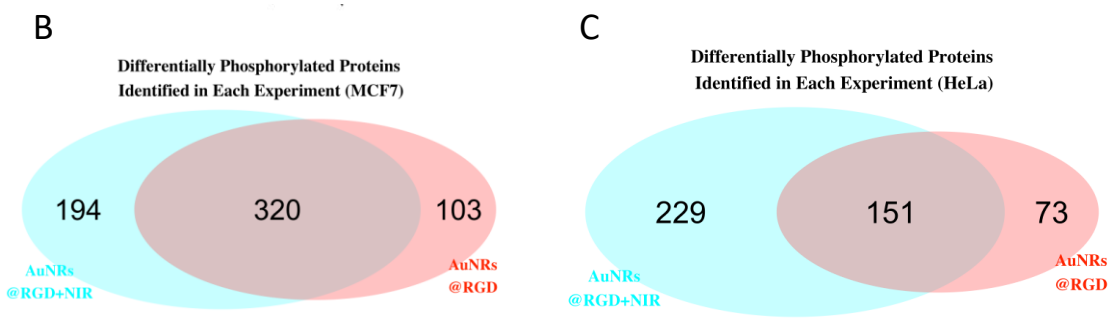

FIGURE 4.21. (A) Numbers of regulated/unregulated phosphorylated sites identified in each experiment. (B-C) Venn diagram showing the comparison of differentially phosphorylated sites identified in each experiment.

Proteins with their significantly altered phosphorylation sites are listed in heatmaps (**Figure 4.17 B and F**) and **Table 4.1**. In order to understand the biological meanings of these phosphorylation changes, we performed pathway analysis (**Figure 4.17 C** for AuNRs and **G** for AuNRs+PPTT), which revealed the significant perturbations to the signaling pathways related to the cytoskeleton and cell junctions. To further confirm the mass spectrometric results, the varied phosphorylated sites of p120 catenin (pS268), and glycogen synthase kinase (GSK3, pY216), which are highly related to cell adhesive junctions, and are regulators to actin cytoskeleton and microtubules [372], respectively, have been validated by Western blot results (**Figure 4.17 D, E, H, and J**).

Table 4.1. Selected significantly dysregulated phosphorylation sites of the cytoskeletal and junction proteins, specifying the phosphorylation sites and biological functions.

Category	Protein	Protein Function	Phosphorylation sites altered	Phosphorylation sites function
Cytoskeleton	Paxillin	Form focal adhesions	pS303, pS302, pS106, pS85	Increase of pS85 has an important function in cell adhesion [373]
	MYH9	Form stress fibers and create a contraction force in cell migration [444]	pS1943	pS1943 could alter cell motility[374]
	MLCP		pS299, pS445, pS871	pS445 is closely related to cell adhesion [375]
	MAP4	Promotes microtubule assembly	pS1073, pS787, pS280, pS789	pS1073 is related to cancer cell metastasis potential [376] and pS787 could promote tubulin polymerization [377] thereby changing the microtubule organization.
Cells junctions	α-catenin	Form cell-cell adhesion complexes, anchoring actin cytoskeleton and interacting with cadherins [378]	pT654, pS641, pT634, pS652, pS655	S641 affects cell motility[379]
	ZO-2	Connect cytoskeletons of adjacent cells and act as barriers for the passage of molecules and ions[380]	pS966, pS986, pS978, pS266, pS986, pS1159, pS130	*No information found*
	Vimentin	A hallmark protein of epithelial to mesenchymal transition (EMT), which is related to the increase of migration and invasive properties[381]	pS459, pS56, pT458	pS56 was reported with the function of cytoskeleton reorganization [382]
	Keratin 18	Keratin 18 and its filament partner keratin 8 are regarded as the most commonly found members of the intermediate filament family.	pS34, pT65, pS420, pS42	pS34 affects cell motility and cytoskeleton [383]

We observed that our treatments can change the phosphorylation of the actin network, including i) proteins forming the focal adhesions (FAs), such as paxillin, zyxin, vinculin; ii) the myosin related proteins, such as myosin-9 and myosin-light-chain phosphatase (MLCP); iii) the actin-binding proteins, such as filamin, cortactin and drebrin. Moreover, changes of cell junctions, such as tight junction proteins ZO-1 and ZO-2 were also observed upon AuNRs stimulation. More changes were observed to ZO-2 after PPTT, indicating an enhanced perturbation in the tight junctions. In addition, cell junction protein catenins, including alpha, beta, and p120 catenins, have altered phosphorylated sites upon treatment. Phosphorylation change of desmosomes junction related proteins, including desmoplakin, epiplakin, plectin, Keratin 18 and vimentin were observed. In addition, the phosphorylation of several microtubule (MT)-related proteins were changed, including microtubule associated proteins MAP4, microtubule associated protein 1B (MAP1B) and glycogen synthase kinase-3 alpha (GSK3A). Besides, Phosphorylation changes of many protein kinases that could regulate the cytoskeleton filaments and cell motility were observed, such as RAF proto-oncogene serine/threonine-protein kinase (Raf1), mitogen-activated protein kinase kinase 2 (MAP2K2), cyclin-dependent kinase (CDK1), RAC-alpha serine/threonine-protein kinase (AKT1), *etc*.

Integrins are adhesive molecules located in the cell membrane and responsible of transporting signals and cell-cell communications [384]. The ability of integrin-targeted AuNRs to alter the junction proteins is linked to the coordination and interdependence manner of integrin and cell junction to form adhesive networks, by connecting through the actin cytoskeleton and sharing common signaling molecules [385]. For instance, integrin-induced signaling molecules focal adhesion kinase (FAK) and paxillin regulate

the N-cadherin junctions in Hela cells [386]; α-catenin links cadherin to the actin cytoskeleton[387]; and p120 catenin cooperates with cortactin to regulate lamellipodial dynamics and cell adhesion[388]. Here, we observed possible signal cross-talk between the cytoskeleton and cell junctions, such as the altered phosphorylation of paxillin, α-, β-, and p120- catenin, as well as cortactin. Based on the phosphoproteomics results, a schematic diagram is constructed to show the signal transduction upon AuNRs and PPTT stimulation (**Figure 4.22**). By targeting integrins, our treatments induced the protein phosphorylation change of the downstream actin cytoskeletal and junction proteins.

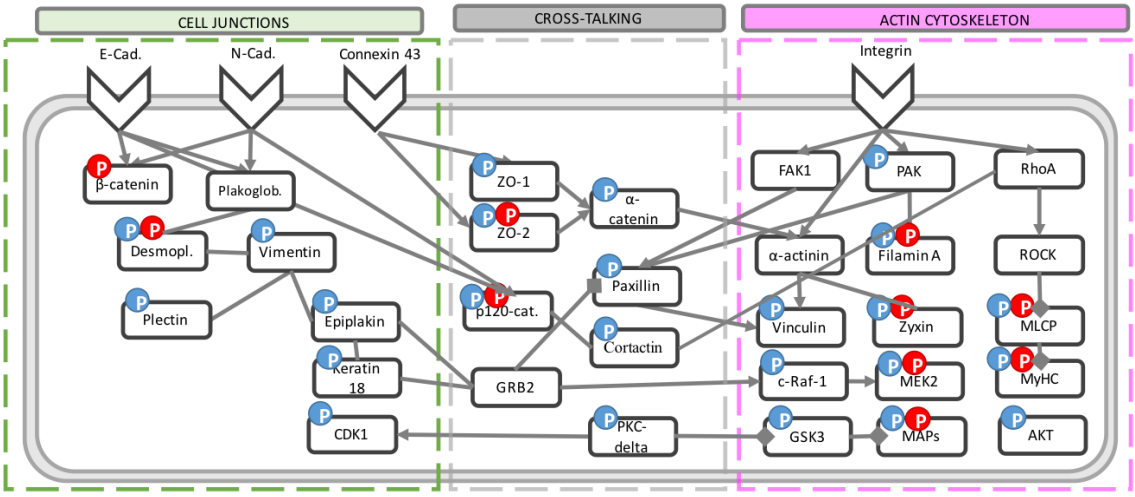

FIGURE 4.22. Schematic diagram of the signaling pathways that are engaged with the cytoskeleton and cell junctions upon the AuNRs and PPTT treatment. The blue and red "P"s indicate the altered phosphorylation level upon AuNRs treatment and PPTT treatment (AuNRs+NIR), respectively.

1.13.2.3 Super-resolution Imaging for Confirming Disturbed Cytoskeletal and Cell Junction Proteins

Collective cell migration requires the cells are effectively coupled by cell junctions, coordinating their actin dynamics and intracellular signaling thereby forming a

functioning unit [367]. The actin cytoskeletons of neighboring cells are coupled by the cell junctions. The drag force between the cells is provided by actomyosin contractility [389], which is important in maintaining effective cell junction and collective migration [390]. Although the phosphorylation signal transduction takes place within a few minutes, the protein expression level may take hours to change. Therefore, to clearly observe the protein expression level changes, we monitored the actin filament structures after 24 hours of AuNRs incubation with or without PPTT (**Figure 4.23**). Under a normal fluorescence microscope, it is difficult to differentiate changes of actin structure before and after treatments due to the insufficient resolution, as shown in **Figure 4.23 A-C**. Stochastic optical reconstruction microscopy (STORM) provides superior spatial resolution than conventional fluorescence microscopy to reveal the detailed actin cytoskeletal structures (**Figure 4.24**). By using STORM, we observed the morphological changes of the circumferential actin filaments at the cell-cell junctions. Before AuNRs treatment, the well-aligned stress fibers (contractile actin bundles) are clearly visualized, with polymerized and stable structure (**Figure 4.23 D**). However, after AuNRs treatment, the actin bundles became thinner, showing a clear sign of disturbance (**Figure 4.23 E**). Furthermore, after NIR exposure, the circumferential actin filaments at cell junctions exhibited obvious changes (**Figure 4.23 F**): the stress fibers were greatly decreased, while coil, depolymerized and reorganized structures appeared, which possibly indicated the heating effect on harming the actin filaments polymerization at the junction sites. In addition, the actin structure at the cell leading edges (filopodia and lamellipodia) was also imaged (**Figure 4.25**), and the observed decrease in stress fibers in the cell leading edges hinted a decrease in cell motility.

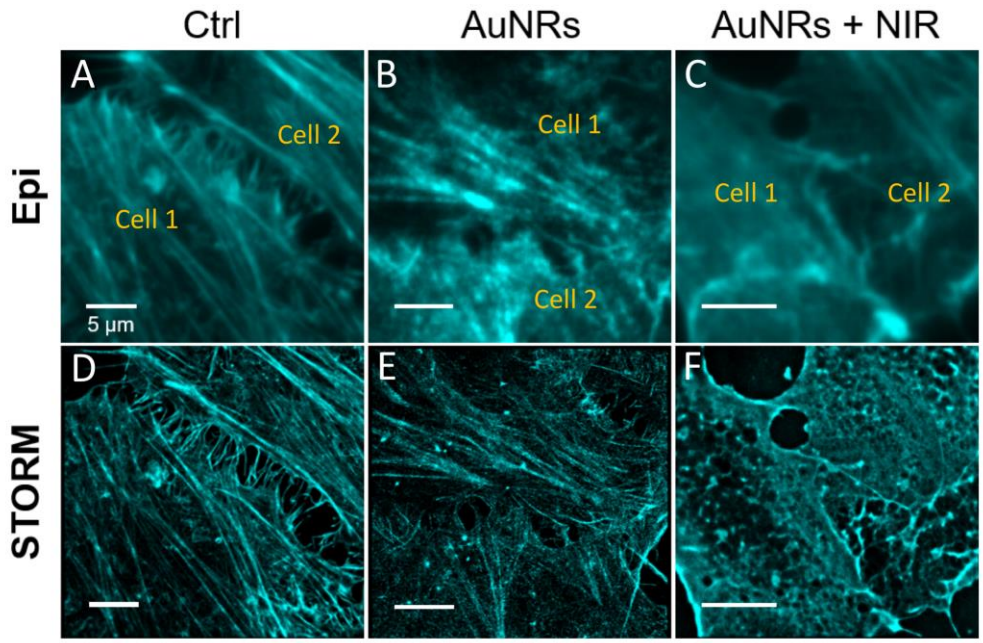

FIGURE 4.23. STORM and epifluorescence images of actin filaments in the cell-cell junction upon different treatments: (A, D) Control; (B, E) AuNRs; (C, F) AuNRs + NIR. After NIR exposure, the actin filaments at cell junctions exhibited clearly altered morphology (scale bar = 5 μm).

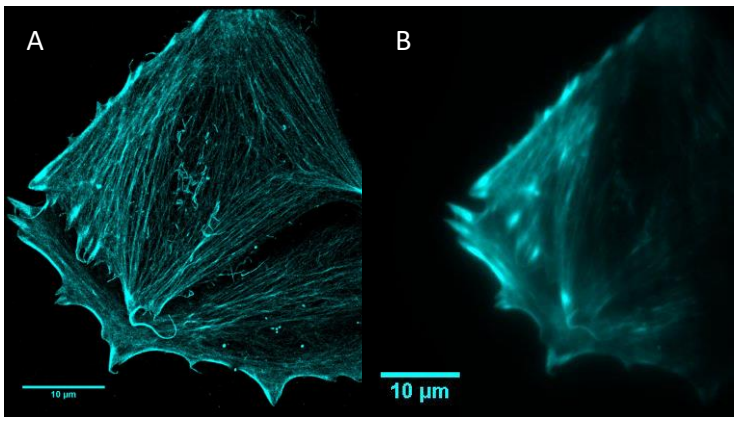

FIGURE 4.24. Comparison of the resolution of STORM (A) and conventional fluorescence microscopy imaging (B) for actin filaments.

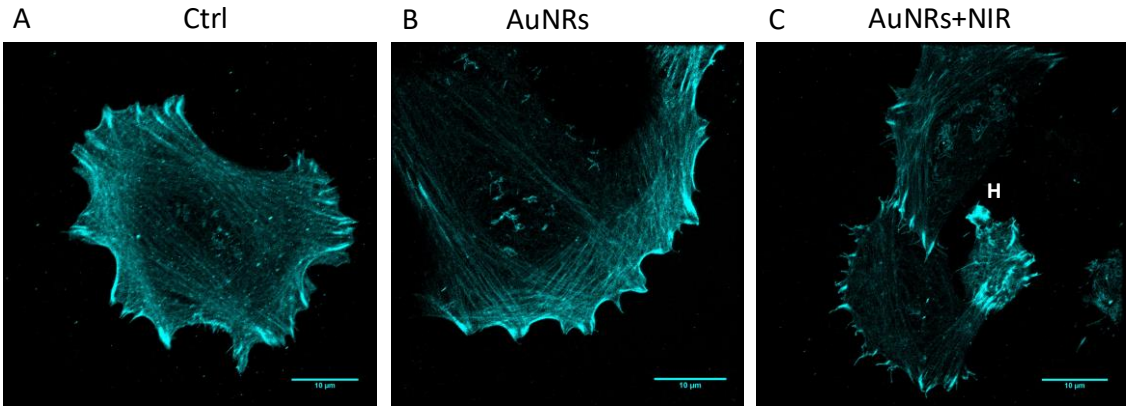

FIGURE 4.25. STORM images of actin filaments in individual HeLa cells.

We further examined the AuNRs and PPTT effects on cell junctions in faster-migrating HeLa cells and slower-migrating MCF-7 cells. Different cell lines could have highly diverse populations of cell junction proteins. The expression level of neural (N)-cadherin in HeLa was found to be much higher than that in the MCF-7 cells[391] (not detectable in MCF-7 cells in our study). On the other hand, MCF-7 cells show significantly higher expression levels of tight junction proteins than HeLa cells (**Figure 4.26**). Therefore, we used HeLa cells as a model for studying the N-cadherin junction and MCF-7 cells for the tight junction.

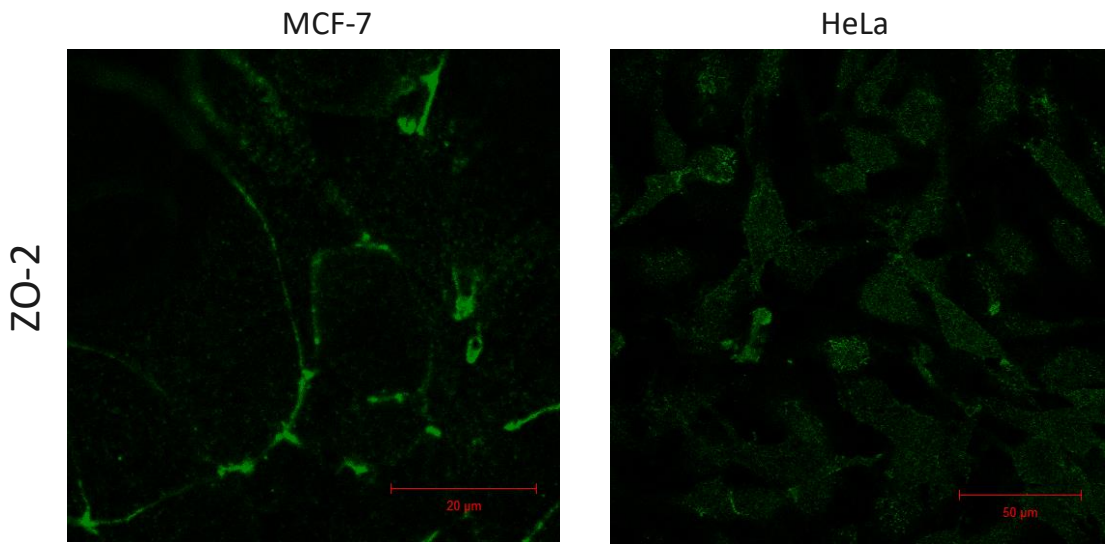

Figure 4.26. Low expression of tight junctions in HeLa cells compared with MCF-7 cells.

The N-cadherin junction is well known to be highly expressed in many aggressive tumors and promote metastasis[392]. It is reported that N-cadherin holds the cohesive cell clusters together, which tend to migrate persistently[393], a key role in collective migration [393, 394]. The expression level of N-cadherin junction is largely known as a marker for cancer motility and invasiveness. We observed a decreased expression level of N-cadherin (**Figure 4.27 A-E and 4.28)** upon the AuNRs treatments by fluorescence intensity and Western blot analysis.

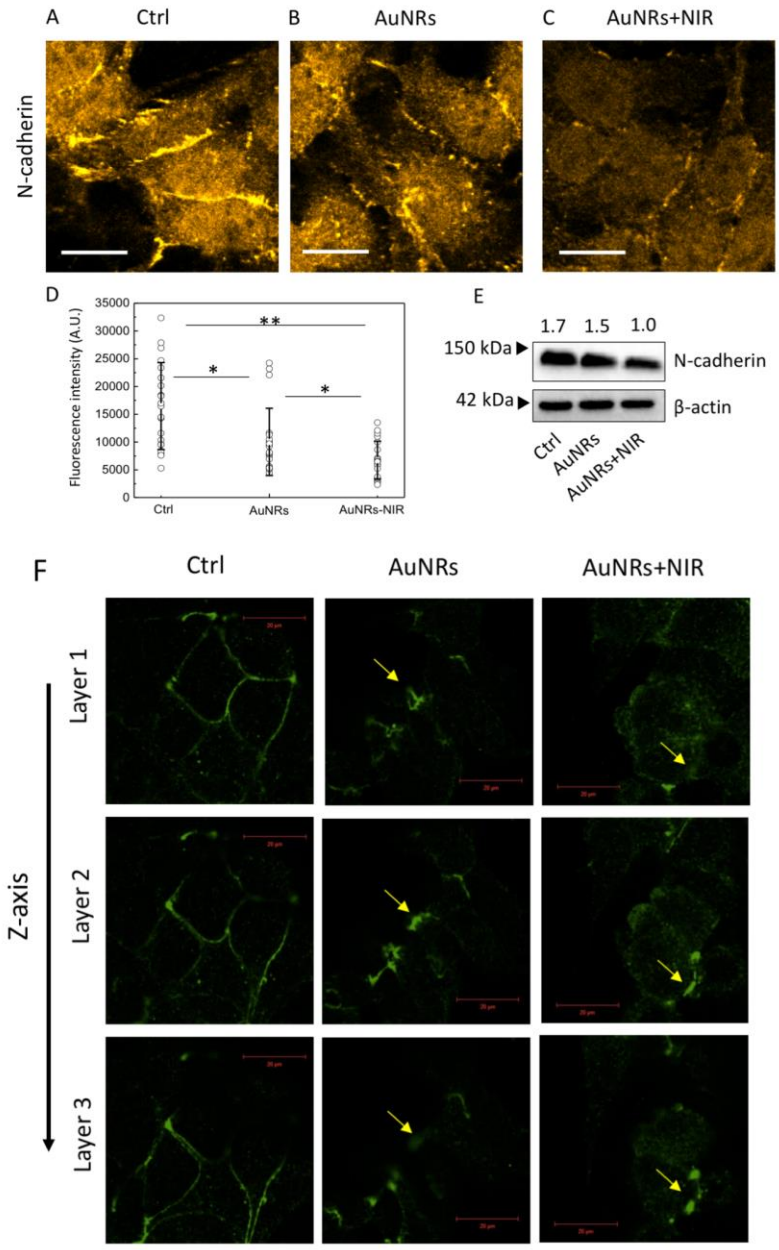

FIGURE 4.27. (A-C) Immunofluorescence images of N-cadherin in HeLa cells before (A) and after AuNRs (B) and AuNRs+PPTT (C) treatments (more images in Figure S14). The fluorescence intensities in these images are normalized together. (D) The fluorescence quantification of the N-cadherin (n=20 cells, ±SEM). (E) Western blot results also indicate a decreased expression level of N-cadherin after treatments. (F) Immunofluorescence images of tight junction protein ZO-2 in MCF-7 cells, before and after AuNRs or AuNRs+PPTT treatments. The morphology of ZO-2 change from a normal and continuous line-like structure in the control group to a

discontinuous dot-like structure after treatments. The figures showed 3D scanning of ZO-2, where Layer 1 is close to the bottom of the cells, and Layer 3 is close to the top of the cells. Scale bar = 20 μm.

Tight junctions create strong intercellular links [395] at the invasion zone of tumors [367]. During tumor development, tight junctions are remodeled, enabling cancer cells to adopt a migratory behavior [396]. It has been reported that tight junction protein Zonula occludens ZO-1 can directly bind to integrin and regulate the mechanical properties of integrin-fibronectin links[397]. In addition, the tight junction proteins ZO-1, ZO-2 and ZO-3 can bind to the cytoskeleton[398]. Here, we studied the tight junction changes by labeling ZO-2. We observed the morphology of ZO-2 change from a normal and continuous line-like structure in the control group to a discontinuous dot-like structure after treatment, indicating possible impaired tight junctions (**Figure 4.27 F**). If only treated with same dose of NIR light (no AuNRs added), no changes in the actin filaments, N-cadherins, and ZO-2 were observed (**Figure 4.29**).

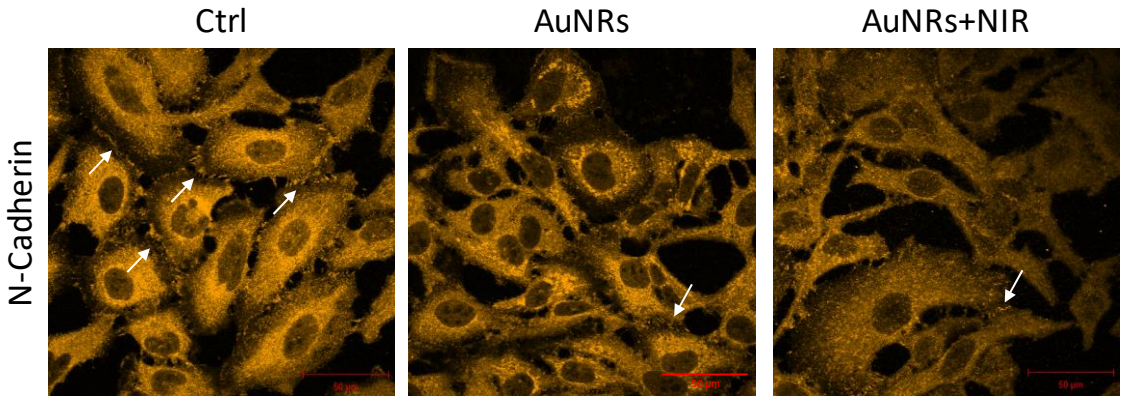

FIGURE 4.28. Immunofluorescence images of N-cadherin in HeLa cells before and after AuNRs or AuNRs/PPTT treatments. The arrows indicate the N-cadherin junctions.

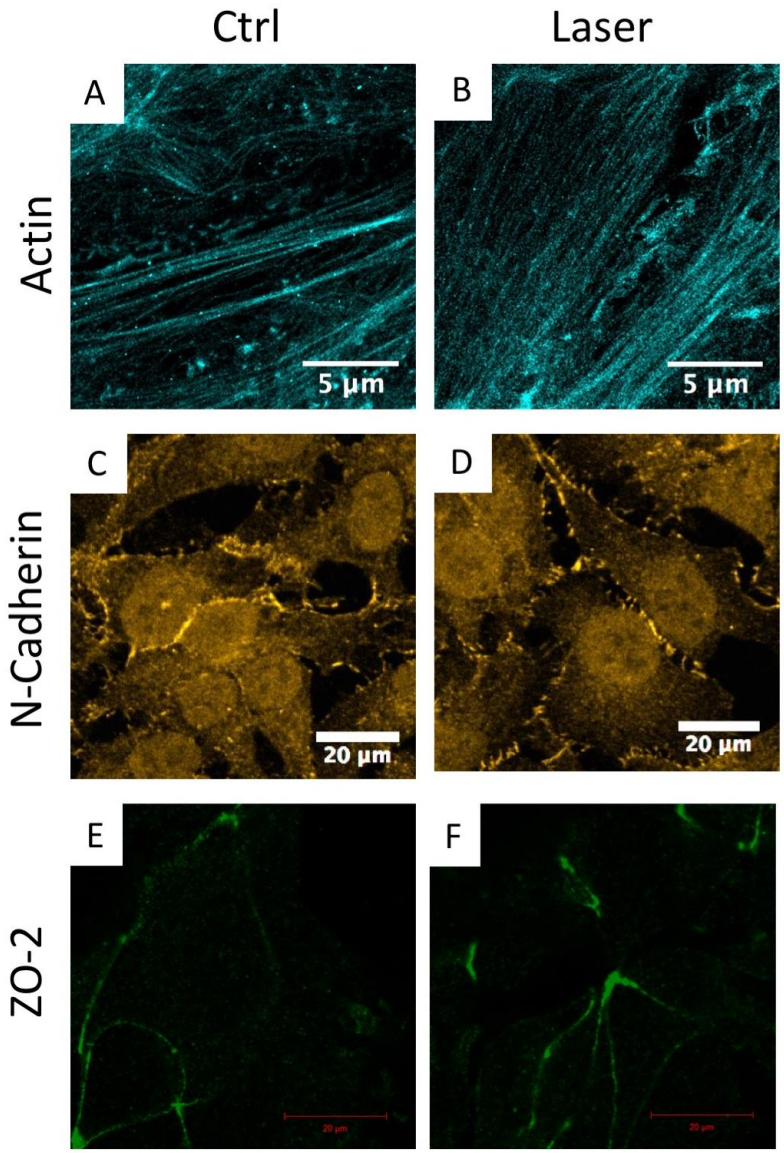

FIGURE 4.29. STORM images of actin filaments in the cell-cell junction for control (A) and laser control (no AuNRs) (B). Scale bar = 5 μm. Immunofluorescence images of N-cadherin in HeLa cells for control (C) and laser control (no AuNRs) (D). Scale bar = 20 μm. Immunofluorescence images of tight junction protein ZO-2 in MCF-7 cells, for control (E) and laser control (no AuNRs) (F). Scale bar = 20 μm.

This study differs from the previous works mainly in the following points: 1) Early signaling (30 min) was studied upon AuNRs and mild PPTT treatments using phosphoproteomics, while most of other work studied longer time scale, such as overnight or after several days [399]. 2) The alterations of cell junction were reported here,

while our previous work was focused on the cytoskeleton proteins after 24 h AuNRs and/or PPTT treatments [10]. 3) In addition, super-resolution imaging technique (STORM) revealed more detailed structural information on the effects of our treatment.

We have previously studied the PPTT for triggering apoptosis[9, 40]. However, due to several reasons (such as the inhomogeneous distribution of AuNRs or the laser penetration ability), some locations within tumor might not generate apoptosis. In addition, it is possible for some cancer cells to develop thermal tolerance[223]. For those cells that not able to receive enough dose or resistant to the treatment to cause apoptosis, their ability towards metastasis could decrease upon treatment.

Collective migration is widely observed in metastasis *in vivo* [400]. The relationship of cell mechanical properties (cell junction and adhesion, actomyosin contractility, geometry confinement, *etc*.) and cell collective migration *in vivo* has been reported previously [369, 401]. For instance, it has been reported that lipoma preferred partner (LPP), an actin-binding protein that could degrade N-cadherin in lung cancer, could inhibit collective cell migration during lung metastasis in mice model [402]. Regarding our treatment, future studies on metastatic mice models will be performed.

As metastasis is a highly complex process, multiple factors, such as cytoskeleton, adhesion, extracellular matrix (ECM), tumor microenvironment, blood or lymphatic vessels, *etc.*, will need to be considered for a comprehensive understanding of AuNRs-PPTT in inhibiting metastasis. Zhang *et al*. have shown that photodynamic therapy (using liposome with porphyrin-18) can greatly disturb the ECM, therefore decrease the attachment of the cells with the ECM and affect the actomyosin contractility[403]. It will

be interesting to look into how AuNRs and PPTT affect ECM, tumor microenvironment, blood or lymphatic vessels in future studies.

1.13.3 Methods.

Experimental design. The experiment is based our hypothesized that integrin-targeting AuNRs and PPTT treatment could affect the cytoskeleton and cell junctions, thus result in the inhibition of cancer cell collective migration. To test this hypothesis, phosphoproteomics was performed to understand the signal transduction among the integrin, cytoskeleton and cell junctions. Super-resolution imaging tools, as well as Western blot, were used to observe the changes of the actin cytoskeleton and cell junctions.

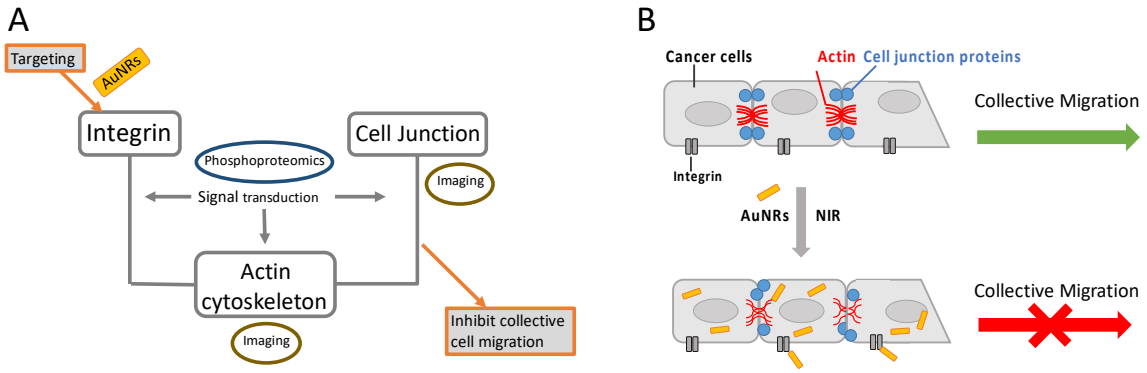

FIGURE 4.30. Experimental design (A) and proposed mechanism (B) of AuNRs and PPTT in inhibiting cancer collective migration. Targeting integrin could affect the actin cytoskeleton and cell junctions to result in the inhibition of cancer cell collective migration. Phosphoproteomics and super-resolution fluorescence imaging, as well as Western blot, were the main experimental tools used in the current study.

Materials. Dulbecco's modified Eagle's medium (DMEM), phosphate buffered saline (PBS), fetal bovine serum (FBS), antibiotic/antimycotic solution, and 0.25% trypsin/2.2 mM EDTA solution were purchased from VWR. Methoxypolyethylene

glycol-thiol (mPEG-SH, MW 5000) was purchased from Laysan Bio, Inc. Cell penetrating peptide RGD (RGDRGDRGDRGDPGC) was purchased from GenScript, Inc. Mammalian cell protease inhibitors and phosphatase inhibitors were purchased from Roche Applied Sciences, and sequencing grade trypsin was purchased from Promega. Tetrachloroauric acid trihydrate ($HAuCl_4.3H_2O$), ascorbic acid, cetyltrimethylammonium bromide (CTAB), $AgNO_3$, $NaBH_4$, 4-(2- hydroxyethyl)-1-piperazineethanesulfonic acid (HEPES), NaCl, sodium deoxycholate, sodium dodecyl sulfate (SDS), paraformaldehyde, glutaraldehyde, formaldehyde-D2 (DCDO), sodium cyanoborohydride ($NaBH_3CN$), formic acid (FA), trypsin (TPCK treated), iodoacetamide (IAA), dithiothreitol (DTT), trifluoroacetic acid (TFA) and triethylammonium bicarbonate buffer (TEAB), Triton X-100, 2-(N-Morpholino)ethanesulfonic acid hemisodium salt (MES), NaCl, EGTA, glucose, $MgCl_2$, $NaBH_4$, BSA, Anti-BAX and anti-beta-actin primary antibody, (H+L) HRP conjugate, Alexa 647-phalloidin, 100 mM Tris pH 8.0, glucose oxidase, catalase, β-mercaptoethanol were purchased from Sigma (St. Louis, MO). Urea were from Shanghai Sangon Biotech (Shanghai, China). BCA protein assay kit was from Beyotime Institute of Biotechnology (Shanghai, China). HPLC-grade acetonitrile (ACN) was from Merck (Darmstadt, Germany). Fused silica capillaries with dimensions of 75 and 200 μm i.d. were obtained from Yongnian Optical Fiber Factory (Hebei, China). C18 AQ beads (3 and 5 μm, 120 Å) were purchased from Daiso (Osaka, Japan). Anti-ZO-2 (Cell Signaling Technology) and Anti-N-Cadherin (ABclonal) Alexa Fluor-568 conjugated anti-rabbit IgG (H+L) (Abcam), goat anti-rabbit IgG Antibody. All the water used in experiments was purified with a Milli-Q system from Millipore (Milford, MA).

Instrumentation. AuNRs were imaged using a JEOL 100CX-2 transmission electron microscope (TEM) microscope, with their average size being measured by ImageJ software (NIH). UV−vis spectra were obtained by an Ocean Optics HR4000CG UV-NIR spectrometer. A Nikon Eclipse 80i upright microscope and a back-illuminated scientific complementary metal oxide semiconductor (sCOMS) camera (Dhyana 400BSI, Tucsen) were used to record high magnification (up to 200 ×) differential interference contrast (DIC) images. Phosphoproteomics analysis was performed on a hybrid dual-cell quadrupole linear ion trap − Orbitrap mass spectrometer LTQ Orbitrap Elite (Thermo Fisher) with XCalibur 3.0.63 software. An 808 nm cw laser (0.7 W/cm^2) was used for PPTT. STORM imaging was conducted on modified Zeiss Axiovert 100 TV microscope equipping with a high sensitive back-illuminated sCOMS camera (Dhyana 95, Tucsen).

Synthesis, Conjugation and Characterization of AuNRs. AuNRs with an average size of 25 × 6 nm (length × width) were synthesized using a seedless growth method according to our previous reports [10, 228]. Briefly, 5 ml of 1.0 mM $HAuCl_4$ was added to a solution of 5 mL of 0.2 M cetyltrimethylammonium bromide (CTAB), 250 μL of 4.0 mM $AgNO_3$, and 8 μL of 37% HCl. Then, 70 μL of 78.8 mM ascorbic acid was added, followed by immediate injection of 15 μL of 0.01M of ice-cold $NaBH_4$. The solution was left undisturbed for 12 hours. To remove extra cytotoxic CTAB, the AuNRs were centrifuged at 21000 g for 1 hour and dispersed in DI water, followed by a second centrifugation at 19000 g for 40 min. The sizes and homogeneity of the AuNRs were measured by TEM. AuNRs were then conjugated with surface ligands PEG and RGD. For first-step preparation of AuNRs@PEG, mPEG-SH (1 mM in H_2O) was added to the nanoparticles overnight to achieve about 1000 ligands per AuNR. Then, RGD (1 mM)

was added to achieve 10000 molar excess per AuNR. The solution was allowed to shake overnight at room temperature. Excess of ligands were removed by centrifugation. UV-vis spectrometer and zetasizer were used to test the successful conjugation of the ligands.

Cell Culture, AuNRs Treatments, and PPTT. HeLa and MCF-7 cells were grown in Dulbecco's modified Eagles' medium DMEM containing 10% (v/v) fetal bovine serum and 1% antibiotic solution at 37 ^{o}C in a humidified incubator under 5% CO_2. Cells were cultured for 24 hours followed by incubation with AuNRs (5 nM) for 24 hours. Then, a cw 808 nm laser (0.75 W/cm^2) was applied to the cells for 2 minute. The temperature range of the photothermal effect mediated by AuNRs is 42 ±1 ^{o}C.

Toxicity and uptake of AuNRs to Cancer Cells. In order to examine the nanoparticle cytotoxicity in cells, XTT assay was performed. The uptake of AuNRs to HeLa and MCF-7 cells was visualized under a DIC microscope. Plasmonic AuNRs can be easily discerned from the cellular features as they appeared with high DIC contrast at/near SPR wavelength.

Measuring Cell Migration Speed upon AuNRs Treatment. The 2D scratch assay was performed according to previous report [291]. For measuring cell migration rate, a scratch assay will be used where cells will be cultured in a 6 well plate to form a confluent monolayer. A p200 pipet tip will be used to scrape the cell monolayer in a straight line to create an empty gap. Then the cells will be allowed for migration into the gap and imaged to track their migration rates. The cells were imaged on an inverted Nikon Eclipse Ti-E microscope using bright field microscopy. A Nikon Plan Fluor 10 × objective (Numerical aperture: 0.30, working distance: 16.0 mm) and a 12 V/100 W

halogen lamp as light source was used. The output power of the light source was kept constant for all the imaging experiments and the exposure time of 30 ms was used to provide optimal contrast and brightness. Images were then recorded by a sCOMS camera (Dhyana 400BSI, Tucsen).

Super-resolution imaging setup: The STORM imaging system was integrated into an inverted microscope (Zeiss Axiovert 100 TV, Jena, Germany). 405 nm and 660 nm lasers (Newport Excelsior one 405 nm, 200 mW, Irvine, CA; Laser Quantum Gem 660, 200 mW, Stockport, Cheshire, England) were collimated into a single light path after the beam expander (Thorlabs BE03M-A, Newton, NJ) with 3 × magnification. Collimation of multicolor lasers was done by using a dichroic mirror (Thorlabs, DMLP425T), thus allowing simultaneous illumination of the sample at multi-wavelengths. Uniblitz mechanical shutters (Vincent Associates, LS2Z2, Rochester, NY) in front of each laser were used to control the illumination conditions, either pulsed or continuous illumination profiles. The collimated light was expanded by a telescope of a pair of achromatic lenses (Thorlabs, AC127–025-A & AC254–150-A) and then focused at the back focal plane of a high refractive index oil immersion objective (Olympus, 60X Oil, N.A. 1.49) using another achromatic lens (Thorlabs, AC508–300-A). The incident angle of illumination light is controlled by the lateral shift of the light path, through a three-dimensional stage (Sigma KOKI, SGSP-20-20, Tokyo, Japan), before entering the objective. A multi-edge beam splitter (Semrock, DC-405-388-543-635, Rochester, NY) was used to reflect the light into the working objective to excite the sample. The emission light is collected by the same objective. After the tube lens, provided with the microscope, a pair of relay lenses (Thorlabs, AC127–125-A & AC127–150-A) was used to focus

emission light onto an sCMOS chip (Tucsen, Dhyana 95) enabling a pixel size of ~110 nm. A combination of filters (Semrock, 664 nm RazorEdge long-pass edge filter (LP02-664RU-25), 658 nm StopLine single-notch filter (NF03-658E-25), 708/75 nm BrightLine single-band bandpass filter (FF01-708/75-25)) were inserted in front of the camera to reduce the background noise. Both epi-fluorescence images and STORM images were performed using the customized system.

Briefly, cells were cultured in an 8-well glass chamber (ibidi) and washed once with pre-warmed PBS buffer (Invitrogen). Cells were then fixed and permeabilized with 0.3% glutaraldehyde (Sigma) and 0.25% Triton X-100 (Sigma) in a cytoskeleton buffer containing 10 mM MES pH 6.1 (Sigma), 150 mM NaCl (Sigma), 5 mM EGTA (Sigma), 5 mM glucose (Sigma), and 5 mM $MgCl_2$ (Sigma). Freshly prepared 0.1% $NaBH_4$ (Sigma) in a PBS buffer was used to reduce the autofluorescence background generated during the cell fixation. The cells were then washed with a PBS buffer three times followed by applying a blocking buffer (3% BSA (Sigma) + 0.2% Triton-X100 in PBS buffer) for 60 min. The cells were first incubated with beta-catenin primary antibody in blocking buffer over 1 h, washed three times with PBS buffer, incubated in Alexa Fluor-568 conjugated goat anti-mouse IgG (H+L) (Invitrogen) at 2 μg mL^{-1} in blocking buffer over 60 min and washed three times with PBS buffer again. To label the actin, cells were stained with 0.5 μM Alexa 647-phalloidin (Invitrogen) in a PBS buffer, wrapped with aluminum foil to protect from light and incubated at 4^{o} C overnight. Remove the staining solution and briefly wash once with a PBS buffer. Immediately mount the sample for STORM imaging in an imaging buffer containing 100 mM Tris pH 8.0 (Invitrogen), 10

mM NaCl (Sigma), 0.5mg/mL glucose oxidase (Sigma), 40μg/mL catalase (Sigma), 10% (w/v) glucose (Sigma) and 1% (v/v) β-mercaptoethanol (Sigma) for STORM imaging.

STORM imaging data processing. In our experiments, an imaging sequence of 30,000–40,000 frames recorded at 60 Hz was used to reconstruct a high resolution STORM image. In each frame, individual molecules were identified and fit by an elliptical Gaussian function to determine their centroid positions, widths, intensities and ellipticities. Molecules that were too dim, too wide or too elliptical to yield high localization accuracy were eliminated in order to generate high resolution images. Furthermore, positions for those molecules that were appealing continuously in several imaging frames were determined using the weighted centroid positions in all consecutive frames. To generate the super-resolution images, molecular positions were assigned as one point and their sizes were rendered as a normalized 2D Gaussian distribution. The width of 2D rendered spot depends the localization accuracy calculated from the number of photons detected for that localization event. The reconstructed STORM images have a pixel size of 10 nm.

Sample Preparation for Phosphoproteomics Experiment. Cells were cultured in 100 mm dishes (Corning). The cells were then harvested for MS analysis, with a final confluence about 80-90%. After AuNRs treatment for 30 min, cells were washed twice with PBS before directly adding the lysis buffer (50 mM HEPES (pH =7.4), 150 mM NaCl, 0.1% SDC, 10 units/ mL benzonase, protease inhibitor cocktail and phosphatase inhibitors) to the cells followed by scraping and collecting the cell lysate on ice. Lysates were vortexed and sonicated on ice, followed by centrifugation at 18000 g for 20 min at 4

^{o}C to remove cell debris. The proteins in the supernatant were precipitated by adding 4 × excess volumes of ice-cold precipitation solvents (acetone: ethanol: acetic acid=50:50:0.1) and kept at -20 ^{o}C for overnight. The proteins were obtained after centrifugation, and were re-dissolved in 8 M urea and 50 mM HEPES (pH=8). The protein concentration was determined by Bradford assay. For mass spectrometry analysis, the disulfide bonds of proteins were firstly reduced by 1 mM dithiothreitol (DTT), followed by alkylation with 5.5 mM iodoacetamide. Then, trypsin (1:50 w/w) was used for protein digestion overnight [337].

Stable-isotope dimethyl labeling was performed according to previous reports [404]. Briefly, for light, intermediate and heavy dimethyl labeling, 4 μL of CH_2O (4%, v/v), CD_2O (4%, v/v) or $^{13}CD_2O$ (4%, v/v) was added into 100 μg cell protein digest, respectively. Then 4 μL of freshly prepared $NaBH_3CN$ (0.6 M), $NaBH_3CN$ (0.6 M), and $NaBD_3CN$ (0.6 M) was added. The mixtures were then incubated for 1 h at room temperature for labeling reaction. For quenching the reaction, 16 μL of ammonia (1%, v/v) and 8 μL formic acid (5% v/v) were successively added.

Phosphorylation enrichment was conducted according to previous reports by using Ti^{4+}-IMAC microspheres after dimethyl labeling [336]. Briefly, the microspheres were suspended in the sample loading buffer containing 80% (vol/vol) ACN and 6% (v/v) TFA, and mixed with protein digest with a ratio of 10:1 (w/w), followed by violent vibration for 30 min. After removing the supernatant by centrifugation, the microspheres were washed with washing buffer 1 (50% (v/v) ACN, 6% (v/v) TFA containing 200 mM NaCl) and washing buffer 2 (30% (v/v) ACN and 0.1% (v/v) TFA) for 20 min,

respectively. Finally, the phosphopeptides were eluted by adding 10% (v/v) ammonia-water and lyophilized to powder for following analysis.

RPLC-MS/MS Analysis for Quantitative Phosphoproteomics. LTQ-Orbitrap Elite (Thermo Scientific) coupled with Dionex UltiMate 3000 RSLCnano system (Thermo Scientific) was used for all proteomic analyses. The lyophilized phosphopeptide samples were re-dissolved in aqueous solution with 1% FA and loaded onto a 4 cm × 200 μm i.d. C18 trap column packed with C18 AQ beads (5 μm, 120 Å) and separated by a 50 cm × 75 μm i.d C18 (5 μm, 120 Å) capillary column kept in 50℃ with a flow rate 300 nL/min. Aqueous solution with 0.1% FA (solvent A) and 80% ACN with 0.1% FA (solvent B) were used for the reversed phase (RP) binary gradient separation, and the RP binary gradient was set as: from 0-3% solvent B in 3 min, from 3-30% solvent B in 135 min, from 30-45% solvent B in 15 min, from 45%-100% solvent B in 2 min, after flush with 100% solvent B for 11 min the whole system was equilibrated by using solvent A for 13 min. The MS full scan was acquired from m/z 350 to 1650 in an LTQ-Orbitrap Elite with a mass resolution of 60 000 at m/z 400, and the MS/MS scan was acquired in ion trap. All MS and MS/MS spectra were acquired in the data dependent analysis (DDA) mode, in which the 20 most intense ions in the MS scan were selected for MS/MS scan by collision induced dissociation (CID) with the normalized collision energy at 35%. The dynamic exclusion function was: repeat count 1, repeat duration 30 s, and exclusion duration 90 s.

Phosphoproteomics data processing. MS data were processed using MaxQuant (version 1.5.3.30, http://www.maxquant.org/) using Andromeda as search engine against

the Uniprot human protein database (69712 sequences, downloaded from http://www.uniprot.org/) with precursor mass tolerance of 4.5 ppm and fragment mass deviation of 0.5 Da. Variable modifications consisted of methionine oxidation, acetylation of protein N-term and phosphorylation (STY). Fixed modification contained cysteine carbamidomethylation. Trypsin was set as specific proteolytic enzyme. Peptides with a minimum of six amino acids and a maximum of two missed cleavages were allowed for the analysis. For peptide and protein identification, the false discovery rate (FDR) cutoffs were both set to 0.01. Triplets were selected as the quantification mode with the dimethyl Lys 0 and N-term 0 as light labels, dimethyl Lys 4 and N-term 4 as median labels and dimethyl Lys 8 and N-term 8 as heavy labels. All other parameters are the default setting in MaxQuant.

Bioinformatics analysis. Bioinformatics analysis of phosphoproteomics study was performed. Three biological replications for each condition (control, AuNRs@RGD, AuNRs@RGD+NIR) in MCF7 and HeLa cells were conducted. Raw data from phosphoproteomics was normalized using supervised normalization of the microarray (SNM) [405]. In the SNM procedure, variance due to biological replicates was adjusted by setting them as variables in the model. Variance explained by different experimental treatments (control, AuNRs@RGD, and AuNRs@RGD+NIR) was fitted as a biological variable in the model. Hierarchical clustering was done with statistical software R. Phosphoproteomics data were log2-transformed before analysis of variance (ANOVA), which was used to detect differential phosphorylated proteins between two treatment groups (e.g., AuNRs@RGD vs. AuNRs@RGD+NIR), with treatment conditions set as fixed effects. P value threshold at 0.1 was set to select differential phosphorylated

proteins. The proteins identified as being affected were subjected to pathway analysis using the MetaCore pathway analysis software ("MetaCore from Thomson Reuters").

Western-blot Analysis. Cells were lysed in RIPA buffer (20 mM Tris pH 7.4, 150 mM NaCl, 2 mM EDTA, 2 mM EGTA, 0.1% sodium deoxycholate, 1% Triton X-100, 0.1% SDS) supplemented with protease inhibitors (Sigma-Aldrich) and phosphatase inhibitors (25 mM sodium fluoride, 10 mM sodium pyrophosphate, 50 mM β-glycerophosphate, 1 mM sodium orthovanadate). Protein concentrations were measured by BCA assay (Pierce), and equal amounts of protein were loaded on a SDS-PAGE gel. After SDS-PAGE, the resulting gels were transferred to PVDF membranes (Millipore) by Bio-Rad trans blot turbo (Bio-Rad). Afterwards, the membranes were treated with blocking buffer (5% BSA in TBS (20 mM Tris, 150 mM NaCl)). The primary antibodies p120 catenin (pS268), GSK3 (pY216), N-Cadherin, and BAX were incubated with the membranes for different sets of experiments overnight in 4° C with shaking, followed by adding the secondary antibodies (Goat Anti-Rabbit IgG Antibody, (H+L) HRP conjugate, purchased from Millipore Sigma). Blots were washed three times for 10 m in TBS after primary and secondary antibodies.

Immunofluorescence Labeling and Confocal Microscopy. Cells were cultured on 8 well μ-Slide with glass bottom (Ibidi). After treatment, cells were fixed in 3% Paraformaldehyde/0.1% Glutaraldehyde for 7 min at room temperature, followed by treated with 0.1 % (m/v) $NaBH_4$ for 7 min and the wash three times with PBS. Cells were then blocked with 3% (w/v) BSA and 0.5% (v/v) Triton-X100 in PBS for 30 minutes at room temperature with mild shaking. Primary antibody was diluted to a working concentration in a blocking solution, and incubated at 4 ^{o}C overnight. After three times

washing with PBS, secondary antibody (Goat Anti-Rabbit IgG H&L (Alexa Fluor® 568) from abcam) was added for 1 h, followed by wash 3 X with PBS before mounting with Prolong Gold (Invitrogen). Images were taken with a Zeiss LSM 700–405 confocal microscopes.

Statistical information. For the other experiments in this study if not mentioned, two-tailed t-tests were performed and the differences between data sets were considered significant when $P < 0.05$.

1.13.4 Conclusion.

In this study, we investigated the mechanism of integrin-targeted AuNRs and PPTT in inhibiting collective cancer cell migration. Our phosphoproteomics results revealed the phosphorylation changes to many cytoskeletal and cell junction proteins, setting the foundation for current and future studies of the underlying mechanism at the molecular level. Using super-resolution fluorescence microscopy and Western blotting, we verified the changes to *selected* key proteins related to the actin cytoskeleton and cell junctions. The morphological changes of actin filaments and extensive phosphorylation changes to actin-associated proteins, such as filamin, paxillin, vinculin, zyxin, PAK, MLCP, MyHC, *et al*., upon integrin-targeted AuNRs and PPTT treatment also indicated weakened cell adhesion and stress fiber generation. Furthermore, in HeLa cells, we found a significantly lower expression level of N-cadherin, as well as the phosphorylation changes to α-, β- and p120-catenin that connect N-cadherin to the actin cytoskeleton, while in MCF-7 cells, a discontinuation and altered morphology of the tight junction protein ZO-2. All of the current experimental evidence has led to a proposed mechanism that the interactions between the integrin-targeted AuNRs and cells could trigger the phosphorylation changes of essential components associated with cytoskeleton filaments and cell-cell junctions, and cause their morphological or expression level changes, therefore inhibiting cancer collective migration. Further studies of the perturbations to individual related proteins will be carried out to provide a more complete understanding of the inhibition effect.

GOLD NANOPARTICLES AND PLASMONIC PHOTOTHERMAL EFFECT ON ANIMALS IN INHIBITING METASTASIS

After studying the AuNPs impact *in viro* (on cells) in Chapter 3 and 4, the purpose of Chapter 5 is to check the feasibility of applying the AuNPs treatments on animals for inhibiting cancer metastasis. We have applied the AuNRs based photothermal therapy on animals (dogs and cats with spontaneous breast cancer), and observed that the treatments could significantly affect blood vessels inside the tumor, which might lead to decrease of cancer metastasis. In addition, our proteomics study on cat tumor samples showed a broad regulation of cytoskeleton and cell adhesion proteins, indicating an impeded function in cancer metastasis.

1.14 Gold Nanorod-assisted Photothermal Therapy Decreases Bleeding During Breast Cancer Surgery on Dogs and Cats

Summary. Cancer is the second leading cause of death in the world. Gold nanorods-assisted plasmonic photothermal therapy (AuNRs-PPTT) is a potentially more effective and efficient alternative to replace traditional surgery for localized tumors in which AuNRs absorb near-infrared (NIR) light and convert to heat in order to destruct cancer cells. However, for large tumors (volume $\geq$ 20 cm^3), PPTT could be ineffective due to an uneven distribution of injected AuNRs, which might cause possible inhomogeneity of the heat distribution inside the tumor. However, surgery is frequently recommended for removing large tumors with a high risk of cancer recurrence and metastasis. Here, we applied PPTT before surgery, which showed improved treatment for large tumors. We divided the animals (2 cats and 6 dogs with 21 tumors total) into two

different groups: Group I (control group), where three cases were solely treated with surgery, laser, or AuNRs alone; and Group II, where animals were treated with PPTT (AuNRs and Laser together) before surgery. The animals were monitored for 1-2 years after treatments. Group I had recurrence and metastasis, and all the patients died within a few months. In Group II, 4 out of the 5 cases had tumor recession without any recurrence or metastasis. Interestingly, we observed that applying PPTT before surgery did not show any bleeding during tumor removal in all cases. Our histopathology results supported this observation with the presence of altered blood vessels after PPTT. In conclusion, our study showed that applying AuNRs-PPTT before tumor excision could significantly affect blood vessels inside the tumor, leading to a decreased amount of bleeding during surgery. In summary, our study suggests that the presence of AuNRs-PPTT before surgery potentially avoids the risk of blood loss during surgery, proving it to be beneficial for use prior to any surgical operation.

1.14.1 Introduction.

Gold nanorods (AuNRs)-based plasmonic photothermal therapy (PPTT) is a cancer therapy in which AuNRs are injected into the tumor before exposure to the near-infrared (NIR) light[20, 406]. The NIR light capable of deeply penetrating the tissue is transiently applied to the tumor, producing localized heat that could lead to tumor necrosis and apoptosis[407]. PPTT modulation to induce cell apoptosis might be a more favorable way than necrosis, as during necrosis, the broken plasma membrane leads to the leaking of cytoplasmic components and inflammation, which could further induce cancer growth and metastasis [9, 223, 408]. The high efficiency of PPTT in getting rid of cancer cells by inducing apoptosis has been demonstrated *in vitro* and *in vivo*[40, 407]. We

have shown the efficacy of this treatment in tumor-bearing mice [40, 409] and recently demonstrated the treatment of mammary carcinoma in dogs and cats, where the malignant mammary tumors of volume ≤20 cm^3 could be treated by intratumor inoculation of AuNRs, followed by PPTT[9]. During these studies, we observed that animals with induced or spontaneous tumors have noteworthy regression without recurrence nor metastasis. Our recent studies also shown the ability of gold nanorod-assisted plasmonic photothermal therapy (AuNRs-PPTT) *in vitro* to inhibit cancer cell migration[10, 410]. In addition, the toxicity of this treatment has been examined in mice, dogs, and cats, which indicates that there is no toxicity effect on the animals for a long period[9, 40]. Therefore, PPTT is believed to be a favorable alternative for treating solid tumors with relatively small sizes and preventing metastasis[44].

For large tumors (volume ≥20 cm^3), PPTT could be hard to achieve due to an uneven distribution of injected AuNRs that causes inhomogeneity of the heat in the tumor. In these cases, surgery is usually recommended to remove primary solid tumors. However, the surgical resection of primary breast tumors commonly has a risk for metastatic recurrence[411]. It has been recognized that the tumors contain large amounts of blood vessels that provide nutrients to support tumor growth[412]. Blood vessels are also critical for metastasis as extensive and highly permeable blood vessels provide ways for cancer cells to exit primary tumor sites and go to the blood stream. Surgery usually disrupts the blood and lymphatic vessels, releasing cancer cells in the vasculature that, in turn, promotes the process of metastasis[413]. Therefore, the development of novel therapies that aid in the surgical process to prevent blood loss, tumor recurrences, and metastasis are of great importance.

In this study, we are focusing on introducing a new treatment regime featuring the combination of PPTT and surgery in dogs and cats with large tumors as well as examining the efficacy of this new regime. Interestingly, we observed that applying AuNRs-PPTT before surgery could significantly decrease the bleeding, which could potentially avoid the risk of metastasis caused by surgery.

1.14.2 Methods.

Synthesis and surface modification of AuNRs. AuNRs were prepared according to the seedless method [7]. Briefly, 5 mL of 1 mM $HAuCl_4$ (Sigma-Aldrich, St. Louis, MO, USA) were mixed with 5 mL of 0.20 M cetyltrimethylammonium bromide (CTAB; Sigma-Aldrich), followed by adding 250 μL of 4 mM $AgNO_3$ (Sigma-Aldrich) and adjusting the pH of the solution to be 1–1.15 by 37% HCl. Then, 70 μL of 78.8 mM ascorbic acid (Sigma-Aldrich) were added to the solution until the solution became clear. 15 μL of 0.01 M ice-cold $NaBH_4$ (Sigma-Aldrich) were injected into the growth solution immediately, and the solution was left unstirred for 6 hours. To remove the extra CTAB and prepare for surface modification, the AuNRs were centrifuged at 19,000 rcf for 1 h, and the pellet was redispersed in deionized water and centrifuged at 14,000 rcf for 15 minutes. The AuNRs were rinsed with water, then conjugated with different surface ligands (PEG and RGD). For surface modification, methoxy polyethylene glycol (PEG) thiol (m-PEG-Th, PEG; Laysan Bio, Arab, AL, USA) was added to AuNRs and stirred overnight to achieve a concentration of around 1000 PEG molecules per AuNR. For preparation of the AuNRs@RGD, the PEGylated nanoparticles (1 nM) were treated with RGD (1 mM) to achieve 10,000 ligands on each AuNR. Afterwards, the solution was

kept for overnight to be shaken at normal temperature, and the extra ligands were removed by centrifugation. UV-vis spectrometer was used to confirm the conjugation.

Characterization of AuNRs: A JEOL 100 CX transmission electron microscope (TEM) (JEOL Ltd., Tokyo, Japan) was used to measure the size and homogeneity of the samples. A Cary 500 UV–Vis Spectrometer (Agilent Technologies, Santa Clara, CA, USA) was used for measuring the absorbance of the AuNRs. To characterize the surface conjugation with PEG, a ZetaSizer 3000 HAS (Malvern Instruments, Worcestershire, UK) was used for measuring the surface Zeta potentials. In addition, Ellman's reagents (Sigma-Aldrich), which react with free -SH groups (calorimetrically measured at 412 nm), were used to quantify the number of PEG molecules bound to the surface of the AuNRs.

Animal diagnosis, and X-ray examination: All animals were handled in accordance with Association for Assessment and Accreditation of Laboratory Animal Care and Office of Laboratory Animal Welfare guidelines under the direction of the Institutional Animal Care and Use Committee (IACUC) at Cairo University. The pet animals were admitted to the Department of Surgery Clinic of the Faculty of Veterinary Medicine at Cairo University. All pets' owners claimed that their animals did not receive any treatment before their arrival at the university. Written informed consent was provided by the owners of the pets for the treatments. 8 female animals were treated in this study, including 2 canines and 6 felines, with a total of 21 tumors with varied grades (I to III). The tumor dimensions were measured using calipers. Histopathology tests were used to diagnose the tumors types/grades. At the tumor site, the animal's hair was shaved, and subsequently, radiographic recordings were taken with an X-ray machine (Fischer, Berlin, Germany). The radiographic setting factors were 58 to 70 kVp, 10 mAs, and a 90 cm

focal spot–film distance. The radiographic exposures were conducted dorsoventrally and right laterally. The blood loss was quantified by measuring the blood volume and weighing surgical sponges used for blood collection before and after the surgery.

General anesthesia was applied for animals during surgical mastectomy and postsurgical application of PPTT. Under general injectable anesthesia, each animal was pre-medicated with atropine sulphate (1%®, 0.05–0.1 mg/kg b.wt.; AdwiaCo. S.A.E., Egypt) and xylazine (Xyla-Ject 2%®, 1 mg/kg b.wt.; Adwia Co. S.A.E.), and then anesthesia was induced using ketamine HCl (Ketalar®, 10–15 mg/kg b.wt.; Sigma-Tec, Egypt) and maintained by ketamine HCl [414], [415].

Performing PPTT in animals: Each animal was subjected to three sessions of PPTT treatment in 2-week intervals using an 808 nm diode laser with a power of 0.5 W/cm^2 and a spot size of around 5.6 mm^2. An effective dose of AuNRs solution (7.5 nM AuNRs) for each 100 cm^3 was used for 2 minutes, and the amount used was scaled up based on the volume of the tumor and then injected directly into the tumor. Five minutes after injection, the entirety of the tumor was irradiated with the laser. The AuNRs concentration was decreased by 50% for each subsequent treatment. The temperature increase of a tumor during the laser irradiation was measured by placing a 33-gauge hypodermic thermocouple (OMEGA Engineering, Inc., Stamford, CT, USA) needle directly inside the tumor (42°C–44°C).

Histopathology evaluation of the animal tumors: The detailed pathologic evaluation of tumors was conducted by members of the pathology department of the Faculty of Veterinary Medicine at Cairo University. Histopathological analysis was

performed on 5 µm sections from tumor tissue that were fixed in 10% buffered formalin. The samples were stained with hematoxylin and eosin to assess pathology.

1.14.3 Results and Discussion.

1.14.3.1 Preparation and Characterization of AuNRs

AuNRs with an average size of 27±5 × 6 ±1 nm (length × width) were used in this study, as they showed enhanced efficacy of PPTT [416]. AuNRs were synthesized using our reported method [7], and these AuNRs are shown in the TEM image (**Figure 5.1 A**). AuNRs have a surface plasmon resonance wavelength of around 800 nm (**Figure 5.1 B**). After synthesis, AuNRs were successfully coated with mPEG-SH and RGD as evidenced by the red-shift of the surface plasmon peak (**Figure 5.1 B**). The average number of ligands on each particle is quantified to be 1,000 mPEG-SH and 10,000 RGD on each particle.

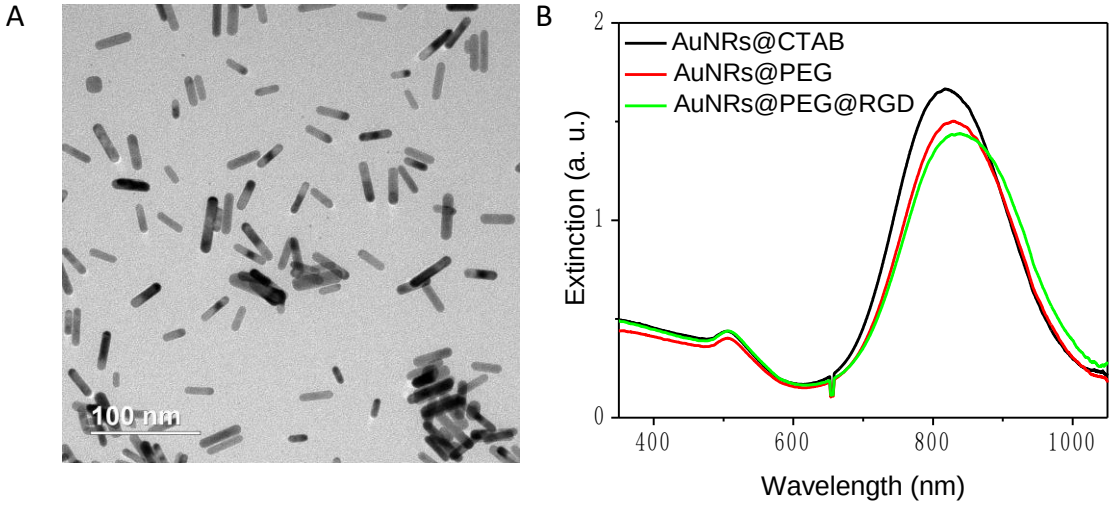

FIGURE 5.1. Characterization of Gold nanorods (Length 27±5, width 6±1 nm). (A) TEM image with 100 nm scale bar. (B) UV-Vis absorbance spectra showing the surface plasmon resonance peaks of AuNRs after synthesis (AuNRs@CTAB), then

after conjugation with PEG (AuNRs@PEG), then after conjugation with RGD (AuNRs@PEG@RGD).

1.14.3.2 PPTT Decreases Bleeding During Surgery

In our earlier studies, we optimized the PPTT conditions for treating dogs and cats, including the AuNRs dosage and the laser conditions (7.5 nM of AuNRs irradiated by NIR laser with 0.5 W/cm^2 intensity for 2 minutes). The optimized conditions were conducted multiple times (2 weeks apart) until complete regression *via* apoptosis was shown and that proved to be better than necrosis[9]. Herein, we devised a new treatment regime for treating animals with tumor volumes ≥20 cm^3 by combining surgery with PPTT.

Before treatment, all animal tumors showed variant growth, as shown in **Tables 5. 1& 5.2**. In control group (I), 3 cases with 10 tumors were solely treated by mastectomy, laser, or AuNRs treatment alone. As shown in **Figure 5.2 A and B**, photographic images of case 1 (GI-1) reveal 3 large tumors located at cranioabdominal and inguinal lymph nodes. All the three tumors connect to form one chain. **Figure 5.2 C** is a picture of tumor during surgery with obvious bleeding (over 100 gram). **Figure 5.2 D** is a histopathology of the tumor tissue showing ductal carcinoma in situ grade II.

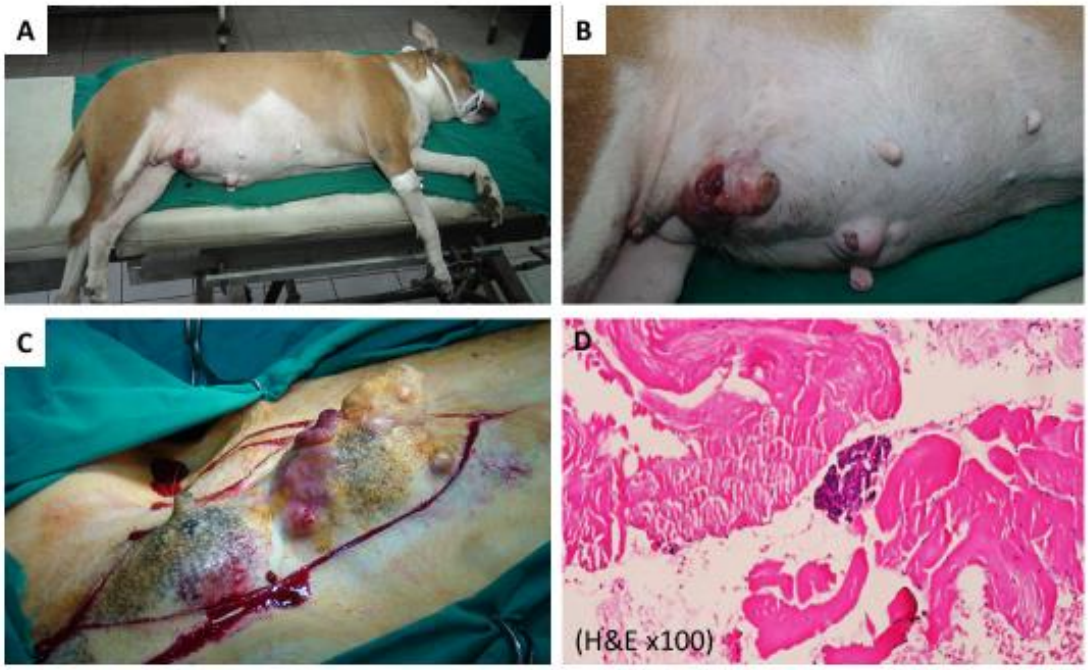

FIGURE 5.2. (A) Photographic image of control case 1 (GI-1) treated with surgery. (B) A magnified figure of A for the tumor area. C) Photo of case during surgery with high amount of bleeding. (D) Photo-micrograph of tumor tissue showing ductal carcinoma in situ grade II (H&E X100).

In Group (II), 5 cases with 11 tumors were treated with 3 sessions of PPTT (in 2 week intervals) and followed by surgery after the last PPTT session. **Figure 5.3 A and B** show case 1 (GI-1) that treated animals with surgery only, and **Figure 5.3 C and D** show one case with surgery after PPTT. Interestingly, we observed that when applying PPTT before surgery, almost no bleeding during the surgery was observed for any of the treated tumors in Group II when compared to Group I (**Figure 5.3A and C** and **Videos S1** (surgery only), **S2,** (surgery after PPTT)).

The decrease of the bleeding might be explained by the histopathology of the tumor bed vasculature (**Figure 5.3 B and D**). With surgery only, the blood vessels are normal and intact (**Figure 5.3 B**) while after PPTT, tumor bed vasculature shows swelling and sloughing of endothelial lining and destruction of blood vessel wall (H&E x400) (**Figure 5.3 D**).

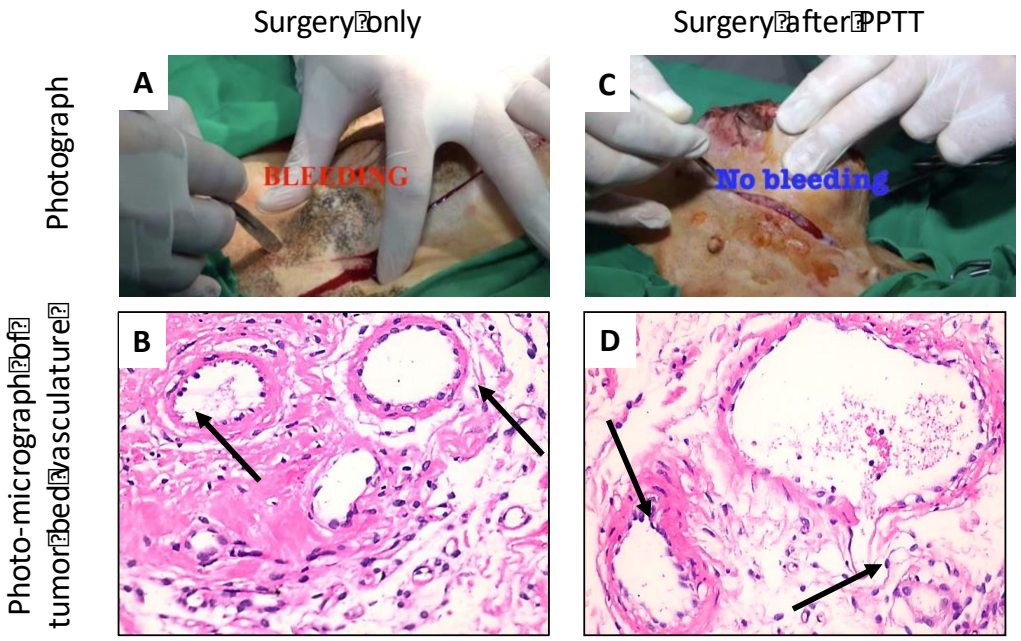

FIGURE 5.3. Left side (A, B) shows case 1 in GI (surgery only). Right side (C, D) shows one case in GII (treated with PPTT for three sessions (2-weeks intervals) before the surgery). (A and C) Photographic images taken from the videos (Movies S1 and S2), indicating decrease of bleeding after PPTT (C), compared with control (A). (B and D) Photo-micrograph of tumor bed vasculature showing (B) normal intact blood vessels with surgery only and (D) swelling and sloughing of endothelial lining and destruction of blood vessel wall (arrow) after PPTT (H&E X400).

In addition, the regime of PPTT before surgery has shown to be effective for achieving complete tumor recession shown in **Table 5.2.** For example, in one case from group 2, a 9-year-old mixed breed cat suffered from mammary neoplasms as shown in **Figure 5.4 A**. The site of 2 tumors located at her left axillary lymph node (black arrow) and left cranial thoracic (blue arrow) is demonstrated in **Figure 5.4 B**. After PPTT, followed by surgical excision of the tumors (**Figure 5.4 C**), tumor recession was achieved. The histopathology showed that after PPTT, well-developed granulation tissues were observed, indicating tumor recovery (**Figure 5.4 D**). After 12 months, this case showed complete recovery from the surgery (**Figure 5.4 E**) without evidence of recurrence or chest metastasis (**Figure 5.4 F**).

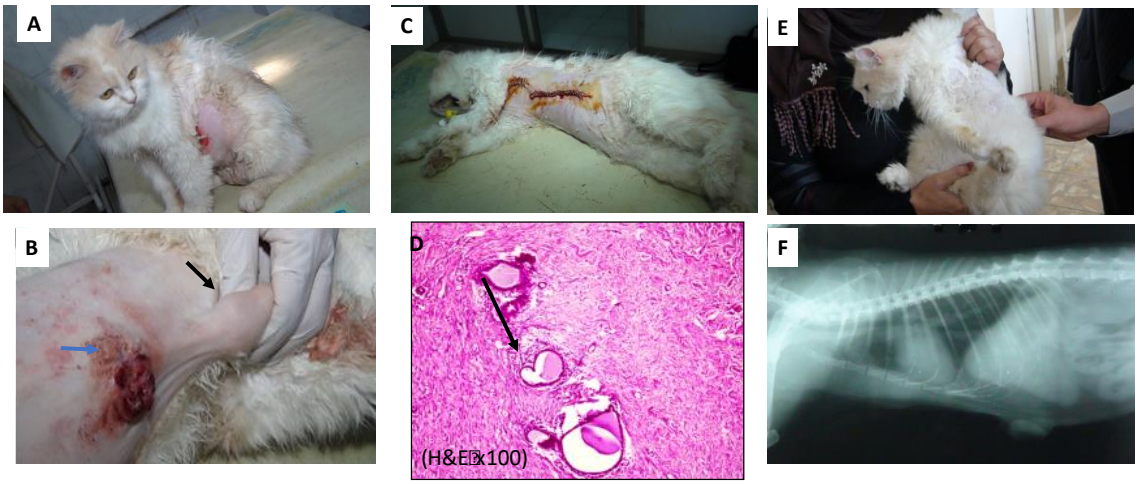

FIGURE 5.4. (A) A 9-year-old mixed breed cat suffered from mammary neoplasm. (B) the sites of tumors at left axillary lymph node (black arrow) and left cranial thoracic (blue arrow) (C) after surgical excision and (D) Subcutaneous layer showing well developed granulation tissue at the site of suture (arrow) (H&E x100). (E) the case after 12 months showed complete recovery from the surgery without any evidence of recurrence. (F) X-ray shows no metastasis in the chest.

Three cases among the five in Group II died a few months after PPTT and surgery treatment due to lung failure, but evidence of tumor reoccurrence or metastasis was not observed. Earlie, we have shown in our study on mice that there is no toxicity after 15 month of AuNRs injection, whose bio-distribution mainly locates at liver and spleen [40], proving that the lung failure might not related to PPTT. However, we do find that other types of nanoparticles, such as TiO_2, iron, Cr^{3+}-doped zinc gallate, silver, could accumulate in the lung and might cause toxicity [417], while AuNPs has better biocompatibility than these nanoparticles. To the best of our knowledge, there is no much systematic studies for discussing the blood circulating (not airborne) AuNRs and their relation with the lung failure so far.

In this report, we observed that PPTT has affected the tumor blood vessels that, in turn, decrease the blood flow inside tumor. The reason is still not fully understood.

Previous reports have shown that AuNPs could affect blood vessels and tumor angiogenesis [81, 418]. In addition, the temperature increase will cause the destruction of blood vessels. For instance, it has been reported that photothermal ablation of breast cancer in mice models using doxorubicin-loaded DNA-wrapped AuNRs could disturb the blood vessels [95]. Furthermore, It is reported that AuNPs with sizes around 30 nm could induce tumor endothelial leakiness [419]. The abnormal vascular nature of the tumor tissues allows them to uptake more AuNRs [420], which might explain why the AuNRs-PPTT is more effective on the tumor blood vessels. The importance of applying the AuNRs-PPTT before surgery could be very important in decreasing blood loss, especially for the patients who have injury-healing problems, including chronic diseases such as diabetes, and need tumor surgery.

Table 5.1. Animal groups, tumor clinical features, and therapeutic approaches

No. #	Case name	Species& age	Site of tumors	Size of tumors cm	Grade	Therapy
GI/1	1a	Dog Mixed Boxer 14 years	1-R caudoabdominal ulcerated	(8x5)	II	Only Mastectomy
	1b		2-R cranioabdominal	(18x4)		
	1c		3-R inguinal LN. All the three connected to form one chain			
GI/2	2	Dog Griffon 7 years	1-R Cranioinquinal	(4.1x 2.9)	II	Laser only followed by mastectomy
GI/3	3a	Cat 15 years	1-R caudo abdominal	(4 x4.5).	II	1+2+3 tumors form chain Laser only followed by mastectomy
	3b					
	3c		2-R inguinal LN	(3 x2.1).		
	3d		3-L cranioabdominal	(5x2)		
	3e		4-R inguinal	(1x2)	I	4+5+6 tumors treated by AuNRs only followed by mastectomy
	3f		5-L inguinal	(1x1)		
			6-L caudothoracic	(1x1)		
GII/1	4a	Cat 9 years	L caudothoracic	(4.5x4)	III	Three sessions of PPTT followed by surgery
	4b		R caudothoracic	(4 x4)		
GII/2	5	Dog Griffon 10 years	R Caudoquinal	(3.1 x 3.6)	III	Three session of PPTT followed by surgery
GII/3	6a	Dog Griffon 11 years	1-L inguinal	(5 x5)	II	Three session of PPTT followed by surgery
	6b		2-L inguinal	(2 x 1.5)		PPTT only
	6c		3 small tumor	(1.5 x1)		PPTT only
GII/4	7a	Dog Griffon 5 years	1-R caudo thoracic	(3x2.5)	II	Three sessions of PPTT followed by surgery

Table 5.1. continued

	7b		2-R cranio abdominal both tumors form chain	(8x6.5)		surgery
GII/5	8a	Dog Griffon 8 years	1-L inguinal large calcified.	(5x5)	III	Three session of PPTT followed by surgery.
	8b		2-small caudal abdomenial	(2x1.5)		2&3 treated by PPTT only
	8c		3-two attached small tumors	(1.5 x1)		

Notes: The control group, GI, included 3 cases (2 dogs and 1 cat with 10 tumors) treated with either surgery only, laser only, or AuNRs only. All cases developed metastasis and died after treatment. Group II (GII) included 5 cases (4 dogs and 1 cat with 11 tumors) treated with PPTT (AuNRs and laser together) for 3 sessions followed by surgery. All were cured from tumor; 1 case had metastasis then died. **Abbreviations:** L, left; LN, lymph node; R, right; PPTT, plasmonic photothermal therapy.

Table 5.2. Survival, bleeding loss and met astasis for both GI and GII

No. #	EBL (g)	LR	DM(time mo)	OSS (mo)	Status
GI-1	>100	+ 1 month	+(CS, LN)	3	DOD
GI-2	66.5	-	+(CS, LN)	1	DOC
GI-3	47.5	-	+(LN)	1	DOC
GII-1	<1	-	-	24	ADF
GII-2	<1	-	-	48	ADF
GII-3	<1	-	-	3	DOC (pneumonia)
GII-4	<1	-	+(LN,CS)	1	DOD
GII-5	<1	-	-	6	DOC(pneumonia)

Notes: Group I (GI) were solely treated with surgery, laser, or AuNrs alone. Group II (GII) were treated with PPTT (AuNrs and laser together) before surgery. Estimate blood loss significant test *P*-value and statistical significance: The two-tailed *P*-value = 0.0010. By conventional criteria; this difference is considered to be very statistically significant. **Abbreviations:** ADF, alive disease free; Cs, clinical stage; DM, distant metastases; DOC, dead of other cause; DOD, dead of disease; EBL, estimated blood loss; LN, lymph node; LR, local recurrence.

Estimate blood loss significant test

P value and statistical significance: The two-tailed P value equals 0.0010. By conventional criteria; this difference is considered to be very statistically significant.

1.14.4 Conclusion.

Surgery is often used for tumor removal; however, it might trigger metastasis [421]. PPTT could be a better alter- native to replace traditional chemotherapy and radio-therapy for localized tumors, especially for tumors with a volume ≤20 cm^3 [9]. Therefore, for effective treatment of large tumors (volume ≥20 cm^3), we applied PPTT before surgical resection to naturally occurring tumors in the mammary glands of dogs and cats. Five cases were treated with this regime and showed complete remission without any recurrence after therapy. Three cases died in the few months following treatment, but in two cases from three, there was no evidence of any tumors upon examination (died due to other reasons, such as pneumonia). Histopathology results showed a decrease in cancer grades compared before (variant grades from 1 to 4) and after 2 weeks of treatment via PPTT and surgery (grade 0). X-ray diffraction revealed an absence of metastasis 1–2 years after treatment. In conclusion, our study demonstrates the feasibility of applying PPTT before surgery to large tumors in dogs and cats. Applying AuNRs-PPTT before surgery in treating large tumors could significantly affect blood vessels inside the tumor and potentially avoid the risk of bleeding during surgery. PPTT could be incorporated before the surgery to decrease the bleeding and potentially avoid the risk of bleeding during surgery that could lead to excessive blood loss and metastasis.

1.15 A Mechanistic Analysis of Gold Nanorod-assisted Photothermal Therapy on a Cat with Contentious Mammary Gland Tumor.

Summary. To understand the mechanism of PPTT in spontaneous breast cancer in animals, we conducted comprehensive proteomics analysis on cat tumor before and after the treatment, which showed a broad regulation of signaling pathways related to 1)

blood circulation system; 2) the cytoskeleton and cell mobility, and 3) immmune response, indicating an impeded function in cancer metastasis.

1.15.1 Methods.

Synthesis Proteomics sample preparation: The tumor sample collected from a cat case (before treatment (A1 and A2), 1st section of PPTT (B1 and B2), and 2 nd section of PPTT (C1 and C2)) was immediately frozen in liquid N_2 and stored at -80 ^oC for proteomics study. The samples were homogenized in lysis buffer (8 M urea, 50 mM HEPES, pH 8, 100 mM sodium chloride, 25 mM sodium fluoride, 10 mM sodium pyrophosphate, 50 mM β-glycerophosphate, 1 mM sodium orthovanadate, EDTA free protease inhibitor cocktail (Roche) 1 pill per 10 ml of lysis buffer) followed by ultrasonic tissue ablation on ice (10 s x 4 cycles). The cell debris was discarded by centrifugation 17000 x g for 16 min at at 4 ^oC the supernatant that contains proteins was kept. The disulfide bonds of the proteins were reduced by adding DTT to the supernatant to reach a final concentration of 10 mM (incubate in 65 ^oC for 25 min), and subsequently alkylated by adding IAA to a final concentration of 14 mM (in dark for 30 min at room temperature). The proteins were precipitated in 4 folds' sample volume of CH_3OH, 1-fold sample volumn of $CHCl_3$ and 3 folds' sample volume of H_2O. After precipitation, the samples were dried in N_2 gas flow and weighted, followed by digestion by trypsin (1: 50) in buffer (1.6 M Urea, 50 mM HEPEs, 5 % ACN, pH 8, 6) in 37 ^oC overnight. The lyophilized peptides were labeled with 6-plex TMT reagents (Thermo) following the manufacturer's protocol. Briefly, peptides were dissolved in 100 μL triethylammonium bicarbonate buffer (100 mM, pH 8.5). Each channel of the TMT reagents was dissolved in 41 μL of anhydrous ACN and mixed with the peptides. The reaction was kept for 1 h at

room temperature, and was then quenched by adding 8 μL of 5% hydroxylamine. We used 100 ug for each group for TMT labeling (A1, A2, B1, B2, C1, C2), corresponding to ion (126,127,128,129,130,131). Peptides from all six tubes with different TMT labels were mixed, desalted again using a tC18 SepPak cartridge, and lyophilized overnight. Then the TMT-labeled peptides were fractionated by high-pH reversed-phase high performance liquid chromatography (HPLC) into 15 fractions using a 4.6×250 mm 5μm particle reversed phase column (Waters) with a 40-min gradient of 5-55% ACN in 10 mM ammonium formate (pH=10). The collected fractions were further purified by the Stage Tip method.

LC-MS/MS Analysis: Each dried peptide sample was suspended in a solvent of 5% ACN and 4% formic acid (FA), and 2 μl was loaded onto a microcapillary column packed with C18 beads (Magic C18AQ, 5 μm, 200 Å, 75 μm x 16 cm) by a Dionex WPS-3000TPLRS autosampler (UltiMate 3000 Thermostatted Pulled Loop Rapid Separation Wellplate Sampler). Peptides were separated by reversed-phase HPLC using an UltiMate 3000 binary pump with three 112-minute gradients of 4-17%, 8-24%, or 10-28% ACN (0.125% FA) for different fractions of the TMT labeled samples. The full MS and MS2 were detected in a hybrid dual-cell quadrupole linear ion trap – Orbitrap mass spectrometer (LTQ Orbitrap Elite, Thermo Scientific, with Xcalibur 3.0.63 software) using a data-dependent Top15 method[422]. Each cycle has one full MS scan (resolution: 60,000) in the Orbitrap at the AGC target of 10^6, followed by up to 15 MS/MS for the most intense ions. The selected ions were excluded from further analysis for 90 s. Ions with a single or unassigned charge were not sequenced. MS/MS scan was activated by

HCD at 40.0% normalized collision energy with 1.2 m/z isolation width. Fragments were detected in the Orbitrap cell with high resolution and high mass accuracy.

Database search, data filter and protein quantification: Raw data files recorded from the mass spectrometer were first converted into the mzXML format. All MS/MS spectra were searched using the SEQUEST algorithm (version 28) [423] and matched against a database encompassing sequences of all proteins downloaded from the Uniprot cat (Felis catus) database. Each protein sequence was listed in both forward and reversed orientations to estimate false discovery rate (FDR) of peptide and protein identifications. Database search was performed by using the following parameters: 10 ppm precursor mass tolerance; 0.025 Da product ion mass tolerance; fully digested with trypsin; up to three missed cleavages; variable modifications: oxidation of methionine (+15.9949); fixed modifications: carbamidomethylation of cysteine (+57.0214) and TMT modification of lysine and N-termini (+229.1630).

The target-decoy method was employed to evaluate and control FDRs of peptide and protein identifications [424]. Linear discriminant analysis (LDA) was used to distinguish correct and incorrect peptide identifications using numerous parameters such as XCorr, ΔCn, and precursor mass error[425]. After scoring, peptides fewer than seven amino acids in length were discarded and peptide spectral match was filtered to a less than 1% FDR based on the number of decoy sequences in the final data set. The TMT reporter ion intensities in the MS/MS spectra were used to quantify peptides. The isotopic information provided by Thermo was utilized to calibrate the ion intensities.

For proteomics analysis: Proteomics data was log2 transformed before analysis of variance (ANOVA) which was used to detect differential levels of proteins between control (CTRL) and treatment groups (S1, S2) using the Bioconductor LIMMA package [426]. We set false discovery rate (FDR) threshold at 0.05 to select differential proteins. Hierarchical clustering was performed with statistical software R [340]. Proteins identified as being affected were subjected to pathway analysis using the MetaCore from Thomson Reuters.

1.15.2 Results and discussions.

Six breast tumor samples from a cat case was collected and subjected to mass spectrometry analysis: they are Ctrl_B1 and Ctrl_B2 (tumor samples before treatment, two biological replications from different locations of the tumor); S1_B1 and S1_B2 (tumor samples after first PPTT treatment, two biological replications from different locations of the tumor); and S2_B1 and S2_B1 (tumor samples after second PPTT treatment, two biological replications from different locations of the tumor). The samples are labeled isotopically by TMT reagents and the relative protein concentrations are determined quantitatively. **Figure 5.5 A** shows the protein expression heat map of 1598 proteins quantifies in the samples. The clustering analysis in **Figure 5.5 B** shows that the control and experimental groups were separately clustered with good reproducibility. A first level clustering of Ctrl_B1 with Ctrl_B2, S1_B1 with S1_B2, and S2_B1 with S2_B1 was first observed. The PPTT treated samples are then clustered in the next level, showing more similarities within the PPTT treated samples compared with the controls.

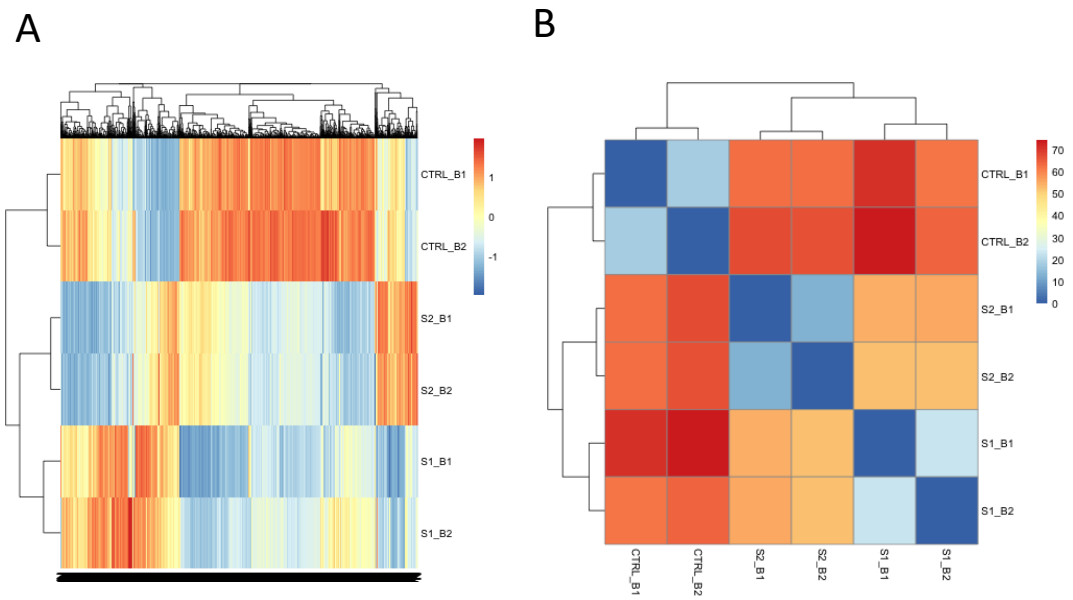

FIGURE 5.5. (A) The heatmap of the quantified proteins in different samples. (B) The clustering analysis of the samples. Ctrl_B1 and Ctrl_B2 (tumor samples before treatment, two biological replications from different locations of the tumor); S1_B1 and S1_B2 (tumor samples after first PPTT treatment, two biological replications from different locations of the tumor); and S2_B1 and S2_B1 (tumor samples after second PPTT treatment, two biological replications from different locations of the tumor).

For proteomics analysis, we set [-1, 1] as a threshold for fold change (log 2) detection (**Figure 5.6 A**). Following the first PPTT treatment, 444 proteins were decreased and 127 proteins were increased. In addition, second PPTT treatment led to down-regulation of 324 and up-regulation of 122 proteins (**Figure 5.6 B**). Overlap in altered proteins in the first and second PPTT is shown in **Figure 5.6 C**.

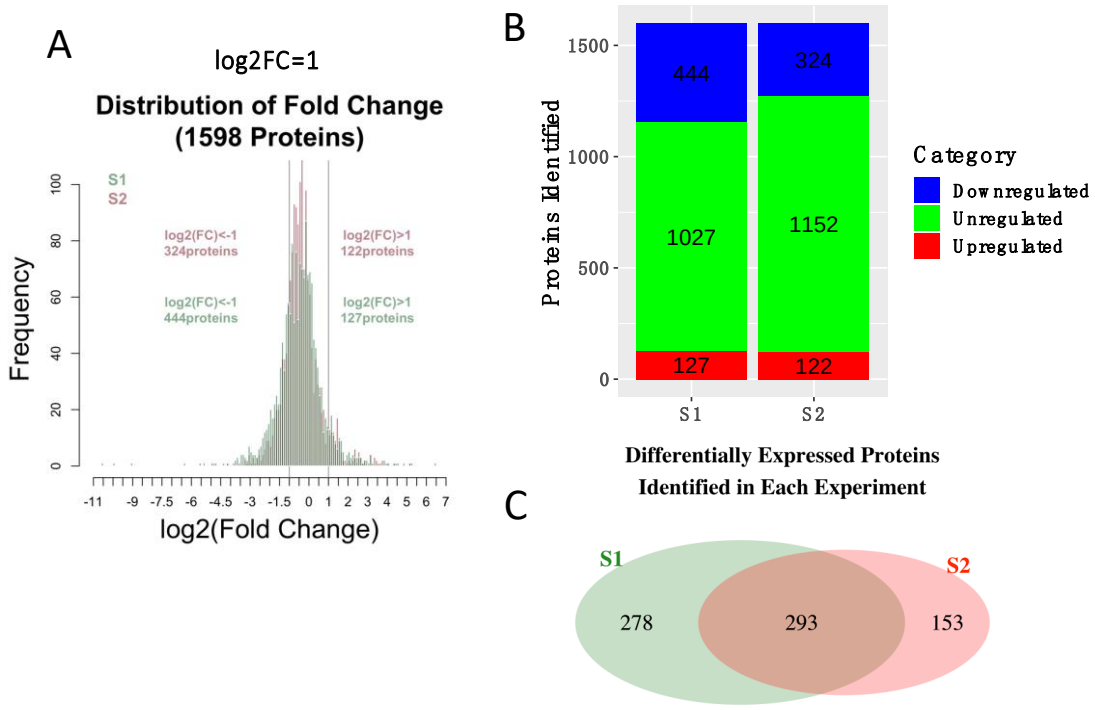

FIGURE 5.6. (A) Distribution of log2 (fold changes) in proteins perturbed by the first and second PPTT treatments compared with control group. (C) Bar graph showing numbers of proteins unregulated, upregulated, and downregulated in each group. (D) Venn diagram showing the common and unique differentially expressed proteins that identified in the first and second PPTT treatments.

To understand the biological process of PPTT in cat, we performed pathway analysis (**Figure 5.7**), which revealed significant perturbations to the signaling pathways related to 1) blood circulation system; 2) the cytoskeleton and cell mobility, and 3) immmune response.

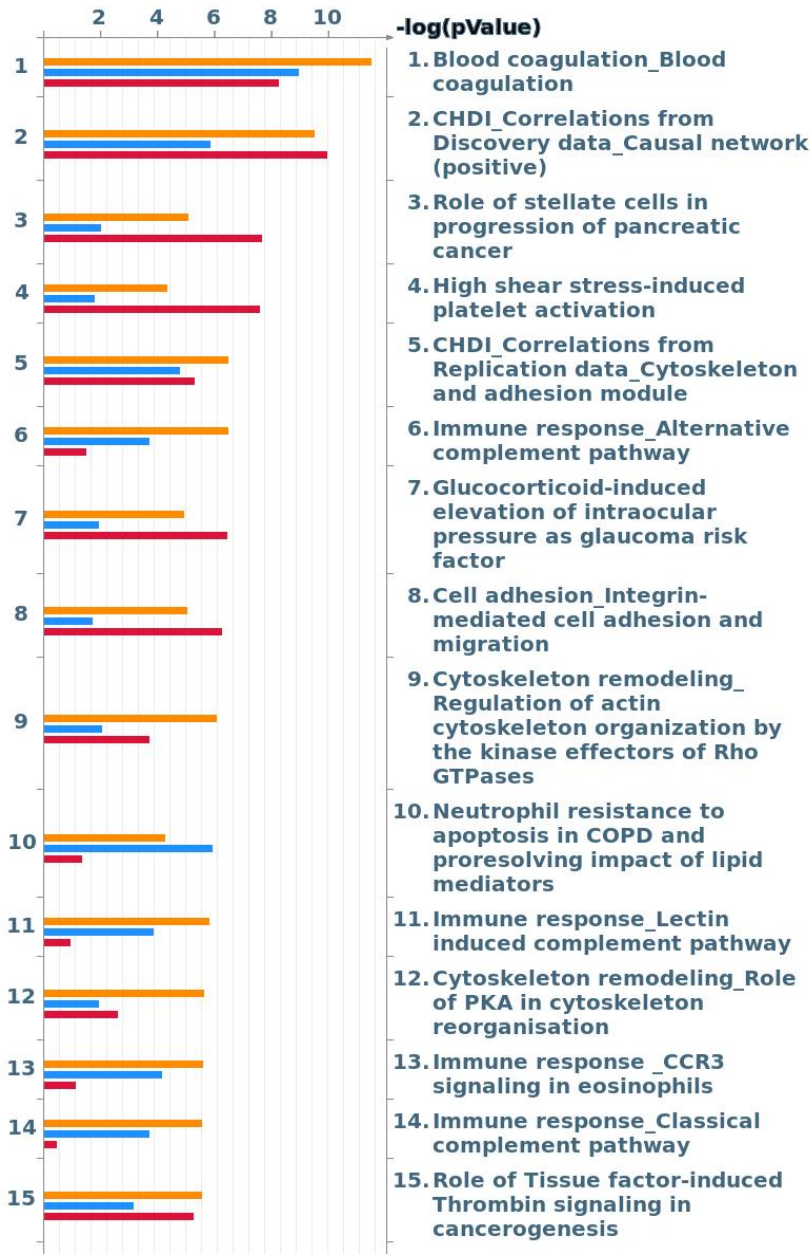

FIGURE 5.7. Pathway analysis showing the top most significant pathways. Orange bar, S1 *vs* Ctrl; blue bar, S2 *vs* Ctrl; Red bar, S2 *vs* S1.

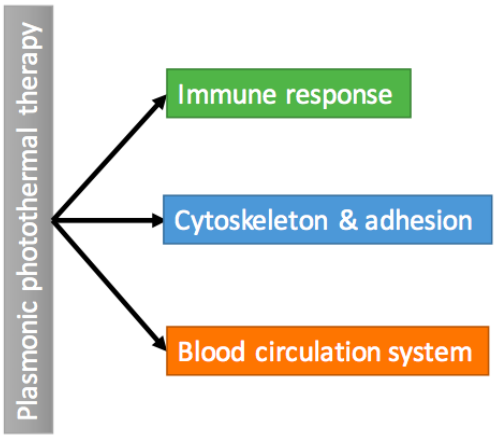

FIGURE 5.8. A simple scheme showing the three main pathways of PPTT in cat.

1.15.3 Conclusion.

We conducted a comprehensive proteomics analysis on a cat case before and after first and second the PPTT treatments, which showed a broad regulation of signaling pathways related to 1) blood circulation system; 2) the cytoskeleton and cell mobility, and 3) immmune response, indicating the mechanism of PPTT in real animal patients for an impeded function in cancer metastasis.

REFERENCES

[1] P. K. Jain, K. S. Lee, I. H. El-Sayed, M. A. El-Sayed, *J Phys Chem B* **2006**, 110, 7238.

[2] M. C. Daniel, D. Astruc, *Chem Rev* **2004**, 104, 293.

[3] M. Faraday, *Philosophical Transactions of the Royal Society of London* **1857**, 147, 145.

[4] B. Nikoobakht, M. El-Sayed, *Chemistry of Materials* **2003**, 15, 1957.

[5] C. J. Murphy, T. K. Sau, A. M. Gole, C. J. Orendorff, J. Gao, L. Gou, S. E. Hunyadi, T. Li, *J Phys Chem B* **2005**, 109, 13857; M. Hu, J. Chen, Z. Y. Li, L. Au, G. V. Hartland, X. Li, M. Marquez, Y. Xia, *Chem Soc Rev* **2006**, 35, 1084; Y. Sun, Y. Xia, *Science* **2002**, 298, 2176.

[6] E. C. Dreaden, A. M. Alkilany, X. Huang, C. J. Murphy, M. A. El-Sayed, *Chem Soc Rev* **2012**, 41, 2740.

[7] M. R. Ali, B. Snyder, M. A. El-Sayed, *Langmuir* **2012**, 28, 9807.

[8] O. Neumann, A. S. Urban, J. Day, S. Lal, P. Nordlander, N. J. Halas, *ACS Nano* **2013**, 7, 42; C. J. Murphy, A. M. Gole, S. E. Hunyadi, J. W. Stone, P. N. Sisco, A. Alkilany, B. E. Kinard, P. Hankins, *Chem Commun (Camb)* **2008**, 544; M. Turner, V. B. Golovko, O. P. Vaughan, P. Abdulkin, A. Berenguer-Murcia, M. S. Tikhov, B. F. Johnson, R. M. Lambert, *Nature* **2008**, 454, 981.

[9] M. R. Ali, I. M. Ibrahim, H. R. Ali, S. A. Selim, M. A. El-Sayed, *Int J Nanomedicine* **2016**, 11, 4849.

[10] M. R. K. Ali, Y. Wu, Y. Tang, H. Xiao, K. Chen, T. Han, N. Fang, R. Wu, M. A. El-Sayed, *Proc Natl Acad Sci U S A* **2017**, 114, E5655.

[11] X. Huang, M. A. El-Sayed, *Journal of Advanced Research* **2010**, 1, 13.

[12] A. K. Oyelere, P. C. Chen, X. Huang, I. H. El-Sayed, M. A. El-Sayed, *Bioconjug Chem* **2007**, 18, 1490; D. Dam, J. Lee, P. Sisco, D. Co, M. Zhang, M. Wasielewski, T. Odom, *Acs Nano* **2012**, 6, 3318.

[13] S. Eustis, M. A. el-Sayed, *Chem Soc Rev* **2006**, 35, 209; R. Bardhan, S. Lal, A. Joshi, N. J. Halas, *Acc Chem Res* **2011**, 44, 936; E. C. Cho, C. Glaus, J. Chen, M. J. Welch, Y. Xia, *Trends Mol Med* **2010**, 16, 561.

[14] C. J. Murphy, A. M. Gole, J. W. Stone, P. N. Sisco, A. M. Alkilany, E. C. Goldsmith, S. C. Baxter, *Acc Chem Res* **2008**, 41, 1721.

[15] J. Turkevich, P. C. Stevenson, J. Hillier, *Discussions of the Faraday Society* **1951**, 55.

[16] P. Zhao, N. Li, D. Astruc, *Coordination Chemistry Reviews* **2013**, 257, 638.

[17] M. Grzelczak, J. Pérez-Juste, P. Mulvaney, L. M. Liz-Marzán, *Chem Soc Rev* **2008**, 37, 1783.

[18] N. Jana, L. Gearheart, C. Murphy, *Journal of Physical Chemistry B* **2001**, 105, 4065; C. Murphy, N. Jana, *Advanced Materials* **2002**, 14, 80; J. Gao, *Abstracts of Papers of the American Chemical Society* **2003**, 226, U690; L. Gou, C. Murphy, *Chemistry of Materials* **2005**, 17, 3668.

[19] L. Scarabelli, A. Sánchez-Iglesias, J. Pérez-Juste, L. M. Liz-Marzán, *J Phys Chem Lett* **2015**, 6, 4270.

[20] X. Huang, I. H. El-Sayed, W. Qian, M. A. El-Sayed, *J Am Chem Soc* **2006**, 128, 2115.

[21] S. Nie, S. Emery, *Science* **1997**, 275, 1102.

[22] X. Huang, W. Qian, I. H. El-Sayed, M. A. El-Sayed, *Lasers Surg Med* **2007**, 39, 747.

[23] X. H. Huang, P. K. Jain, I. H. El-Sayed, M. A. El-Sayed, *Lasers Med. Sci.* **2008**, 23, 217.

[24] S. Link, M. El-Sayed, *International Reviews in Physical Chemistry* **2000**, 19, 409.

[25] H. Knosp, R. Holliday, C. Corti, *Gold Bulletin* **2003**, 36, 93.

[26] S. P. Pricker, *Gold Bulletin* **1996**, 29, 53.

[27] T. G. Benedek, *Journal of the History of Medicine and Allied Sciences* **2004**, 59, 50; W. Kean, L. Hart, W. Buchanan, *Rheumatology* **1997**, 36, 560.

[28] J. H. Breasted, *The Edwin Smith Surgical Papyrus: published in facsimile and hieroglyphic transliteration with translation and commentary in two volumes*, University of Chicago Press Chicago, **1930**.

[29] J. M. Torpy, A. E. Burke, R. M. Glass, *JAMA* **2010**, 303, 2544.

[30] X. Huang, P. K. Jain, I. H. El-Sayed, M. A. El-Sayed, *Lasers in Medical Science* **2007**, 23, 217.

[31] Y. Liu, P. Bhattarai, Z. Dai, X. Chen, *Chem Soc Rev* **2018**.

[32] J. A. Schwartz, A. M. Shetty, R. E. Price, R. J. Stafford, J. C. Wang, R. K. Uthamanthil, K. Pham, R. J. McNichols, C. L. Coleman, J. D. Payne, *Cancer Res* **2009**, 69, 1659.

[33] R. T. Bronson, *Am J Vet Res* **1982**, 43, 2057.

[34] E. MACEWEN, *Cancer and Metastasis Reviews* **1990**, 9, 125.

[35] R. Shafiee, J. Javanbakh, N. Atyabi, P. Kheradmand, D. Kheradmand, A. Bahrami, H. Daraei, F. Khadivar, *Cancer Cell International* **2016**, 16; E. Antuofermo, M. A. Miller, S. Pirino, J. Xie, S. Badve, S. I. Mohammed, *Cancer Epidemiol Biomarkers Prev* **2007**, 16, 2247.

[36] A. S. Abdoon, E. A. Al-Ashkar, O. M. Kandil, A. M. Shaban, H. M. Khaled, M. A. El Sayed, M. M. El Shaer, A. H. Shaalan, W. H. Eisa, A. A. Eldin, H. A. Hussein, M. R. El Ashkar, M. R. Ali, A. A. Shabaka, *Nanomedicine* **2016**, 12, 2291.

[37] E. M. Schuh, R. Portela, H. L. Gardner, C. Schoen, C. A. London, *BMC Vet Res* **2017**, 13, 294.

[38] R. A. Sperling, P. R. Gil, F. Zhang, M. Zanella, W. J. Parak, *Chemical Society Reviews* **2008**, 37, 1896.

[39] A. M. Alkilany, C. J. Murphy, *Journal of Nanoparticle Research* **2010**, 12, 2313.

[40] M. R. Ali, M. A. Rahman, Y. Wu, T. Han, X. Peng, M. A. Mackey, D. Wang, H. J. Shin, Z. G. Chen, H. Xiao, R. Wu, Y. Tang, D. M. Shin, M. A. El-Sayed, *Proc Natl Acad Sci U S A* **2017**, 114, E3110.

[41] E. Boisselier, D. Astruc, *Chem Soc Rev* **2009**, 38, 1759.

[42] N. Khlebtsov, L. Dykman, *Chem Soc Rev* **2011**, 40, 1647.

[43] S. C. Gad, K. L. Sharp, C. Montgomery, J. D. Payne, G. P. Goodrich, *Int J Toxicol* **2012**, 31, 584.

[44] L. Zou, H. Wang, B. He, L. Zeng, T. Tan, H. Cao, X. He, Z. Zhang, S. Guo, Y. Li, *Theranostics* **2016**, 6, 762.

[45] Z. Heidari, M. Salouti, R. Sariri, *Nanotechnology* **2015**, 26, 195101.

[46] S. Wang, X. Ma, X. Hong, Y. Cheng, Y. Tian, S. Zhao, W. Liu, Y. Tang, R. Zhao, L. Song, Z. Teng, G. Lu, *ACS Nano* **2018**, 12, 662.

[47] J. Nam, S. Son, L. J. Ochyl, R. Kuai, A. Schwendeman, J. J. Moon, *Nat Commun* **2018**, 9, 1074.

[48] E. Dickerson, E. Dreaden, X. Huang, I. El-Sayed, H. Chu, S. Pushpanketh, J. McDonald, M. El-Sayed, *Cancer Letters* **2008**, 269, 57.

[49] B. Zhou, J. Song, M. Wang, X. Wang, J. Wang, E. W. Howard, F. Zhou, J. Qu, W. R. Chen, *Nanoscale* **2018**, 10, 21640.

[50] A. S. Bear, L. C. Kennedy, J. K. Young, S. K. Perna, J. P. Mattos Almeida, A. Y. Lin, P. C. Eckels, R. A. Drezek, A. E. Foster, *PLoS One* **2013**, 8, e69073; W. Lu, C. Xiong, G. Zhang, Q. Huang, R. Zhang, J. Z. Zhang, C. Li, *Clin Cancer Res* **2009**, 15, 876.

[51] S. Y. Liu, Z. S. Liang, F. Gao, S. F. Luo, G. Q. Lu, *J Mater Sci Mater Med* **2010**, 21, 665.

[52] H. Wan, J. Yue, S. Zhu, T. Uno, X. Zhang, Q. Yang, K. Yu, G. Hong, J. Wang, L. Li, Z. Ma, H. Gao, Y. Zhong, J. Su, A. L. Antaris, Y. Xia, J. Luo, Y. Liang, H. Dai, *Nat Commun* **2018**, 9, 1171.

[53] S. Lal, S. E. Clare, N. J. Halas, *Acc Chem Res* **2008**, 41, 1842.

[54] J. Chen, C. Glaus, R. Laforest, Q. Zhang, M. Yang, M. Gidding, M. J. Welch, Y. Xia, *Small* **2010**, 6, 811.

[55] H. Yuan, A. Fales, T. Vo-Dinh, *Journal of the American Chemical Society* **2012**, 134, 11358.

[56] M. Pérez-Hernández, P. Del Pino, S. G. Mitchell, M. Moros, G. Stepien, B. Pelaz, W. J. Parak, E. M. Gálvez, J. Pardo, J. M. de la Fuente, *ACS Nano* **2015**, 9, 52.

[57] Y. Liu, Z. Wang, G. Zhu, O. Jacobson, X. Fu, R. Bai, X. Lin, N. Lu, X. Yang, W. Fan, J. Song, G. Yu, F. Zhang, H. Kalish, G. Niu, Z. Nie, X. Chen, *ACS Nano* **2017**, 11, 10539.

[58] Y. Xia, X. Ma, J. Gao, G. Chen, Z. Li, X. Wu, Z. Yu, J. Xing, L. Sun, H. Ruan, L. Luo, L. Xiang, C. Dong, W. Ren, Z. Shen, A. Wu, *Small* **2018**, 14, e1800094.

[59] R. S. Riley, E. S. Day, *Wiley Interdiscip Rev Nanomed Nanobiotechnol* **2017**, 9.

[60] J. E. Talmadge, I. J. Fidler, *Cancer Research* **2010**, 70, 5649.

[61] I. J. Fidler, *Nature Reviews Cancer* **2003**, 3, 453.

[62] C. L. Chaffer, R. A. Weinberg, *Science* **2011**, 331, 1559.

[63] C. L. Chaffer, R. A. Weinberg, *Science* **2011**, 331, 1559.

[64] C. M. Fife, J. A. McCarroll, M. Kavallaris, *British Journal of Pharmacology* **2014**, 171, 5507.

[65] D. Hanahan, R. A. Weinberg, *Cell* **2011**, 144, 646.

[66] C. M. Fife, J. A. McCarroll, M. Kavallaris, *Br J Pharmacol* **2014**, 171, 5507.

[67] G. F. Weber, *Cancer Lett* **2013**, 328, 207.

[68] F. Morgillo, H. Y. Lee, *Drug Resist Update* **2005**, 8, 298; C. Holohan, S. Van Schaeybroeck, D. B. Longley, P. G. Johnston, *Nature Reviews Cancer* **2013**, 13, 714.

[69] C. J. Murphy, A. M. Gole, J. W. Stone, P. N. Sisco, A. M. Alkilany, E. C. Goldsmith, S. C. Baxter, *Accounts Chem Res* **2008**, 41, 1721.

[70] S. M. Moghimi, A. C. Hunter, J. C. Murray, *Faseb J* **2005**, 19, 311.

[71] R. A. Petros, J. M. DeSimone, *Nat. Rev. Drug. Discov.* **2010**, 9, 615.

[72] L. R. Hirsch, R. J. Stafford, J. A. Bankson, S. R. Sershen, B. Rivera, R. E. Price, J. D. Hazle, N. J. Halas, J. L. West, *Proceedings of the National Academy of Sciences of the United States of America* **2003**, 100, 13549; D. Peer, J. M. Karp, S. Hong, O. C. FaroKHzad, R. Margalit, R. Langer, *Nat Nanotechnol* **2007**, 2, 751.

[73] J. A. Yang, H. T. Phan, S. Vaidya, C. J. Murphy, *Nano Letters* **2013**, 13, 2295.

[74] C. Y. Tay, P. Q. Cai, M. I. Setyawati, W. R. Fang, L. P. Tan, C. H. L. Hong, X. D. Chen, D. T. Leong, *Nano Letters* **2014**, 14, 83.

[75] S. J. H. Soenen, N. Nuytten, S. F. De Meyer, S. C. De Smedt, M. De Cuyper, *Small* **2010**, 6, 832.

[76] T. Zhou, M. F. Yu, B. Zhang, L. M. Wang, X. C. Wu, H. J. Zhou, Y. P. Du, J. F. Hao, Y. P. Tu, C. Y. Chen, T. T. Wei, *Advanced Functional Materials* **2014**, 24, 6922.

[77] E. Doolittle, P. Peiris, G. Doron, A. Goldberg, S. Tucci, S. Rao, S. Shah, M. Sylvestre, P. Govender, O. Turan, Z. Lee, W. Schiemann, E. Karathanasis, *Acs Nano* **2015**, 9, 8012.

[78] Z. Wang, Y. Yu, W. Dai, J. Cui, H. Wu, L. Yuan, H. Zhang, X. Wang, J. Wang, X. Zhang, Q. Zhang, *Biomaterials* **2013**, 34, 756.

[79] Y. Zhao, D. Y. Alakhova, A. V. Kabanov, *Adv Drug Deliv Rev* **2013**, 65, 1763.

[80] T. M. Sun, Y. C. Wang, F. Wang, J. Z. Du, C. Q. Mao, C. Y. Sun, R. Z. Tang, Y. Liu, J. Zhu, Y. H. Zhu, X. Z. Yang, J. Wang, *Biomaterials* **2014**, 35, 836.

[81] C. Roma-Rodrigues, A. Heuer-Jungemann, A. R. Fernandes, A. G. Kanaras, P. V. Baptista, *Int J Nanomedicine* **2016**, 11, 2633.

[82] P. M. Peiris, P. Deb, E. Doolittle, G. Doron, A. Goldberg, P. Govender, S. Shah, S. Rao, S. Carbone, T. Cotey, M. Sylvestre, S. Singh, W. P. Schiemann, Z. Lee, E. Karathanasis, *J Pharm Sci* **2015**, 104, 2600.

[83] M. Kanapathipillai, A. Brock, D. E. Ingber, *Adv Drug Deliv Rev* **2014**, 79-80, 107.

[84] R. R. Arvizo, S. Saha, E. Wang, J. D. Robertson, R. Bhattacharya, P. Mukherjee, *Proc Natl Acad Sci U S A* **2013**, 110, 6700.

[85] M. Ali, Y. Wu, D. Ghosh, B. Do, K. Chen, M. Dawson, N. Fang, T. Sulchek, M. El-Sayed, *Acs Nano* **2017**, 11, 3716.

[86] T. Zhou, M. Yu, B. Zhang, L. Wang, X. Wu, H. Zhou, Y. Du, J. Hao, Y. Tu, C. Chen, T. Wei, *Advanced Functional Materials* **2014**, 24, 6922.

[87] E. Faghfuri, M. H. Yazdi, M. Mahdavi, Z. Sepehrizadeh, M. A. Faramarzi, F. Mavandadnejad, A. R. Shahverdi, *Arch Med Res* **2015**, 46, 31; M. H. Yazdi, M. Mahdavi, N. Setayesh, M. Esfandyar, A. R. Shahverdi, *Daru* **2013**, 21, 33.

[88] S. Yang, H. Gao, *Pharmacol Res* **2017**.

[89] Y. Zhang, J. Wei, S. Liu, J. Wang, X. Han, H. Qin, J. Lang, K. Cheng, Y. Li, Y. Qi, G. J. Anderson, S. Sukumar, S. Li, G. Nie, *Theranostics* **2017**, 7, 1062.

[90] M. R. K. Ali, Y. Wu, D. Ghosh, B. H. Do, K. Chen, M. R. Dawson, N. Fang, T. A. Sulchek, M. A. El-Sayed, *ACS nano* **2017**, 11, 3716.

[91] T. Okuno, S. Kato, Y. Hatakeyama, J. Okajima, S. Maruyama, M. Sakamoto, S. Mori, T. Kodama, *J Control Release* **2013**, 172, 879.

[92] A. R. Burke, R. N. Singh, D. L. Carroll, J. C. Wood, R. B. D'Agostino, P. M. Ajayan, F. M. Torti, S. V. Torti, *Biomaterials* **2012**, 33, 2961.

[93] X. He, X. Bao, H. Cao, Z. Zhang, Q. Yin, W. Gu, L. Chen, H. Yu, Y. Li, *Advanced Functional Materials* **2015**, 25, 2831.

[94] Y. Wu, M. R. K. Ali, B. Dong, T. Han, K. Chen, J. Chen, Y. Tang, N. Fang, F. Wang, M. A. El-Sayed, *ACS Nano* **2018**.

[95] D. Wang, Z. Xu, H. Yu, X. Chen, B. Feng, Z. Cui, B. Lin, Q. Yin, Z. Zhang, C. Chen, J. Wang, W. Zhang, Y. Li, *Biomaterials* **2014**, 35, 8374.

[96] H. Sun, J. Su, Q. Meng, Q. Yin, L. Chen, W. Gu, Z. Zhang, H. Yu, P. Zhang, S. Wang, Y. Li, *Advanced Functional Materials* **2017**, 27.

[97] R. L. Atkinson, M. Zhang, P. Diagaradjane, S. Peddibhotla, A. Contreras, S. G. Hilsenbeck, W. A. Woodward, S. Krishnan, J. C. Chang, J. M. Rosen, *Sci Transl Med* **2010**, 2, 55ra79.

[98] H. Qiu, Y. Min, Z. Rodgers, L. Zhang, A. Z. Wang, *Wiley Interdiscip Rev Nanomed Nanobiotechnol* **2017**, 9.

[99] Z. Amoozgar, M. S. Goldberg, *Adv Drug Deliv Rev* **2015**, 91, 38.

[100] L. J. Cruz, R. A. Rosalia, J. W. Kleinovink, F. Rueda, C. W. Löwik, F. Ossendorp, *J Control Release* **2014**, 192, 209.

[101] R. A. Rosalia, L. J. Cruz, S. van Duikeren, A. T. Tromp, A. L. Silva, W. Jiskoot, T. de Gruijl, C. Löwik, J. Oostendorp, S. H. van der Burg, F. Ossendorp, *Biomaterials* **2015**, 40, 88.

[102] R. H. Fang, C. M. Hu, B. T. Luk, W. Gao, J. A. Copp, Y. Tai, D. E. O'Connor, L. Zhang, *Nano Lett* **2014**, 14, 2181.

[103] C. Wang, L. Xu, C. Liang, J. Xiang, R. Peng, Z. Liu, *Adv Mater* **2014**, 26, 8154.

[104] Q. Chen, L. Xu, C. Liang, C. Wang, R. Peng, Z. Liu, *Nature Communications* **2016**, 7.

[105] F. Zhou, J. Yang, Y. Zhang, M. Liu, M. L. Lang, M. Li, W. R. Chen, *Clin Cancer Res* **2018**, 24, 5335.

[106] M. J. Ernsting, M. Murakami, A. Roy, S. D. Li, *J Control Release* **2013**, 172, 782.

[107] Y. Chen, Y. Hung, I. Liau, G. Huang, *Nanoscale Research Letters* **2009**, 4, 858; K. Jiang, D. Smith, A. Pinchuk, *Journal of Physical Chemistry C* **2013**, 117, 27073.

[108] J. Hillyer, R. Albrecht, *Journal of Pharmaceutical Sciences* **2001**, 90, 1927.

[109] S. Fraga, A. Brandão, M. E. Soares, T. Morais, J. A. Duarte, L. Pereira, L. Soares, C. Neves, E. Pereira, M. de Lourdes Bastos, *Nanomedicine: Nanotechnology, Biology and Medicine* **2014**, 10, 1757.

[110] Y. Wang, Y. Liu, H. Luehmann, X. Xia, P. Brown, C. Jarreau, M. Welch, Y. Xia, *ACS Nano* **2012**, 6, 5880.

[111] G. Zhang, Z. Yang, W. Lu, R. Zhang, Q. Huang, M. Tian, L. Li, D. Liang, C. Li, *Biomaterials* **2009**, 30, 1928.

[112] L. Shang, K. Nienhaus, G. U. Nienhaus, *Journal of Nanobiotechnology* **2014**, 12, 5.

[113] Y. Pan, A. Leifert, D. Ruau, S. Neuss, J. Bornemann, G. Schmid, W. Brandau, U. Simon, W. Jahnen-Dechent, *Small* **2009**, 5, 2067.

[114] R. Coradeghini, S. Gioria, C. P. García, P. Nativo, F. Franchini, D. Gilliland, J. Ponti, F. Rossi, *Toxicology letters* **2013**, 217, 205.

[115] S. Pattanayak, S. Chakraborty, M. M. R. Mollick, I. Roy, S. Basu, D. Rana, S. S. Gauri, D. Chattopadhyay, M. Chakraborty, *New Journal of Chemistry* **2016**, 40, 7121.

[116] E. E. Connor, J. Mwamuka, A. Gole, C. J. Murphy, M. D. Wyatt, *Small* **2005**, 1, 325.

[117] J. A. Khan, B. Pillai, T. K. Das, Y. Singh, S. Maiti, *ChemBioChem* **2007**, 8, 1237.

[118] W.-S. Cho, M. Cho, J. Jeong, M. Choi, B. S. Han, H.-S. Shin, J. Hong, B. H. Chung, J. Jeong, M.-H. Cho, *Toxicology and applied pharmacology* **2010**, 245, 116.

[119] A. P. Leonov, J. Zheng, J. D. Clogston, S. T. Stern, A. K. Patri, A. Wei, *Acs Nano* **2008**, 2, 2481.

[120] C. M. Goodman, C. D. McCusker, T. Yilmaz, V. M. Rotello, *Bioconjugate chemistry* **2004**, 15, 897.

[121] N. M. Schaeublin, L. K. Braydich-Stolle, A. M. Schrand, J. M. Miller, J. Hutchison, J. J. Schlager, S. M. Hussain, *Nanoscale* **2011**, 3, 410.

[122] A. M. Alkilany, P. K. Nagaria, C. R. Hexel, T. J. Shaw, C. J. Murphy, M. D. Wyatt, *Small* **2009**, 5, 701.

[123] T. Niidome, M. Yamagata, Y. Okamoto, Y. Akiyama, H. Takahashi, T. Kawano, Y. Katayama, Y. Niidome, *Journal of Controlled Release* **2006**, 114, 343.

[124] S. D. Li, L. Huang, *Mol Pharm* **2008**, 5, 496.

[125] D. Lankveld, R. Rayavarapu, P. Krystek, A. Oomen, H. Verharen, T. van Leeuwen, W. De Jong, S. Manohar, *Nanomedicine* **2011**, 6, 339.

[126] R. Su, S. A. Ermilov, A. V. Liopo, A. A. Oraevsky, *Journal of biomedical optics* **2012**, 17, 1015061.

[127] J. M. Stern, V. V. Kibanov Solomonov, E. Sazykina, J. A. Schwartz, S. C. Gad, G. P. Goodrich, *Int J Toxicol* **2016**, 35, 38.

[128] A. Gandalovičová, D. Rosel, M. Fernandes, P. Veselý, P. Heneberg, V. Čermák, L. Petruželka, S. Kumar, V. Sanz-Moreno, J. Brábek, *Trends Cancer* **2017**, 3, 391.

[129] R. A. Petros, J. M. DeSimone, *Nat Rev Drug Discov* **2010**, 9, 615.

[130] D. Peer, J. M. Karp, S. Hong, O. C. Farokhzad, R. Margalit, R. Langer, *Nature nanotechnology* **2007**, 2, 751.

[131] Q. Mu, H. Wang, M. Zhang, *Expert Opin Drug Deliv* **2017**, 14, 123.

[132] C. Y. Tay, P. Cai, M. I. Setyawati, W. Fang, L. P. Tan, C. H. Hong, X. Chen, D. T. Leong, *Nano Lett* **2014**, 14, 83.

[133] S. J. Soenen, N. Nuytten, S. F. De Meyer, S. C. De Smedt, M. De Cuyper, *Small* **2010**, 6, 832.

[134] A. Schroeder, D. A. Heller, M. M. Winslow, J. E. Dahlman, G. W. Pratt, R. Langer, T. Jacks, D. G. Anderson, *Nat Rev Cancer* **2011**, 12, 39.

[135] Y. Wu, M. R. Ali, K. Chen, N. Fang, M. A. El-Sayed, *Nano Today* **2019**.

[136] S. Maier, M. Brongersma, P. Kik, S. Meltzer, A. Requicha, H. Atwater, *Advanced Materials* **2001**, 13, 1501.

[137] M. A. van Dijk, A. L. Tchebotareva, M. Orrit, M. Lippitz, S. Berciaud, D. Lasne, L. Cognet, B. Lounis, *Phys Chem Chem Phys* **2006**, 8, 3486; V. Myroshnychenko, J. Rodríguez-Fernández, I. Pastoriza-Santos, A. M. Funston, C. Novo, P. Mulvaney, L. M. Liz-Marzán, F. J. García de Abajo, *Chem Soc Rev* **2008**, 37, 1792.

[138] L. Opilik, T. Schmid, R. Zenobi, *Annu Rev Anal Chem (Palo Alto Calif)* **2013**, 6, 379.

[139] Y. Gu, W. Sun, G. Wang, N. Fang, *J Am Chem Soc* **2011**, 133, 5720; N. J. Durr, T. Larson, D. K. Smith, B. A. Korgel, K. Sokolov, A. Ben-Yakar, *Nano Lett* **2007**, 7, 941.

[140] A. G. Tkachenko, H. Xie, Y. Liu, D. Coleman, J. Ryan, W. R. Glomm, M. K. Shipton, S. Franzen, D. L. Feldheim, *Bioconjug Chem* **2004**, 15, 482.

[141] P. K. Jain, X. Huang, I. H. El-Sayed, M. A. El-Sayed, *Acc Chem Res* **2008**, 41, 1578.

[142] C. Rosman, S. Pierrat, A. Henkel, M. Tarantola, D. Schneider, E. Sunnick, A. Janshoff, C. Sönnichsen, *Small* **2012**, 8, 3683.

[143] S. H. Wang, C. W. Lee, F. G. Tseng, K. K. Liang, P. K. Wei, in *J Biophotonics*, 2015.

[144] M. Liu, Q. Li, L. Liang, J. Li, K. Wang, M. Lv, N. Chen, H. Song, J. Lee, J. Shi, L. Wang, R. Lal, C. Fan, *Nat Commun* **2017**, 8, 15646.

[145] X. Nan, P. A. Sims, X. S. Xie, *Chemphyschem* **2008**, 9, 707.

[146] R. Schneider, T. Glaser, M. Berndt, S. Diez, *Opt Express* **2013**, 21, 3523.

[147] W. Qian, X. Huang, B. Kang, M. A. El-Sayed, *J Biomed Opt* **2010**, 15, 046025.

[148] X. Y. Wan, L. L. Zheng, P. F. Gao, X. X. Yang, C. M. Li, Y. F. Li, C. Z. Huang, *Sci Rep* **2014**, 4, 4529.

[149] G. Rong, H. Wang, L. R. Skewis, B. M. Reinhard, *Nano Lett* **2008**, 8, 3386.

[150] B. Xiong, Z. Huang, H. Zou, C. Qiao, Y. He, E. S. Yeung, *ACS Nano* **2017**, 11, 541.

[151] D. Riveline, E. Zamir, N. Q. Balaban, U. S. Schwarz, T. Ishizaki, S. Narumiya, Z. Kam, B. Geiger, A. D. Bershadsky, *J Cell Biol* **2001**, 153, 1175.

[152] D. R. Stabley, C. Jurchenko, S. S. Marshall, K. S. Salaita, *Nat Methods* **2011**, 9, 64; Y. Liu, K. Yehl, Y. Narui, K. Salaita, *J Am Chem Soc* **2013**, 135, 5320.

[153] K. Lee, Y. Cui, L. P. Lee, J. Irudayaraj, *Nat Nanotechnol* **2014**, 9, 474.

[154] C. Lambertz, A. Martos, A. Henkel, A. Neiser, T. T. Kliesch, A. Janshoff, P. Schwille, C. Sönnichsen, *Nano Lett* **2016**, 16, 3540.

[155] L. Zhang, Y. Li, D. W. Li, C. Jing, X. Chen, M. Lv, Q. Huang, Y. T. Long, I. Willner, *Angew Chem Int Ed Engl* **2011**, 50, 6789.

[156] Y. Liu, J. R. Ashton, E. J. Moding, H. Yuan, J. K. Register, A. M. Fales, J. Choi, M. J. Whitley, X. Zhao, Y. Qi, Y. Ma, G. Vaidyanathan, M. R. Zalutsky, D. G. Kirsch, C. T. Badea, T. Vo-Dinh, *Theranostics* **2015**, 5, 946.

[157] E. D. SoRelle, O. Liba, J. L. Campbell, R. Dalal, C. L. Zavaleta, A. de la Zerda, *Elife* **2016**, 5.

[158] O. Betzer, N. Perets, A. Angel, M. Motiei, T. Sadan, G. Yadid, D. Offen, R. Popovtzer, *ACS Nano* **2017**, 11, 10883.

[159] C. Sonnichsen, B. Reinhard, J. Liphardt, A. Alivisatos, *Nature Biotechnology* **2005**, 23, 741; Y. Cui, J. Irudayaraj, *Wiley Interdiscip Rev Nanomed Nanobiotechnol* **2015**, 7, 387.

[160] H. Ueno, S. Nishikawa, R. Iino, K. V. Tabata, S. Sakakihara, T. Yanagida, H. Noji, *Biophys J* **2010**, 98, 2014.

[161] P. Zhang, S. Lee, H. Yu, N. Fang, S. H. Kang, *Sci Rep* **2015**, 5, 11447.

[162] X. Cheng, X. Cao, B. Xiong, Y. He, E. Yeung, *Nano Research* **2017**, 10, 1423.

[163] K. Chen, **2015**, Graduate Theses and Dissertations.

[164] T. M., I. D., Y. E.S., *Journal of Microscopy* **2008**, 232, 207.

[165] J. Zhu, J. He, J. Y. Chen, D.-R. Lu, L. Zhou, **2008**; E. D. Salmon, P. Tran, in *Methods in Cell Biology*, Vol. 72 (Eds: L. Wilson, P. Matsudaira), Academic Press **2003**, p. 289; N. E. Ziv, J. Schiller, *CSH Protoc* **2007**, 2007, pdb prot4787.

[166] A. S. Stender, K. Marchuk, C. Liu, S. Sander, M. W. Meyer, E. A. Smith, B. Neupane, G. Wang, J. Li, J. X. Cheng, B. Huang, N. Fang, *Chem Rev* **2013**, 113, 2469.

[167] W. Sun, G. Wang, N. Fang, E. S. Yeung, *Anal Chem* **2009**, 81, 9203.

[168] B. D. Chithrani, W. C. Chan, *Nano Lett* **2007**, 7, 1542.

[169] F. Zhao, K. Chen, B. Dong, K. Yang, Y. Gu, N. Fang, *Opt Express* **2017**, 25, 9860.

[170] J. Chen, Y. Xu, X. Lv, X. Lai, S. Zeng, *Opt Express* **2013**, 21, 112.

[171] Y. Gu, X. Di, W. Sun, G. Wang, N. Fang, *Anal Chem* **2012**.

[172] Y. Gu, G. Wang, N. Fang, *Acs Nano* **2013**, 7, 1658.

[173] K. Chen, Y. Gu, W. Sun, Bin Dong, G. Wang, X. Fan, T. Xia, N. Fang, *Nat Commun* **2017**, 8, 887.

[174] A. E. Augspurger, A. S. Stender, R. Han, N. Fang, *Anal Chem* **2014**, 86, 1196.

[175] P. Kukura, H. Ewers, C. Müller, A. Renn, A. Helenius, V. Sandoghdar, *Nat Methods* **2009**, 6, 923.

[176] J. Ortega-Arroyo, P. Kukura, *Phys Chem Chem Phys* **2012**, 14, 15625.

[177] K. J. Mickolajczyk, N. C. Deffenbaugh, J. O. Arroyo, J. Andrecka, P. Kukura, W. O. Hancock, *Proc Natl Acad Sci U S A* **2015**, 112, E7186.

[178] J. Andrecka, Y. Takagi, K. Mickolajczyk, L. Lippert, J. Sellers, W. Hancock, Y. Goldman, P. Kukura, M. Spies, Y. Chemla, *Single-Molecule Enzymology: Fluorescence-Based and High-Throughput Methods* **2016**, 581, 517.

[179] K. J. Mickolajczyk, E. A. Geyer, T. Kim, L. M. Rice, W. O. Hancock, *bioRxiv* **2018**, 418053.

[180] C. L. Hsieh, S. Spindler, J. Ehrig, V. Sandoghdar, *J Phys Chem B* **2014**, 118, 1545.

[181] H. M. Wu, Y. H. Lin, T. C. Yen, C. L. Hsieh, *Sci Rep* **2016**, 6, 20542.

[182] D. Nedosekin, E. Galanzha, E. Dervishi, A. Biris, V. Zharov, *Small* **2014**, 10, 135.

[183] D. Boyer, P. Tamarat, A. Maali, B. Lounis, M. Orrit, *Science* **2002**, 297, 1160.

[184] J. F. Li, Y. F. Huang, Y. Ding, Z. L. Yang, S. B. Li, X. S. Zhou, F. R. Fan, W. Zhang, Z. Y. Zhou, D. Y. Wu, B. Ren, Z. L. Wang, Z. Q. Tian, *Nature* **2010**, 464, 392.

[185] K. L. Wustholz, A. I. Henry, J. M. McMahon, R. G. Freeman, N. Valley, M. E. Piotti, M. J. Natan, G. C. Schatz, R. P. Van Duyne, *J Am Chem Soc* **2010**, 132, 10903.

[186] F. De Angelis, F. Gentile, F. Mecarini, G. Das, M. Moretti, P. Candeloro, M. Coluccio, G. Cojoc, A. Accardo, C. Liberale, R. Zaccaria, G. Perozziello, L. Tirinato, A. Toma, G. Cuda, R. Cingolani, E. Di Fabrizio, *Nature Photonics* **2011**, 5, 683.

[187] S. Yang, X. Dai, B. Stogin, T. Wong, *Proceedings of the National Academy of Sciences of the United States of America* **2016**, 113, 268.

[188] S. Tanwar, K. K. Haldar, T. Sen, *J Am Chem Soc* **2017**, 139, 17639.

[189] P. Zhan, T. Wen, Z. G. Wang, Y. He, J. Shi, T. Wang, X. Liu, G. Lu, B. Ding, *Angew Chem Int Ed Engl* **2018**, 57, 2846.

[190] J. Ando, K. Fujita, N. I. Smith, S. Kawata, *Nano Lett* **2011**, 11, 5344.

[191] K. C. Huang, K. Bando, J. Ando, N. I. Smith, K. Fujita, S. Kawata, *Methods* **2014**, 68, 348.

[192] M. R. Ali, Y. Wu, T. Han, X. Zang, H. Xiao, Y. Tang, R. Wu, F. M. Fernández, M. A. El-Sayed, *J Am Chem Soc* **2016**, 138, 15434.

[193] C. Sun, M. Gao, X. Zhang, *Anal Bioanal Chem* **2017**, 409, 4915.

[194] R. Lahr, P. Vikesland, *Acs Sustainable Chemistry & Engineering* **2014**, 2, 1599.

[195] X. Qian, X. H. Peng, D. O. Ansari, Q. Yin-Goen, G. Z. Chen, D. M. Shin, L. Yang, A. N. Young, M. D. Wang, S. Nie, *Nat Biotechnol* **2008**, 26, 83.

[196] Y. Wang, S. Kang, A. Khan, G. Ruttner, S. Y. Leigh, M. Murray, S. Abeytunge, G. Peterson, M. Rajadhyaksha, S. Dintzis, S. Javid, J. T. Liu, *Sci Rep* **2016**, 6, 21242.

[197] L. Sinha, Y. Wang, C. Yang, A. Khan, J. G. Brankov, J. T. Liu, K. M. Tichauer, *Sci Rep* **2015**, 5, 8582.

[198] M. F. Kircher, A. de la Zerda, J. V. Jokerst, C. L. Zavaleta, P. J. Kempen, E. Mittra, K. Pitter, R. Huang, C. Campos, F. Habte, R. Sinclair, C. W. Brennan, I. K. Mellinghoff, E. C. Holland, S. S. Gambhir, *Nat Med* **2012**, 18, 829.

[199] M. F. Kircher, *Nanomedicine (Lond)* **2017**, 12, 171.

[200] N. Stone, K. Faulds, D. Graham, P. Matousek, *Anal Chem* **2010**, 82, 3969.

[201] G. von Maltzahn, A. Centrone, J. H. Park, R. Ramanathan, M. J. Sailor, T. A. Hatton, S. N. Bhatia, *Adv Mater* **2009**, 21, 3175.

[202] J. Qian, L. Jiang, F. Cai, D. Wang, S. He, *Biomaterials* **2011**, 32, 1601.

[203] J. W. Kang, P. T. So, R. R. Dasari, D. K. Lim, *Nano Lett* **2015**, 15, 1766.

[204] N. Gandra, S. Singamaneni, *Adv Mater* **2013**, 25, 1022.

[205] E. P. Perillo, Y.-L. Liu, K. Huynh, C. Liu, C.-K. Chou, M.-C. Hung, H.-C. Yeh, A. K. Dunn, *Nature Communications* **2015**, 6, 7874; E. Toprak, H. Balci, B. H. Blehm, P. R. Selvin, *Nano Letters* **2007**, 7, 2043; M. Speidel, A. Jonáš, E.-L. Florin, *Opt. Lett.* **2003**, 28, 69; S. R. P. Pavani, R. Piestun, *Opt. Express* **2008**, 16, 22048; B. Huang, W. Wang, M. Bates, X. Zhuang, *Science* **2008**, 319, 810.

[206] K. A. Willets, A. J. Wilson, V. Sundaresan, P. B. Joshi, *Chem Rev* **2017**, 117, 7538.

[207] W. Sun, E. Boulais, Y. Hakobyan, W. L. Wang, A. Guan, M. Bathe, P. Yin, *Science* **2014**, 346, 1258361; X. Lan, X. Lu, C. Shen, Y. Ke, W. Ni, Q. Wang, *J Am Chem Soc* **2015**, 137, 457; L. Sun, H. Lin, D. J. Park, M. R. Bourgeois, M. B. Ross, J. C. Ku, G. C. Schatz, C. A. Mirkin, *Nano Lett* **2017**, 17, 2313; M. B. Ross, J. C. Ku, V. M. Vaccarezza, G. C. Schatz, C. A. Mirkin, *Nat Nanotechnol* **2015**, 10, 453.

[208] J. Park, M. Kim, J. Hwang, J. Nam, *Small Methods* **2017**, 1.

[209] X. M. Qian, X. H. Peng, D. O. Ansari, Q. Yin-Goen, G. Z. Chen, D. M. Shin, L. Yang, A. N. Young, M. D. Wang, S. M. Nie, *Nature Biotechnology* **2008**, 26, 83.

[210] J. Kneipp, H. Kneipp, K. Kneipp, *Chemical Society Reviews* **2008**, 37, 1052.

[211] C. X. Ma, J. M. Harris, *Applied Spectroscopy* **2013**, 67, 801.

[212] L. A. Austin, B. Kang, M. A. El-Sayed, *Nano Today* **2015**, 10, 542.

[213] P. K. Jain, X. H. Huang, I. H. El-Sayed, M. A. El-Sayed, *Accounts of Chemical Research* **2008**, 41, 1578.

[214] K. A. Willets, R. P. Van Duyne, in *Annual Review of Physical Chemistry*, Vol. 58, Annual Reviews, Palo Alto **2007**, p. 267.

[215] P. L. Stiles, J. A. Dieringer, N. C. Shah, R. R. Van Duyne, in *Annual Review of Analytical Chemistry*, Vol. 1, Annual Reviews, Palo Alto **2008**, p. 601.

[216] B. Kang, L. A. Austin, M. A. El-Sayed, *Acs Nano* **2014**, 8, 4883.

[217] S. Keskin, E. Efeoglu, K. Kececi, M. Culha, *Journal of Biomedical Optics* **2013**, 18.

[218] A. M. Alkilany, L. B. Thompson, S. P. Boulos, P. N. Sisco, C. J. Murphy, *Advanced Drug Delivery Reviews* **2012**, 64, 190.

[219] X. H. Huang, I. H. El-Sayed, W. Qian, M. A. El-Sayed, *Journal of the American Chemical Society* **2006**, 128, 2115.

[220] Z. M. Li, P. Huang, X. J. Zhang, J. Lin, S. Yang, B. Liu, F. Gao, P. Xi, Q. S. Ren, D. X. Cui, *Molecular Pharmaceutics* **2010**, 7, 94; T. Niidome, Y. Akiyama, M. Yamagata, T. Kawano, T. Mori, Y. Niidome, Y. Katayama, *Journal of Biomaterials Science-Polymer Edition* **2009**, 20, 1203.

[221] X. H. Peng, M. A. Macke, H. J. C. Shin, S. Nannapaneni, N. Chen, S. Kim, Z. Chen, M. A. El-Sayed, D. Shin, *Cancer Research* **2015**, 75.

[222] E. B. Dickerson, E. C. Dreaden, X. Huang, I. H. El-Sayed, H. Chu, S. Pushpanketh, J. F. McDonald, M. A. El-Sayed, *Cancer letters* **2008**, 269, 57.

[223] M. R. Ali, H. R. Ali, C. R. Rankin, M. A. El-Sayed, *Biomaterials* **2016**, 102, 1.

[224] M. Aioub, B. Kang, M. A. Mackey, M. A. El-Sayed, *Journal of Physical Chemistry Letters* **2014**, 5, 2555.

[225] G. Y. Zhu, X. Zhu, Q. Fan, X. L. Wan, *Spectrochimica Acta Part a-Molecular and Biomolecular Spectroscopy* **2011**, 78, 1187.

[226] N. C. Maiti, M. M. Apetri, M. G. Zagorski, P. R. Carey, V. E. Anderson, *Journal of the American Chemical Society* **2004**, 126, 2399.

[227] G. L. ELLMAN, *Arch Biochem Biophys* **1959**, 82, 70.

[228] M. R. K. Ali, B. Snyder, M. A. El-Sayed, *Langmuir* **2012**, 28, 9807.

[229] M. A. Mackey, M. R. K. Ali, L. A. Austin, R. D. Near, M. A. El-Sayed, *Journal of Physical Chemistry B* **2014**, 118, 1319.

[230] G. Prencipe, S. M. Tabakman, K. Welsher, Z. Liu, A. P. Goodwin, L. Zhang, J. Henry, H. Dai, *Journal of the American Chemical Society* **2009**, 131, 4783.

[231] E. Ruoslahti, M. D. Pierschbacher, *Cell* **1986**, 44, 517.

[232] D. Kalderon, B. L. Roberts, W. D. Richardson, A. E. Smith, *Cell* **1984**, 39, 499.

[233] M. R. K. Ali, S. R. Panikkanvalappil, M. A. El-Sayed, *Journal of the American Chemical Society* **2014**, 136, 4464.

[234] M. R. K. Ali, H. R. Ali, C. R. Rankin, M. A. El-Sayed, *Biomaterials* **2016**, 102, 1.

[235] S. R. Panikkanvalappil, M. A. Mackey, M. A. El-Sayed, *Journal of the American Chemical Society* **2013**, 135, 4815.

[236] S. R. Panikkanvalappil, S. M. Hira, M. A. Mahmoud, M. A. El-Sayed, *Journal of the American Chemical Society* **2014**, 136, 15961.

[237] B. Kang, L. A. Austin, M. A. El-Sayed, *Nano Letters* **2012**, 12, 5369.

[238] S. P. A. Fodor, R. A. Copeland, C. A. Grygon, T. G. Spiro, *Journal of the American Chemical Society* **1989**, 111, 5509.

[239] B. Hernandez, F. Pfluger, S. G. Kruglik, M. Ghomi, *Journal of Raman Spectroscopy* **2013**, 44, 827; J. J. Zhang, Q. Huang, G. H. Yao, Z. G. Ke, H. Zhang, Y. L. Lu, *Journal of Molecular Structure* **2014**, 1072, 195.

[240] S. R. Panikkanvalappil, S. M. Hira, M. A. El-Sayed, *Chem Sci* **2016**, 7, 1133.

[241] S. K. Kim, M. S. Kim, S. W. Suh, *Journal of Raman Spectroscopy* **1987**, 18, 171.

[242] M. Okada, N. I. Smith, A. F. Palonpon, H. Endo, S. Kawata, M. Sodeoka, K. Fujita, *Proceedings of the National Academy of Sciences of the United States of America* **2012**, 109, 28.

[243] K. Hamada, K. Fujita, N. I. Smith, M. Kobayashi, Y. Inouye, S. Kawata, *Journal of Biomedical Optics* **2008**, 13.

[244] Y. Wu, F. Wang, Z. Liu, H. Qin, C. Song, J. Huang, Y. Bian, X. Wei, J. Dong, H. Zou, *Chem Commun (Camb)* **2014**, 50, 1708.

[245] Y. W. Lo, S. T. Lin, S. J. Chang, C. H. Chan, K. W. Lyu, J. F. Chang, E. W. May, D. Y. Lin, H. C. Chou, H. L. Chan, *J Cell Mol Med* **2015**, 19, 744.

[246] V. M. Gonzalez, M. A. Fuertes, C. Alonso, J. M. Perez, *Molecular pharmacology* **2001**, 59, 657.

[247] T. Kageyama, R. Nagashio, S. Ryuge, T. Matsumoto, A. Iyoda, Y. Satoh, N. Masuda, S. X. Jiang, M. Saegusa, Y. Sato, *Asian Pac J Cancer Prev* **2011**, 12, 3457.

[248] X. Huang, Z. Lu, Z. Lv, T. Yu, P. Yang, Y. Shen, Y. Ding, D. Fu, X. Zhang, Q. Fu, Y. Yu, *Plos One* **2013**, 8, e71553.

[249] A. Sato, A. Hiramoto, A. Satake, E. Miyazaki, T. Naito, Y. Wataya, H. S. Kim, *Nucleosides Nucleotides Nucleic Acids* **2008**, 27, 433.

[250] A. Freund, R. M. Laberge, M. Demaria, J. Campisi, *Mol Biol Cell* **2012**, 23, 2066.

[251] L. Rao, D. Perez, E. White, *J Cell Biol* **1996**, 135, 1441.

[252] J. Zha, H. Harada, E. Yang, J. Jockel, S. J. Korsmeyer, *Cell* **1996**, 87, 619; A. Schurmann, A. F. Mooney, L. C. Sanders, M. A. Sells, H. G. Wang, J. C. Reed, G. M. Bokoch, *Mol Cell Biol* **2000**, 20, 453; S. Jin, Y. Zhuo, W. Guo, J. Field, *J Biol Chem* **2005**, 280, 24698.

[253] T. Iwasaki, T. Katayama, K. Kohama, Y. Endo, T. Sawasaki, *Mol Biol Cell* **2013**, 24, 748.

[254] N. Fehrenbacher, L. Bastholm, T. Kirkegaard-Sorensen, B. Rafn, T. Bottzauw, C. Nielsen, E. Weber, S. Shirasawa, T. Kallunki, M. Jaattela, *Cancer Res* **2008**, 68, 6623.

[255] Y. Zhang, X. Gu, X. Yuan, *European Journal of Neuroscience* **2007**, 25, 1341; M. Koyanagi, J. Takahashi, Y. Arakawa, D. Doi, H. Fukuda, H. Hayashi, S. Narumiya, N. Hashimoto, *J Neurosci Res* **2008**, 86, 270.

[256] S. Kaufman, *Adv Enzymol Relat Areas Mol Biol* **1993**, 67, 77; A. Martinez, P. M. Knappskog, S. Olafsdottir, A. P. Doskeland, H. G. Eiken, R. M. Svebak, M. Bozzini, J. Apold, T. Flatmark, *Biochem J* **1995**, 306 (Pt 2), 589; N. Moller, S. Meek, M. Bigelow, J. Andrews, K. S. Nair, *Proc Natl Acad Sci U S A* **2000**, 97, 1242.

[257] B. Kang, M. A. Mackey, M. A. El-Sayed, *J Am Chem Soc* **2010**, 132, 1517.

[258] D. Vanhecke, L. Rodriguez-Lorenzo, M. Clift, F. Blank, A. Petri-Fink, B. Rothen-Rutishauser, *Nanomedicine* **2014**, 9, 1885.

[259] E. Cho, Q. Zhang, Y. Xia, *Nature Nanotechnology* **2011**, 6, 385.

[260] J. Park, M. K. Ha, N. Yang, T. H. Yoon, *Anal Chem* **2017**, 89, 2449.

[261] X. Liu, M. Atwater, J. Wang, Q. Huo, *Colloids Surf B Biointerfaces* **2007**, 58, 3; C. J. Orendorff, C. J. Murphy, *J Phys Chem B* **2006**, 110, 3990.

[262] H. Suzuki, T. Toyooka, Y. Ibuki, *Environ Sci Technol* **2007**, 41, 3018.

[263] R. M. Zucker, K. M. Daniel, *Methods Mol Biol* **2012**, 906, 497.

[264] Y. Ibuki, T. Toyooka, *Methods Mol Biol* **2012**, 926, 157.

[265] R. M. Zucker, K. M. Daniel, E. J. Massaro, S. J. Karafas, L. L. Degn, W. K. Boyes, *Cytometry A* **2013**, 83, 962; C. Greulich, J. Diendorf, T. Simon, G. Eggeler, M. Epple, M. Köller, *Acta Biomater* **2011**, 7, 347.

[266] Y. Toduka, T. Toyooka, Y. Ibuki, *Environ Sci Technol* **2012**, 46, 7629.

[267] R. P. Friedrich, C. Janko, M. Poettler, P. Tripal, J. Zaloga, I. Cicha, S. Dürr, J. Nowak, S. Odenbach, I. Slabu, M. Liebl, L. Trahms, M. Stapf, I. Hilger, S. Lyer, C. Alexiou, *Int J Nanomedicine* **2015**, 10, 4185.

[268] I. J. Fidler, *Nature reviews. Cancer* **2003**, 3, 453.

[269] F. Morgillo, H. Y. Lee, *Drug resistance updates : reviews and commentaries in antimicrobial and anticancer chemotherapy* **2005**, 8, 298.

[270] *Lancet (London, England)* **2005**, 365, 1687.

[271] L. R. Hirsch, R. J. Stafford, J. A. Bankson, S. R. Sershen, B. Rivera, R. E. Price, J. D. Hazle, N. J. Halas, J. L. West, *Proceedings of the National Academy of Sciences* **2003**, 100, 13549.

[272] M. R. Ali, I. M. Ibrahim, H. R. Ali, S. A. Selim, M. A. El-Sayed, *International Journal of Nanomedicine* **2016**, 11, 4849.

[273] H. R. Ali, M. R. Ali, Y. Wu, S. A. Selim, H. F. Abdelaal, E. A. Nasr, M. A. El-Sayed, *Bioconjugate Chemistry* **2016**, 27, 2486.

[274] Y.-w. Jun, Y.-M. Huh, J.-s. Choi, J.-H. Lee, H.-T. Song, KimKim, S. Yoon, K.-S. Kim, J.-S. Shin, J.-S. Suh, J. Cheon, *Journal of the American Chemical Society* **2005**, 127, 5732; P. K. Jain, K. S. Lee, I. H. El-Sayed, M. A. El-Sayed, *The Journal of Physical Chemistry B* **2006**, 110, 7238; M. R. Ali, S. R. Panikkanvalappil, M. A. El-Sayed, *Journal of the American Chemical Society* **2014**, 136, 4464.

[275] F. Danhier, O. Feron, V. Preat, *Journal of controlled release : official journal of the Controlled Release Society* **2010**, 148, 135; E. B. Dickerson, W. H. Blackburn, M. H. Smith, L. B. Kapa, L. A. Lyon, J. F. McDonald, *BMC Cancer* **2010**, 10, 10.

[276] R. R. Arvizo, S. Saha, E. Wang, J. D. Robertson, R. Bhattacharya, P. Mukherjee, *Proceedings of the National Academy of Sciences of the United States of America* **2013**, 110, 6700.

[277] V. Swaminathan, K. Mythreye, E. T. O'Brien, A. Berchuck, G. C. Blobe, R. Superfine, *Cancer research* **2011**, 71, 5075.

[278] S. E. Cross, Y. S. Jin, J. Tondre, R. Wong, J. Rao, J. K. Gimzewski, *Nanotechnology* **2008**, 19, 384003; D. Wirtz, K. Konstantopoulos, P. C. Searson, *Nature reviews. Cancer* **2011**, 11, 512.

[279] L. A. Lautscham, C. Kammerer, J. R. Lange, T. Kolb, C. Mark, A. Schilling, P. L. Strissel, R. Strick, C. Gluth, A. C. Rowat, C. Metzner, B. Fabry, *Biophysical journal* **2015**, 109, 900.

[280] K. N. Dahl, A. J. S. Ribeiro, J. Lammerding, *Circulation Research* **2008**, 102, 1307; P. Isermann, J. Lammerding, *Current Biology* **2013**, 23, R1113; A. L. McGregor, C. R. Hsia, J. Lammerding, *Current opinion in cell biology* **2016**, 40, 32.

[281] J. Swift, I. L. Ivanovska, A. Buxboim, T. Harada, P. C. Dingal, J. Pinter, J. D. Pajerowski, K. R. Spinler, J. W. Shin, M. Tewari, F. Rehfeldt, D. W. Speicher, D. E. Discher, *Science* **2013**, 341, 1240104.

[282] T. Harada, J. Swift, J. Irianto, J. W. Shin, K. R. Spinler, A. Athirasala, R. Diegmiller, P. C. Dingal, I. L. Ivanovska, D. E. Discher, *The Journal of cell biology* **2014**, 204, 669.

[283] J. S. Lee, C. M. Hale, P. Panorchan, S. B. Khatau, J. P. George, Y. Tseng, C. L. Stewart, D. Hodzic, D. Wirtz, *Biophys J* **2007**, 93, 2542; P. M. Davidson, C. Denais, M. C. Bakshi, J. Lammerding, *Cell Mol Bioeng* **2014**, 7, 293.

[284] L. Kong, G. Schafer, H. J. Bu, Y. Zhang, Y. X. Zhang, H. Klocker, *Carcinogenesis* **2012**, 33, 751.

[285] M. A. Mackey, M. R. K. Ali, L. A. Austin, R. D. Near, M. A. El-Sayed, *The Journal of Physical Chemistry B* **2014**, 118, 1319.

[286] B. Kang, L. A. Austin, M. A. El-Sayed, *ACS Nano* **2014**, 8, 4883.

[287] L. A. Austin, S. Ahmad, B. Kang, K. R. Rommel, M. Mahmoud, M. E. Peek, M. A. El-Sayed, *Toxicology in Vitro* **2015**, 29, 694.

[288] G. Bao, S. Suresh, *Nature Materials* **2003**, 2, 715.

[289] S. E. Cross, Y. S. Jin, J. Rao, J. K. Gimzewski, *Nature Nanotechnology* **2007**, 2, 780.

[290] S. E. Cross, Y. S. Jin, J. Rao, J. K. Gimzewski, *Nat Nanotechnol* **2007**, 2, 780.

[291] C. C. Liang, A. Y. Park, J. L. Guan, *Nature protocols* **2007**, 2, 329.

[292] J. L. Hutter, J. Bechhoefer, *Rev. Sci. Instrum.* **1993**, 64, 3342; A. Renger, *ZAMM - Journal of Applied Mathematics and Mechanics / Zeitschrift für Angewandte Mathematik und Mechanik* **1989**, 69, 214.

[293] W. W. Xu, N. Chahine, T. Suchek, *Langmuir* **2011**, 27, 8470.

[294] B. D. Chithrani, A. A. Ghazani, W. C. W. Chan, *Nano Letters* **2006**, 6, 662.

[295] I. H. El-Sayed, X. H. Huang, M. A. El-Sayed, *Nano Letters* **2005**, 5, 829.

[296] G. Prencipe, S. M. Tabakman, K. Welsher, Z. Liu, A. P. Goodwin, L. Zhang, J. Henry, H. J. Dai, *J. Am. Chem. Soc.* **2009**, 131, 4783.

[297] H. R. Ali, M. R. K. Ali, Y. Wu, S. A. Selim, H. F. M. Abdelaal, E. A. Nasr, M. A. El-Sayed, *Bioconjugate Chemistry* **2016**.

[298] W. W. Xu, R. Mezencev, B. Kim, L. J. Wang, J. McDonald, T. Sulchek, *Plos One* **2012**, 7.

[299] E. C. Cho, Y. Liu, Y. N. Xia, *Angewandte Chemie-International Edition* **2010**, 49, 1976.

[300] E. C. Cho, Q. Zhang, Y. N. Xia, *Nature nanotechnology* **2011**, 6, 385.

[301] A. Pietuch, B. R. Bruckner, D. Schneider, M. Tarantola, C. Rosman, C. Sonnichsen, A. Janshoff, *Beilstein Journal of Nanotechnology* **2015**, 6, 223; C. W. Lee, L. L. Jang, H. J. Pan, Y. R. Chen, C. C. Chen, C. H. Lee, *Journal of Nanobiotechnology* **2016**, 14.

[302] B. Kang, M. A. Mackey, M. A. El-Sayed, *Journal of the American Chemical Society* **2010**, 132, 1517.

[303] S. Patel, D. Jung, P. T. Yin, P. Carlton, M. Yamamoto, T. Bando, H. Sugiyama, K. B. Lee, *Acs Nano* **2014**, 8, 8959.

[304] G. F. Wang, A. S. Stender, W. Sun, N. Fang, *Analyst* **2010**, 135, 215; A. S. Stender, K. Marchuk, C. Liu, S. Sander, M. W. Meyer, E. A. Smith, B. Neupane, G. Wang, J. Li, J.-X. Cheng, B. Huang, N. Fang, *Chem. Rev.* **2013**, 113, 2469; W. Sun, G. Wang, N. Fang, E. S. Yeung, *Anal. Chem.* **2009**, 81, 9203.

[305] P. L. Paine, *Journal of Cell Biology* **1975**, 66, 652.

[306] J. D. Pajerowski, K. N. Dahl, F. L. Zhong, P. J. Sammak, D. E. Discher, *Proceedings of the National Academy of Sciences of the United States of America* **2007**, 104, 15619.

[307] J. Lammerding, L. G. Fong, J. Y. Ji, K. Reue, C. L. Stewart, S. G. Young, R. T. Lee, *J Biol Chem* **2006**, 281, 25768.

[308] E. C. Dreaden, M. A. Mackey, X. H. Huang, B. Kang, M. A. El-Sayed, *Chemical Society Reviews* **2011**, 40, 3391.

[309] P. Sandin, L. W. Fitzpatrick, J. C. Simpson, K. A. Dawson, *Acs Nano* **2012**, 6, 1513; A. J. Kim, N. J. Boylan, J. S. Suk, S. K. Lai, J. Hanes, *Journal of Controlled Release* **2012**, 158, 102.

[310] Z. Q. Chu, K. K. Miu, P. S. Lung, S. L. Zhang, S. S. Zhao, H. C. Chang, G. Lin, Q. Li, *Scientific Reports* **2015**, 5; M. Morille, C. Passirani, A. Vonarbourg, A. Clavreul, J. P. Benoit, *Biomaterials* **2008**, 29, 3477.

[311] M. R. K. Ali, Y. Wu, T. G. Hang, X. L. Zang, H. P. Xiao, Y. Tang, R. H. Wu, F. M. Fernandez, M. A. El-Sayed, *Journal of the American Chemical Society* **2016**, 138, 15434.

[312] A. C. Rowat, J. Lammerding, J. H. Ipsen, *Biophysical journal* **2006**, 91, 4649.

[313] Y. Ge, M. Bruno, K. Wallace, W. Winnik, R. Y. Prasad, *Proteomics* **2011**, 11, 2406.

[314] J. Lammerding, J. Hsiao, P. C. Schulze, S. Kozlov, C. L. Stewart, R. T. Lee, *Journal of Cell Biology* **2005**, 170, 781; J. M. Berk, K. E. Tifft, K. L. Wilson, *Nucleus-Austin* **2013**, 4, 298.

[315] H. S. Choi, W. Liu, P. Misra, E. Tanaka, J. P. Zimmer, B. I. Ipe, M. G. Bawendi, J. V. Frangioni, *Nature Biotechnology* **2007**, 25, 1165.

[316] M. Semmler-Behnke, W. G. Kreyling, J. Lipka, S. Fertsch, A. Wenk, S. Takenaka, G. Schmid, W. Brandau, *Small* **2008**, 4, 2108.

[317] E. Sadauskas, G. Danscher, M. Stoltenberg, U. Vogel, A. Larsen, H. Wallin, *Nanomedicine-Nanotechnology Biology and Medicine* **2009**, 5, 162.

[318] C. Dumontet, M. A. Jordan, *Nat Rev Drug Discov* **2010**, 9, 790.

[319] J. R. Stehn, N. K. Haass, T. Bonello, M. Desouza, G. Kottyan, H. Treutlein, J. Zeng, P. R. B. B. Nascimento, V. B. Sequeira, T. L. Butler, M. Allanson, T. Fath, T. A. Hill, A. McCluskey, G. Schevzov, S. J. Palmer, E. C. Hardeman, D. Winlaw, V. E. Reeve, I. Dixon, W. Weninger, T. P. Cripe, P. W. Gunning, *Cancer Research* **2013**, 73, 5169.

[320] R. A. Patel, Y. Liu, B. Wang, R. Li, S. M. Sebti, *Oncogene* **2014**, 33, 550; R. Prudent, E. Vassal-Stermann, C. H. Nguyen, C. Pillet, A. Martinez, C. Prunier, C. Barette, E. Soleilhac, O. Filhol, A. Beghin, G. Valdameri, S. Honore, S. Aci-Seche, D. Grierson, J. Antonipillai, R. Li, A. Di Pietro, C. Dumontet, D. Braguer, J. C. Florent, S. Knapp, O. Bernard, L. Lafanechere, *Cancer Research* **2012**, 72, 4429.

[321] S. Banerjee, D. J. Hwang, W. Li, D. D. Miller, *Molecules* **2016**, 21.

[322] R. R. Arvizo, S. Saha, E. F. Wang, J. D. Robertson, R. Bhattacharya, P. Mukherjee, *Proceedings of the National Academy of Sciences of the United States of America* **2013**, 110, 6700.

[323] L. Yildirimer, N. T. K. Thanh, M. Loizidou, A. M. Seifalian, *Nano Today* **2011**, 6, 585; W. S. Lin, Y. W. Huang, X. D. Zhou, Y. F. Ma, *Toxicology and Applied Pharmacology* **2006**, 217, 252; Z. Pan, W. Lee, L. Slutsky, R. A. F. Clark, N. Pernodet, M. H. Rafailovich, *Small* **2009**, 5, 511.

[324] M. Ali, Y. Wu, D. Ghosh, B. Do, K. Chen, M. Dawson, N. Fang, T. Sulchek, M. El-Sayed, *ACS nano* **2017**.

[325] L. Parrotta, C. Faleri, M. Cresti, G. Cai, *Planta* **2016**, 243, 43; W. T. Coakley, *Symposia of the Society for Experimental Biology* **1987**, 41, 187; L. P. Gavrilova, I. I. Korpacheva, S. G. Semushina, V. A. Yashin, *Cell and Tissue Biology* **2013**, 7, 54.

[326] E. B. Dickerson, E. C. Dreaden, X. H. Huang, I. H. El-Sayed, H. H. Chu, S. Pushpanketh, J. F. McDonald, M. A. El-Sayed, *Cancer Letters* **2008**, 269, 57.

[327] J. Wang, G. Zhu, M. You, E. Song, M. I. Shukoor, K. Zhang, M. B. Altman, Y. Chen, Z. Zhu, C. Z. Huang, W. Tan, *ACS Nano* **2012**, 6, 5070; H. Sugimoto, T. Chen, R. Wang, M. Fujii, B. M. Reinhard, L. Dal Negro, *ACS Photonics* **2015**, 2, 1298; B. Nikoobakht, M. A. El-Sayed, *Chemistry of Materials* **2003**, 15, 1957.

[328] K. A. DeMali, K. Wennerberg, K. Burridge, *Current opinion in cell biology* **2003**, 15, 572; A. J. Ridley, M. A. Schwartz, K. Burridge, R. A. Firtel, M. H. Ginsberg, G. Borisy, J. T. Parsons, A. R. Horwitz, *Science* **2003**, 302, 1704.

[329] A. Howe, A. E. Aplin, S. K. Alahari, R. L. Juliano, *Curr Opin Cell Biol* **1998**, 10, 220.

[330] N. Chattopadhyay, Z. Wang, L. K. Ashman, S. M. Brady-Kalnay, J. A. Kreidberg, *The Journal of Cell Biology* **2003**, 163, 1351; F. Zhang, C. C. Tom, M. C. Kugler, T. T. Ching, J. A. Kreidberg, Y. Wei, H. A. Chapman, *J Cell Biol* **2003**, 163, 177.

[331] A. Kren, V. Baeriswyl, F. Lehembre, C. Wunderlin, K. Strittmatter, H. Antoniadis, R. Fassler, U. Cavallaro, G. Christofori, *Embo Journal* **2007**, 26, 2832.

[332] B. Feldinghabermann, B. M. Mueller, C. A. Romerdahl, D. A. Cheresh, *J Clin Invest* **1992**, 89, 2018; E. J. Filardo, P. C. Brooks, S. L. Deming, C. Damsky, D. A. Cheresh, *J Cell Biol* **1995**, 130, 441.

[333] E. Ruoslahti, M. D. Pierschbacher, *Cell* 44, 517.

[334] E. Ruoslahti, *Annual Review of Cell and Developmental Biology* **1996**, 12, 697; J. D. Humphries, A. Byron, M. J. Humphries, *Journal of cell science* **2006**, 119, 3901.

[335] H. D. Han, L. S. Mangala, J. W. Lee, M. M. K. Shahzad, H. S. Kim, D. Y. Shen, E. J. Nam, E. M. Mora, R. L. Stone, C. H. Lu, S. J. Lee, J. W. Roh, A. M. Nick, G. Lopez-Berestein, A. K. Sood, *Clinical Cancer Research* **2010**, 16, 3910.

[336] Y. Wu, F. J. Wang, Z. Y. Liu, H. Q. Qin, C. X. Song, J. F. Huang, Y. Y. Bian, X. L. Wei, J. Dong, H. F. Zou, *Chemical Communications* **2014**, 50, 1708.

[337] C. Choudhary, C. Kumar, F. Gnad, M. L. Nielsen, M. Rehman, T. C. Walther, J. V. Olsen, M. Mann, *Science* **2009**, 325, 834.

[338] M. R. K. Ali, Y. Wu, T. Han, X. Zang, H. Xiao, Y. Tang, R. Wu, F. M. Fernandez, M. A. El-Sayed, *Journal of the American Chemical Society* **2016**.

[339] B. H. Mecham, P. S. Nelson, J. D. Storey, *Bioinformatics* **2010**, 26, 1308.

[340] R Core Team, R Foundation for Statistical Computing, 2016.

[341] M. A. Mackey, M. R. Ali, L. A. Austin, R. D. Near, M. A. El-Sayed, *The Journal of Physical Chemistry B* **2014**, 118, 1319.

[342] Y.-H. Kim, J. Jeon, S. H. Hong, W.-K. Rhim, Y.-S. Lee, H. Youn, J.-K. Chung, M. C. Lee, D. S. Lee, K. W. Kang, J.-M. Nam, *Small* **2011**, 7, 2052.

[343] S. Elmore, *Toxicologic pathology* **2007**, 35, 495.

[344] H. Guillou, A. Depraz-Depland, E. Planus, B. Vianaya, J. Chaussy, A. Grichine, C. Albiges-Rizo, M. R. Block, *Experimental Cell Research* **2008**, 314, 478.

[345] D. A. Lauffenburger, A. F. Horwitz, *Cell* **1996**, 84, 359; H. Yamaguchi, J. Condeelis, *Biochimica Et Biophysica Acta-Molecular Cell Research* **2007**, 1773, 642.

[346] W. T. Arthur, L. A. Petch, K. Burridge, *Curr Biol* **2000**, 10, 719.

[347] J. D. Hood, D. A. Cheresh, *Nature Reviews Cancer* **2002**, 2, 91; C. Huang, K. Jacobson, M. D. Schaller, *Journal of cell science* **2004**, 117, 4619.

[348] P. S. Chen, M. Y. Wang, S. N. Wu, J. L. Su, C. C. Hong, S. E. Chuang, M. W. Chen, K. T. Hua, Y. L. Wu, S. T. Cha, M. S. Babu, C. N. Chen, P. H. Lee, K. J. Chang, M. L. Kuo, *Journal of cell science* **2007**, 120, 2053.

[349] M. Canel, A. Serrels, M. C. Frame, V. G. Brunton, *Journal of cell science* **2013**, 126, 393.

[350] A. Chen, H. Beetham, M. A. Black, R. Priya, B. J. Telford, J. Guest, G. A. Wiggins, T. D. Godwin, A. S. Yap, P. J. Guilford, *BMC Cancer* **2014**, 14, 552.

[351] T. T. Onder, P. B. Gupta, S. A. Mani, J. Yang, E. S. Lander, R. A. Weinberg, *Cancer Res* **2008**, 68, 3645.

[352] M. Tamura, J. Gu, K. Matsumoto, S. Aota, R. Parsons, K. M. Yamada, *Science* **1998**, 280, 1614; D. Cai, S. C. Chen, M. Prasad, L. He, X. Wang, V. Choesmel-Cadamuro, J. K. Sawyer, G. Danuser, D. J. Montell, *Cell* **2014**, 157, 1146; J. G. Gu, M. Tamura, K. M. Yamada, *Journal of Cell Biology* **1998**, 143, 1375.

[353] S. Etienne-Manneville, A. Hall, *Nature* **2002**, 420, 629; A. J. Ridley, A. Hall, *Cell* **1992**, 70, 389; C. D. Nobes, A. Hall, *Cell* **1995**, 81, 53.

[354] P. Friedl, K. Wolf, *Nat Rev Cancer* **2003**, 3, 362; J. T. Parsons, A. R. Horwitz, M. A. Schwartz, *Nat Rev Mol Cell Biol* **2010**, 11, 633; S. J. Heasman, A. J. Ridley, *Nat Rev Mol Cell Biol* **2008**, 9, 690.

[355] P. Kanchanawong, G. Shtengel, A. M. Pasapera, E. B. Ramko, M. W. Davidson, H. F. Hess, C. M. Waterman, *Nature* **2010**, 468, 580.

[356] P. Friedl, D. Gilmour, *Nat Rev Mol Cell Biol* **2009**, 10, 445.

[357] J. Al-Bassam, R. S. Ozer, D. Safer, S. Halpain, R. A. Milligan, *Journal of Cell Biology* **2002**, 157, 1187.

[358] S. Etienne-Manneville, *Traffic* **2004**, 5, 470.

[359] I. Bock-Marquette, A. Saxena, M. D. White, J. M. DiMaio, D. Srivastava, *Nature* **2004**, 432, 466.

[360] Z. Yan, H. Yin, R. Wang, D. Wu, W. Sun, B. Liu, Q. Su, *Acta Histochemica* **2014**, 116, 527.

[361] F. Ciardiello, G. Tortora, *European Journal of Cancer* 39, 1348.

[362] Z. Zhong, Z. Wen, J. E. Darnell, Jr., *Science* **1994**, 264, 95.

[363] M. R. Ali, M. A. Rahman, Y. Wu, T. Han, X. Peng, M. A. Mackey, D. Wang, H. J. Shin, Z. G. Chen, H. Xiao, *Proceedings of the National Academy of Sciences* **2017**, 201619302.

[364] C. G. Galbraith, K. M. Yamada, J. A. Galbraith, *Science* **2007**, 315, 992; P. K. Mattila, P. Lappalainen, *Nature Reviews Molecular Cell Biology* **2008**, 9, 446.

[365] M. Ali, M. Rahman, Y. Wu, T. Han, M. Mackeya, M. Mackey, D. Wang, H. Shin, Z. Chen, H. Xiao, R. Wu, Y. Tang, D. Shin, M. El-Sayed, *Proceedings of the National Academy of Sciences of the United States of America* **2017**, 114, E3110.

[366] A. G. Clark, D. M. Vignjevic, *Curr Opin Cell Biol* **2015**, 36, 13.

[367] O. Ilina, P. Friedl, *J Cell Sci* **2009**, 122, 3203.

[368] B. Ladoux, R. M. Mège, *Nat Rev Mol Cell Biol* **2017**, 18, 743.

[369] C. De Pascalis, S. Etienne-Manneville, *Mol Biol Cell* **2017**, 28, 1833.

[370] C. Bertocchi, M. Vaman Rao, R. Zaidel-Bar, *J Signal Transduct* **2012**, 2012, 125295; S. M. Ritchie, N. H. Battery, *Phosphorylation and the Cytoskeleton*, Springer, **1996**.

[371] A. Grada, M. Otero-Vinas, F. Prieto-Castrillo, Z. Obagi, V. Falanga, *J Invest Dermatol* **2017**, 137, e11.

[372] T. Sun, M. Rodriguez, L. Kim, *Dev Growth Differ* **2009**, 51, 735.

[373] A. Efimov, N. Schiefermeier, I. Grigoriev, R. Ohi, M. C. Brown, C. E. Turner, J. V. Small, I. Kaverina, *J Cell Sci* **2008**, 121, 196; T. K. Kwak, M. S. Lee, J. Ryu, Y. J. Choi, M. Kang, D. Jeong, J. W. Lee, *J Biol Chem* **2012**, 287, 27499.

[374] N. G. Dulyaninova, R. P. House, V. Betapudi, A. R. Bresnick, *Mol Biol Cell* **2007**, 18, 3144.

[375] A. Zagórska, M. Deak, D. G. Campbell, S. Banerjee, M. Hirano, S. Aizawa, A. R. Prescott, D. R. Alessi, *Sci Signal* **2010**, 3, ra25.

[376] Y. T. Wang, C. F. Tsai, T. C. Hong, C. C. Tsou, P. Y. Lin, S. H. Pan, T. M. Hong, P. C. Yang, T. Y. Sung, W. L. Hsu, Y. J. Chen, *J Proteome Res* **2010**, 9, 5582.

[377] H. Kitazawa, J. Iida, A. Uchida, K. Haino-Fukushima, T. J. Itoh, H. Hotani, K. Ookata, H. Murofushi, J. C. Bulinski, T. Kishimoto, S. Hisanaga, *Cell Struct Funct* **2000**, 25, 33.

[378] A. Hartsock, W. J. Nelson, *Biochim Biophys Acta* **2008**, 1778, 660.

[379] H. Ji, J. Wang, H. Nika, D. Hawke, S. Keezer, Q. Ge, B. Fang, X. Fang, D. Fang, D. W. Litchfield, K. Aldape, Z. Lu, *Mol Cell* **2009**, 36, 547.

[380] C. Zihni, C. Mills, K. Matter, M. S. Balda, *Nat Rev Mol Cell Biol* **2016**, 17, 564.

[381] M. G. Mendez, S. Kojima, R. D. Goldman, *FASEB J* **2010**, 24, 1838.

[382] Q. F. Li, A. M. Spinelli, R. Wang, Y. Anfinogenova, H. A. Singer, D. D. Tang, *J Biol Chem* **2006**, 281, 34716.

[383] E. W. Flitney, E. R. Kuczmarski, S. A. Adam, R. D. Goldman, *FASEB J* **2009**, 23, 2110; P. S. Kakade, S. Budnar, R. D. Kalraiya, M. M. Vaidya, *J Biol Chem* **2016**, 291, 12003; N. O. Ku, S. Michie, E. Z. Resurreccion, R. L. Broome, M. B. Omary, *Proc Natl Acad Sci U S A* **2002**, 99, 4373; C. Stumptner, M. B. Omary, P. Fickert, H. Denk, K. Zatloukal, *Am J Pathol* **2000**, 156, 77.

[384] R. L. Juliano, *Annu Rev Pharmacol Toxicol* **2002**, 42, 283.

[385] G. F. Weber, M. A. Bjerke, D. W. DeSimone, *J Cell Sci* **2011**, 124, 1183; K. L. Mui, C. S. Chen, R. K. Assoian, *J Cell Sci* **2016**, 129, 1093.

[386] H. Yano, Y. Mazaki, K. Kurokawa, S. K. Hanks, M. Matsuda, H. Sabe, *J Cell Biol* **2004**, 166, 283.

[387] R. Desai, R. Sarpal, N. Ishiyama, M. Pellikka, M. Ikura, U. Tepass, *Nat Cell Biol* **2013**, 15, 261.

[388] S. Boguslavsky, I. Grosheva, E. Landau, M. Shtutman, M. Cohen, K. Arnold, E. Feinstein, B. Geiger, A. Bershadsky, *Proc Natl Acad Sci U S A* **2007**, 104, 10882.

[389] P. Pandya, J. L. Orgaz, V. Sanz-Moreno, *Curr Opin Cell Biol* **2017**, 48, 87.

[390] R. M. Mège, J. Gavard, M. Lambert, *Curr Opin Cell Biol* **2006**, 18, 541.

[391] R. B. Hazan, L. Kang, B. P. Whooley, P. I. Borgen, *Cell Adhes Commun* **1997**, 4, 399.

[392] R. B. Hazan, G. R. Phillips, R. F. Qiao, L. Norton, S. A. Aaronson, *J Cell Biol* **2000**, 148, 779.

[393] W. Shih, S. Yamada, *J Cell Sci* **2012**, 125, 3661.

[394] W. Shih, S. Yamada, *Cell Adh Migr* **2012**, 6, 513.

[395] T. A. Martin, W. G. Jiang, *Histol Histopathol* **2001**, 16, 1183; A. B. Singh, A. Sharma, P. Dhawan, *J Oncol* **2010**, 2010, 541957.

[396] G. Mandicourt, S. Iden, K. Ebnet, M. Aurrand-Lions, B. A. Imhof, *J Biol Chem* **2007**, 282, 1830; G. S. Karagiannis, D. F. Schaeffer, C. K. Cho, N. Musrap, P. Saraon, I. Batruch, A. Grin, B. Mitrovic, R. Kirsch, R. H. Riddell, E. P. Diamandis, *Mol Oncol* **2014**, 8, 178.

[397] V. González-Tarragó, A. Elosegui-Artola, E. Bazellières, R. Oria, C. Pérez-González, P. Roca-Cusachs, *Mol Biol Cell* **2017**, 28, 1847; S. Tuomi, A. Mai, J. Nevo, J. O. Laine, V. Vilkki, T. J. Ohman, C. G. Gahmberg, P. J. Parker, J. Ivaska, *Sci Signal* **2009**, 2, ra32.

[398] A. S. Fanning, C. M. Van Itallie, J. M. Anderson, *Mol Biol Cell* **2012**, 23, 577.

[399] S. Bhattacharya, M. Ahir, P. Patra, S. Mukherjee, S. Ghosh, M. Mazumdar, S. Chattopadhyay, T. Das, D. Chattopadhyay, A. Adhikary, *Biomaterials* **2015**, 51, 91; Y. Zhang, L. Hu, D. Yu, C. Gao, *Biomaterials* **2010**, 31, 8465.

[400] E. H. Barriga, K. Franze, G. Charras, R. Mayor, *Nature* **2018**, 554, 523; D. Cai, W. Dai, M. Prasad, J. Luo, N. S. Gov, D. J. Montell, *Proc Natl Acad Sci U S A* **2016**, 113, E2134.

[401] X. Trepat, M. Wasserman, T. Angelini, E. Millet, D. Weitz, J. Butler, J. Fredberg, *Nature Physics* **2009**, 5, 426; S. R. Vedula, M. C. Leong, T. L. Lai, P. Hersen, A. J. Kabla, C. T. Lim, B. Ladoux, *Proc Natl Acad Sci U S A* **2012**, 109, 12974.

[402] S. Kuriyama, M. Yoshida, S. Yano, N. Aiba, T. Kohno, Y. Minamiya, A. Goto, M. Tanaka, *Oncogene* **2016**, 35, 952.

[403] D. Zhang, F. Feng, Q. Li, X. Wang, L. Yao, *Biomaterials* **2018**, 173, 22.

[404] P. J. Boersema, R. Raijmakers, S. Lemeer, S. Mohammed, A. J. Heck, *Nat Protoc* **2009**, 4, 484.

[405] B. H. Mecham, P. S. Nelson, J. D. Storey, *Bioinformatics* **2010**, 26, 1308.

[406] I. H. El-Sayed, X. Huang, M. A. El-Sayed, *Cancer Lett* **2006**, 239, 129.

[407] M. Perez-Hernandez, P. Del Pino, S. G. Mitchell, M. Moros, G. Stepien, B. Pelaz, W. J. Parak, E. M. Galvez, J. Pardo, J. M. de la Fuente, *ACS Nano* **2015**, 9, 52.

[408] P. Orosz, B. Echtenacher, W. Falk, J. Ruschoff, D. Weber, D. N. Mannel, *J Exp Med* **1993**, 177, 1391; J. R. Melamed, R. S. Edelstein, E. S. Day, *ACS Nano* **2015**, 9, 6.

[409] E. B. Dickerson, E. C. Dreaden, X. Huang, I. H. El-Sayed, H. Chu, S. Pushpanketh, J. F. McDonald, M. A. El-Sayed, *Cancer Lett* **2008**, 269, 57.

[410] Y. Wu, M. R. K. Ali, B. Dong, T. Han, K. Chen, J. Chen, Y. Tang, N. Fang, F. Wang, M. A. El-Sayed, *ACS Nano* **2018**, 12, 9279.

[411] S. Tohme, R. L. Simmons, A. Tsung, *Cancer Res* **2017**, 77, 1548.

[412] M. Potente, H. Gerhardt, P. Carmeliet, *Cell* **2011**, 146, 873.

[413] Y. Park, T. Kitahara, R. Takagi, R. Kato, *Oncology* **2011**, 81, 199.

[414] H. Farghali, N. AbdElKader, M. Khattab, H. AbuBakr, *Stem Cell Research & Therapy* **2017**, 8.

[415] H. Farghali, N. AbdElKader, M. Khattab, H. AbuBakr, *Bioscience Reports* **2017**, 37.

[416] M. A. Mackey, M. R. Ali, L. A. Austin, R. D. Near, M. A. El-Sayed, *J Phys Chem B* **2014**, 118, 1319.

[417] J. A. Tate, A. A. Petryk, A. J. Giustini, P. J. Hoopes, *Proc SPIE Int Soc Opt Eng* **2011**, 7901, 790117; D. Elgrabli, R. Beaudouin, N. Jbilou, M. Floriani, A. Pery, F. Rogerieux, G. Lacroix, *PLoS One* **2015**, 10, e0124490; X. Sun, J. Shi, X. Fu, Y. Yang, H. Zhang, *Sci Rep* **2018**, 8, 10595; L. Yang, H. Kuang, W. Zhang, Z. Aguilar, H. Wei, H. Xu, *Scientific Reports* **2017**, 7.

[418] R. R. Arvizo, S. Rana, O. R. Miranda, R. Bhattacharya, V. M. Rotello, P. Mukherjee, *Nanomedicine* **2011**, 7, 580; M. Wu, Y. Zhang, Y. Zhang, M. Wu, M. Wu, H. Wu, L. Cao, L. Li, X. Li, X. Zhang, *Rsc Advances* **2018**, 8, 1706.

[419] M. I. Setyawati, C. Y. Tay, B. H. Bay, D. T. Leong, *ACS Nano* **2017**, 11, 5020.

[420] K. Greish, *Methods Mol Biol* **2010**, 624, 25.

[421] J. A. Krall, F. Reinhardt, O. A. Mercury, D. R. Pattabiraman, M. W. Brooks, M. Dougan, A. W. Lambert, B. Bierie, H. L. Ploegh, S. K. Dougan, R. A. Weinberg, *Sci Transl Med* **2018**, 10.

[422] W. Chen, J. M. Smeekens, R. Wu, *Chemical Science* **2016**, 7, 1393.

[423] J. K. Eng, A. L. McCormack, J. R. Yates, *J Am Soc Mass Spectrom* **1994**, 5, 976.

[424] J. E. Elias, S. P. Gygi, *Nat Methods* **2007**, 4, 207; J. Peng, J. E. Elias, C. C. Thoreen, L. J. Licklider, S. P. Gygi, *J Proteome Res* **2003**, 2, 43.

[425] E. L. Huttlin, M. P. Jedrychowski, J. E. Elias, T. Goswami, R. Rad, S. A. Beausoleil, J. Villen, W. Haas, M. E. Sowa, S. P. Gygi, *Cell* **2010**, 143, 1174.

[426] M. E. Ritchie, B. Phipson, D. Wu, Y. Hu, C. W. Law, W. Shi, G. K. Smyth, *Nucleic Acids Res* **2015**, 43, e47.

VITA

YUE WU

YUE WU was born Mar 8, 1989 in Zhejiang, China. She received her B.S. in chemistry from Zhejiang University of Technology, China in 2007 and M.S. in analytical chemistry from Dalian Institute of Chemical Physics, Chinese Academy of Sciences in 2011. She is currently pursuing a PhD in chemistry at Georgia Institute of Technology under the supervision of Professor Mostafa A. El-Sayed. Her current research focuses on the development of gold nanomaterials for applications related with cancer treatment and biological optical imaging.